THE CATHOLIC UNIVERSITY OF AMERICA

A Quantitative Analysis of Star-Forming Galaxies at Intermediate Redshifts: Number Counts, Morphological Sequences, and Evolutionary Timescales

A DISSERTATION

Submitted to Faculty of the

Department of Physics

School of Arts and Sciences

Of The Catholic University of America

In Partial Fulfillment of the Requirements

For the Degree

Doctor of Philosophy

By

Elysse Nicole Voyer

Washington, D.C.

2011

A Quantitative Analysis of Star-Forming Galaxies at Intermediate Redshifts: Number Counts, Morphological Sequences, and Evolutionary Timescales

Elysse Nicole Voyer, Ph.D.

Director: Duilia F. de Mello, Ph.D.

How did local galaxies obtain their Hubble morphologies and to what effect did star formation drive the transformations of past galaxies into these Hubble types? To answer these questions, galaxies at different epochs must be untangled from deep imaging and pieced together to analyze their evolution over time. This thesis probes an epoch when the Universe experienced a sharp decline in star-formation-rate density $\sim$4.6Gyr ago, i.e. intermediate redshifts ($0.2<z<1.2$). Multiwavelength data was used to detect and analyze rest-frame ultraviolet (UV) star-forming galaxies in order to to establish what types of galaxies were forming stars during this time, and detect evolution within and between these galaxies populations.

First, an initial study on UV galaxies in the Hubble Ultra Deep Field (HUDF) is performed. A photometric catalog of 96 sources in first targeted space-based U-band image of the HUDF is produced. By matching this with other catalogs, optical photometry, redshifts, spectral types (STs), and visual morphologies are obtained. This reveals that the majority of galaxies have spiral visual morphologies that are split between STs of late-type spirals and starburst galaxies. When compared to more distant star-forming Lyman Break Galaxies (LBGs) and their local counterparts, the sample is 14% less luminous. No evolution is detected in the overall galaxy sizes, however sub-galactic clumps are found to increase in size by a factor of 2–3.5 from high- to intermediate-z.

Expanding upon this study, a sample of 333 far-UV (FUV) sources are detected in imaging of Great Observatories Origins Deep Survey -North and -South fields. FUV number counts are measured, covering 4 times larger area than the most recent study at these wavelengths (1610Å) and magnitudes (21–29), reducing cosmic variance effects. Moreover, the extragalactic background light was measured and found unlikely

to be greater than 100 photons/cm^2/s/sr/Å.

Finally, an analysis of the optical morphologies of the FUV sample is presented based on measurements of their STs and light profiles as a function of radius (Sérsic index). Results show star formation was primarily occurring in disk and merger morphologies over $0.1<z<1.2$. Additionally, galaxies with irregular and spiral STs demonstrate a good correlation with Sérsic index.

This dissertation by Elysse Nicole Voyer fulfills the dissertation requirement for the doctoral degree in Physics approved by Duilia F. de Mello, Ph.D., as Director and by Steven B. Kraemer, Ph.D., and Jonathan P. Gardner, Ph.D. as Readers.

Duilia F. de Mello, Ph.D., Director

Steven B. Kraemer, Ph.D., Reader

Jonathan P. Gardner, Ph.D., Reader

To the memory of my mother,

Patricia Ann Kammes

Contents

List of Figures

List of Tables

Acknowledgements

I am eternally grateful to my advisor, Dr. Duilia de Mello, for all of the wisdom, guidance, and education she has provided to me over the past four years as her student. The joy that she obtains from her profession will always radiate to those around her, inspiring them to learn about the Universe as she has inspired me. She has taught me how to grow as a scientist and how to believe in my own abilities. *Muito Obrigada!* I am also very thankful to my NASA GSRP technical advisor, Dr. Jonathan Gardner, who has worked with me on much of this thesis for the past three years at Goddard Space Flight Center. It has been a privilege to learn from him and to be a part of the NASA community.

I want to thank those who I have collaborated with in the process of this thesis work. Thank you to Dr. Harry Teplitz for providing the HST ultraviolet imaging that has been the foundation of my research, as well as for many helpful conversations on my analysis. Thank you to Dr. Brian Siana for his collaborative effort in working on these data with me and for all of his suggestions for the improvement of this work down to the very fine details. Finally, thank you to Sandra Blevins for her hard work on the final research for this thesis and for her wonderful friendship and eternally positive attitude towards all things in life that has helped uplift me over the past year.

A very sincere thank you to the faculty and staff of the Catholic University department of Physics, it has been a pleasure to work with you and learn from you as a graduate student. In particular, I would like to thank Drs. Steven Kraemer and Fred Bruhweiler for teaching me about the 'physics' in astrophysics, for always challenging me to learn, and for believing in my capabilities.

Thank you to my colleagues and friends at NASA's GSFC, Drs. Antara Basu-Zych, Ann Hornschemeier, Leigh Jenkins, Bret Lehmer, Amber Straughn, Panayiotis Tzanavaris, and Derek Hammer. I have greatly enjoyed our weekly galaxy discussion group over the past few years. Thank you for making science fun!

I would like to thank Yaireska Collado-Vega for her amazing friendship and support throughout our years together in graduate school. She has helped me to survive this difficult journey. Much love and gratitude. I would also like to express deep thanks to Dr. Sara Petty for her unwavering guidance and friendship. Also thank you to my dear friends, Sarah, Christina, Maria, Jen, Kathleen, Rafael, Andreza, and

Javier for their friendship and encouragement during this process. I would like to thank my family for their truly unconditional love and support in choosing this path for my life and career.

To my amazing fiancé and best friend, Ryan, there are no words for how you've helped and supported me over the past 5 years during graduate school and during our time as undergraduates. I will always love you and be here for you.

Much gratitude and thanks to the New Mexico State University Astronomy Department for providing me with office space and computer resources during the final stages of writing this thesis.

This work has been supported by NASA Graduate Student Research Program Fellowship grant.

1

Introduction

One of the foremost questions being asked by modern astronomy is how and when galaxies obtained the morphologies that Edwin Hubble originally divided in four visual classes: elliptical, lenticular, spiral, and irregular (Hubble, 1936). Recent engineering and technological advances in ground and space-based astronomical instrumentation have facilitated large observational surveys that have produced a much deeper view of the universe than ever before over the entire electromagnetic spectrum. These data have shown that not all galaxies fit within the standard Hubble classifications. For example, many galaxies are interacting, live in groups and clusters, have tidal tails and extended halos. They collide, transform, and merge during their evolution, existing beyond the original Hubble sequence. Studies of galaxy evolution are critical because they allow us to test the evolution of the universe itself, improving our understanding of how the universe has matured since the Big Bang. However, it is not possible to directly see how galaxies assemble, grow, and age. Epochs of different galaxies must be untangled from deep imaging and pieced together sequentially in order to analyze their evolution over time.

1.1 The Historical Origins of Extragalactic Astronomy

It was not until the early 18th century that philosophers and scientists began to speculate on the idea that our solar system exists within a larger aggregation of stars, i.e. the Milky Way, and that other such systems may exist outside its bounds, i.e. galaxies. "Island Universe" was the term coined by German philosopher Immanuel Kant in the mid-18th century to describe the faint nebulae observed in the nighttime sky. Along with English astronomer, Thomas Wright, Kant hypothesized that some of these "nebulae" actually existed outside of the Milky Way galaxy as independent conglomerates of stars. Physical evidence for these philosophical predictions first arrived with the observations of comet hunter Charles Messier when he recorded 103 of the brightest nebulae including several galaxies such as our nearest neighbor, the Andromeda galaxy in his *Catalog of Nebulae and Star Clusters*. Inspired by this work, Sir William Herschel, together with his sister Caroline Herschel, observed and cataloged $\sim$2500 nebulae by the beginning of the 19th century. However, it was not until the mid-19th century that William Parsons discovered distinct spiral structure in several nebulae using his 72$''$ "Leviathan " telescope located in Ireland. Individual stars were not yet resolvable in these sources, and so it remained an open question as to the nature of these spiral nebulae. Nearly twenty years later through spectroscopic observations Sir William Huggins determined that diffuse nebulae could be divided into two categories, those with emission line features (later determined to be planetary nebulae within our own Galaxy) and those with spectra similar to stars. All observed spiral nebulae fit into the second category imparting the first viable evidence of the "Island Universes" theory - that spiral nebulae are in fact other galaxies exterior to our own.

When photographic methods were adopted for astronomical observations during the turn of the 20th century more detailed studies of spiral morphologies were carried out. Furthermore, many spectral studies of spirals, the most notable done by American astronomer Vesto Slipher in 1912, were detecting Doppler shifts in their spectral features yielding measurements of both radial and rotational velocities. The

measured radial velocities were positive (i.e redshifted) indicating overall recessional motion and had magnitudes much greater than what had been measured for stellar sources, indicating that the spirals were not gravitationally bound and thus not permanent components of the Milky Way. However, not all astronomers felt these data were compelling enough to solidify the universal nature of spiral nebulae, particularly because the nature of our own galaxy was still undetermined. In 1920 a "Great Debate" on the scale of the Universe was held at the Smithsonian Museum of Natural History in Washington, D.C between astronomers Harlow Shapley and Herber Curtis. Shapley argued that spiral nebulae were part of the Milky Way and that the Milky Way spanned the entire universe, while Curtis claimed that the universe was made up of many spiral nebulae, including the Milky Way. Since both sides lacked sound evidence, the debate was not settled until three years later when Edwin Hubble observed the Andromeda galaxy (M31) with the 100″ telescope at the Mount Wilson Observatory and distinguished individual stars within the nebulae including several Cepheid variables. The strict relationship between the pulsation period and the luminosity of Cepheids together with their apparent brightness allow for the determination of their distances. Thus, Hubble was able to establish the distance to Andromeda, discovering it was much larger than the size of the Milky Way, and therefore was an extragalactic source.

Hubble's discovery paved the way for a new exciting area of extragalactic astronomical research that would fundamentally change our view of the universe. In the 1926 paper *Extra-Galactic Nebulae* and later in the book *The Realm of Nebulae* (1936) Hubble mapped out the morphologies of the numerous galaxies he had observed onto a "tuning-fork diagram" of ellipticals, spirals, and irregulars, and believing it may represent a potential linear sequence of evolution (Figure 1.1). Elliptical morphologies were placed towards the left side of the sequence and were categorized as "early-types" while morphologies of an increasing spiral nature were placed towards the right of the sequence and categorized as "late-types". The actual "fork" occurs where spiral sources diverge into barred and unbarred populations. These terminologies are still commonly used in modern extragalactic research, although it

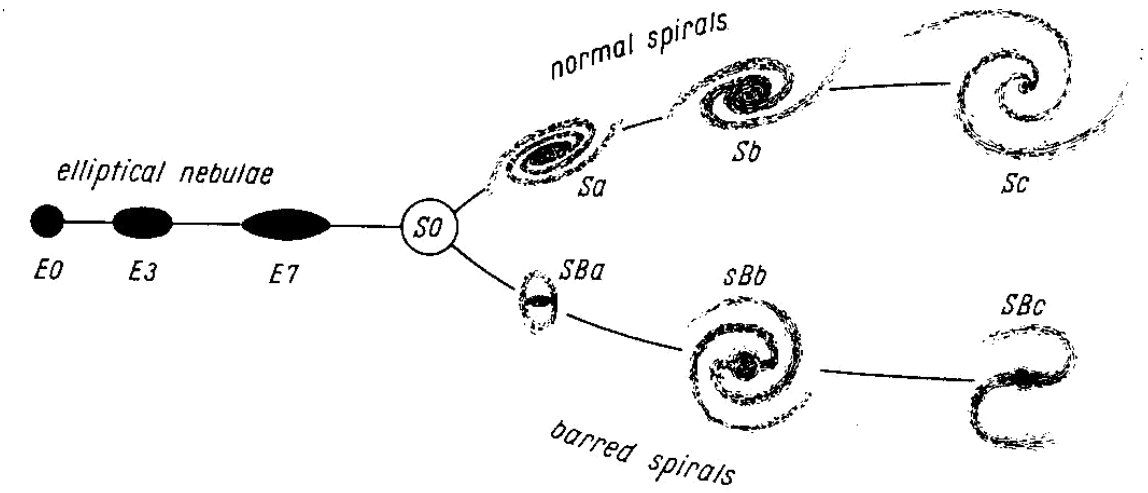

Figure 1.1 *Hubble "tuning-fork" diagram including the S0 type (Hubble, 1936).*

is now understood that the progression on the tuning-fork has no realistic bearings on the actual evolution of galaxies which is much more complex and intricate than originally hypothesized by Hubble. Several researchers continued with this type of morphological work dividing and expanding upon the initial Hubble sequence. In his work, Erik Holmberg discovered galaxies could be subdivided within their Hubble classifications by their apparent color indices (Holmberg, 1958). Different colors represent different stellar populations within a galaxy. Holmberg demonstrated that the colors of galaxies changed sequentially from red ellipticals to various degrees of blue spirals along the Hubble sequence, thus indicating that morphology is correlated to the mean age of the stars within a galaxy. Gérard De Vaucouleurs divided spirals into a more complex classification, removed two irregular subtypes, and added galaxies with ring-like structure to the Hubble sequence (de Vaucouleurs, 1959). Sydney van den Bergh used observations from the Palomar Sky Survey to study the relationship between morphology and luminosity of a galaxy, breaking down Hubble's spiral bins using additional luminosity class parameters (van den Bergh, 1960a,b). Others developed systems based upon spectral classifications that showed correlations with both Hubble and de Vaucouleurs classifications (Morgan, 1958, 1959a,b; Morgan & Osterbrock, 1969). Peculiar systems of irregular and interacting galaxies were first

largely cataloged by Arp (1966) in his *Atlas of Peculiar Galaxies*. He surmised that these visual laboratories could contain evidence towards the formation mechanisms of regular Hubble types. An even more extensive catalog of ∼850 interacting systems was compiled by Russian astronomer Vorontsov-Velyaminov, as well as a larger four volume catalog of 29,000 galaxies of all types, *The Morphological Catalog of Galaxies*, based on the Palomar Sky Survey plates (Vorontsov-Vel'Yaminov, 1959; Vorontsov-Vel'Yaminov & Krasnogorskaya, 1962; Vorontsov-Vel'Yaminov & Arkhipova, 1963, 1968, 1974; Vorontsov-Velyaminov, 1977).

Despite the unarguable scientific impact of early morphological research, it is important to understand the caveats of this work. All early visual classifications schemes were done based on visible wavelengths that probe the main sequence stellar content together with emission from the gas and dust of a galaxy. Optical data provide an overall view of extragalactic sources, but miss information about other galactic components and features that reveal themselves at both bluer and redder wavelengths. Additionally, due to the technological limitations of the times, these classification schemes were based upon galaxies at relatively close proximity to the Milky Way leaving out fainter more distant galaxies that existed at earlier times in the universe. Several additional important correlations between the physical properties of galaxies and their morphologies along the Hubble sequence are discussed in the review by Roberts & Haynes (1994), including optical linear size, optical luminosity functions, optical surface brightness, far infrared flux, X-ray emission, neutral hydrogen (HI) mass and content, and regions of ionized hydrogen (i.e., HII regions).

1.1.1 Modern Galaxy Surveys

The remarkable advancements in optics and engineering throughout the 20th century have delivered a deeper and more diverse view of the universe that has decisively transformed our understanding of galactic structure and evolution. These include the ability to launch observatories above the Earth's atmosphere and the advent of 8-10 meter ground based telescopes. Astronomers have conducted large scale mul-

tiwavelength surveys that probe deeper than ever before into the current state and past histories of galaxies over the entire electromagnetic spectrum. NASA's four "Great Observatories", the Hubble Space Telescope (HST), the Compton Gama Ray Observatory (CRO), the Chandra X-ray Observatory (CXO), and the Spitzer Space Telescope, have produced some of the highest quality space-based data ever taken at a multitude of wavelengths. HST is equipped with detectors covering ultraviolet (UV), optical, and near-infrared (IR) wavelengths. It has been used to conduct several modern astronomical surveys including the Hubble Deep Fields (HDF; Williams et al., 1996), the Great Observatories Origins Deep Survey (GOODS; Giavalisco et al., 2004), Galaxy Evolution From Morphology And SEDs (GEMS; Rix et al., 2004), the Hubble Ultra Deep Field (HUDF; Beckwith et al., 2006), the Cosmological Evolution Survey (COSMOS; Scoville et al., 2007), and the currently ongoing Cosmic Assembly Near-infrared Deep Extragalactic Legacy Survey (CANDELS; P.I.'s S. Faber and H. Ferguson). CXO has produced two deep X-ray surveys of the Chandra Deep Fields-North and -South (CDF-N & -S Alexander et al., 2003; Giacconi et al., 2001) and Spitzer has covered several of these survey fields in mid- to far-IR wavelengths as well as completing independent IR surveys. From the ground, several large telescopes have contributed largely to optical and near-IR imaging and spectroscopy. These include including Keck, the European Southern Observatory Very Large Telescopes (VLTs), Gemini-North & -South, the National Observatory of Japan's Subaru telescope, the Hobby-Eberly Telescope, and the Large Binocular Telescope. Two examples of extensive spectroscopic surveys carried out by these instruments are the Deep Evolutionary Extragalactic Probe surveys (DEEP; Koo, 1998) on Keck and the VIMOS VLT Deep Survey (VVDS; Le Fèvre et al., 2004).

With the wide range of data delivered by these modern observatories it has been possible to resolve the details of the morphological, dynamical, kinematic, and chemical characteristics of galaxies over multiple wavelengths and redshifts from both imaging and spectroscopic observations. These data have revealed distant galaxies that are the progenitors of the local Hubble types. They have discovered that the appearance of galaxies changes with different wavelengths of light, and that the in-

tensity and spatial distribution of emissions at different wavelengths vary with galaxy morphology. Thus, it has become critical to make quantitative connections between galaxy properties at local and earlier epochs to formulate and confirm theories of the galaxy evolution scenario.

1.2 Galaxies Across the Electromagnetic Spectrum

Before probing into the past histories of galaxies, it is important to understand their characteristics at the present epoch. A basic understanding of the features of galaxies over multiple wavelengths has been derived from observational analysis of the local populations (Figure 1.2). Radio observations reveal both neutral hydrogen (HI) 21-cm line regions and high-energy synchrotron processes in galaxies. The latter is detected in most types of "active galaxies", while the former is the cold fuel of star formation and can be found in different morphological types at low and high redshift. Submillimeter and far- to mid-infrared (IR) detections primarily reveal thermal dust grain emission within galaxies either due to re-processing of radiation from young stars at shorter wavelengths (such as optical and ultraviolet). Observations in the near-IR are sensitive to the older, redder, stars populating galaxies and thus the integrated near-IR emission is one of the best tracers of total underlying stellar mass. The ultraviolet (UV) radiation from galaxies reveals the most recent episodes of star formation that are unobscured by gas and dust as well as activity from active galactic nuclei (AGN). X-ray observations are associate with extremely hot interstellar and intergalactic gas, discrete stellar systems such as X-ray binaries, and emission from the inner accretion regions around black holes in the central regions of galaxies. At the shortest observable wavelengths gamma ray radiation has detected beams from rotating neutron stars, high-energy jets emanating from the central regions of galaxies, and the bursting deaths of massive stars.

Observed features of local galaxies are typically described as seen at rest-frame wavelengths, i.e. light observed at the same frequency at which it was emitted. However, when viewing deeper observations of the extragalactic universe, the light we

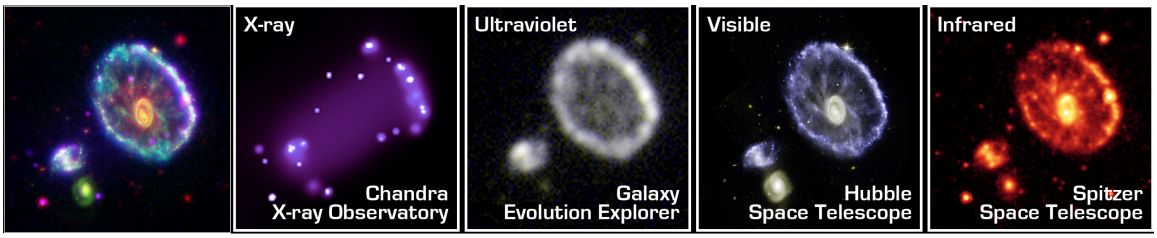

Figure 1.2 *The Cartwheel galaxy in X-ray to IR wavelengths with a composite image on the far left. Images are credited to NASA/JPL-Caltech/P. N. Appleton (SSC-Caltech).*

observe is no longer in the rest-frame, but has been "band-shifted" towards longer, redder, wavelengths as galaxies recede away from us. This is commonly known in physics as a Doppler effect and is described mathematically as,

$$\lambda_{observed} = (1 + z)\lambda_{emitted} \tag{1.1}$$

Here, "z" is defined as the cosmological redshift of the receding source and is equal to its recessional velocity over the speed of light for non-relativistic speeds (i.e. speeds $\ll$ the speed of light, c). If the source were moving relativistically (a large fraction of c) special relativity considerations would need to be accounted for in the redshift measurement. In flat Minkowski space-time the redshift equation is affected by time dilation of a relativistic source as viewed by an observer. The derived expression for time dilation,

$$t_o = \frac{t_{restframe}}{\sqrt{1 - \frac{v^2}{c^2}}} \tag{1.2}$$

is based upon the postulate that the speed of light must remain constant in all rest-frames. As, a result time in a given rest-frame as viewed by an observer moving away at some velocity, v, is measured as being longer than what is measured in the rest-frame itself. The resulting relativistic cosmological redshift can be derived as,

$$z_{rel} = \sqrt{\frac{1 + \frac{v}{c}}{1 - \frac{v}{c}}} - 1 \tag{1.3}$$

where, v/c is the Lorentz factor commonly noted as β in relativity theory.

When observing galaxies at higher redshifts astronomers must take care to understand and interpret the observed data in the rest-frame. In deep surveys of galaxies, such as those done by HST, it is critical to have redshift information on the observed sources in order to place them at the correct rest-frame. Usually photometric analysis is the preferred method for deriving redshifts since the process uses observing time than taking individual spectra of thousands of sources to determine shifts in spectral lines. If surveys are preformed in multiple broadband colors the photometry for each source at several wavelengths can be fit to Doppler-shifted synthetic spectral energy distributions (SEDs) to determine the photometric redshifts for large data sets.

1.3 Theoretical Scenarios of Galaxy Evolution

Conflicting theories of overall galaxy evolution have emerged and continuously develop with the flow of observational and theoretical research. Currently, there are two main competing models of galaxy evolution proposed in the literature (Figure 1.3). The monolithic collapse scenario predicts that galaxies were formed after an initial free fall collapse of gas clouds that continued to evolve quiescently (i.e. not involving any sort of interactions from other bodies), forming spiral galaxies through gas accretion if supported by rotation, and ellipticals otherwise (Eggen et al., 1962; Larson, 1974; Arimoto & Yoshii, 1987; Chiosi et al., 1994). Alternatively, the theory of hierarchical formation is largely based on lambda-cold-dark-matter (ΛCDM) cosmological simulations. Big Bang cosmology leads to the derivation of the flat ΛCDM governed Universe (i.e. the "standard model") which includes dark energy as denoted by the cosmological constant, Λ. This quantity is used to mathematically explain the acceleration of expanding space that has been observed observationally from distant supernova explosions. Within this cosmology, hierarchical formation predicts that smaller mass galaxies formed first and acted as the building blocks of higher mass galaxies (such as giant ellipticals) merging together over time (Kauffmann & Charlot, 1998; Kitzbichler & White, 2007). The end state of a galaxy is then determined by

its history of merger events. In addition, a third scenario, known as secular evolution, has recently become favored to explain the formation of disk galaxies at specific epochs in such a way that the formation is internally regulated, thus removing the need for merging events and/or a merging history (Kormendy & Kennicutt, 2004; Combes, 2010). Certainly, the overall formation history of galaxies is not so clear-cut as to fit neatly into one scenario or another. In order to sort out these theories the predictions of each scenario must be explored observationally.

1.4 The Star-Formation Rate Density of the Universe

Star formation is one of the primary drivers of galaxy evolution over cosmic time and has thus become the focus of much observational research aimed to probe this evolution. Great efforts have been poured into analyzing the star-formation rates (SFR) from various populations of galaxies at both high and low redshifts in order to assemble a picture of the cosmic SFR density history of the universe, i.e. mass per unit time per unit volume as a function of redshift or look-back time. The basic recipe for constructing a piece of this picture is as follows: first, star-formation sensitive data of several galaxies with known or derivable redshifts must be assembled. Next, the intrinsic luminosity of each source can be determined from its measured flux and redshift, and the luminosity function of the sample is formulated (i.e. the relative number of galaxies at each luminosity as a function of apparent magnitude). The luminosity function is then converted to a function of SFR through a relation that has been derived from models simulating the stellar population synthesis for similar types of galaxies (Kennicutt, 1998). Lastly, the SFR density is calculated by integrating under the SFR function to attain the final volume information. This integrated value is plotted at the center of the redshift bin. A quest to pepper the SFR density plot with measurements in order to assemble the most accurate possible star-formation history has been undertaken by numerous research groups. Each approach this task through different galaxy demographics and targeted redshift ranges.

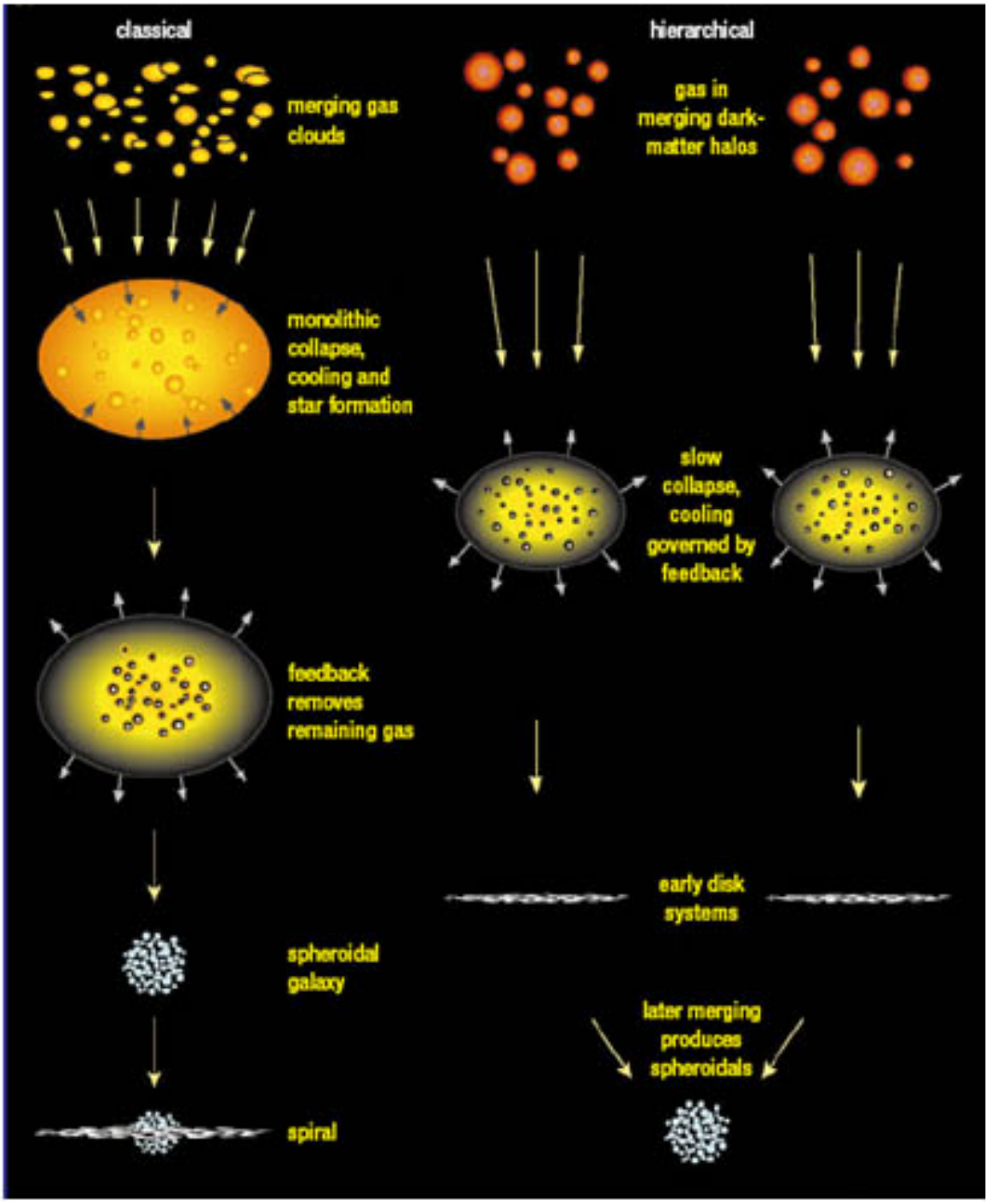

Figure 1.3 *Cartoon of the monolithic (or classic) collapse (left) and hierarchical formation (right) scenarios (Ellis et al., 2000).*

Lilly et al. (1996) determined the SFRs in three bands (2800Å, 4400Å, 1μm) for a large sample of i-band selected galaxies from $0 < z < 1$ in the Canada-France-Hawaii Redshift Survey. Soon after, Madau et al. (1996) compiled this data, along with their own for ranges of $2 < z < 3.4$ and $3.5 < z < 4.5$, into the Madau-Lilly plot (Figure 1.4). This was the first SFR density compilation to show data for $z \gtrsim 1$, revealing that the SFR density steadily built up until $z \sim 1$ after which there was a sharp decline to local epochs. The Madau et al. study used a sample of star-forming Lyman break, or "drop-out", galaxies (LBGs) to make these measurements. This nomenclature results from the technique used to detect LBGs developed by several authors in anticipation of the HDF data sets (Steidel & Hamilton, 1992, 1993; Yoshii & Peterson, 1994; Madau, 1995; Steidel et al., 1995). Light short-ward of the Lyman break (912Å) in a galaxy spectrum is used up in ionizing any neutral-hydrogen gas in the interstellar and intergalactic medium between the star-forming galaxy and the observer. This allows for little to no UV detections at shorter wavelengths. The spectra of galaxies detected at higher redshifts are band-shifted (i.e. Doppler shifted) to redder observed wavelengths as compared to the actual wavelength at which light is emitted by the source itself (See Section 1.2 for more details). Band-shifting of the Lyman break to redder wavelengths for high redshift star-forming galaxies causes them to drop-out of observations made in bluer bandpass images, while still appearing in redder ones. Based on this, a color criteria can be developed to select large numbers of LBGs in a common redshift range from broad-band survey observations. A majority of the initial SFR density studies used LBGs as a high-redshift star-forming galaxy sample.

As redshift estimates and survey data continued to grow and improve, numerous authors continued to add to the picture of cosmic star formation. Connolly et al. (1997) added data for $0.5 < z < 2$, shifting the peak of the SFR density to $\sim$1.5 and filling the gap between the Madau and Lilly data. Steidel et al. (1999) improved the measurements at $z \sim 3$ and ~ 4 doing a spectroscopic study of LBGs that moved these points upwards on the Madau-Lilly plot, showing the SFR density out to high redshift might have been relatively constant. This consistency towards high redshift seemed

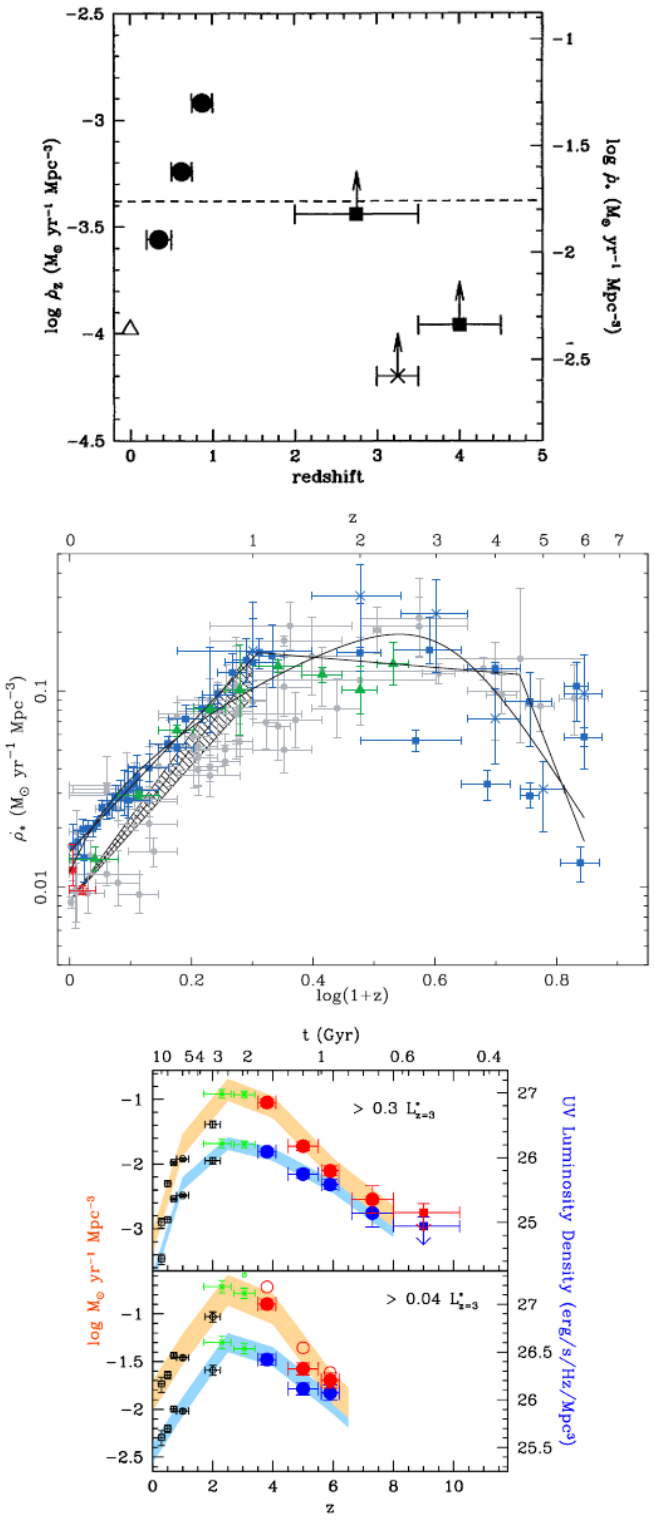

Figure 1.4 *Evolution of the SFR density Madau-Lilly diagram from its original publication (top; Madau et al., 1996), to the first largest compilation of measurements (middle; Hopkins & Beacom, 2006), to the most recent measurements (bottom; Bouwens et al., 2009)*

to be confirmed by observations of LBGs at z $\sim$ 5 (Iwata et al., 2003), but became questionable due to conflicting results at z $\sim$ 6 (Bouwens et al., 2003; Stanway et al., 2003). In 2004, Hopkins assembled all the measurements of SFR in the literature to date, converting them to a consistent cosmology and making corrections for dust (Hopkins, 2004). His compilation included not only LBG populations, but SFR from several star-forming galaxy populations and SFR indicators including narrowband optical emission features, mid-IR galaxies, and radio galaxies. At this point the SFR density from $0 < z < 1$ was well constrained, but it took several more years of research to show that the number of star-forming galaxies actually decreases significantly from z = 3 to z = 7 (Bunker et al., 2004; Bouwens et al., 2006; Wadadekar et al., 2006; McLure et al., 2009; Reddy & Steidel, 2009; Bouwens et al., 2009), adjusting the previous results at high redshift.

Currently, the picture stands that $\sim$800 Myr after the Big Bang (z $\sim$ 7) the SFR density of the universe was dramatically increasing, meaning star formation in galaxies on a whole was on the rise, for $\sim$1.4 Gyr, up to z $\sim$ 3, where it began to level out, eventually peaking at rates on the order of 0.15 $M_{\odot}$ yr^{-1} Mpc^{-3} between $1 < z < 2$. After z $\sim$ 1 there was a sharp decline in the SFR density to the current epoch, indicating that over the past $\sim$7.7 Gyr star formation has been shutting down in galaxies. Observations reveal that Hubble type galaxies form during the course of this decline in star formation. It remains a largely open question as to what were the physical processes and mechanisms within galaxies that caused this decline and influenced the morphological transformation of galaxies to their present day appearances. Only through studies of the morphology, kinematics, chemistry, and evolutionary sequences of star-forming galaxies over intermediate redshifts ($0.2 < z < 1.2$) can the evolutionary gap between the distant and local universe be spanned. This is one of the primary goals of the work presented in this thesis.

1.5 Rest-Frame Ultraviolet Galaxies

Emission from small numbers of newly-born massive O and B type stars dominate the total UV light from new regions of star formation. Emissions from these stars peak in UV wavelengths and have short lifetimes on the order of millions of years. The UV spectral range is loosely defined as covering wavelengths between 100Å–3200Å, most of which is opaque to Earth's atmosphere, and opaque to the interstellar medium below 912Å (i.e. the Lyman Limit; photons at this energy or higher are used to ionize HI gas). This leaves a window of $912\text{Å} < \lambda < 3200\text{Å}$ at which relatively close star-forming galaxies can be observed at rest-frame UV wavelengths from space.

Initially, UV observational technology was largely developed in a spectroscopic mode in order to observe the chemical properties of stars at these wavelengths. Not much of an emphasis was put on imaging galaxies in the UV, potentially a result of astronomers believing that this emission was highly sensitive to gas and dust and thus would be absorbed by the intergalactic medium of the extragalactic source itself, or along the line of sight through the Milky Way. Interestingly, the very first image of an external galaxy at UV wavelengths was taken from the moon by Apollo 16 astronauts using the Naval Research Lab S201 camera between 1250Å-1600Å (Figure 1.5). They imaged the Large Magellanic Cloud with a 3 arcminute spatial resolution, but still managed to capture the undeniable morphological transformation from its well known optical appearance to a star-forming galaxy decoupled from its older stellar population. Other UV cameras were mounted on balloons and rockets acquiring further UV imaging of nearby extragalactic sources (e.g., Carruthers et al., 1978). Two of NASA's very first successful space satellites launched in the late 1960's and early 1970's, the Orbiting Astronomical Observatory 2 and 3 (OAO2 and Copernicus; Code et al., 1970) carried several UV telescopes on board and implemented the first photometric and imaging surveys of galaxies in the UV. From these data astronomers learned that local galaxies with early-type morphologies were much less luminous in the UV than late-type morphologies, and more generally, that galaxies were brighter in the UV than expected from previous analysis of their optical colors. Other productive

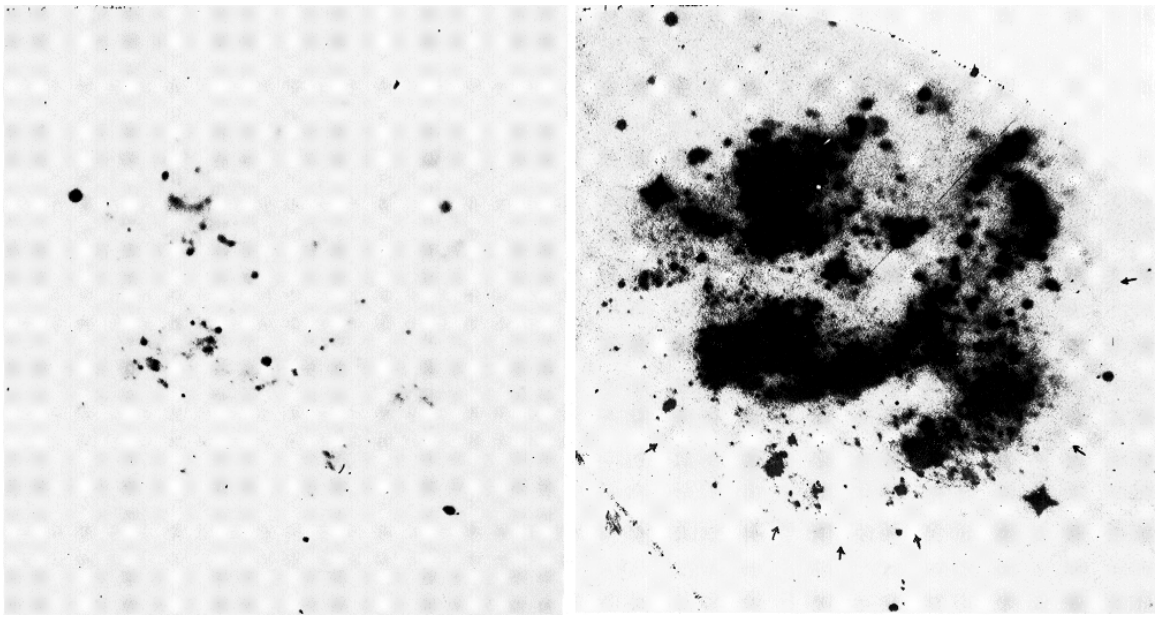

Figure 1.5 *A 3 minute exposure (left) and 30 minute exposure (right) of the Large Magellanic Cloud taken with the NRL S201 camera in FUV (1230Å–1600Å). This is the first ever UV image of another galaxy taken on the moon by the crew of Apollo 16 Page & Carruthers (1981).*

UV imaging observatories included the SCAP and FOCA balloon borne experiments run by a French and Swiss collaboration between the 1970's and early 1990's and the Ultraviolet Imaging Telescope (UIT) carried on NASA's ASTRO-1 Spacelab from 1990 to 1995. Overall, these missions revealed the morphological change between the UV and optical wavelengths in local galaxies, but lacked the necessary resolution for detailed analysis of stellar populations. At the time, this task was left to the efforts of the near-UV detectors on HST. However, a smaller UV mission that commenced nearly 13 years after Hubble's launch has singularly made one of the largest contributions to our understanding of galaxies in the rest-frame UV.

The Galaxy Evolution Explorer (GALEX) is a small explorer mission launched by NASA in April of 2003 (Martin et al., 2005). Its observational capabilities include near-UV (NUV) and far-UV (FUV) imaging and spectroscopy over a wavelengths 1350Å–2750Å. GALEX has completed the largest ever all-sky survey in the UV, providing high resolution imaging of local star-forming galaxies. These data make a

significant contribution to our understanding of the endpoint of galaxy evolution in the universe, setting a benchmark with which to compare and interpret detections of star-forming galaxies at higher redshifts. More specifically in the interest of this thesis, the GALEX survey has provided a library of local rest-frame UV morphologies which can be compared and connected to the high-redshift broadband optical and near-IR band-shifted rest-UV morphologies mapped by the high resolution cameras on HST.

1.5.1 Piecing Together the Ultraviolet Puzzle

In order to detect star-forming galaxies at higher redshifts a series of techniques have been developed to exploit the band-shifting of certain characteristic features of the UV spectrum or UV color information in combinations with other bands. The following entails a brief discussion of the different populations of star-forming galaxies targeted by these methods.

Starbursts: Starbursts do not generally fit into the classical Hubble "tuning-fork" diagram because this phenomenon occurs in a mixed bag of types, from small dwarf galaxies to large spirals. They were first identified by their extremely blue broadband colors (Larson & Tinsley, 1978), and later, by their strong optical Hα emission lines, a primary spectral signature of star formation. Many local galaxies categorized as starbursts are undergoing, or have undergone, major and minor mergers that induce tidal (i.e. gravitational) features in these systems (e.g., Liu & Kennicutt, 1995a,b). Non-interacting starbursts show enhanced star formation in their central bulges and it has been suggested that bar structures in spiral galaxies act as triggering mechanisms, driving cold gas (star formation fuel) to in-fall on these central regions, triggering excess star formation (Ishizuki et al., 1990; Schinnerer et al., 2003). All starburst systems have extremely high SFR, two or more orders of magnitude greater than measured in normal star-forming spirals. Direct stellar light in the far-UV and re-processed stellar light in the far-IR dominates their emission features. One technique used to study distant starburst sources is via construction and analysis of SEDs from their broad-band colors (Kinney et al., 1996). Spectral types (STs)

can then be determined from these SEDs. Using this method many systems with starburst emission features have been identified at higher redshift. Studies have shown that starbursts are represented in all visual morphologies at high redshift including spirals, clump clusters, chains, doubles, and tadpoles, and they have been detected out to z $\sim$ 5 (de Mello et al., 2006b; Elmegreen et al., 2007). However, these data add further confusion to how we define starbursts, given that at high redshift they also cover a wide range of galaxy demographics. Connections between local and high-redshift starbursts are not yet clear in the scheme of galaxy evolution.

LBGs and UVLGs: The basic method for identifying LBGs at high redshift has been briefly described in Section 1.4. Cuts defined in the color-color plots of large survey samples have are used to select LBGs in specific redshift ranges when compared with spectroscopic measurements. Much work has been done to try to connect LBGs to a star-forming population of galaxies at lower redshifts, essentially low redshift LBGs. Heckman et al. (2005) and Hoopes et al. (2007) used GALEX observations to study a population of UV luminous galaxies (UVLGs) with far-UV luminosities greater than 2×10^{10} $L_{\odot}$ at z = 0 that are thought to be local LBG analogs. Overzier et al. (2008, 2009, 2010) have studied the morphological connections between LBGs at $2 < z < 4$, UVLGs, and starbursts at $z < 0.3$. They show that there are similarities in the UV/optical colors and sizes of these populations, and find the asymmetric morphologies, which are signs of starbursts at low redshift, are not resolvable at higher redshifts. Burgarella et al. (2007) have detected a population of LBGs at z $\sim$ 1 using the drop-out technique in GALEX far-UV imaging. Their sample is defined by two different populations of LBGs: red LBGs that have corresponding observations in Spitzer mid-IR 24μ images and are also categorized as luminous infrared galaxies (LIRGs), and a blue LBGs that are not detected in the mid-IR. Through SED analysis they find that both subsets have similar stellar populations, with the red being slightly dustier, and they make connection between the median red LBG SED to a dusty starburst galaxy at z $\sim$ 1.44.

LAEs: Narrow-band imaging has been used to target a population of star-forming galaxies designated as Lyman-α emitters (LAEs) (Hu & McMahon, 1996). The

Lyman-α spectral line is detected at 1216Å as the energy transition between n=2 and n=1 orbitals in a hydrogen atom. Photons emitted in this transition are highly dust-sensitive resulting from their resonant scattering in HI, requiring LAEs to be a dust deprived population. Thus, either recent starburst episodes due to potential merger activity or the very initial burst of star formation is being observed in these sources. LAEs were initially detected at redshifts ~ 4, but have been subsequently observed at both earlier and later epochs (Moller & Warren, 1993; Cowie & Hu, 1998; Kulkarni et al., 2006; Nilsson & Møller, 2009). Due to their strong emission lines this population is an excellent candidate for narrow-band surveys at very high redshift.

1.5.2 Ultraviolet Morphologies of High-Redshift Galaxies

The rest-frame UV is detectable in broadband observations of redder, longer wavelengths when imaging sources in the distant universe. However, there is a large contrast between the rest-frame UV morphologies of galaxies and their rest-frame optical morphologies (de Mello et al., 2006b; Teplitz et al., 2006). In many cases rest-frame UV morphologies can appear to be clumpy and irregular due to the distribution of star formation (Law et al., 2007), while their rest-frame optical (B-,V-, i-, and z-bands) morphologies are generally more uniform because they detect older stellar populations, gas, and regions obscured by dust, revealing the overall structure of a galaxy (see Figure 1.6). The differences between rest-UV and rest-optical morphologies have been observed to decrease in star-forming galaxies towards higher redshifts (Papovich et al., 2005). Regardless, at all redshifts UV morphologies are patchy and clumpy or extremely compact in nature (Gordon et al., 2004; Law et al., 2007; Oesch et al., 2010). Considering the scenarios of galaxy evolution, these morphological signatures could result from either merger interactions between two or multiple systems that trigger star formation as predicted by the hierarchical theory of evolution, cloud collapse via gravitational instabilities in a gaseous disk that is fed by cold gas spiraling inwards along filamentary structures predicted by secular evolution theories, or another mechanism still to be discovered. Several non-parametric measurements of

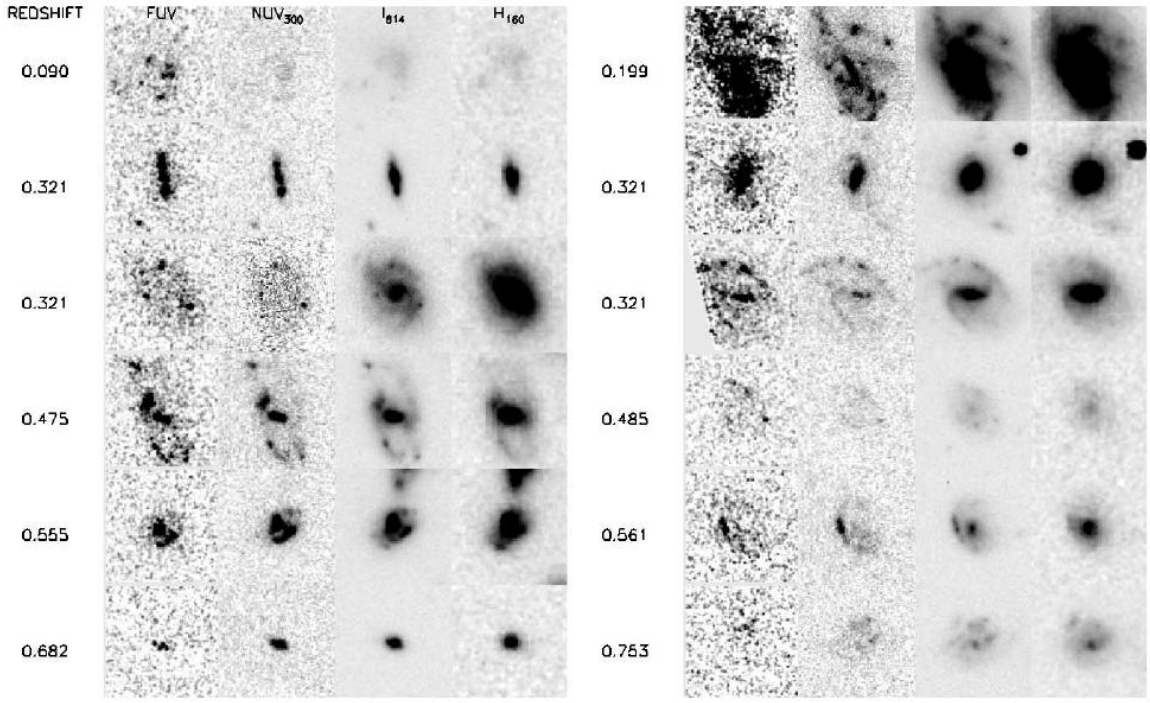

Figure 1.6 *Rest-frame star-forming galaxies show transformations in their morphologies between the UV, optical and IR observed wavelengths. Image is from Teplitz et al. (2006).*

the light distributions in galaxies have been developed to test for merger morphologies at high redshift. These include Concentration-Asymmetry-Clumpiness (CAS) (Conselice et al., 2003), the Gini coefficient (Abraham et al., 2003), and M_{20} (Lotz et al., 2004). These quantitative parameters are optimized for merger classifications because they do not attempt to fit light profiles with well defined functions as traditionally done by parametric measurements such as the half-light radii, Petrosian radii, bulge-to-disk ratio, and Sérsic index[1]. However, studies in the literature choose to use a wide combination of these techniques to quantify morphological changes in star-forming galaxies over time.

Several studies have focused on rest-UV morphologies of LBGs at $z \gtrsim 2.5$ finding the majority of these sources to be either multi-compact regions, disturbed morpholo-

[1]See Section 3.3 of this thesis for a more complete discussion of these measurements.

gies, or exponential disks (Giavalisco et al., 1996; Ferguson et al., 2004; Lotz et al., 2006; Ravindranath et al., 2006). Only ∼30% of these LBG samples have de Vaucouleurs $r^{1/4}$ spheroidal profiles. Most recently, Oesch et al. (2010) have completed the deepest morphological analysis of rest-UV galaxies ever, analyzing LBGs at z ∼ 7–8 in WFC3 IR imaging of the HUDF. Of the 16 galaxies in their LBG sample only two possess non-compact extended morphologies harboring double compact regions. Thus, there is a multiplication in rest-UV LBG cores towards low redshifts, as well as a development of disky/extended morphologies. However, the sizes of the cores do not evolve greatly since z ∼ 7. Rest-UV morphologies of low redshift star-forming populations, including starburst galaxies between $0.95 \leqslant z \leqslant 1.5$ (Ravindranath et al., 2006) and emission-line galaxies between $1.2 \leqslant z \leqslant 1.8$ (Lotz et al., 2006), are found to generally have the same fraction of exponential and disturbed/merger morphologies as high-redshift LBGs, but a decreased fraction of spheroidal morphologies. The same change in statistics is also determined from a broadband-selected census of rest-UV (2800Å) morphologies over $0.5 \leqslant z \leqslant 2.2$ (Dahlen et al., 2007). However, studying the rest-UV morphology alone has not provided a clear picture as to whether a merging or secular evolution scenario dominated at $z \gtrsim 2.5$.

Another way to test for merger mechanisms in high-redshift galaxies is through direct comparison to merger candidates in the local universe. Petty et al. (2009) artificially redshifted 8 local starburst galaxies to z ∼ 1.5 and z ∼ 4 to compare their quantitative morphologies to large samples of LBGs, as well as clumpy and merger-like galaxies at these redshifts. They found that 20–30% of the high-redshift populations are similar to the redshifted local starbursts, and also that three of the local starbursts share morphological properties of clumpy and merger-like galaxies at higher-z. Technical effects, such as surface-brightness dimming and decrease in resolution, were measured out to higher-z, and are found to bias rest-frame morphological quantification at these epochs. Thus, in order to concretely detect the evolutionary path of UV star-forming galaxies better resolutions are needed and non-parametric techniques require further adjustments.

Overall these observations suggest a scenario where star formation turns off in

ellipticals at higher redshifts but is quiescently on-going in the majority of extended sources down to the present epoch. In combination with the fact that the present population of galaxies was assembled over the past ∼8 Gyr (since z ∼ 1) there remains an open question as to how quiescent star formation could primarily drive these final stages of morphological transformations.

1.5.3 Star Formation and the Epoch of Disk Formation

Four and a half billion years ago our Sun was born within a cloud of gas nestled far in the outskirts of the Milky Way. This is equivalent to a redshift of ∼0.43 (or ∼4.5 Gyr ago). It is not so straightforward how the Milky Way's relaxed spiral structure came to being or if this spiral structure was already well established at the Sun's birth. If one makes a census of the local galaxy population they will find a majority have disk morphologies like our Milky Way. This begs the question, when was the epoch of disk formation in the universe?

Delgado-Serrano et al. (2010) did a study constructing the Hubble sequence as it would have appeared 6 Gyr ago. They find that peculiar/irregular galaxies represent 52% of this past sequence compared to representing only ∼10% of the local Hubble sequence. Although Hubble types have been observed up to z ∼ 1.5, a great deal of evolution in the irregular galaxy population must have contributed to forming the local spirals. The next logical step in this investigation is to search through existing survey data to evaluate a large sample of disks and peculiar galaxies over several redshifts. Furthermore, a multiwavelength view is essential for identifying how rest-frame optical morphologies changed with respect to rest-frame star-formation morphologies.

Ravindranath et al. (2004) gathered a sample of 1508 disk galaxies between 0.25 $\leqslant$ z $\leqslant$ 1.25 in the rest-frame B-band with Sérsic values of exponential disks. They tracked their size evolution over time using measurements of half-light radii values. A null result was reached with the sample showing no significant size evolution with redshift. Physical measurements of the irregular galaxy population are also useful

in tracking any morphological transformations to disks. Elmegreen et al. (2009) have measured the sizes of star-forming clumps in clump cluster and chain galaxies detected in the GOODS and GEMS fields out to z $\sim$ 1.5 (see Section 2.6 for more detail on these classifications). These morphologies have been classified through visual identifications, contour plots, and radial profiles in the observed i-band. Their results provide evidence towards eventual clump dispersion to form smooth disks and clump coalescence to build up bulges at later epochs. Because these clumpy galaxies do not show any classic tidal signatures, and ones that did were rejected from the sample, Elmegreen et al. (2009) suggest that clump clusters and chains are not currently interacting with other galaxies and are believed to be undergoing secular evolution. However, as mentioned previously, searches for LBG analogs at low redshifts have revealed that evidence of tidal features disappear in the rest-frame UV when these objects are convolved to the resolutions of the GOODS fields. Therefore this debate remains open.

Several groups have approached the puzzle of disk evolution through an alternative approach looking for changes in the internal kinematic motions of galaxies over time. The most recent kinematic studies use novel ground-based observing techniques with integral field unit (IFU) spectroscopy and adaptive optics (AO) to obtain spatial and spectral information from targeted sources. So far this work has probed normal disks and clumpy galaxies between $0.1 < z < 3$ by measuring velocity dispersions from strong rest-frame optical emission features of star formation, such as Hα (Genzel et al., 2008), to search for rotational motions. The interpretation of these results suggest some conflict between evolutionary scenarios proposed between low and high redshift. Studies at all redshifts find the potential for disk-dominated galaxies to have been secularly evolving since their formation. Studies of z $\sim$ 2–3 sources do not seem to find any merger involvement in this process (Förster Schreiber et al., 2006, 2009), while results from observations of a large sample of 544 strong emission-line galaxies between $0.1 < z < 1.2$ find their results consistent with evolutionary scenarios that could still involve major mergers (Kassin et al., 2007). Epinat et al. (2010) warns that when doing kinematic studies to be cautious of selection biases in the interpretation of

results, finding toy models used to fit these data can be biased due to poor resolution.

Observational studies of disky and clumpy galaxies are complemented by simulations of galaxy evolution set in the high-redshift universe, such as those by Agertz et al. (2009, 2011) and Elmegreen et al. (2008). These simulations predict scenarios for galaxy formation in the CDM cosmology, and lend evidence for triggering mechanisms of star formation at high redshift. These simulations target secular evolution as the primary avenue of disk assembly and include merging of small dwarf systems and the coalescence of clumps of material within galaxies. Simulations by Krumholz & Dekel (2010) explore the possibility of star-formation quenching in giant clumps within high-redshift galaxies by stellar feedback. They determine that in order for clumps to remain bound they must form stars at a rate of a few percent of the mass per free-fall time. They suggest that further observational studies of stellar populations in individual clumps are needed to support results of these simulations.

1.6 In This Thesis

The aim of this thesis is to produce a comprehensive multiwavelength study of star-forming galaxies through several observational approaches in order to achieve a better picture of the role of morphology and star formation in galaxy evolution. The focus is on distant star-forming galaxies at intermediate redshifts ($0.2 < z < 1.2$) that populated the universe $\sim$4.5 to 9 billion years after the Big Bang.

In Chapter 2, an initial sample of rest-UV star-forming galaxies is presented and analyzed. The sample is drawn from the first space-based U-band observations of the HUDF area of the GOODS-south (GOODS-S) field taken with HSTs Wide Field Planetary Camera 2 (WFPC2). Photometry presented for these sources and the subsequent catalog is matched with an optically-selected catalog of the entire GOODS-S area (Giavalisco et al., 2004). This provides multi-band photometry, galaxy spectral types (STs), and photometric redshifts (z_{phot}) for all rest-UV HUDF sources. Far-UV (FUV) photometry of these sources measured in images from HST's Advanced Camera for Survey (ACS) Solar Blind Channel (SBC) detector is also be presented.

Distributions of sources with z_{phot}, spectral type (ST), physical size, and U-band magnitude are presented. Plotting the z_{phot} distribution of the sample will gauge the star-formation activity as a function of time during the intermediate-z epoch. Mapping out the ST distribution of the sample will reveal what types of galaxies populated the star-forming regime. From the size distribution of the sample, physical sizes of galaxies are measured over all morphological types.

In Chapter 3, a study of clumpy star-forming galaxies in the HUDF based on the initial U-band catalog is presented. This data set is unique in that only the U-band probes rest-frame far-UV wavelengths for redshifts $0.63 < z < 1.5$ and only HST data has the spatial resolution necessary to conduct this study. Physical sizes of sub-galactic star-forming clumps are measured and compared with results of studies at higher redshifts in order to look for potential clump size evolution within the star-forming field galaxy population. The implications of the results on galaxy evolution are discussed.

In Chapter 4, the number counts of FUV detected galaxies are determined for the entire sample of FUV sources in GOODS-N and -S for magnitudes 21–29. The measured FUV counts will be compared to previous faint HST FUV number count studies and bright FUV number count studies done with GALEX. A comparison with results from the most recent semi-analytic galaxy evolution models will also be presented. This chapter provides a global view of star-forming galaxy evolution at intermediate-z to complement the previous detailed analysis of individual star-forming galaxies.

In Chapter 5, a new measurement of the resolved FUV background light from galaxies is presented along with a comparison to past measurements and measurements of the total UV background light.

In Chapter 6, a larger sample of FUV detected galaxies in the GOODS-N and -S fields is used to do an analysis of morphological evolution over several epochs based on rest-frame V-band morphologies. Galaxy morphologies are measured quantitatively and compared with SED derived STs in order to determine how well this characteristic correlates with galaxy morphology.

In Chapter 7, the overall conclusions of this thesis are discussed as well as future work that will be supported by the results of this study.

2

Rest-Frame Ultraviolet Galaxies in the Hubble Ultra Deep Field

This chapter presents the source catalog of the first space-based high resolution U-band image of the Hubble Ultra Deep Field. Additionally, redshifts, SED based spectral types, multiwavelength photometry and morphologies are also presented and discussed for these sources. The methodology followed for the observations, image processing, object identification, catalog preparation, and catalog matching are depicted within. The goal here is to develop an initial sample of rest-frame UV star-forming galaxies at intermediate redshifts ($0.2 < z < 1.5$) to be analyzed and expanded upon throughout the course of this thesis. The aim of this initial study is to find what types of galaxy morphologies harbor star formation at intermediate redshifts in this well known field.

2.1 Introduction

The Hubble Ultra Deep Field (HUDF) campaign (Beckwith et al., 2006) has produced the deepest optical images of our universe to date. The HUDF was observed by Hubble in 412 orbits that were centered in a region of the Chandra Deep Field

South (CDF-S) which was also the target of the Great Observatories Origins Deep Survey (GOODS, Giavalisco et al., 2004) known as the GOODS-south or GOODS-S. The HUDF used the same Advanced Camera for Surveys (ACS) filters as GOODS, F435W (B_{435}), F606W (V_{606}), F775W (i_{775}), and F850LP (z_{850}), but covered only one field of the 15 GOODS-S fields. The HUDF reached approximately uniform limiting magnitudes $m_{AB} \sim 29$ for point sources, at least two magnitudes deeper than GOODS. Neither campaign included deep imaging in the U bandpass. Taking U-band photometry is a time consuming task because longer integrations are required to achieve comparable depth to optical images. Only three HST U-band deep fields have been taken so far, the original Hubble Deep Field, the Hubble Deep Field South and the deepest U-band ever taken with Hubble which was part of the parallel campaign of the HUDF and lies on the edge of the GOODS-S (Williams et al., 1996; Casertano et al., 2000; de Mello et al., 2006b). GOODS has only partial U-band coverage with HST obtained during parallel observations (de Mello et al., 2006a). Deep U-band ground-based images of the GOODS-S field, such as those taken with the CTIO 4m and ESO 2.2m available in the GOODS webpage[5], are included in the multiwavelength coverage of GOODS. Although ground-based observations can cover larger fields of view than Hubble's cameras more efficiently, they do not possess the same angular resolution as space-based observations (Nonino et al., 2009). This is not a deterrent to studies on color determination of U-band objects (Capak, 2004; Burgarella et al., 2007), but it does inhibit detailed morphological analysis of U-band detected galaxies. Specifically, many low-resolution ground-based images will blend together nearby detections, and/or be contaminated with stars, leading to inaccurate photometric and morphological analysis (e.g., Section 6). Thus, the resolution provided by HST is crucial in achieving important science goals when studying star-forming objects at intermediate-z. The U-band is a critical wavelength in studies at intermediate redshifts ($z < 2$) since the rest-frame UV light is redshifted into the U bandpass. It is in the UV that short-lived, massive, O and B stars radiate most of their energy and therefore the U-band is necessary to probe the unobscured star-

[5]http://www.stsci.edu/science/goods/SupportObs/cdfs_mosaic/

formation activity in galaxies at z < 2. Therefore U-band observations are needed to analyze star-forming galaxies at intermediate redshifts. Furthermore, in order to reveal what types of galaxy morphologies harbor star formation U-band data needs to be analyzed together with multiwavelength observations.

As discussed previously in some detail, several studies have provided observational evidence that at redshifts z ∼ 1–2 there is a sudden decline in the star-formation rate (SFR) density in comparison with the early universe(e.g., Madau et al., 1996; Connolly et al., 1997; Dahlen et al., 2005; Bouwens et al., 2006; Wadadekar et al., 2006). However, it is still an open question as to what population of objects contributes to the SFR density during the decline, and whether downsizing (the shift in star formation being dominated from large to small mass galaxies as the universe aged) plays an important role in this era (Cowie et al., 1996; Savaglio et al., 2005; Mouri & Taniguchi, 2006; Neistein et al., 2006). Therefore, the study of star-forming galaxies at intermediate redshifts (z < 2) can greatly contribute to bridging the gap between these two important epochs, the early universe and the local universe.

Deep multiwavelength images have been used to search for distant galaxies in early evolutionary phases, and in particular galaxies forming stars at z > 2 (early universe) known as LBGs (Steidel et al., 2003). These objects are selected to be (rest-frame) UV bright and thus are identified by Lyman break and Lyα absorption features in their UV spectra. They share similar observed properties with local starburst galaxies, and their spectral lines are indicative of active star formation (Steidel et al., 1996, 1999; Pettini et al., 2001). LBGs have been observed to have a variety of morphological types (disks, irregulars, mergers, spheroids) that show little difference between their rest-frame optical and UV morphologies (observed near-infrared and optical respectively) (Dickinson et al., 2000; Papovich et al., 2003; Ravindranath et al., 2006). An open question is whether these objects are present at lower redshifts (z < 2). Detecting LBGs at z < 2 requires near-UV or far-UV dropouts, and only ground-based, GALEX, and HST observations of deep fields have been available to do this type of study. Ground-based and GALEX data lack the resolution necessary to conduct a detailed search for these objects beyond our local universe. However,

there has been a significant contribution to studying LBGs at z $\sim$ 1 using far-UV drop-out techniques with GALEX (Burgarella et al. 2008). There have also been studies searching for local analogs of LBGs, in particular Heckman et al. (2005) and Hoopes et al. (2007) have found a class of objects called ultraviolet-luminous galaxies (UVLGs).

In the following sections the first HST targeted U-band image of the HUDF is presented, analyzed, and discussed. This thesis assumes a cosmology with $\Omega_{\rm M} = 0.3$, $\Omega_{\Lambda} = 0.7$ and $h = 0.7$, and magnitudes are given in the AB-system.

2.2 Observations

The U-band observations were obtained with the HST Wide Field Planetary Camera 2 (WFPC2) in the Cycle 13 HST Treasury proposal (Teplitz, Program 10403). The HUDF was imaged in the near-UV (NUV) through the WFPC2/F300W filter ($\lambda_{\rm max}$ = 2987Å, $\Delta\lambda$=740Å) in 12 HST orbits divided into 4 roll angles to compensate for the shape of the WFPC2 chevron and achieve uniform depth. On-chip binning (2x2) was applied during WFPC2 observations to reduce the effects of read-out noise, i.e. each Wide Field became 400 $\times$ 400 pixels. A total of 24 WFPC2 images were taken with individual exposure times of 1200s. FUV imaging was also obtained in this same proposal with HST/ACS Solar Blind Channel (SBC) camera at which time WFPC2 parallel observations were also made. The HUDF ACS/SBC images were taken in 50 HST orbits using the long-pass quartz filter (F150LP) ($\lambda_{\rm eff}$ = 1614Å, and FWHM=177Å). The FUV was imaged in 25 pointings. Each pointing had a four point dither pattern with two 650s exposures at each dither position. The total exposure time per pointing was $\sim$5200s (Siana et al., 2007).

2.3 Image Processing

The WFPC2 images were retrieved from the HST archive for further processing. A total of 24 WFPC2 images were combined with the MultiDrizzle code in the PyDrizzle

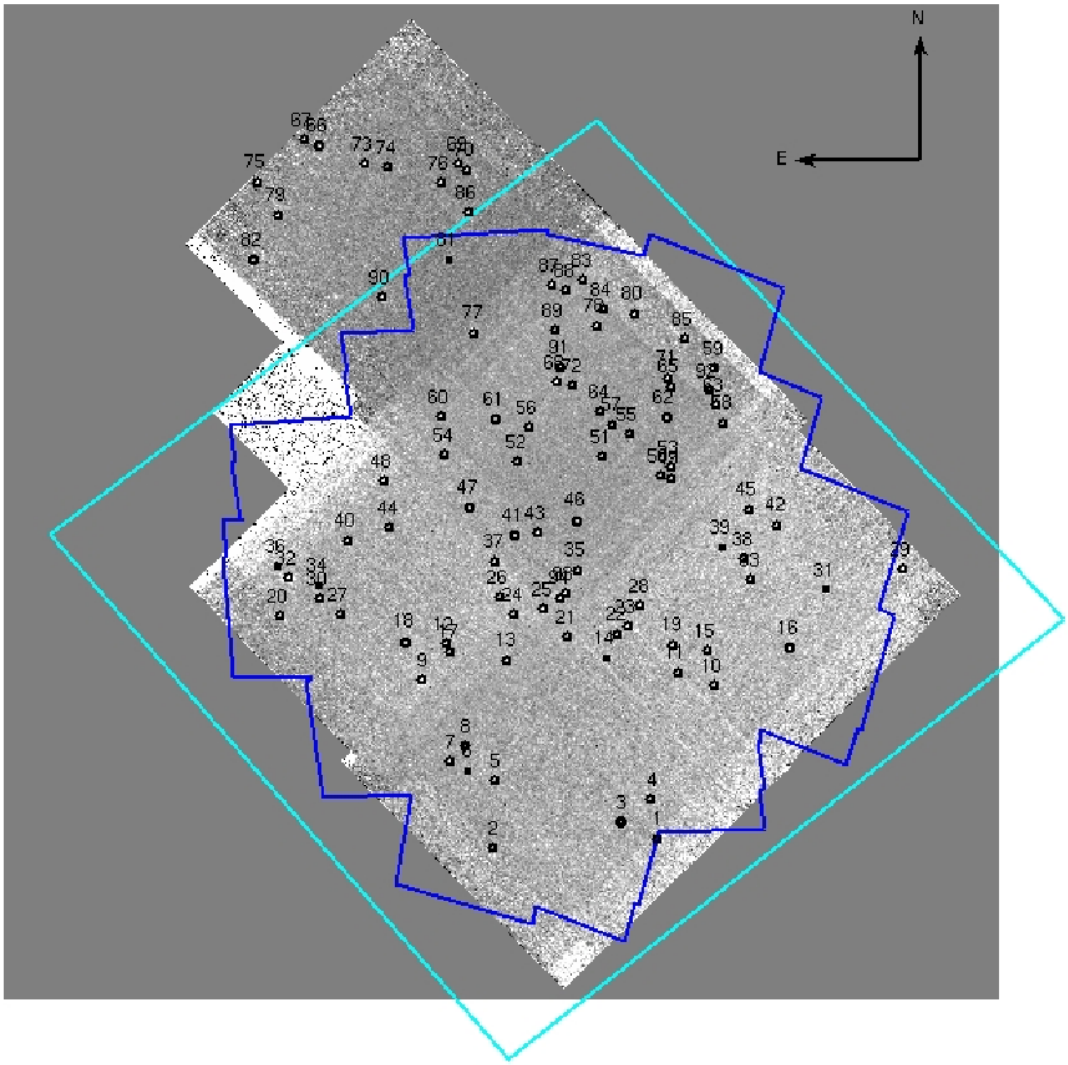

Figure 2.1 *WFPC2 drizzled U-band image and HUDF (cyan) and ACS/SBC (blue) footprints. Note the large number of detections in the second rectangular region from the top of the image due to a higher net exposure time for this region.*

package (Koekemoer et al., 2002). These images were taken using a dithering technique that reduces effects of pixel-to-pixel errors and allows one to better remove hot pixels, bad columns, and charge traps from the image. Dithering also allows the recovery of information lost to undersampling by pixels that are not small compared to the point-spread-function (PSF). MultiDrizzle simplifies and automates the detection of cosmic-rays of these dithered observations. Calibrated flat-fields were used from the HST pipeline in conjunction with the data images to run the MultiDrizzle script through the following steps. First, a static mask was created to identify bad pixels, then each image was sky-subtracted, shifts were determined from header coordinates for each image and were applied in drizzling each image separately onto registered output images. Next, a median image was created from these separate drizzled images and was blotted back to each original input image. Finally, the blotted images were used to compute cosmic ray masks, and the final drizzle combination was performed using these masks.

WFPC2 is composed of four CCD chips: three wide field chips (WF2–4) in and L-shaped 150″x150″ configuration designed for optical and near-UV surveys, and a single 34″x34″ square planetary camera (PC) chip designed for targeted high-resolution imaging in smaller fields of view. Prior to running MultiDrizzle the Planetary Camera (PC) data was removed from all images because its inclusion greatly increased the noise level of the output drizzled image. This was achieved by replacing the PC in each of the 24 images with hot pixels, forcing MultiDrizzle to automatically include the PC in the pixel mask for each individual image. The MultiDrizzle user-inputs were set in such a way that the program would output separate science and weight images for these combined data. All the reduced high-level science data products have been made available online in the Space Telescope Science Institute (STScI) archives at: http://archive.stsci.edu/prepds/udf/udf_hlsp.html.

The drizzled WFPC2 image shown in Figure 2.1 has a total exposure time of 28,800s and an improved plate scale of 0.09″/pixel. Due to the way in which the 24 WFPC2 pointings were positioned, the final drizzled image is not of a uniform depth across the entire field. The majority of pointings overlap in the mid-upper region of

the combined image. Consequently, the majority of UV sources are detected in this area of the HUDF. In addition, the upper-most section of the U-band image lies just outside the original HUDF survey footprint, and sources from this area are marked as such in the catalog. The reduction procedure used for the HUDF ACS/SBC images is outlined in Teplitz et al. (2006).

2.4 Object Identification And Catalog Preparation

The catalog of U-band sources was produced using Source Extractor version 2.5 (Bertin & Arnouts, 1996, hereafter SExtractor). This software was essentially designed to produce galaxy catalogs given an astronomical FITS image. SExtractor takes a specific set of input parameters and uses these to decide which pixels in an image should be considered part of a source, which pixels should be considered to belong to the background of the image, which objects should be segmented into two or more sources, and how to calculate the photometric measurement of all detected sources. There are two steps that the program implements in order to create a single catalog. In the first step the program calculates a sky background for the entire input image. In the second step the calculated background is first subtracted from the image, a smoothing/convolution filter is applied if desired (e.g., Gaussian filter), and the pixel value threshold, below which a pixel is not considered a possible detection, is applied throughout the image. Continuing with the catalog creation, the remaining pixels are deblended into sources, those sources are cleaned based on input parameters, photometry is measured for each source, and finally objects are classified as either galaxies or point sources. The resulting catalog can contain a slew of varying parameters that are selected at the discretion of the user.

For the initial detection of U-band sources, both low-σ (1.5σ above background noise) and high-σ (3σ above background noise) catalogs were created. The high-σ catalog contains all visually confirmed sources in the image, while the low-σ catalog may contain spurious detection. The difference between the SExtractor parameters specified for these two catalogs was the detection threshold relative to the background

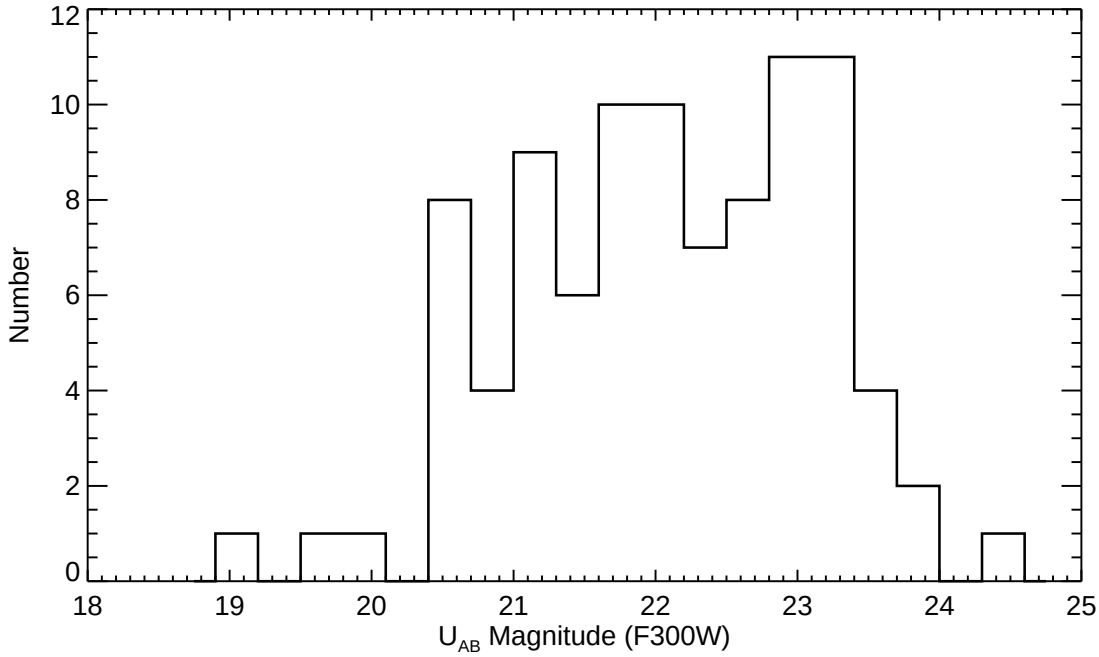

Figure 2.2 *Magnitude distribution of the U-band catalog, MAG_AUTO from SE.*

RMS. For both catalogs, the minimum area of adjoining pixels for a detection was 15 pixels, and the minimum deblending parameter was set at 10%, except for a few cases where the deblending value was specifically set in order to avoid multiple detections in one single object. This is particularly critical for source detection in U-band images since star-forming regions can appear as multiple clumps in one object. SExtractor might detect those clumps as individual objects making false identifications. The GAIN, MAG_ZEROPOINT, and SATUR_LEVEL parameters which are specific to the WFPC2 camera were set to 7 e^-/ADU, 20.77 mag, and 2 ADU/s, respectively. The weight map produced by the drizzling process was used by setting the weight map type to MAP_WEIGHT. Photometric measurements of each source were calculated using SE's automatic aperture magnitudes (MAG_AUTO). MAG_AUTO uses a Kron (1980) flexible elliptical aperture to measure the total magnitude of each

source. Instead of using the classical aperture photometry with a fixed aperture radius, MAG_AUTO has the advantage of limiting the background noise while detecting light from faint sources more effectively. The size of the background mesh which is subtracted from the photometry of each source (BACK_SIZE) was set to 64 pixels, and its RMS value is used to calculate photometric errors. The high-σ and low-σ catalogs were cleaned by removing sources with photometric errors ≥ 1.0.

The resulting U-band catalog includes all detections from the high-σ catalog, and the remaining objects visually confirmed from the low-σ catalog. The U-band 1.5σ limiting magnitude measured within a $1''$ diameter aperture is 23.5mag (AB) (Figure 2.2).

2.4.1 Visual Identification Of U-Band Sources

Each individual SExtractor U-band detection has been checked visually in order to decide (i) if a single source detection is actually multiple sources, (ii) if multiple source detections are single sources, (iii) if a detection is too noisy, or (iv) if there are any faint UV sources which are not detected. When such cases occur, SExtractor parameters can be adjusted to maximize U-band source detections in the HUDF image, and non-detections can be omitted from the catalog.

Additionally, U-band sources within a Hubble ACS/B-band image of the GOODS-S field that overlaps the HUDF have been visually identified. The B-band sources had been cataloged by the GOODS team using SExtractor and have matched aperture photometry in multiple ACS bands (V,i,z) (Dahlen et al., 2007). The B-band catalog also lists spectral types (see §5 for definition) and photometric redshifts with a typical GOODS accuracy of Δ_z=0.08 (where $\Delta_z \equiv \langle |z_{phot} - z_{spec}|/(1+z_{spec}) \rangle$) (Dahlen et al., 2007) for each source. If a U-band detection could not be visually identified as one of the objects in the B-band catalog it was removed from the U-band catalog. This was done because the B-band data is much deeper (limiting 10σ sensitivity is 27.8; Giavalisco et al., 2004) than the U-band, and a source in the U-band is not expected to be a detection without also appearing in the B-band. During this

cleaning the majority of spurious U-band detections located in the borders of the WFPC2 image were removed. There were also five B-band objects discovered that have corresponded to multiple detections in the U-band. This was a result of setting SExtractor's deblending parameters to a low value in an effort to detect as many U-band sources as possible. This parameter was adjusted in an additional SExtractor run to obtain single detections of these sources. The final U-band catalog contains 96 objects.

2.4.2 Catalog Matching

The final U-band catalog was matched to the far-UV catalog of the HUDF created from the ACS/SBC observations described in Section 2.4 (Siana et al., 2007). Each ACS/SBC source was matched to the nearest U-band object within a 2.5″ radius. Thirteen U-band sources do not have FUV detections because they are outside the ACS/SBC footprint. Any ACS/SBC sources with signal to noise $< 3\sigma$ were not considered. In total, 31 of the 96 U-band objects have resolved matching ACS/SBC detections.

The HUDF has also been observed with the Galaxy Evolution Explorer (GALEX) mission in the far and near ultraviolet (FUV: $\lambda_{\rm eff} = 1528$Å, $\Delta\lambda_{FUV} = 269$Å, NUV: $\lambda_{\rm eff} = 2271$Å, $\Delta\lambda_{NUV} = 616$Å; GALEX field of view is 1°.28 and 1°.24 in FUV and NUV, and pixel scale is 1.5″/pixel) and is publicly available in the GALEX Release 4 (GR4) at the Multimission Archive at STScI (MAST). These data are from two different surveys, the All Sky Survey (AIS, 4″.3 FWHM) and the Deep Sky Survey (DIS, 5″.3 FWHM). The 5σ limiting magnitudes of the AIS data are 20.8 in the NUV and 19.9 in the FUV, and for the DIS data 24.4 in the NUV and 24.8 in the FUV (Morrissey et al., 2007).

The need for HST resolution in this thesis was confirmed by comparing HST imaging with available GALEX imaging of the same HUDF sources. First, all the U-band sources were searched for in the GR4 GALEX catalog and 28 and 45 were matched in the FUV and NUV images, respectively. Next, since GALEX resolution

is significantly lower than Hubble's (GOODS ACS image has 0.03″/pixel), objects where confusion between sources might be problematic were searched for. It was determined that one should use the GALEX data with caution. There are 22 objects where confusion is an important factor in the NUV and FUV and they have been flagged in the catalog. In Figure 2.3 an example of a single GALEX NUV detection of at least four identified objects in the U and B-band is shown. The GALEX data was not used any further in this study due to the lack of resolution.

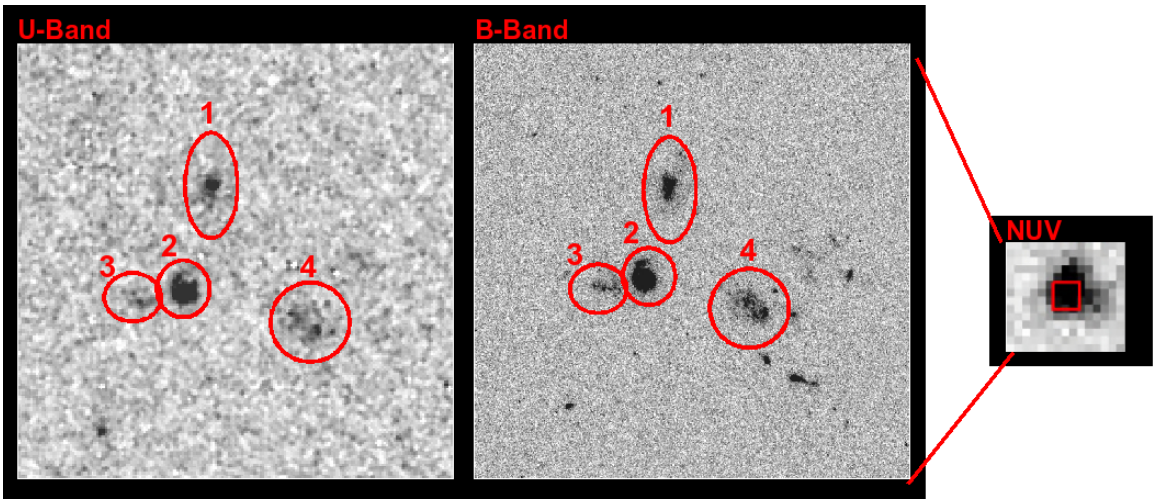

Figure 2.3 *WFPC2 (left), ACS (center), and GALEX (right) images showing four objects (1: 53.1619949 -27.7739410, 2: 53.1623802 -27.7750893, 3: below magnitude limit of the U-band catalog, 4: 53.1608238 -27.7753963) which are within the GALEX beam. All three images are 20″ × 20″.*

2.5 The Catalog

Table A.1 presents the U-band catalog of the HUDF NUV sources. Column (1) provides the reference ID for each source. Three objects with Chandra X-ray detections (Koekemoer et al., 2004) are flagged as "a"[1]. Columns (2) and (3) are the GOODS World Coordinate System (WCS) Right Ascension and Declination in degrees. Columns (4)-(9) are the U, FUV, B, V, i, and z magnitudes and their photomet-

[1]Seven other Chandra X-ray sources found in the HUDF were not detected in the U-band image.

ric errors (MAG_AUTO), respectively. The B, V, i, and z magnitudes were obtained from matching U-band sources to the GOODS-S B-band based catalog. Note that not all U-band detections have FUV photometry because they are either outside the ACS/SBC footprint, are non-detections (S/N $< 3.5\sigma$), or are not resolved in the FUV imaging. Columns (10) and (11) are GALEX NUV and FUV magnitudes from the GR4. Sources with confusion are flagged as "c" in column (1). Columns (12) and (13) list photometric redshifts (z_{phot}) for all objects and available spectroscopic redshifts (z_{spec}) for 41 objects all from the measurements and compilation of Dahlen et al. (2010). Figure 2.4 plots z_{spec} as a function of z_{phot} for these 41 sources. There is excellent agreement between these values except for 2 objects. One of these objects has a low z_{spec} quality flag, and for the other object the good quality z_{spec} is used over the

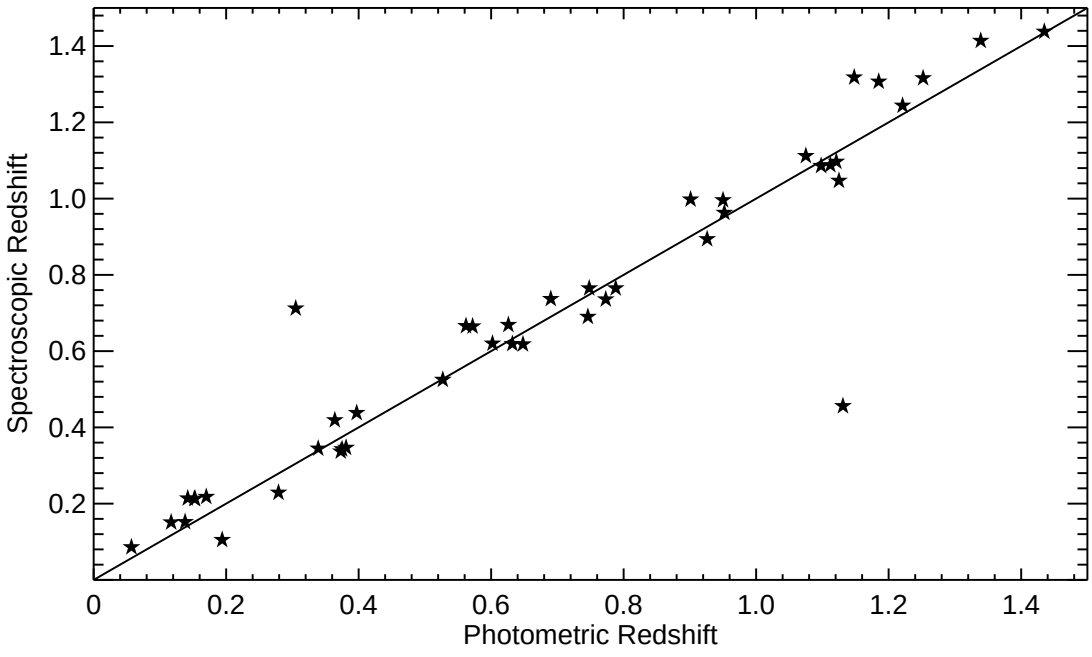

Figure 2.4 *Photometric Redshifts vs. Spectroscopic Redshifts from measurements and the spectroscopic compilation of Dahlen et al. (2010).*

z_{phot} for any further analysis. Column (14) lists the spectral types (STs) measured by Dahlen et al. (2010) that are based on spectral energy distributions (SEDs) from Coleman et al. (1980) and Kinney et al. (1996). Type 1 galaxies are early-types (E, S0, Sa), type 2 are Sbc, type 3 are Scd, type 4 are Magellanic irregulars (Im), and types 5 and 6 are starbursts SB1 and SB2. Some sources have non-integer STs (e.g., ST = 3.67) due to SED fits that were interpolated between subsequent templates (see Section 2.6 for further explanation of templates). The SED templates of SB1s and SB2s are differentiated by the values of intrinsic color excess, E(B-V). SB1 has E(B-V) $\leq$ 0.10, and SB2 has 0.11 $\leq$ E(B-V) $\leq$ 0.21 (Kinney et al., 1996). The 5″x5″ multiwavelength images of all 96 U-band detections (including the two stars) are displayed in the gallery in Figures 2.5(a)–2.5(k) which is also located online with the U-band catalog at: http://goods.gsfc.nasa.gov/release/UDF_F300W/original/gallery/udf_u_fuv.html. From left to right the columns of images are U, B, V, i, z, and composite BVi images. The optical images are from Beckwith et al. (2006) high-level public data products in the STScI archive except if the object is slightly outside of the original HUDF survey field. In this case the GOODS data are used (Giavalisco et al., 2004) for the optical images. The composite images are from the GOODS Cut Out Service on MAST[2]. Objects in the gallery are in the same order of ascending R.A. as in the catalog and have corresponding ID numbers. At the lower right of each image is listed its best quality redshift (z_{phot} or z_{spec}), apparent U-band magnitude (AB), ST, and visual morphology from Elmegreen et al. (2007) (hereafter E07) where 1 = chain, 2 = double, 3 = tadpole, 4 = spiral, 5 = spheroidal, 6 = clump-cluster (see Section 2.6 for more details on E07 classification). If any of the listed values are set to zero then the object is a star or a point source.

2.6 Morphologies and Spectral Types

One of the advantages of using the HUDF, besides the high resolution and depth of the Hubble images, is also the multiwavelength coverage available which is necessary

[2]http://archive.stsci.edu/eidol.php

(a)

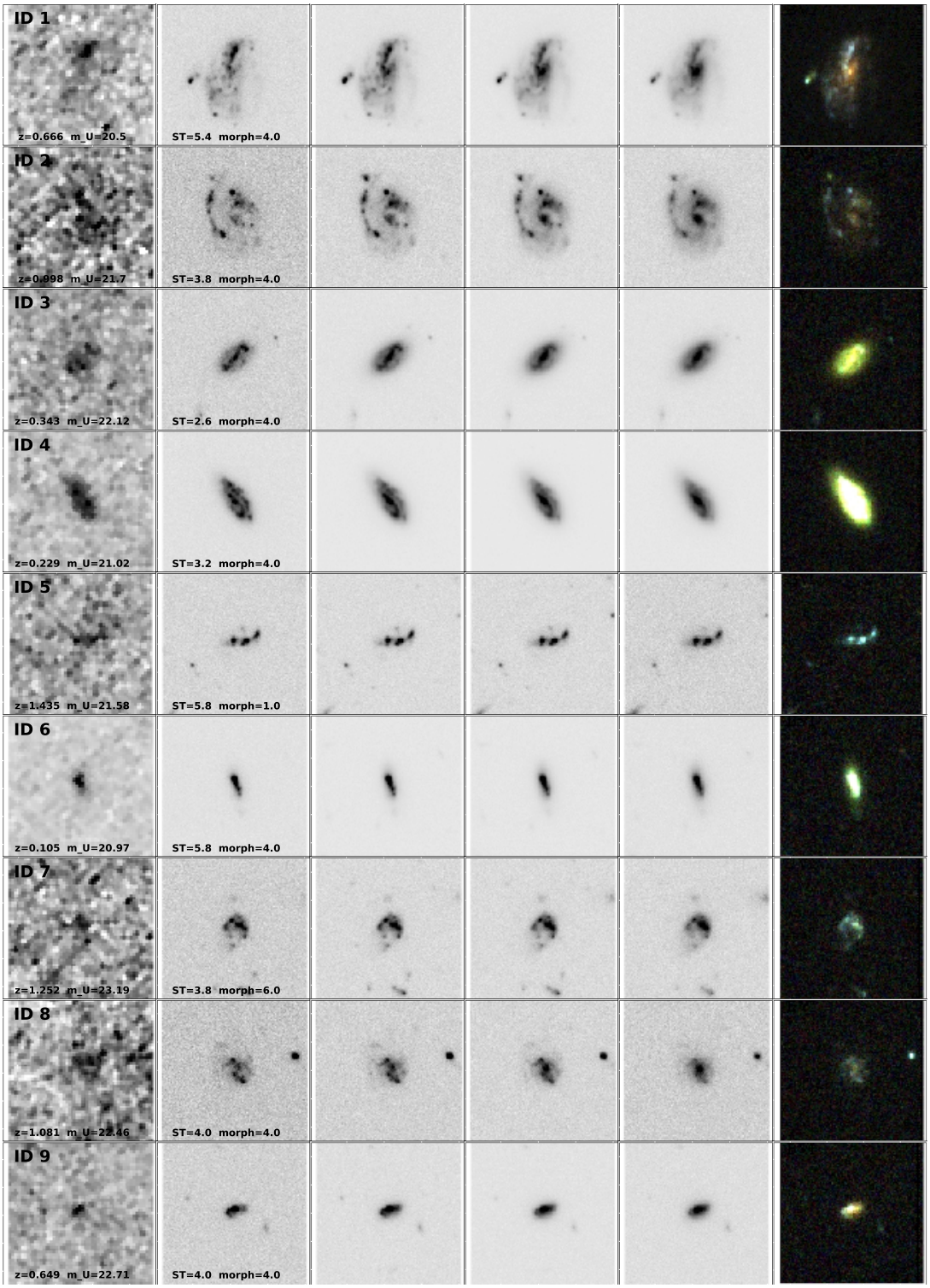

Figure 2.5 *U-band detected galaxy IDs 1–9. See (k) for full description of gallery.*

(b)

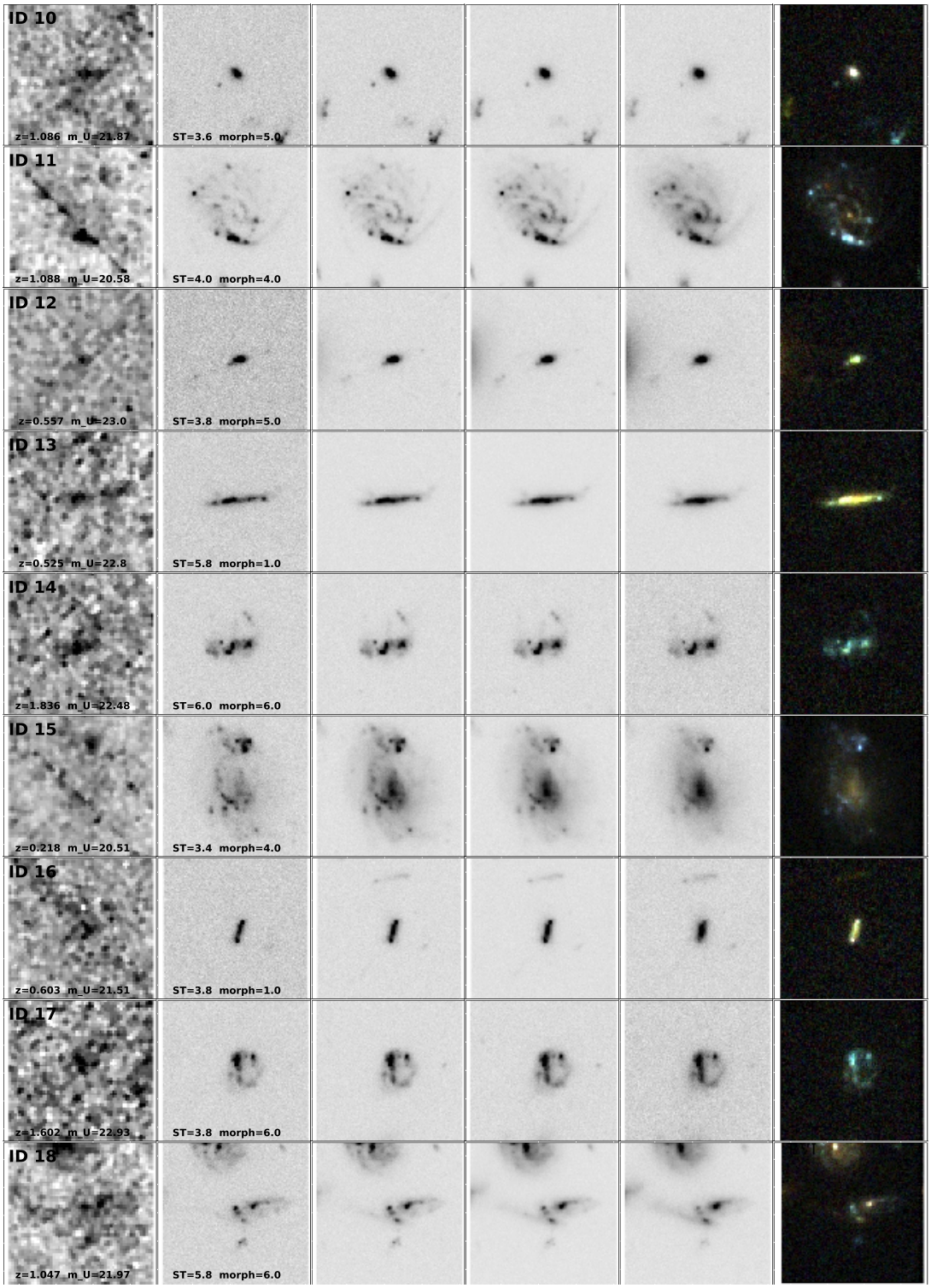

Figure 2.5 *U-band detected galaxy IDs 10–18. See (k) for full description of gallery.*

(c)

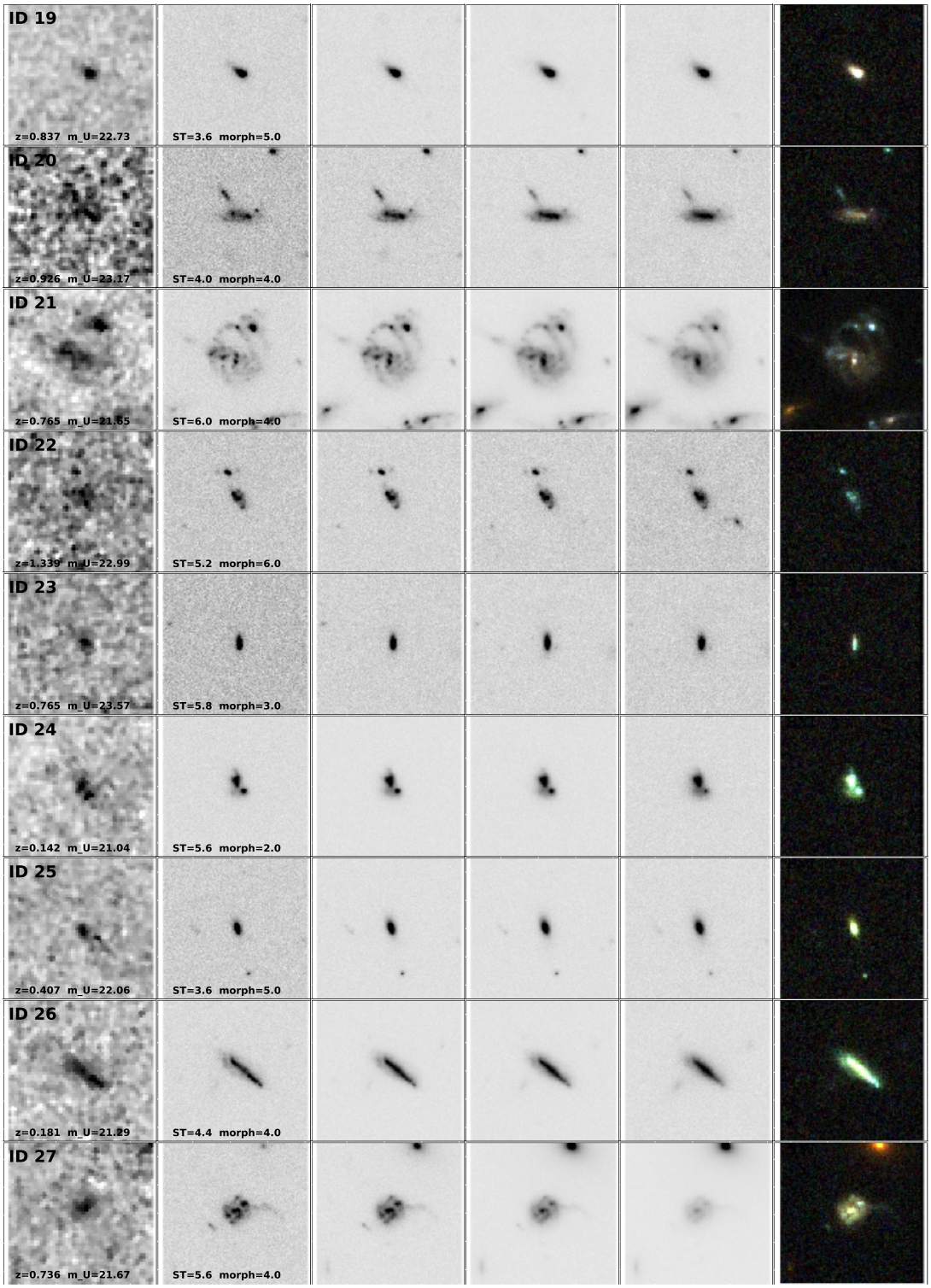

Figure 2.5 *U-band detected galaxy IDs 19–27. See (k) for full description of gallery.*

(d)

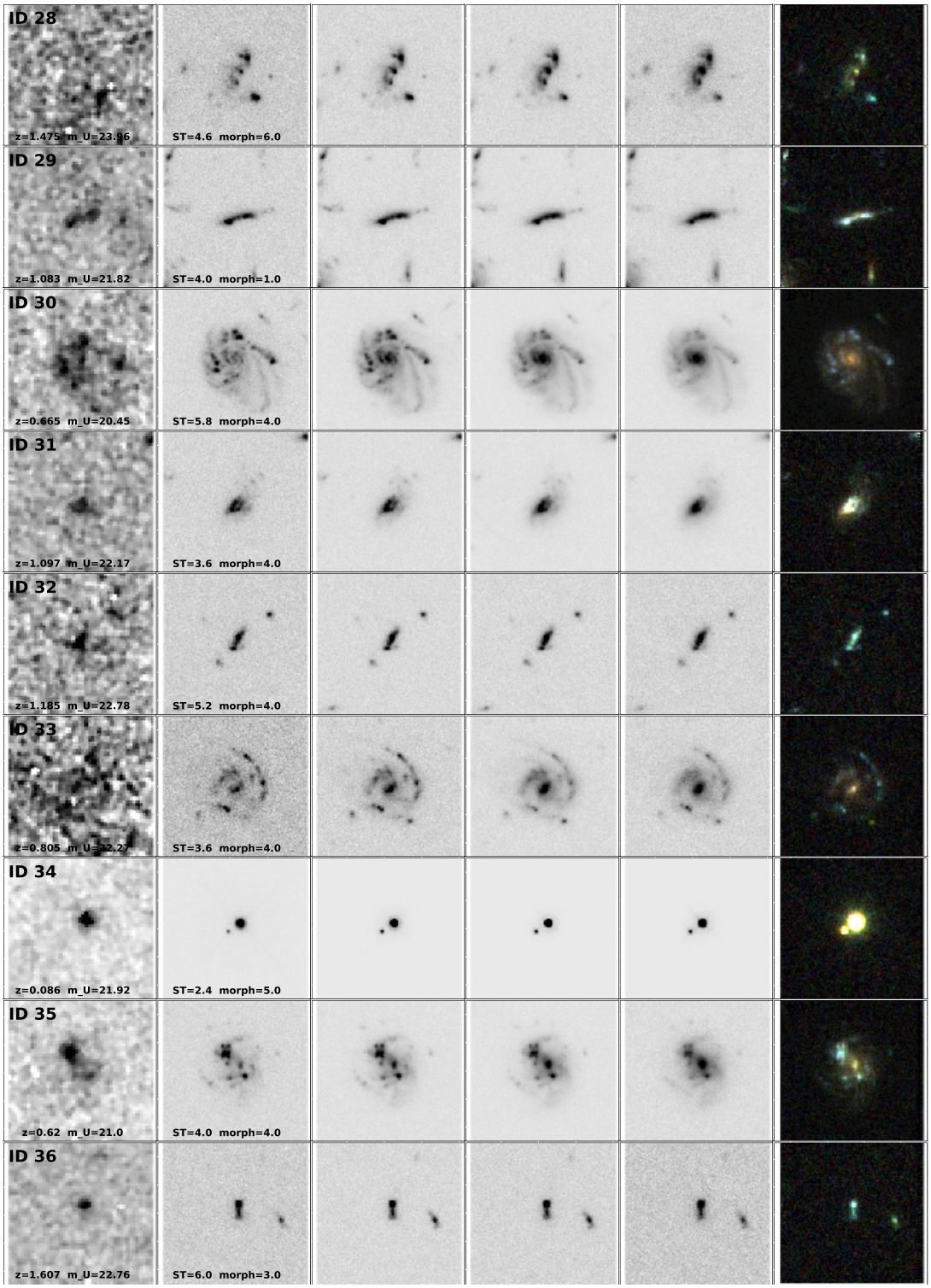

Figure 2.5 *U-band detected galaxy IDs 28–36. See (k) for full description of gallery.*

(e)

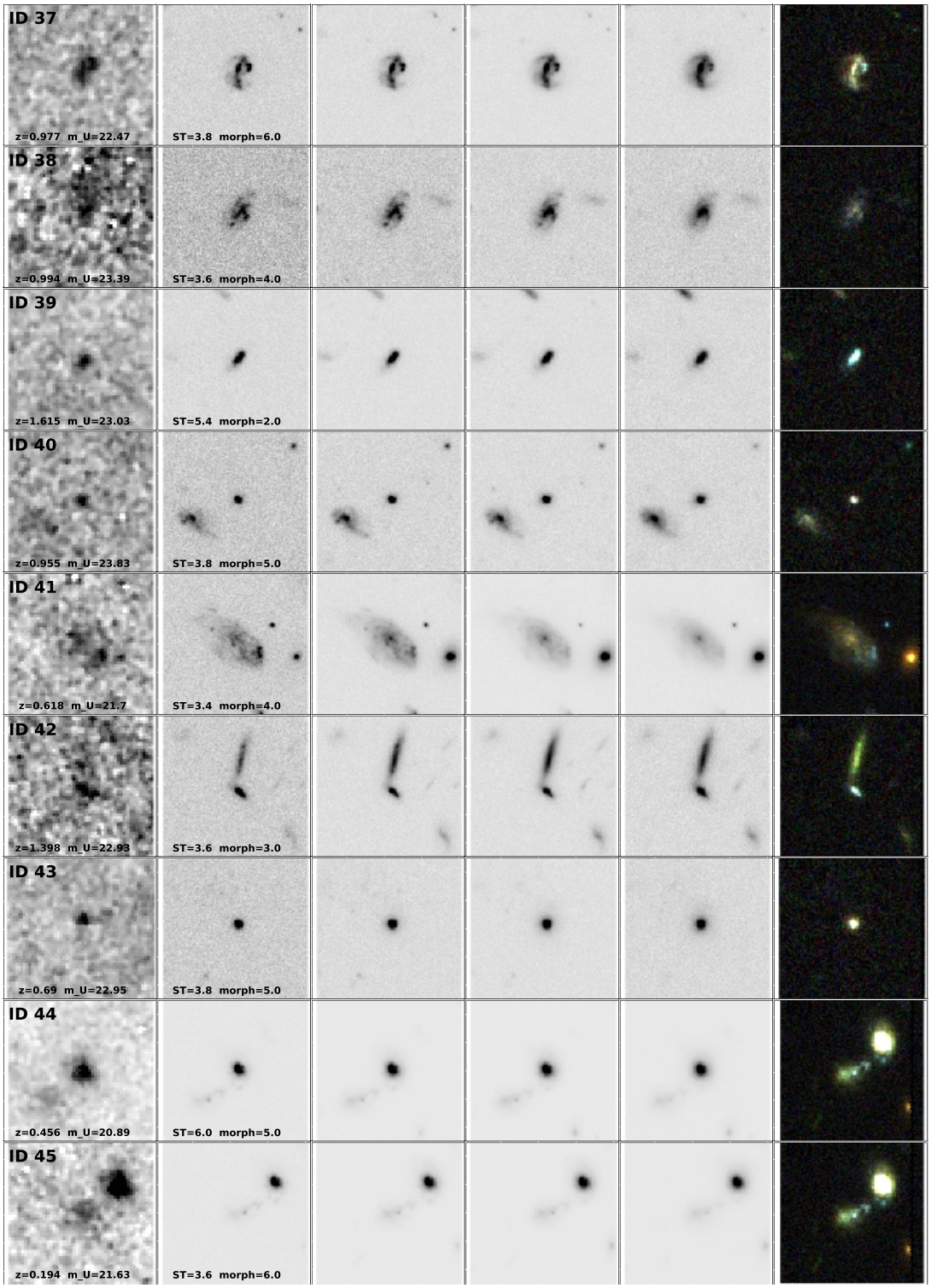

Figure 2.5 *U-band detected galaxy IDs 37–45. See (k) for full description of gallery.*

(f)

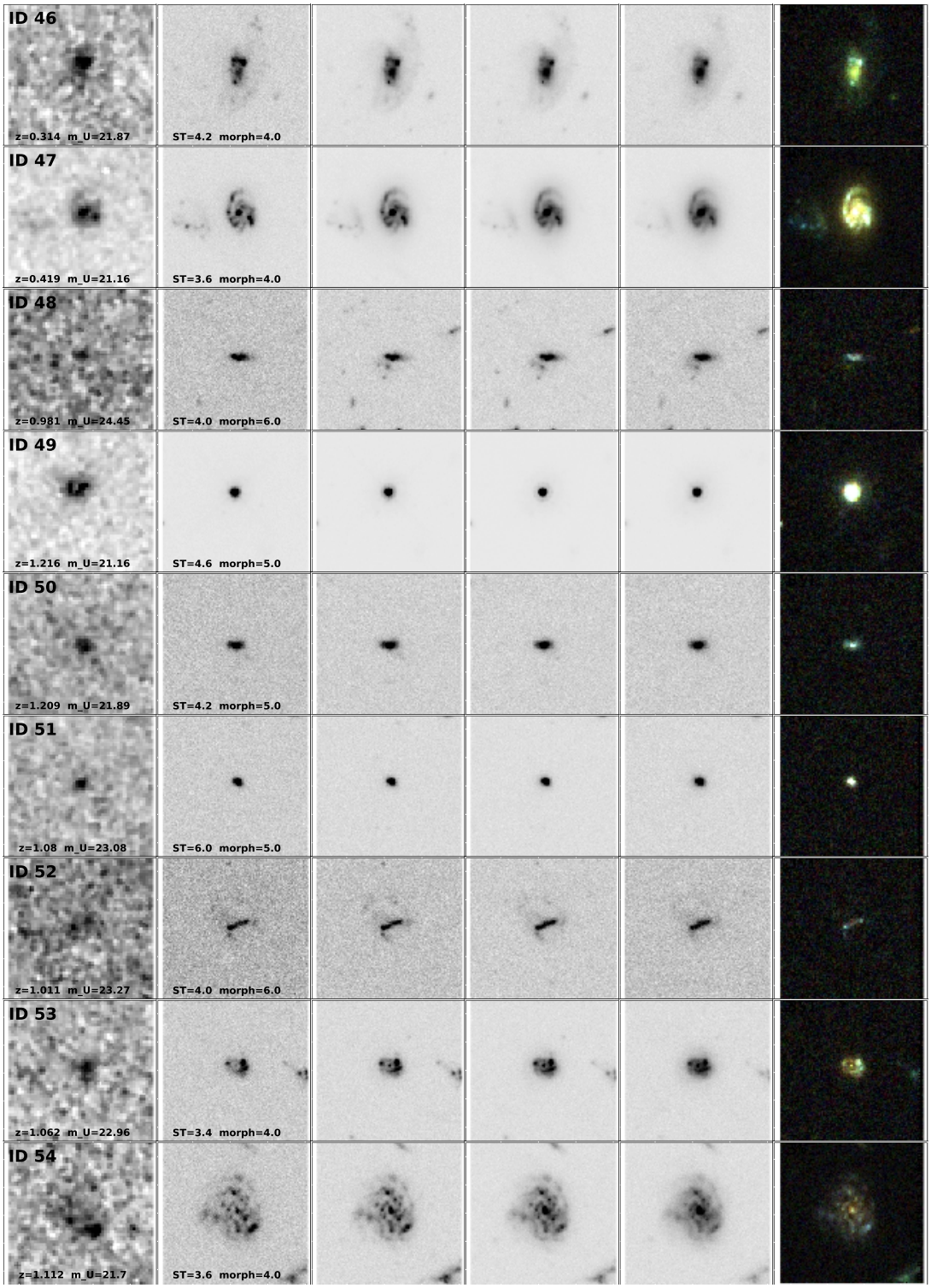

Figure 2.5 *U-band detected galaxy IDs 46–54. See (k) for full description of gallery.*

(g)

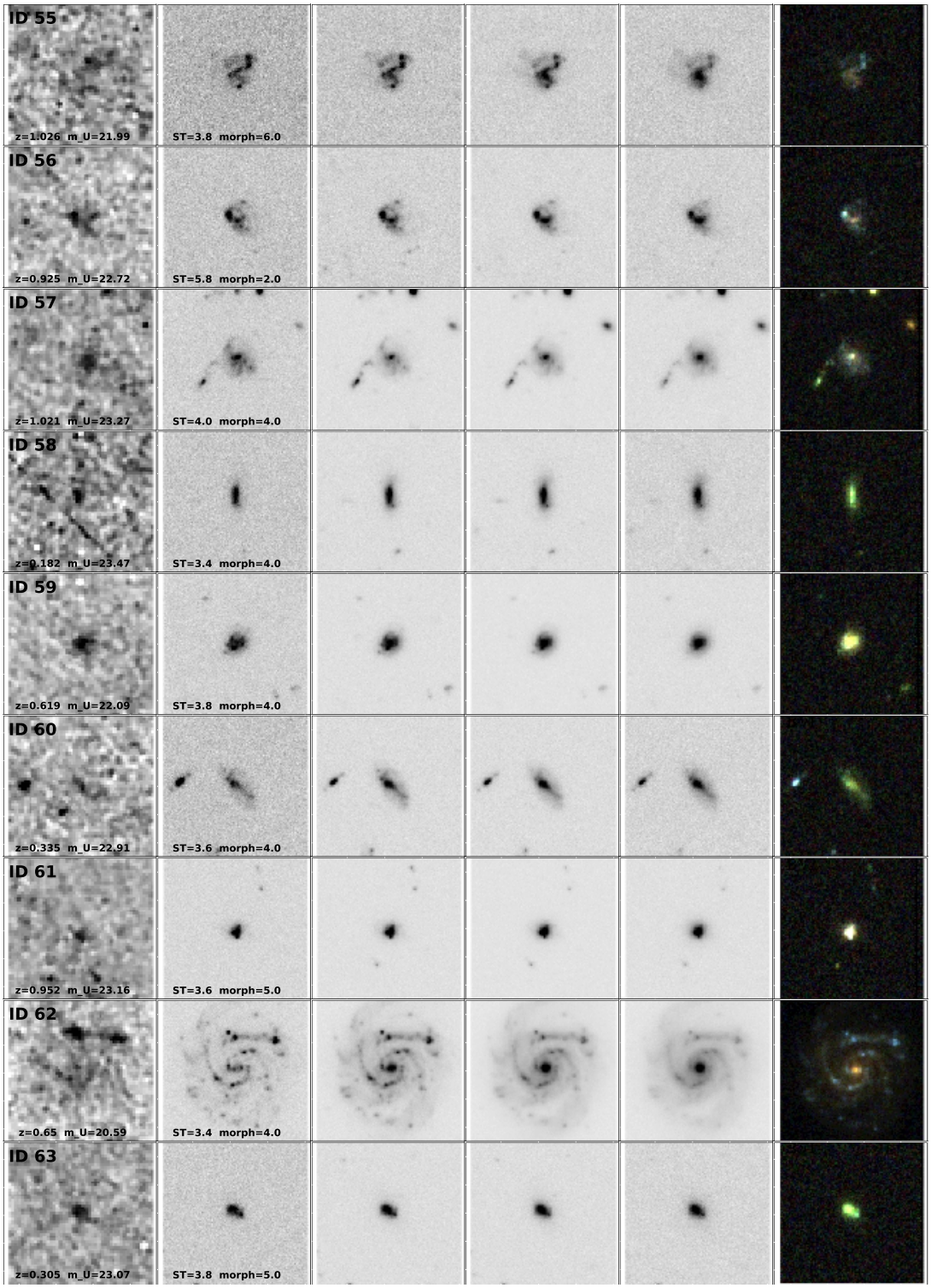

Figure 2.5 *U-band detected galaxy IDs 55–63. See (k) for full description of gallery.*

(h)

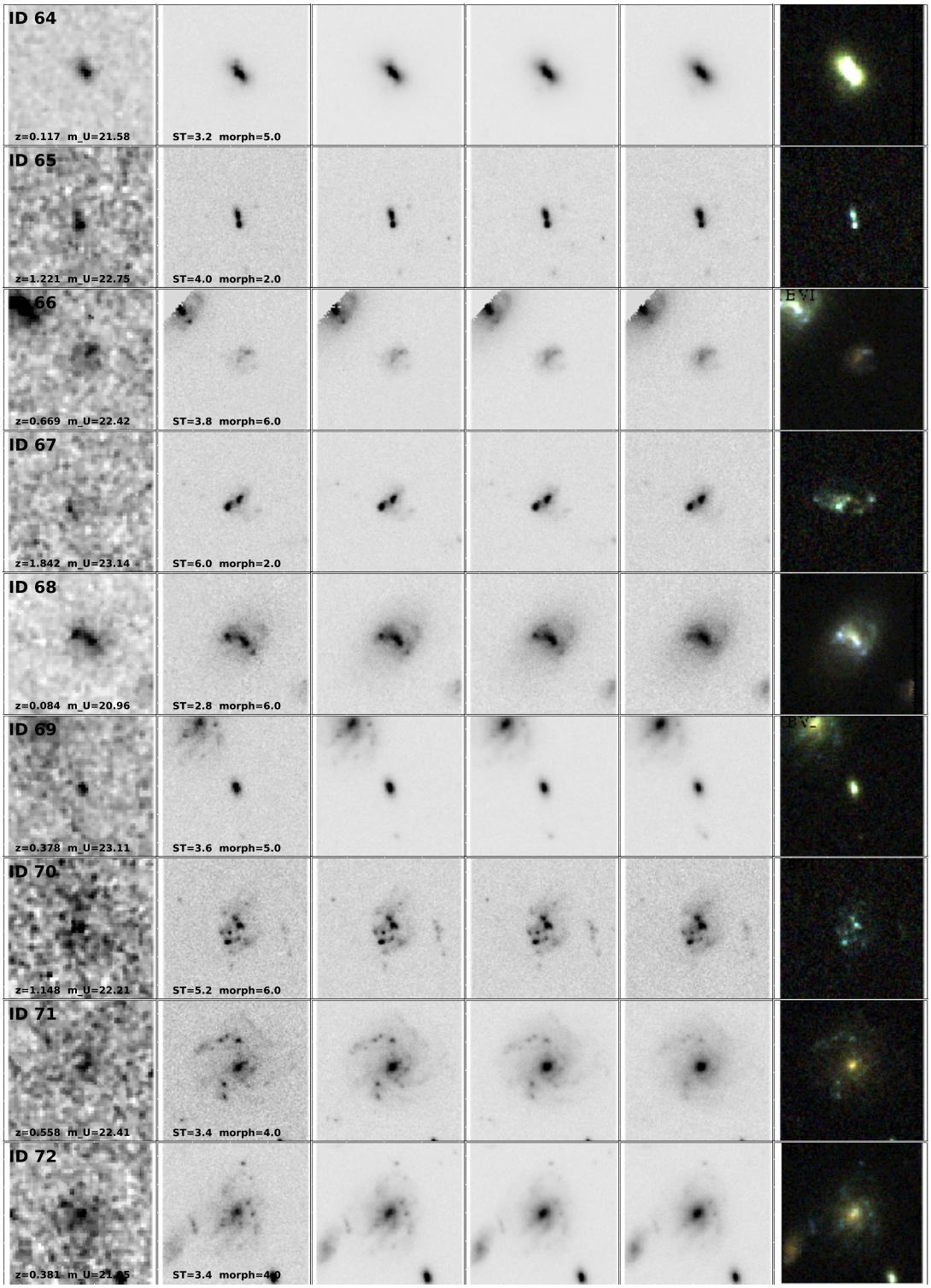

Figure 2.5 *U-band detected galaxy IDs 64–72. See (k) for full description of gallery.*

(i)

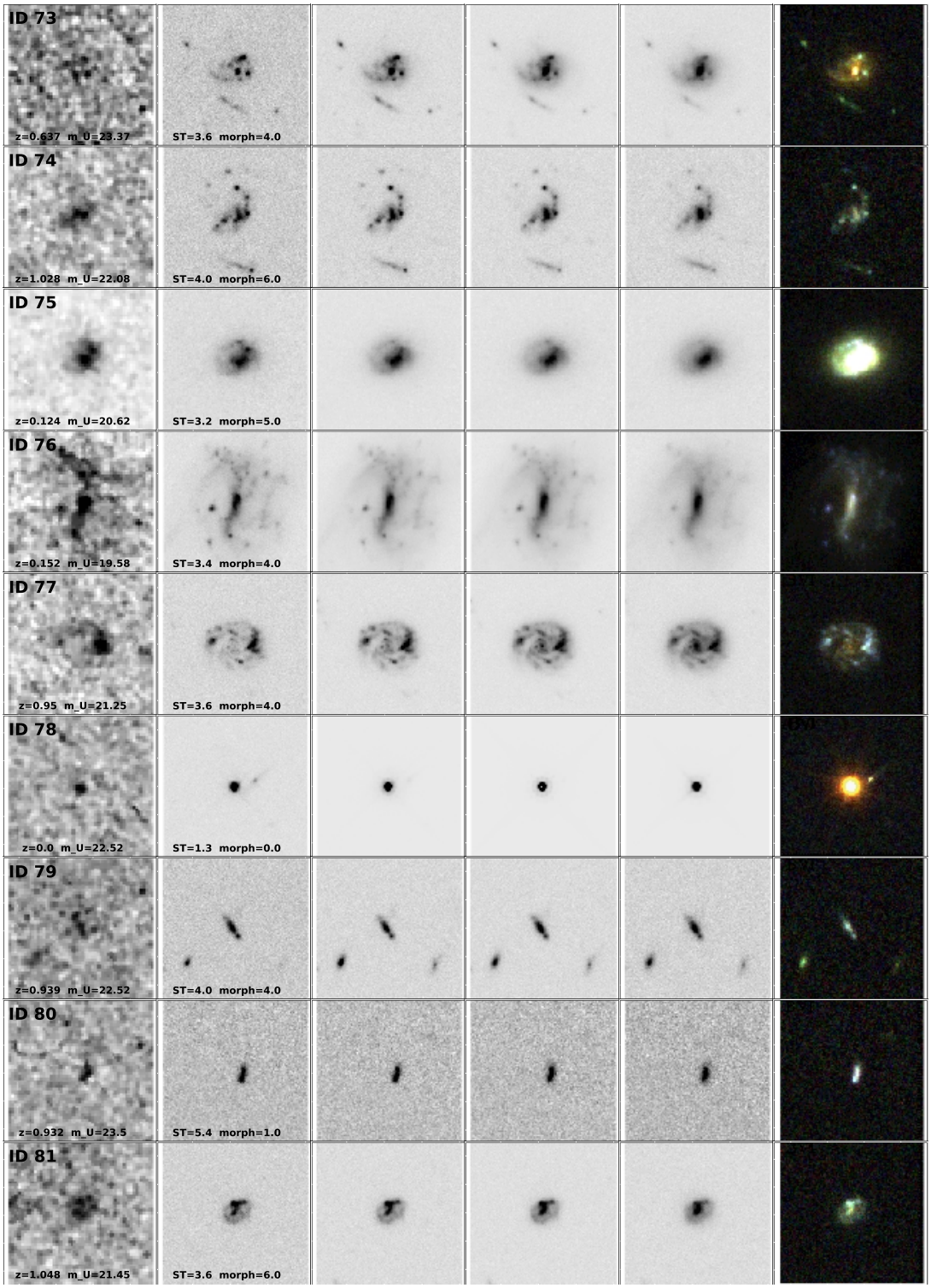

Figure 2.5 *U-band detected galaxy IDs 73–81. See (k) for full description of gallery.*

(j)

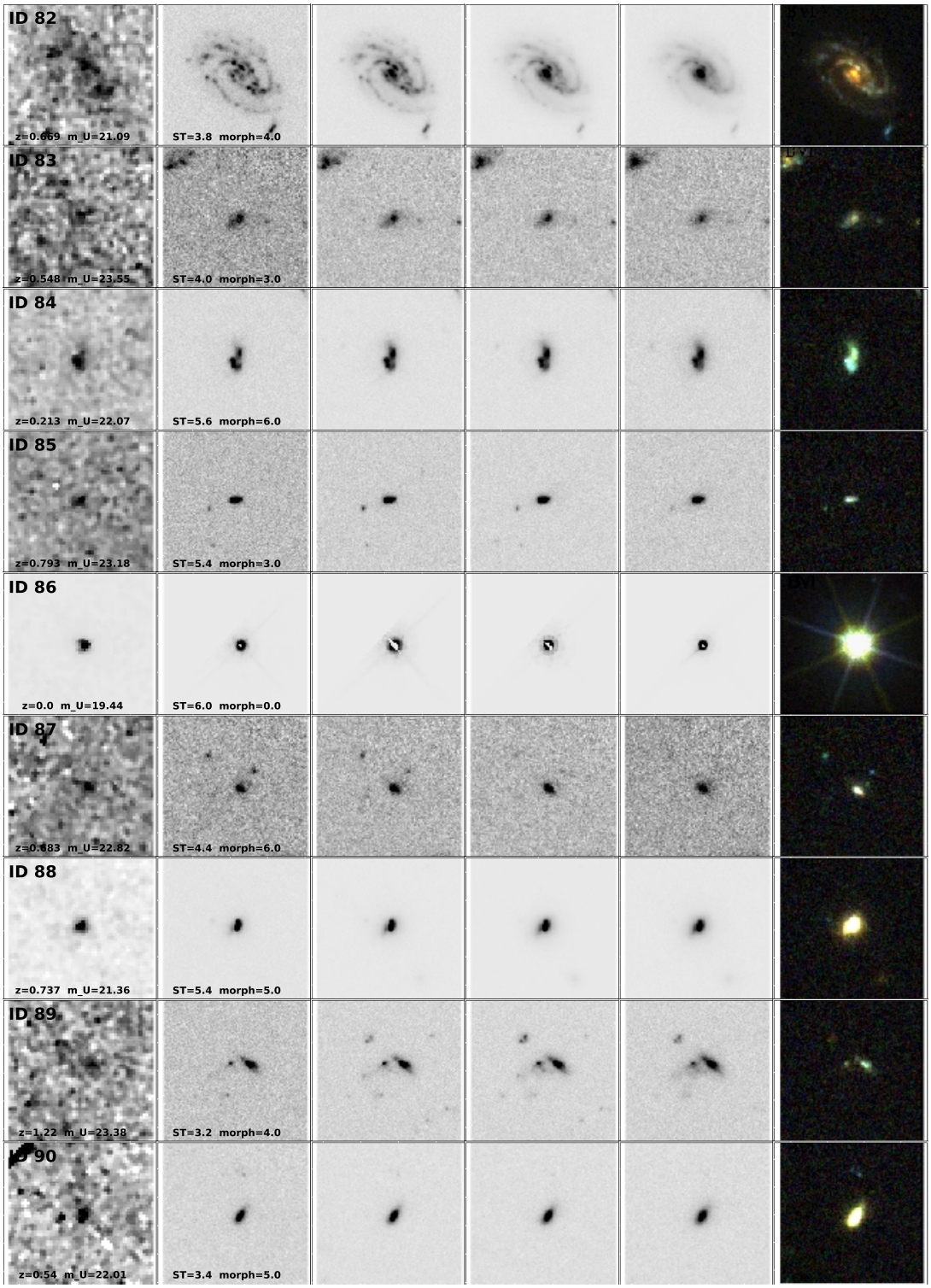

Figure 2.5 *U-band detected galaxy IDs 82–90. See (k) for full description of gallery.*

(k)

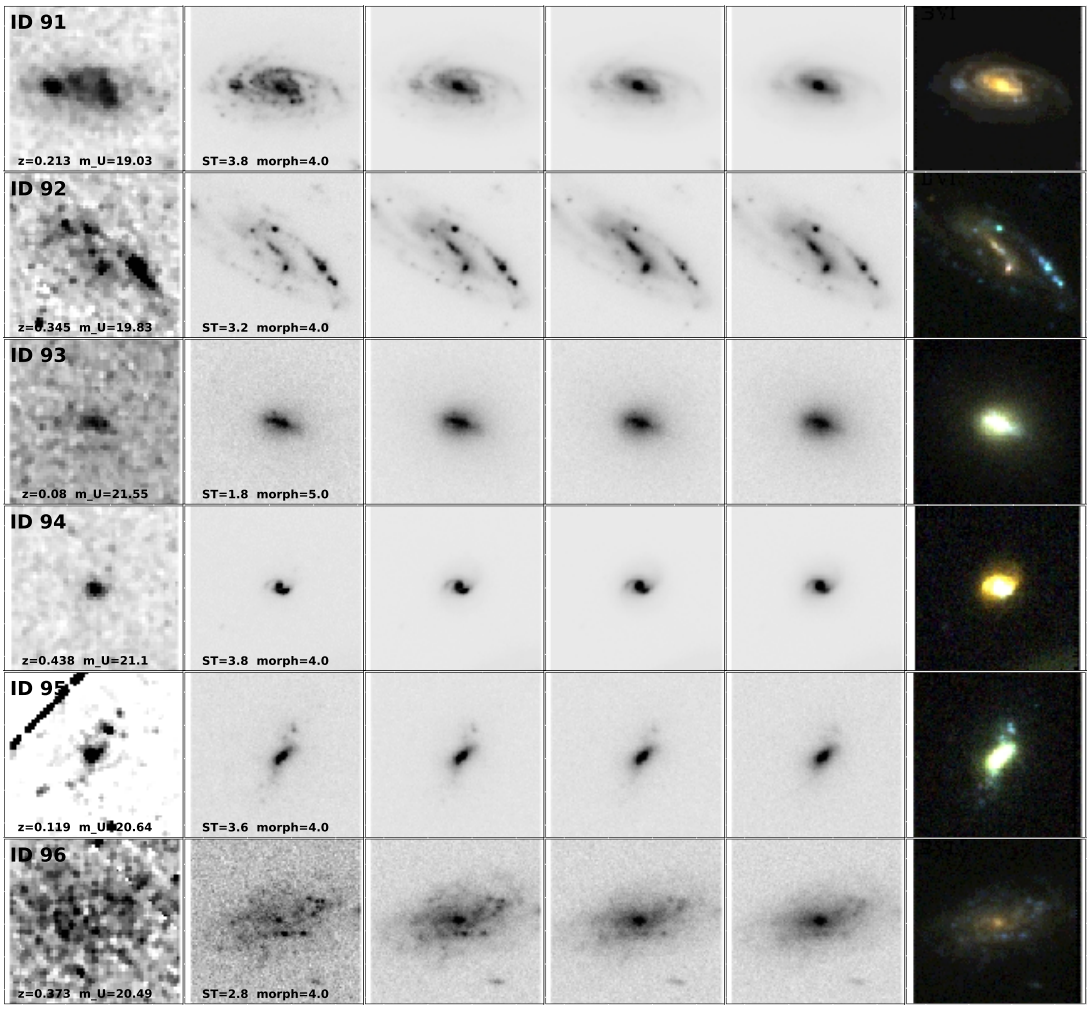

Figure 2.5 *U-band detected galaxy IDs 91–96. From left to right: multiwavelength (U, B, V, i, z and composite BVi) images of the HUDF U-band detected sources. Best quality redshift, U-band magnitude (AB), spectral type, and Elmegreen et al. (2007) visual morphology (1 = chain, 2 = double,3 = tadpole,4 = spiral,5 = spheroidal,6 = clump-cluster) are listed.*

in order to proper evaluate the overall morphology of the galaxies. Rest-frame UV can be misleading when viewed alone because it targets only the regions of new fstar formation in a galaxy instead of its overall structure which also includes the bulk of the stellar population, gas, and dust (e.g., Hibbard and Vacca 1997, Teplitz et al. 2006, de Mello et al. 2006a, b, Toft et al. 2007). Therefore, by using the HUDF multiwavelength coverage, it is also possible to localize where old and new star formation are located within the overall structure of a galaxy. The catalog gallery (Figures 2.5(a)–2.5(k)) shows that there are a wide variety of optical morphologies in the U-band sample.

The U-band detected galaxies can very generally be split into categories of disky and compact objects when looking at their optical images. It appears that only the most compact sources are similar across all bandpasses. This is clearly portrayed in a smaller gallery of four selected compact sources in Figure 2.6. In the color composite images of these compact sources in the larger U-band gallery, objects #39 and 63 appear very blue in their BVi images, while objects #43 and 90 are quite yellow. Despite this apparent color difference, the yellow objects don't appear any fainter in their U-band images than the blue, however they may be slightly smaller compared to their optical images. This could be due to enhanced star formation in the bluer compact galaxies versus those more yellow in color.

Alternatively, Figure 2.7 presents a gallery of four selected disky sources. It is clear that in their rest-UV (U-band) images small knots and large clumps of star formation are primarily detected, while in their rest-optical B- and V-band images older stellar populations and a diffuse disk begin to appear. Spiral arms are also well defined in the B and V images, while none can be viewed in the U-band images for objects #82 and 1, and slight traces of these arms appear in the U-band for objects #30 and 62. However it is not clear from the U-band alone that these are disky sources. In the redder i- and z- bands the knots of star formation nearly completely disappear from all disky sources and only the bulge component and the diffuse disk and spiral arms are visible. Thus, the largest morphological disconnect appears between the observed U-band and the i- and z-bands. It is also interesting to note that the bulge component

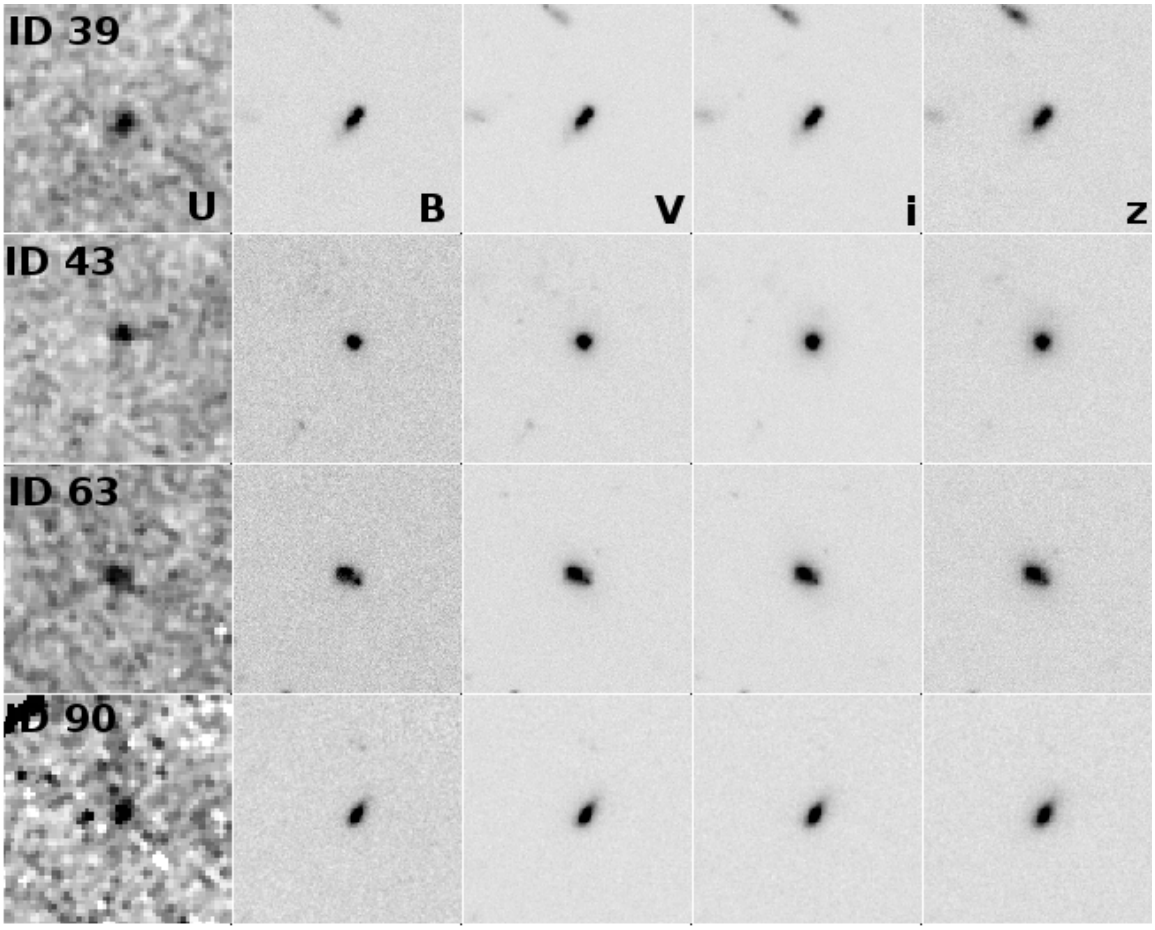

Figure 2.6 *Gallery of four selected compact U-band detected galaxies. Morphologies of compact sources in the U-band catalog are consistent throughout observations in the rest-UV to rest-optical.*

of these sources does not appear until viewed in the V-band, demonstrating that it may be difficult to judge bulge growth by looking at rest-UV data and the shortest wavelength rest-optical data. However, one exception may be object #30 that may be showing a small amount of rest-UV emission from the bulge region when compared to its z-images, but this is quite subjective to the viewer. It would be interesting to further consider the physical locations of this emission more quantitatively in order to determine if there could be trace amounts of star formation in bulges at intermediate redshifts. However, this feature could result from the UV upturn, be a small knot of

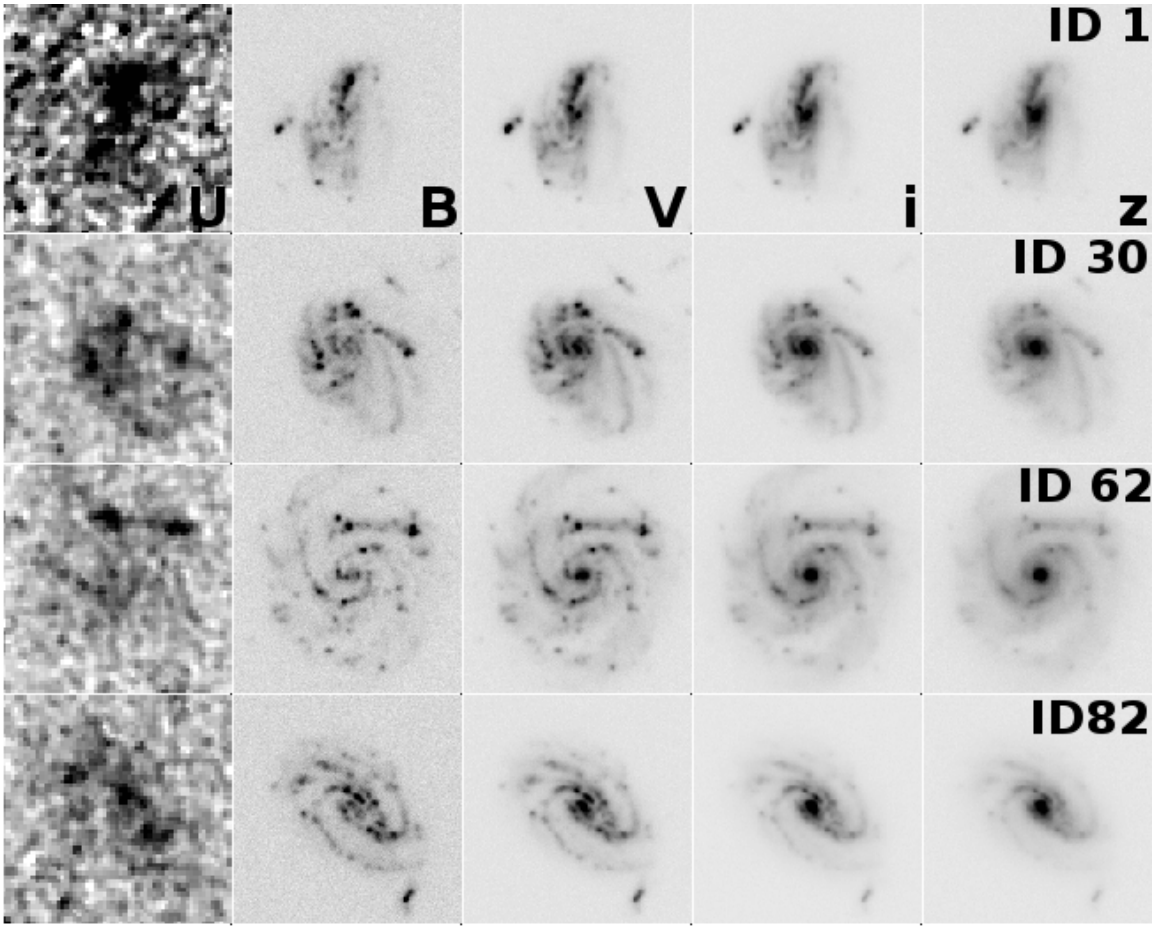

Figure 2.7 *Gallery of four selected disky U-band detected galaxies. Morphologies of disky sources are largely disconnected between their rest-UV and rest-optical morphologies, appearing clumpy and unordered in the rest-UV (U-band) and showing well formed spiral structure in the rest-optical bands (B, V, i, z).*

star formation passing through the galactic nucleus as a result of a minor merger, or indicate AGN activity.

Two primary ways to evaluate morphologies are visually and determining spectral types based on SEDs. In this section both of these methods are used to analyze the U-band sample. As mentioned previously, SED based STs are from (Dahlen et al., 2010). SEDs are a collective overview of the absorption and emission activities of the different physical components of a galaxy. Radiation emitted as a result of nuclear processes inside the stellar constituents of galaxies will either be directly radiated

out of the galaxy, or scattered, absorbed, or re-radiated in another wavelength by other components (primarily gas and dust) of the galaxy. Thus, SEDs are incredibly powerful tools for providing information about the energy budget of galaxies. The well modeled SEDs of local galaxies are extended to more distant sources by applying a k-correction to the spectra which essentially translates it to the rest-frame of the distant source. The Dahlen et al. (2010) photometric redshifts are derived from a large range of the most current deepest available data from VLT/VIMOS U-band observations to Spitzer/IRAC 8μm data. Best fitting spectral types are determined in the course of the SED fitting for the redshift calculations. Figure 2.8 shows the SEDs from Coleman et al. (1980) and Kinney et al. (1996) on which the ST determination is based. For Sbc, Scd, Im, and SB1 the combined effects of the Balmer 3646Å and 4000Å breaks are noticeable in the templates, blending together in some cases. The Balmer 3646Å break is caused by the build up of absorption lines at the termination of the hydrogen Balmer series (n=2), while the 4000Å break is due to an accumulation of absorption lines of

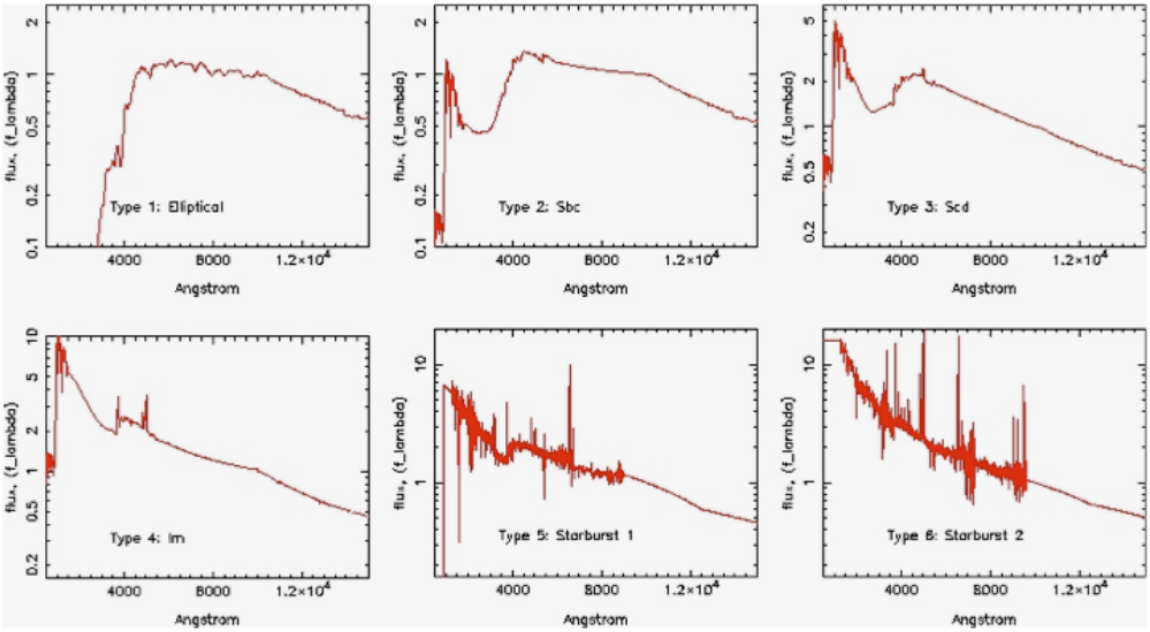

Figure 2.8 *Spectral energy distributions from Coleman et al. (1980) (E, Sbc, Scd, Im) and Kinney et al. (1996) (SB1, SB2) that are the basis for the spectral types (STs) used throughout this thesis (Dahlen et al., 2010).*

ionized metals. Both effects take place within stellar atmospheres and are sensitive to stellar types and ages. The Balmer 3646Å break is strongest in A-type stars, while the 4000Å break strengthens with increasing stellar age as older stellar populations are cooler (more opaque) and contain more metals. The difference between starburst type 1 and 2 STs templates has been discussed in previous Section (2.5). This is the largest, most comprehensive redshift and ST catalog in GOODS-S to date. The visual morphologies of the sample are derived from E07 morphological classifications based on the visual and surface brightness analysis of HUDF ACS i-band images. Their classification types are described as follows: chains, with prominent clumps in a straight row; doubles, with two prominent, apparently connected clumps; clump-clusters, with several apparently connected clumps in a three dimensional or disk arrangement; tadpoles, with one prominent clump and a tail of smaller clumps or diffuse emission; spirals, with a nucleus, spiral-arm-like structure and an exponential-like disk profile; and ellipticals, with a spheroidal central light concentration based on concentric elliptical light contours. Examples of each morphological type are displayed in Figure 2.9.

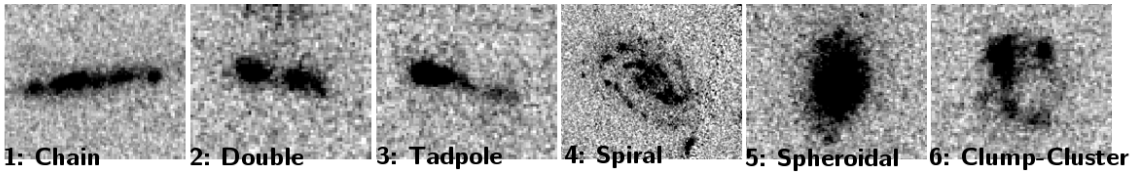

Figure 2.9 *Visual aid of morphological classifications from Elmegreen et al. (2007) used extensively in this thesis. Galaxies are from GOODS-S i-band images. This is the bandpass in which morphological types were originally assigned.*

First looking at the ST distribution of the 94 U-band sources in Figure 2.10 it is clear that spiral types Scd galaxies dominate the sample after which starbursts and Im (Magellanic irregulars, see Coleman et al. (1980)) types compose most of the remaining detections. There are no elliptical STs and only two Sbc sources. Using the E07 visual morphology scheme it is found that, of the 94 U-band galaxies, 42 of are spirals, 19 are spheroidals, 18 are clump-clusters, and there are 5 of each chains and doubles, and 4 tadpoles. In Figure 2.11 ST is plotted as a function of redshift for all

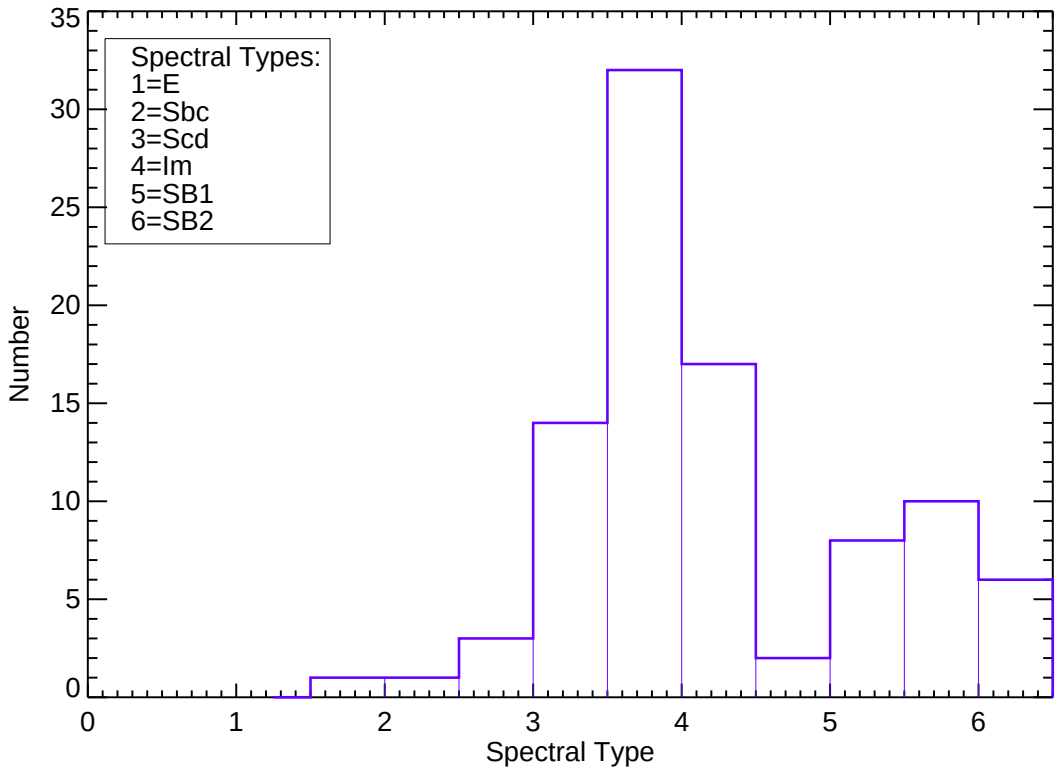

Figure 2.10 *Distribution of SED based spectral types of all 94 U-band detected galaxies. The spectral types are from the compilation of Dahlen et al. (2010) and their values are: 1 = E, 2 = Sbc, 3 = Scd, 4 = Im, 5 = Starburst 1, 6 = Starburst 2. Non-integer STs (e.g., ST = 3.67) are due to SED fits that were interpolated between subsequent templates.*

U-band objects throughout the six different visual morphological classes. Although

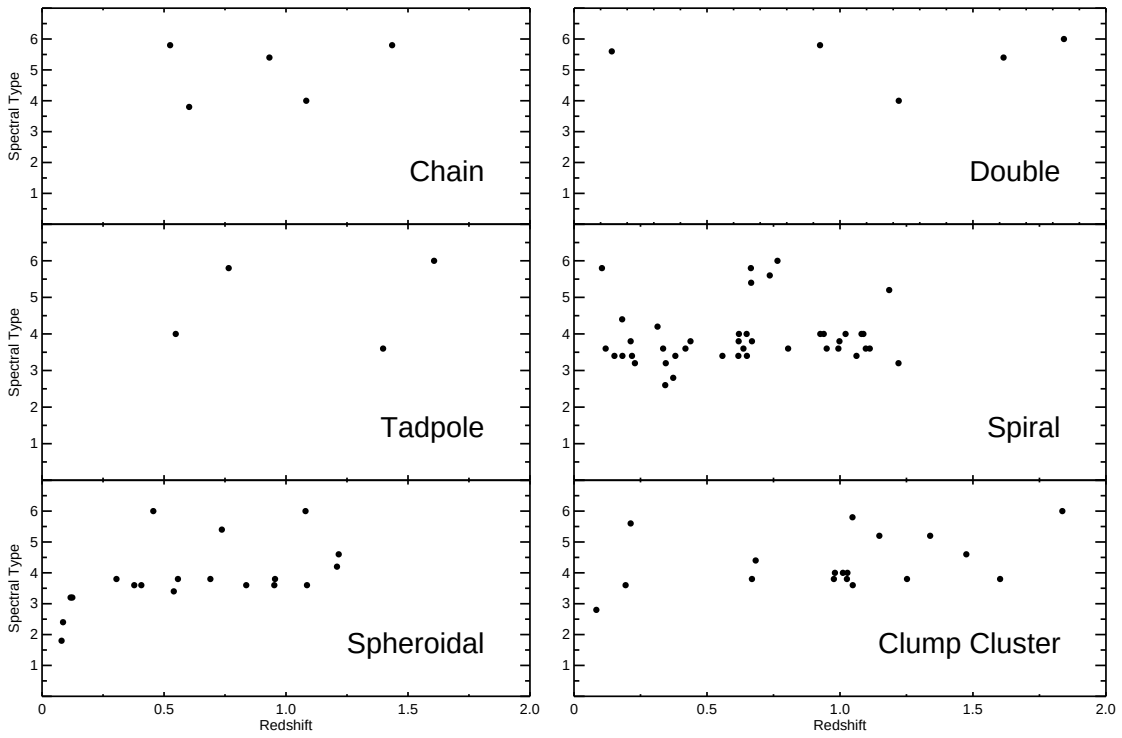

Figure 2.11 *Spectral types of U-band detected galaxies as a function of best available redshift split into bins of visual morphologies (classification from Elmegreen et al. (2007)). No spiral or spheroidal types are detected past $z \sim 1.25$, however all other types are detected at $z > 1.25$, suggesting potential evolution between these populations.*

there are only a few sources in their morphological bins, it appears that chains and doubles tend to have mainly starburst types (ST =5, 6), while the other clumpy morphologies, tadpoles and clump-clusters are split between starbursts and Im types. Past $z > 1.25$ there is a lack of spirals and spheroidals, while clump-clusters dominate at higher redshifts. This lends evidence to the suggestion that clump-clusters are the progenitors of star-forming spirals and spheroidal galaxies E07. The spheroidal U-band sources have very consistent Im (4) STs from $z \sim 0.25$–1.25, with only 3 anomalous starburst STs. Below $z \sim 0.25$ spheroidal distribution dips towards Scd and Sbc STs, hinting that in the local universe these sources would most likely be

visually and spectraly classified as the same types. However, at higher redshifts their ST diverge from any regular type.

Very few tadpoles (4%) and chains (5%) are detected in our U-band image. Because tadpoles might be disks in formation and/or merger remnants, knowing the fraction of star-forming tadpoles is an important detail in understanding the physical significance of these events in the overall galaxy evolution scenario. Straughn et al. (2006) used ACS i-band images to detect a significant sample of tadpole galaxies in the HUDF, and found for each redshift epoch between $0.1 \leq z \leq 4.5$ tadpoles consistently represented $\sim$6% of the overall field galaxy population. Based on this measurement, they reason that all galaxies that formed since re-ionization spend $\sim$0.8 Gyr in a merger/tadpole stage. The small percentage of tadpoles detected in our image suggests that they are either not present at intermediate redshift or that there is a selection effect, e.g. these types of objects may be either too faint to detect in our image, or, are high-redshift U-dropouts only visible at longer wavelengths. It has been checked whether this is really the case by comparing these statistics with those from detections in the U-band parallel image to the ACS HUDF; the deepest U-band image ever taken (de Mello et al., 2006b; Wadadekar et al., 2006). This field lies on the edge of the GOODS-S field and is 4 magnitudes deeper than the HUDF data analyzed here. There are 306 sources analyzed in this image, and of these, they detected a larger fraction of faint tadpole (7%) and double or multiple clumps (13%) at $z < 2$ than what is detected in the HUDF U-band data presented here. Therefore, the fact that the HUDF U-band image only detects a few tadpoles suggests that it is limited to observing only the brightest tadpoles and could be missing $\sim$ 4–10% of the tadpole population that might be present in the HUDF area.

U-band sources are also evaluated in terms of the z_{phot} and STs parameters derived by E07 given in their i-band selected HUDF catalog. Figure 2.12 shows how the U-band sources (filled stars) that have matches in the larger E07 catalog are distributed within this overall catalog (open circles), providing a picture of how intermediate-redshift star-forming sources fit within the larger galaxy population observed in this field, since the E07 catalog is optically selected. The redshifts and STs used in the E07

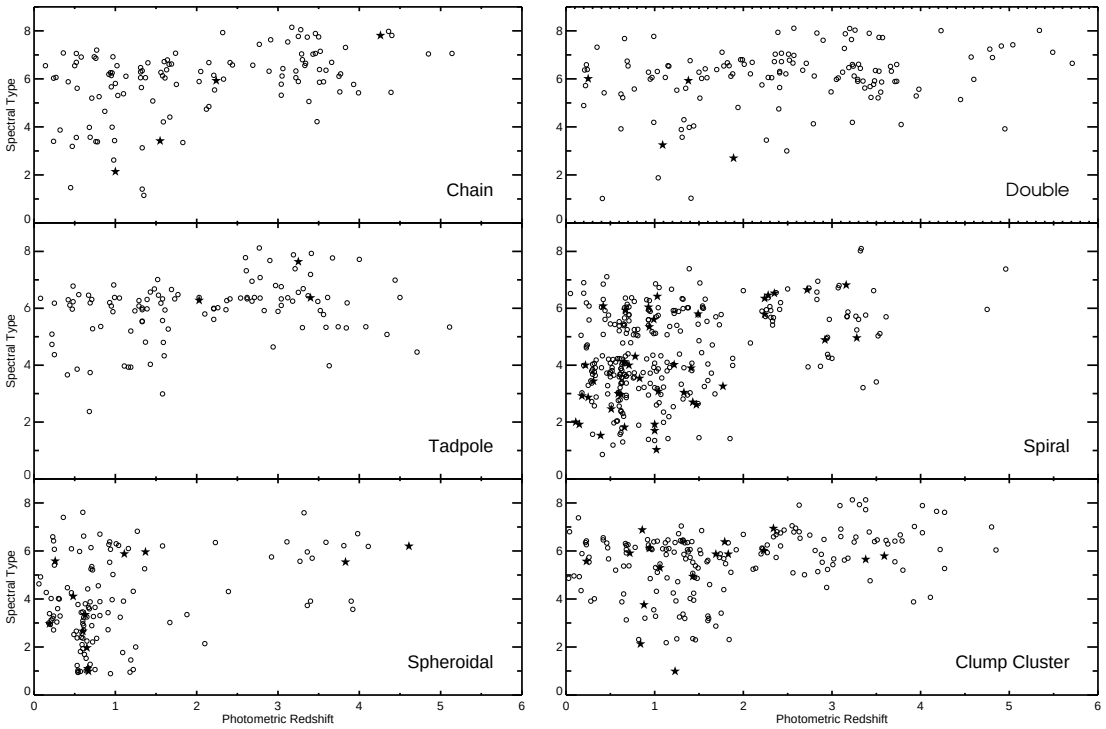

Figure 2.12 *Photometric Redshift vs. Spectral Type, where U-band objects (filled stars) are within E07's i-band selected HUDF catalog (open circles) using their redshifts and STs. The data was scattered at random by ±0.15 added to all ST values in order to better display the distributions.*

catalog and plotted in Figure 2.12 are from Coe et al. (2006) and were measured using the Bayesian method. There is not a good agreement with the Dahlen et al. (2010) redshifts matched with the U-band catalog for objects when compared to those derived by E07. There are 13 objects with GOODS redshifts larger than the U-band dropout limit (z = 2.3) which suggests that photometric redshifts were not well calculated re-emphasizing that the U-band can provide an excellent test of redshift accuracy, and the inclusion of these bandpasses and IR bandpasses in the z_{phot} calculation has made these redshifts highly reliable.

Of all the resolved HUDF objects, the U-band detects 3% of all chains, 3% of all doubles, 3% of all tadpoles, 8% of all clump-clusters, 9% of all spheroidals, and 13% of all spirals.The U-band clump-clusters mainly have STs = 5 and higher, similar to

the results in Figure 2.11. U-band detected spirals have a wide range of STs, as do all HUDF detected spirals. Figure 2.12 also shows five starbursting spheroidal U-band objects. Two of the U-band spheroidals in the group with spectral types between 3-5 appear blue in color, and could be possible blue clumps. In Elmegreen's HUDF catalog object 1 (RA = 53.1635971, DEC = -27.7935085) has ST = 2 and z = 0.65, and object 2 (RA=53.1703148, DEC=-27.7852764) has ST = 1 and z = 0.47. In the U-band catalog, objects 1 and 2 have starburst spectral types 6 and 5.67 and z = 1.54 and 0.29, respectively. Elmegreen & Elmegreen (2005) found that nearly half of all HUDF spheroidal objects with starburst spectral types have blue clumps, agreeing with the GOODS spectral types of objects 1 and 2 used in the U-band catalog.

2.7 Summary

This chapter has presented the first space-based U-band image targeted at the HUDF and its resulting catalog and gallery of star-forming sources in multiple wavelengths. By matching these data with other GOODS-S and HUDF catalogs, redshift and morphological information was attained for these sources. These data demonstrate the importance of multiwavelength data sets in order to gain the best understanding of the morphologies of galaxies. It is clear that most galaxies in this sample that are not compact show a large transformation between rest-UV (observed U-band) and rest-optical (observed B-, V-, i-, z-bands) morphologies at intermediate redshifts. Their rest-UV morphologies are unordered and clumpy, clearly mapping the regions of star formation in the overall optical morphologies. At very high redshifts even the IR will observe galaxies in the rest-frame UV, thus their optical morphologies will no longer be detectable and information on high-redshift galaxy evolution will come only from rest-UV wavelengths. Thus, a better understanding of the physical implications of rest-UV morphologies at intermediate redshifts will provide more clearly their evolutionary connections to high-redshift rest-UV galaxies that will be observed with the next generation of space- and ground-based observatories. The following conclusions can be made about this initial HUDF star-forming sample:

1. Using Elmegreen et al. (2007) morphological classification of the HUDF, it has been found that 42 U-band objects are spirals, 19 are spheroidals, 18 are clump clusters, and 5 are tadpoles, chains, and doubles each.

2. Clumpy type objects mainly have starburst spectral types, while spirals have a wide range of STs, and spheroidals are mainly Im types at $z > 0.25$, but have STs that better coincide with their visual morphologies at low redshifts.

3. Past $z > 1.0$ there is a lack of U-band detected spirals and spheroidals, while clump clusters dominate this epoch suggesting that clump-clusters could be the progenitors of spirals and spheroidal galaxies.

In the next chapter the physical properties of these star-forming sources are explored and analyzed in greater depth to attempt in determining their role in galaxy evolution over intermediate redshifts.

3

Sizes and Luminosities of Star-Forming Galaxies and Sub-Galactic Clumps at Intermediate Redshifts

This chapter focuses on the quantification of sizes and luminosities of star-forming galaxies and sub-galactic star-forming clumps at intermediate redshifts (i.e. $0.2 < z < 1.5$) in order to provide theorists and observers with realistic numbers regarding the physical scales and energy output of these sources and to explore their potential contributions and affects on the evolutionary sequence. The procedure to determine the size distributions and do the luminosity calculations are described within, and the results are presented in context with previous studies of star-forming galaxies at low and high redshift. This chapter addresses the following questions:

1. Do the physical sizes of various galaxy morphologies evolve with decreasing redshift? What does the answer to this question imply about a merger versus a secular evolution scenario of galaxy evolution?
2. What are the typical sizes of sub-galactic star-forming clumps at intermediate redshifts and how do they compare to measurements at high redshift? What

does this imply about the formation mechanisms of disk galaxies seen at the present epoch?

3. Are the intrinsic luminosities (energy output) of star-forming galaxies comparable at different redshifts, and if so is this indicative that these are the same types of galaxy populations?

3.1 Introduction

Galaxy growth as a function of redshift is a direct prediction of hierarchical models of galaxy evolution. For instance Somerville et al. (2008) semi-analytical models, using the hierarchical paradigm of structure formation, predict that at $z \sim 2$ ($\sim$10 Gyr ago) disks at fixed stellar masses were on average 60% as large as they are today. They also predict that there is only mild evolution in the relationship between radial size and stellar mass for galactic disks from $z \sim 1$ ($\sim$7.8 Gyr ago) to the present day. The latter prediction agrees with what is found in surveys of distant galaxies with the Hubble Space Telescope. For example, Ravindranath et al. (2004) does not find any significant signs of size evolution in disks at $z < 1$ in the GOODS survey data. Therefore, whatever physical mechanisms drove galaxy evolution during the $\sim$2.5 Gyr period between $1 < z < 2$ defines disks as seen today. This epoch also marks the turning point of the star-formation rate density of the universe as a function of cosmic time (e.g. Reddy & Steidel (2009); Bouwens et al. (2007); Wadadekar et al. (2006)), and when the majority of star-formation activity shifted from high- to lower-mass galaxies, i.e. downsizing (Cowie et al., 1996; Savaglio et al., 2005; Mouri & Taniguchi, 2006; Neistein et al., 2006). Evidence from several high-redshift studies of star-forming galaxies along with the increasing *star-formation rate density* (see Section 1.4 for definition and discussion) towards lower redshifts at $z > 1$ suggest that mergers of smaller galaxies were more important to the assembly process at high redshifts. These data have shown strong evidence of the hierarchical galaxy assembly scenario. If galaxy build-up due to merging is indeed the case at high redshifts, star-formation in the intermediate-redshift universe would be expected to take place in

two different types of galaxies: disks already assembled and small galaxies.

Morphologically, many of these high-redshift (z $\sim$ 1.5–3) star-forming sources are clumpy galaxies that, in the rest-frame UV, consist of large knots of star-forming regions with no discernible central bulge and disk arrangement (i.e. no exponential light profile). These were first established as a morphological class separate from disk or edge-on disk galaxies by Elmegreen et al. (2004) who named them "clump-clusters". Their initial study of clump-clusters concludes that these sources are face-on versions of chain galaxies. Chain galaxies were first described by Cowie et al. (1995) who discovered several chains as faint sources in the WFPC2 imaging of the Hawaii survey fields (originally surveyed by the Canada-France-Hawaii telescope). Since their initial identification, chains have been studied further by several authors (e.g., van den Bergh et al., 1996; Moustakas et al., 2004; Elmegreen & Elmegreen, 2005) and are identified as having several blue clumps aligned linearly along with no clear bulge or disk component. Current observations and interpretations of high-redshift clumpy galaxies still disagree as to whether this morphology is a signature of secular and/or merger evolution. Studies that simulate local interacting and extreme star-forming galaxies at higher redshifts compare their rest-UV morphologies to knotty LBGs and clump-clusters at these redshifts (Overzier et al. 2008; Petty et al. 2009). They show that morphological signatures of mergers are no longer observable due to surface brightness dimming and decrease in resolution, even in HST images. Thus, to approach the issue from another angle, kinematic studies observe the velocities and velocity dispersions of star-forming spectral signatures (e.g., Hα, Hβ, [OIII], [OII], [NII], [SII])[1] to look for rotation, dispersion, or merging with the theory that the former two are indicative of a secular evolution scenario. Traditionally kinematic studies are conducted with moderate- to high-resolution spectroscopy from which line-of-sight velocity information is derived via the measurement of spatially extended emission lines. The recent improvement of integral field unit (IFU) technology in

[1]These spectral lines are optical emission features created in star-forming regions of galaxies where the surrounding gas has been ionized by young massive stars and appear with high signal-to-noise above the continuum of their spectra.

combination with adaptive optics in infrared bands permits for a powerful and unique observing technique that provides 1-dimensional spectra together with 2-dimensional spectral morphologies for the whole field of view of an instrument.

Förster Schreiber et al. (2009) and Genzel et al. (2008) probed a high-redshift epoch of star-forming galaxies at z $\sim$ 2 using IFU spectroscopy with the Very Large Telescope (VLT). They found large amounts of turbulence in clumpy disks that they interpreted as evidence for rapid ($<$ 1 Gyr) secular evolution at high$-z$ powered by the kinetic energy of cold gas accretion from galactic halos. Elmegreen & Elmegreen (2005) and Elmegreen et al. (2007) (hereafter E05 and E07, respectively) had reported on the presence of lower luminosity/mass analogs of these systems in the Hubble Ultra Deep Field (HUDF) (Beckwith et al., 2006). The E07 classification scheme of HUDF galaxies is based on the visual inspection of HUDF i-band images, size, and surface brightness measurements. A full description can be found in Section 2.6. The observed i-band observations probe rest-frame UV star-formation at z $\gtrsim$ 2 where it samples rest-frame UV wavelengths. Due to the lack of U-band coverage of the HUDF, rest-frame UV star-forming galaxies at intermediate redshifts (z $\sim$ 0.2–1.2) were not properly verified. Star-forming galaxies have also been probed at high redshifts by Förster Schreiber et al. (2009) objects as part of a sample of 80 objects from the Spectroscopic Imaging survey in the Near-Infrared with SINFONI (SINS) by Förster Schreiber et al. (2006). The targets were selected using mixed samples of objects at 1 $<$ z $<$ 3, covering from Lyman-alpha emitters (LAEs) to K20 objects. LAEs have been described in detail in Section 1.5.1 and K20 objects are defined by Förster Schreiber et al. (2009) as being part of a K-band selected survey of sources with $K_s <$ 20 that is unbiased by morphology or color selection. The surprisingly high fraction (1/3) of large star-forming rotating disks in the SINS survey implies that mergers were not the main mechanism forming disks. Thus, the current evidence points to disk formation as being mainly secular at high redshifts, suggesting that this may be the primary mechanism for disk build-up as the SFR density of the universe decreased towards the current epoch. However, merging has not yet been ruled out from this process since it is difficult to discern morphological tidal features at high redshifts

like those observed in local interacting starburst systems.

Combining the recent observational results with theoretical simulations suggests that clumpy galaxies are undergoing this secular evolution through cold gas accretion onto rotating disks. Star-forming clumps in disks could have migrated to the center of the potential well of a galaxy and combined to form a bulge, or, if gravitationally unstable, could have dissipated forming the disk component. Elmegreen et al. (2008) focuses on the formation of bulges formed by coalescing clumps. Their low- and high-resolution numerical simulations all produce thick bulges that are highly rotating and contain trace amounts of dark matter. The only caveat is that in the model in which supernova feedback is boosted and the clumps are destroyed before having chance to form a bulge. Krumholz & Dekel (2010) agree with the outcome of these simulations but discuss that the ultimate survival of clumps at high redshifts is in direct relation to their SFR efficiencies. They calculate that only if clump SFR efficiencies are extremely high, greater than any system yet observed, can feedback from the stellar systems expel star-forming gas from the galaxy and halt bulge formation. The highest spatial resolution simulations of clumpy galaxies to date by Agertz et al. (2009, 2011) were performed in the context of the Λ cold-dark-matter (ΛCDM) cosmology. These simulations support the secular evolution of disk galaxies at high redshifts as cold streams are made to funnel large amounts of gas onto disks resulting in the formation of clumpy chain and clump-cluster galaxy morphologies. Smaller contributions to the development of these morphologies are made by minor mergers.

Here, a study searching for the counterparts of these clumpy galaxies and sub-galactic regions at lower redshifts is presented for the first time. Since E07 and E05 clumps are detected in the rest-frame UV at high redshift ($1.6 < z < 3$), U-band images are required for the intermediate redshift range ($0.5 < z < 1.5$). Considering the small sizes of the star-forming clumps, 1–2 kpc at high redshifts E05, U-band images from space are necessary to provide adequate resolution for this study. Even the deepest U-band images from the ground (Nonino et al., 2009) can not resolve the UV morphologies of galaxies at intermediate redshifts. The purpose here is to analyze for the first time, the sizes of these galaxies and of individual star-forming

clumps in the rest-frame UV at intermediate redshifts. Throughout this chapter a cosmology with $\Omega_{\rm M}$=0.3, Ω_{Λ}=0.7 and h=0.7 is used and magnitudes are given in the AB system.

3.2 The Data and The Galaxy Samples

The galaxy sample consists of the sources detected in the HST targeted U-band image of the HUDF obtained with the WFPC2/F300W (see Chapter 2). All objects are brighter than 23.5 magnitude and are at redshifts z < 2. The drizzled WFPC2 image has a plate scale of 0.09″/pixel, and covers an area ∼9.4 arcmin^2. One star is detected in this image at the coordinates 53.1826210, -27.7681408. Its point-spread-function (PSF) was measured using the IRAF task PSFMEASURE in the noao.obsutil package in order to determine the minimum spatial of the image at which sizes can be measured. Figure 3.1 shows the observed and modeled radial profile of the star from this analysis with a measured FWHM (full width half maximum) = 2.18 pixels, or ∼0.2″, given the plate scale. Typically, stellar FWHMs are on the order of 1 pixel in an image. Here, the FWHM is slightly higher than desired due to on orbit temperature variations known as "thermal breathing" that can cause small displacements in the focus of the telescope over time. To be conservative and to account for errors in measurements, a FWHM = 3 pixels, or 0.27″, is used as the minimum spatial resolution throughout this study. Table 3.1 shows the physical sizes that this spatial scale corresponds to at the intermediate redshifts covered in this study.

3.2.1 Selection of Clumpy Galaxies

For the best possible rest-frame UV comparison to sizes of clumpy galaxies measured at high redshifts (z > 2) in HST ACS i-band images by E05, clumpy galaxies in the intermediate-redshift range representing the equivalent rest-UV wavelengths (∼1200Å–1800Å) in the U-band are selected, i.e. 0.63 ≤ z < 1.5. A total of 46 galaxies in the U-band catalog are within this redshift range. Galaxies were further selected

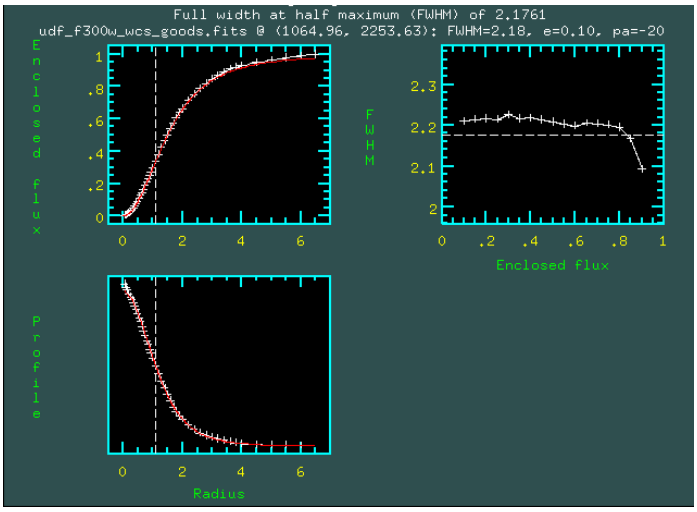

Figure 3.1 *Radial profile and FWHM information for the single star detected in the HUDF U-band image at coordinates 53.1826210, -27.7681408. Analysis was done with IRAF task PSFMEASURE.*

if their morphologies did not look visually similar throughout their multiwavelength images and thus could not be measured in bandpasses other than U. This selection results in a sample of 18 clumpy galaxies from the larger U-band sample. Comparing selected galaxies with their visual morphologies as defined by E05 in the ACS i-band images it is found that 12 sources are spirals, 4 are clump-clusters, 1 is a double, and 1 is a tadpole.

3.3 Sizes of Star-Forming Galaxies

The U-band image of intermediate$-z$ objects (i.e. the rest-frame UV) reveals the sites where star-formation occurs. As pointed out in Law et al. (2007) rest-frame UV morphologies are either statistically decoupled from the majority of physical observables, such as star-formation Rates (SFR) of the objects, or determined by too complex a combination of physical processes to provide characterizations with predictive power. However, the sizes of the objects in the rest-frame UV account for the size of un-obscured star-forming sites which are commonly detected as LBGs at high redshifts and therefore important for our understanding of star formation and

Table 3.1. Selected Intermediate-z HUDF Clumpy Galaxies

Galaxy ID[a]	R.A. deg	Decl. deg	m_U AB	z[b] best	ST	Min. Size[c] kpc
1	53.1784172	-27.7682304	21.09	0.630	3.8	2.19
2	53.1726112	-27.7809887	23.37	0.640	3.6	2.18
3	53.1608238	-27.7753963	21.70	0.650	6.0	1.97
4	53.1699409	-27.7710609	20.59	0.650	3.4	1.89
5	53.1564293	-27.8107758	20.45	0.665	5.8	1.89
6	53.1520653	-27.7747822	21.65	0.750	6.0	1.87
7	53.1552696	-27.7695465	21.67	0.770	5.6	2.23
8	53.1668854	-27.7976780	22.72	0.930	5.8	2.12
9	53.1518974	-27.7819862	23.17	0.930	4.0	1.86
10	53.1761894	-27.7961178	21.25	0.950	3.6	2.14
11	53.1675873	-27.7925072	23.27	1.020	4.0	2.17
12	53.1730003	-27.7779026	22.08	1.030	4.0	2.00
13	53.1782227	-27.7830944	21.45	1.050	3.6	2.19
14	53.1659012	-27.7815647	22.96	1.060	3.4	2.12
15	53.1661797	-27.7875214	21.70	1.080	3.6	2.21
16	53.1518784	-27.7754364	21.97	1.120	5.8	1.83
17	53.1572227	-27.7785568	22.78	1.180	5.2	2.19
18	53.1450996	-27.7894268	23.19	1.250	3.8	2.25

[a]This is the ID number given in Figures3.10(a)–3.10(e) for each selected clumpy galaxy.

[b]Best quality redshift available between z_{phot} and z_{spec} (Dahlen et al., 2010).

[c]This is the minimum spatial size measurable in the HUDF U-band image given the cosmological distance scale (kpc/″) at the objects redshift and using a conservative minimum spatial resolution of 0.27″ for the image.

the evolutionary paths which will lead to modern Hubble types.

The sizes of U-band sources presented in the catalog in Chapter 2 are obtained by measuring their half-light radii (r_h) and Petrosian radii (r_p; Petrosian, 1976) with SExtractor. These are two standard methods by which galaxy sizes are measured via their surface brightness profiles. Since galaxies do not have well defined edges, as for example compared to stars, it is best to make size comparisons between distant galaxies based on a certain fraction of the total apparent brightness of a source. The half-light radius, also known as the effective radius, is defined as the distance from the center of a source where its apparent brightness has decreased by 50% of its maximum values. It assumes that half of the sources brightness is contained within an ellipse defined by a radius equal to the square root of its semi-major axis multiplied by its semi-minor axis. Alternatively, the Petrosian radius was initially defined in such a way to attempt in obtaining the majority of a galaxies light profile using a standard formula. An index, η, defines the fractional percent of the surface brightness, I(R), out to a radius, R, which is equal to the average surface brightness at that radius, $\langle$I(R)$\rangle$,

$$\eta = \frac{2\int_0^R I(R')R'dR'}{R^2 I(R)} \tag{3.1}$$

Thus, η can be defined to set a standard brightness profile at which to systematically measure galaxy radii. Typically, and in this work, η is set to 0.2. Both of these apparent size measurements are used for this study in order to make the analysis conveniently comparable to other galaxy samples.

Figures 3.2 and 3.3 present the kiloparsec distributions of r_h and r_p for all galaxies detected in the U-band image of the HUDF, respectively. Here it is clear that the Petrosian radius measures the majority of the light in each source since the peak of the r_p distribution is at a radial size $\sim$2 times the peak of the r_h distribution. Figures 3.4 and 3.5 show r_h and r_p, respectively, as a function of redshift covering a range spanning $\sim$8.9 Gyr of cosmic evolution. The redshifts plotted are those of best quality between the z*phot* and z_{spec} of each source from Dahlen et al. (2010). In Table 3.2 the sizes of U-band sources are split into four different redshift bins that span $\sim$2

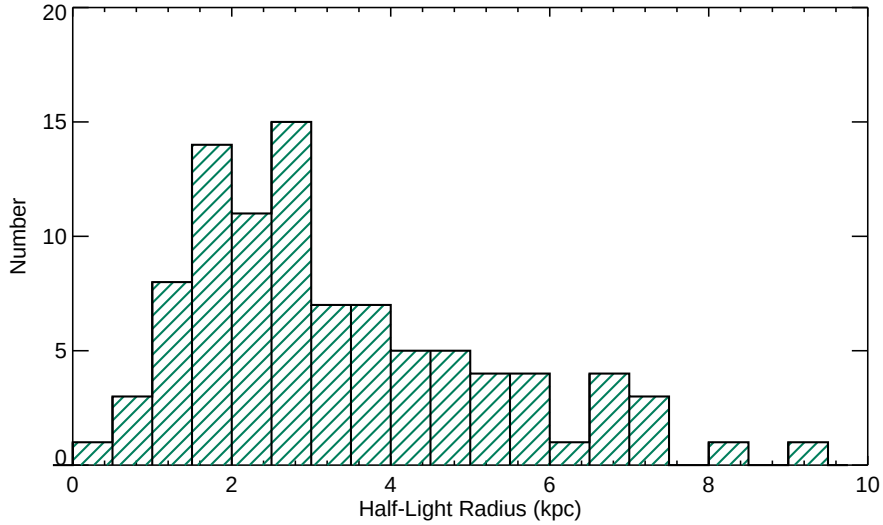

Figure 3.2 *Distribution of the half-light radius, r_h, of U-band detected galaxies in the HUDF.*

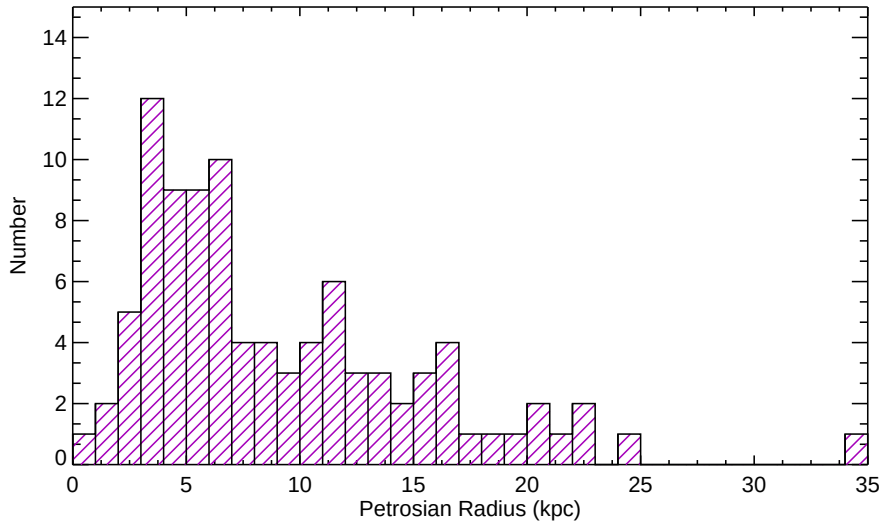

Figure 3.3 *Distribution of the Petrosian radius, r_p, of U-band detected galaxies in the HUDF.*

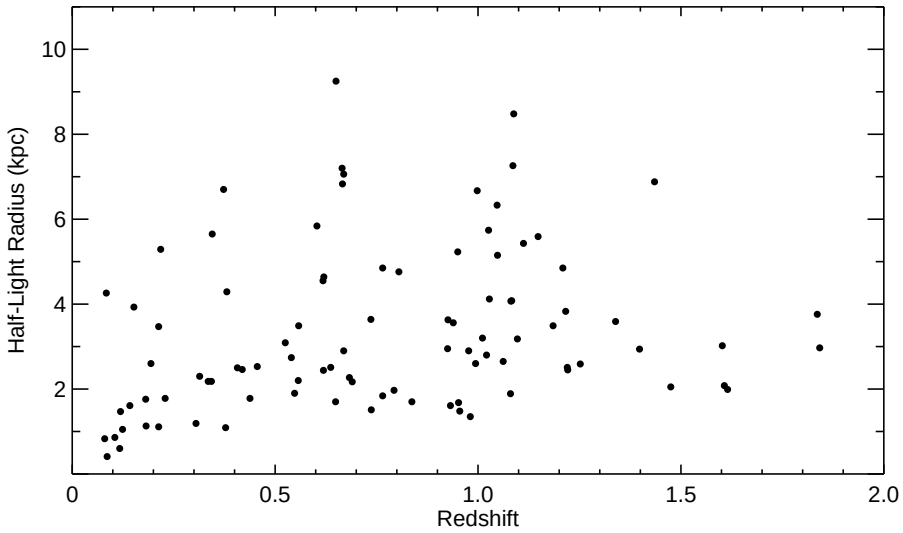

Figure 3.4 *Half-light radius (kpc) as a function of redshift for all U-band detected galaxies in the HUDF. Redshifts are from the compilation of Dahlen et al. (2010).*

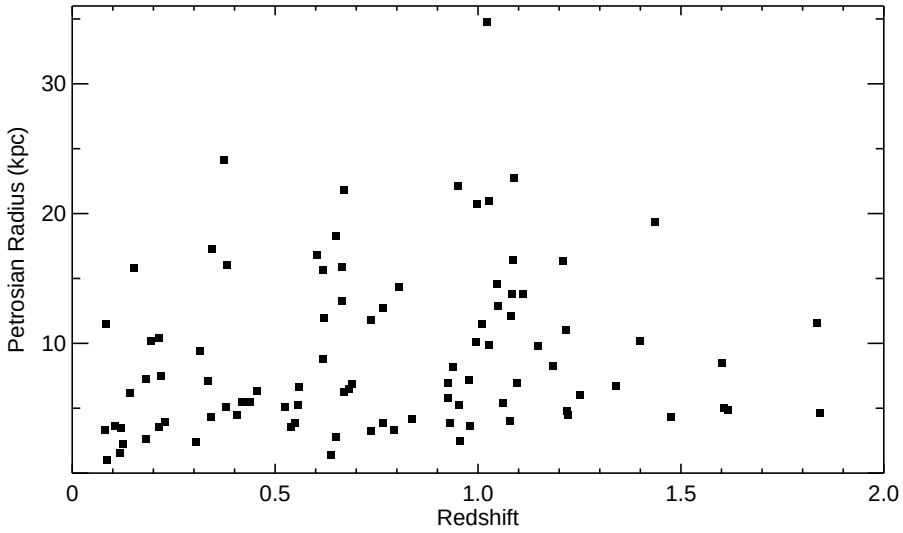

Figure 3.5 *Petrosian radius (kpc) as a function of redshift for all U-band detected galaxies in the HUDF. Redshifts are from the compilation of Dahlen et al. (2010).*

Table 3.2. Sizes of U-band HUDF Galaxies Over ∼2 Gyr Intervals

Redshift	λ_{rest} Å	Number Objs.	Half-light Radius kpc	Ave. r_h	Petrosian Radius kpc	Ave. r_p
$z \leq 0.28$	∼2344	16	$0.41 \leq r_h \leq 5.29$	2.01	$0.99 \leq r_p \leq 15.84$	5.88
$0.28 < z < 0.56$	2344–1923	17	$1.09 \leq r_h \leq 6.70$	2.84	$2.42 \leq r_p \leq 24.13$	7.75
$0.56 < z < 0.98$	1923–1515	29	$1.35 \leq r_h \leq 9.25$	3.59	$1.43 \leq r_p \leq 22.15$	9.15
$0.98 < z \leq 1.84$	1515–1056	32	$1.89 \leq r_h \leq 8.48$	4.01	$4.01 \leq r_p \leq 34.76$	11.46

Gyr each in order track size evolution. While the averages sizes per redshift bin show a decrease in galaxy size with increasing redshift for both r_h and r_p, the plots show that after $z \sim 1.3$ all but a few sources have $r_h \lesssim 4$ kpc ($r_p \lesssim 15$ kpc), indicating that star-forming galaxies could be decreasing in size after $z \sim 1$ out towards high redshift. This is a direct prediction of hierarchical evolution. However, statistically there are fewer objects at $z \leq 1.2$ so the trend is biased against this upper redshift range, and the U-band detects different stellar populations depending on the observed redshift, so one must be careful in interpreting these results. Given the rest-frame wavelength ranges of the redshifts in Table 3.2 all sources are detected at rest-UV wavelengths, however in the near-UV (first two rows) there may be A star interlopers in the observed stellar populations radiating the UV flux, while in the far-UV (last two rows) all the emission is coming from O and B stellar populations.

De Mello et al. (2006b) measure U-band (WFPC2/F300W) half-light radii for sources in GOODS-S parallel observations in the redshift range $0.66 < z_{phot} < 1.5$ and find the average $r_h = 2.07 \pm 0.08$ kpc. The average size of HUDF U-band sources (40 objects or 45% of the total sample) within this redshift range is 4.04 ± 2.11 kpc. We see much more size variation in the HUDF at these redshifts than de Mello et al. (2006b) which is most likely a result of the shallower limit of the HUDF U-band catalog (23.5) versus the 27.5 limiting magnitude of the U-band parallels, i.e. the HUDF observations are biased towards physically larger and brighter galaxies.

Figures 3.6 through 3.9 separate the previous plots of size as a function of redshift into bins of morphological types and SED based spectral types in order to see if

the different types present any evidence of size evolution individually. Morphologies are from E07 and based on observed i-band images, and the STs are from Dahlen et al. (2010) (see Chapter 2 for further descriptions). The stars in each plot represent the selected sample of clumpy galaxies. The sizes and photometric properties of the individual clumps within these galaxies are further analyzed in Section 3.4. Analyzing the bins of visual morphology, doubles and tadpoles have the smallest sizes over the entire redshift range varying between $r_h < 3$ kpc and $r_p < 7$ kpc, except for one tadpole with $r_p = 10.18$ kpc. These small sizes are expect due to the compact nature of these objects. Although there are only 5 chain galaxies, they span a large range in size and redshift for both types of measured radii. Spirals show a similar size distribution to the overall size distribution of the catalog in their given redshift

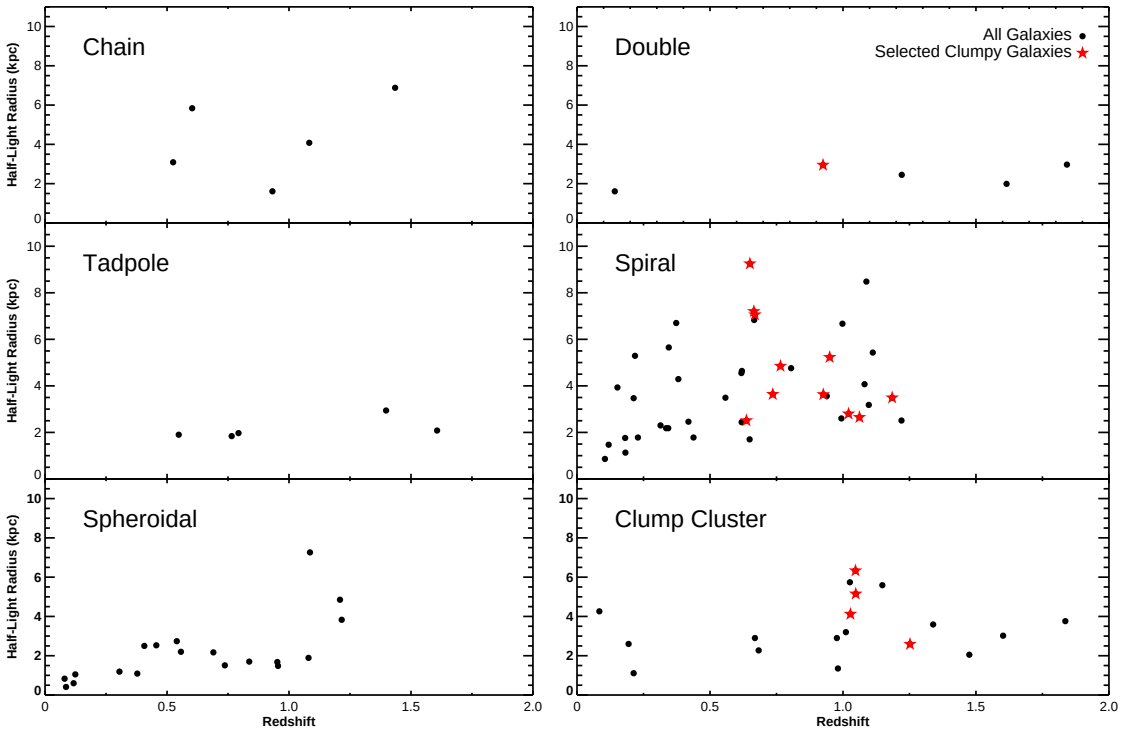

Figure 3.6 *Half-light radius (kpc) vs. redshift of all galaxies in the U-band image of the HUDF. Each panel shows the size distribution for each morphological type classified by Elmegreen et al. (2007). Selected clumpy galaxies are highlighted in the distribution as red stars.*

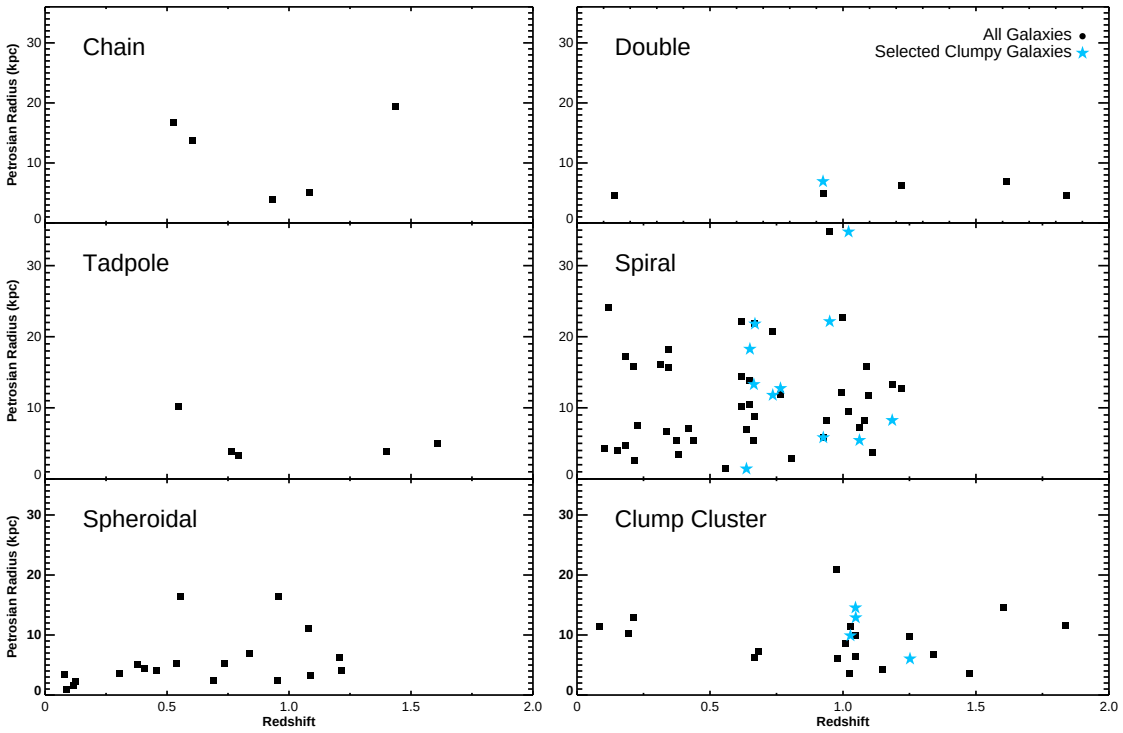

Figure 3.7 *Petrosian radius (kpc) vs. redshift of all galaxies in the U-band image of the HUDF. Each panel shows the size distribution for each morphological type classified by Elmegreen et al. (2007). Selected clumpy galaxies are highlighted in the distribution as stars.*

range, varying primarily between r_h = 1–8 kpc or r_p = 3–23 kpc out to z $\sim$ 1. This result is in agreement with Ravindranath et al. (2004) who have also not detected any significant size evolution of disk galaxies in then GOODS-S field between 0.25 $\leq$ z $\leq$ 1.25 (measured in rest-frame B-band) when selection effects are considered. These data show that the overall sizes of their star-forming morphologies do not show any significant evolution either. The two largest U-band objects are spirals, and we detect only one spiral with size $<$ 1 kpc (r_h = 0.86) at z = 0.105. The spheroidal objects with z $<$ 1 are for the most part quite compact with an interesting up-swing in r_h at higher redshifts. This trend lends itself to the theory of star formation dominating in large spheroidals at earlier times, however the statistics here are quite small, and it should be noted that the r_p of these sources at z $>$ 1 does not follow this same

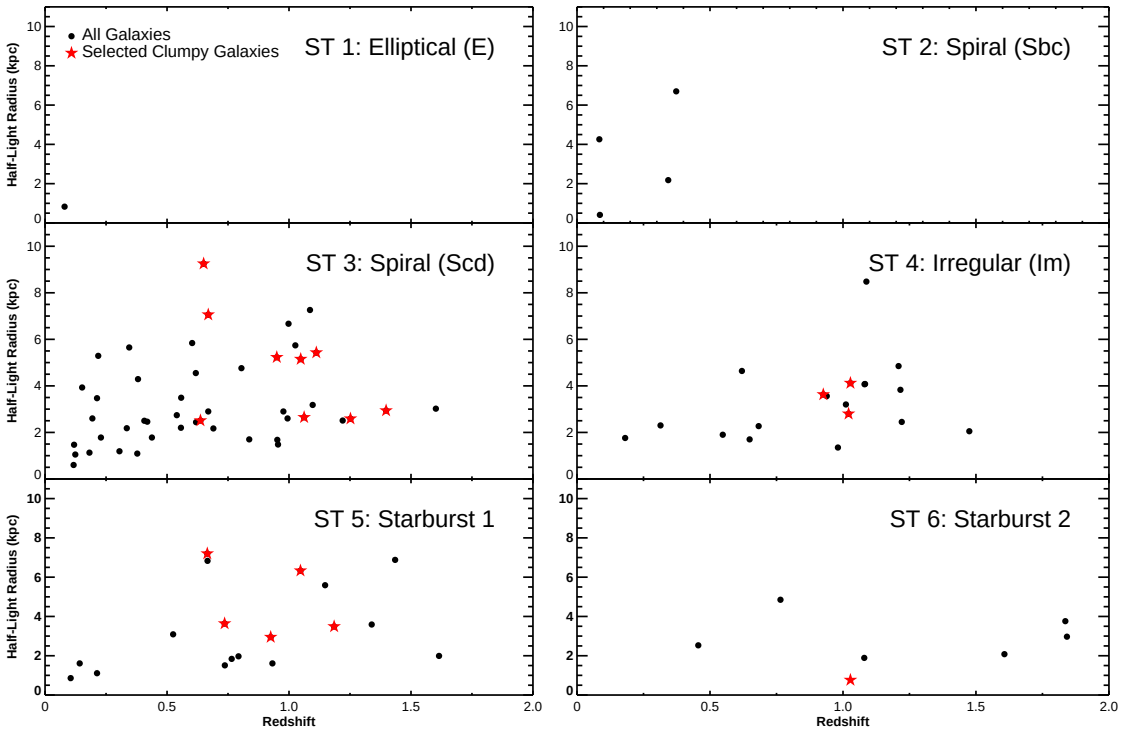

Figure 3.8 *Half-light radius (kpc) vs. redshift of all galaxies in the U-band image of the HUDF. Each panel shows the size distribution for each spectral type from Dahlen et al. (2007) based on the SEDs of Coleman et al. (1980) and Kinney et al. (1996). Selected clumpy galaxies are highlighted in the distribution as blue stars.*

trend, thus pointing out an important caveat in interpreting results with different measures of size based on apparent brightness. The large r_h sizes of spheroidals at z $>$ 1 may also be biased by rest-UV selection of only the brightest, and thus largest, spheroidals at higher redshift. A more detail quantitative analysis of rest-UV sources will be done in Chapter 6.

The U-band size distributions of chains, doubles, tadpoles, clump clusters, and especially spirals are similar to those for all resolvable HUDF sources (E07) with z $<$ 1. The spheroidal U-band size distribution varies much less in size than the distribution of all HUDF spheroidals at these redshifts, however, U-band spheroidals do make up the majority with sizes $<$ 1 kpc at z $<$ 1 which is consistent with the distribution of all HUDF spheroidals. At z $>$ 1, which probes the rest-frame UV

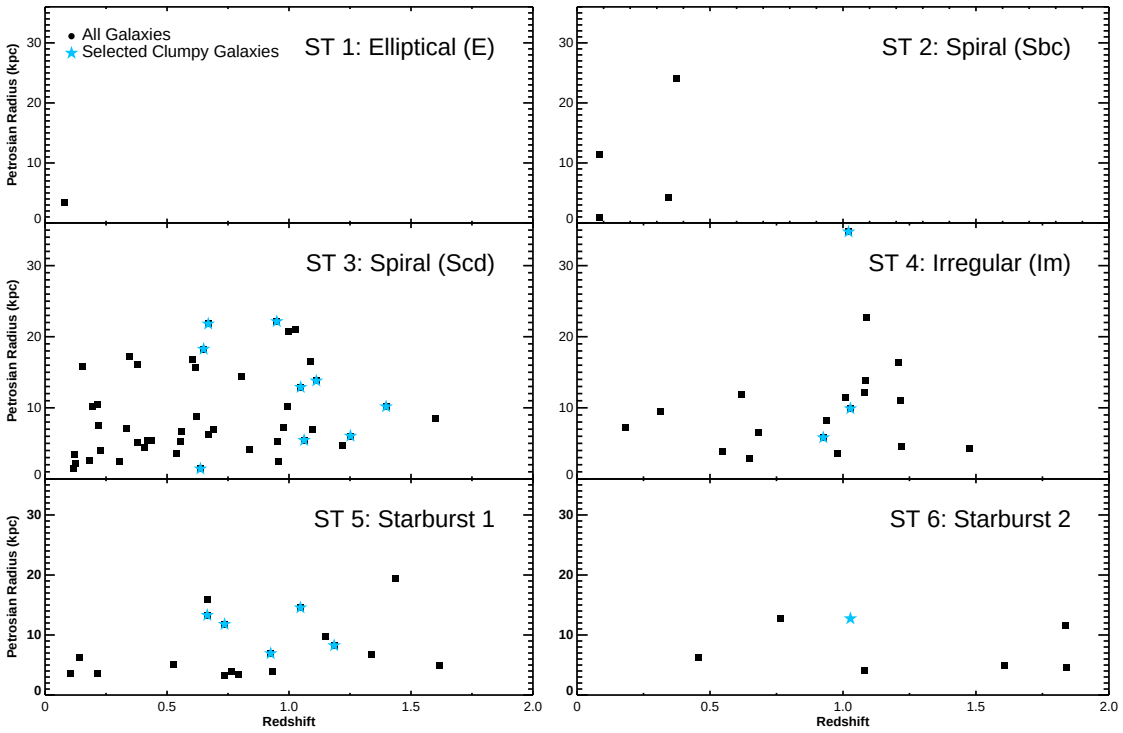

Figure 3.9 *Petrosian radius (kpc) vs. redshift of all galaxies in the U-band image of the HUDF. Each panel shows the size distribution for each spectral type from Dahlen et al. (2007) based on the SEDs of Coleman et al. (1980) and Kinney et al. (1996). Selected clumpy galaxies are highlighted in the distribution as blue stars.*

sizes of all HUDF galaxies in the i-band, E07 finds a significant decrease in size with increasing redshift for all morphological types (decrease by factors of 2–3) except for tadpoles. This evolutionary trend is not detected in the intermediate-redshift HUDF U-band distributions, possibly resulting from incompleteness biases in the catalog at z $>$ 1. Moreover, the fact that no significant size evolution is seen for any morphology at lower redshift suggests that galaxies may be either dynamically settling at this point in time, or there could have been a cessation of major merger events.

Using spectral types (STs - defined in Sections 2.5 and 2.6) as morphological indicators, the Scd spirals have nearly the same size distribution as the visually defined spirals. Only one elliptical source is detected with very small r_h and r_p. Irregular STs show a slight trend towards small sizes at low redshifts in both r_h and r_p. This may

suggest that large irregular galaxies become more ordered in morphology as they evolve and thus large irregular galaxies may become large spirals at these redshifts, or star formation shuts down in them at $z < 1$. Starburst type 1 and 2 galaxies show no evolution in size between $0.5 \lesssim z \lesssim 1.8$, and appear small ($r_h < 2$ kpc; $r_p < 8$ kpc) at $z < 0.25$. Thus, once again there are no clear trends in rest-UV size evolution for HUDF sources < 2, except perhaps for irregular spectral types. However, statistics are too low in this bin to suggest any definite conclusions.

3.4 Clumpy Star-Forming Galaxies

As previously discussed, observational evidence for the developmental mechanisms driving disk evolution can be sought through studies of their properties on a sub-galactic scale. Here, the rest-UV sizes of star-forming clumps at intermediate redshifts are probed for signatures of size evolution. A total of 43 clumps are measured in the 18 selected clumpy galaxies discussed in Section 3.2.1. The redshifts of these sources probe the rest-frame UV between ∼1200–1800Å in order to compare with clump measurements at the same rest-wavelengths at $z > 2$ E05. As shown in Figures 3.6 through 3.9 these clumpy galaxies have primarily spiral optical morphologies, four have clump-cluster morphologies, and only one is a double, while their STs range between spiral, irregular, and starbursts. There is no significant size trend for r_h or r_p in any of these distributions.

In order to define the borders of individual clumps, contours representing pixel levels between 1–10σ above the median background level of the surrounding area of each source were plotted on individual images of each galaxy. Clumps were detected in contours between 2-5σ above the background depending on the galaxy. The highest level contour that detected the majority of visually identifiable clumps for each galaxy was used. Next, the U-band contour images were visually inspected next to their optical B-band ACS images to ensure that the detected peaks in the contours were within the area of the galaxy and not a smaller source near, but unlikely to be part of, the galaxy in the image. The size of each clump was then measured along the

longest diameter bounded by the selected contours using the analysis tools in DS9 (Figure 3.10). To be conservative, only clumps with sizes $> 0.27''$ on the image were considered for this analysis, eliminating 10 potential clumps (see Section 3.2). In the limit of large distances where $D_A >>$ the size of a source the semi-major axis is equal to the diameter of the source. Therefore, angular distances to each source were calculated based on the best redshift for that source (z_{phot} or z_{spec}) and the angular formula was used to determine the kiloparsec size of each clump: $\theta D_A =$ size.

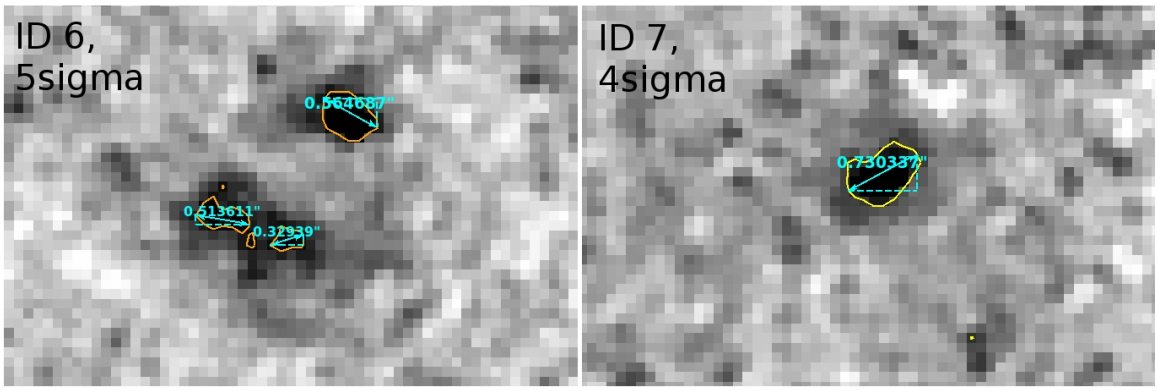

Figure 3.10 *Examples of arcsecond measurements of clump sizes within specified contours above median background levels for two clumpy galaxies.*

Following the methods of E05 and Elmegreen et al. (2009), the task IMSTATISTICS from the IRAF images.imutils package was used to perform photometry on individual clumps. Square photometry apertures were defined by the most distant edges of the contours used to measure the size for each individual clump. This ensured that the majority of the clump's pixelated areas were included in the measurement. With the fluxes of each clump their luminosities were determined via two separate methods. First, the luminosity based on absolute magnitude of the clump was calculated. The absolute magnitude was obtained from the apparent magnitude and the luminosity distance (D_L) in parsecs to the clump,

$$M_U(AB) = m_U(AB) - 5[log(D_L) - 1] \quad (3.2)$$

From this, the U-band luminosity was calculated based upon the absolute magnitude

of the sun in the F300W filter,

$$\frac{L_U}{L_\odot} = 10^{(M_\odot(F300W)_{AB} - M_U(F300W)_{AB})/2.5} \tag{3.3}$$

The solar U-band absolute magnitude was obtained for the Johnson-Cousins system, as $M_\odot(U) = 5.61$ ($m_\odot(U)$ = -25.96, with D_L = 1 AU = 4.85x10^{-6} pc), where the effective U-band wavelength is defined as 3650Å. It was converted to its magnitude in the WFPC2 F300W filter using the zero point conversion factor of 0.04±0.05 determined by O'Neil et al. (1998). Unlike the other WFPC2 filters, the F300W U-band filter was not designed to be a perfect match to the Johnson-Cousins system and so its conversion is not defined in the WFPC2 data handbook. Finally, $M_\odot(F300W)$ was determined with this information along with the formulas given in the HST WFPC2 cookbook,

$$\begin{aligned} ZPT(Johnson - Cousins) &= ZPT(STMAG) - filterconversionfactor \\ ZPT(Johnson - Cousins) &= 19.54 - 0.04 \\ &= 19.41 \end{aligned} \tag{3.4}$$

Then the flux of the sun, $f_\odot$(U), in units of [counts/s] can be determined from,

$$\begin{aligned} m_\odot(U) &= ZPT(Johnson - Cousins) - 2.5log(f_\odot(U)) \\ f_\odot(U) &= 10^{(m_\odot(U)+19.41)/2.5} \end{aligned} \tag{3.5}$$

Next, the raw solar flux can be used to determine its apparent magnitude in the F300W filter in the AB system,

$$\begin{aligned} m_\odot(F300W)_{AB} &= ZPT(F300W)_{AB} - 2.5log(f_\odot(U)) \\ m_\odot(F300W)_{AB} &= 20.77 - 2.5log(f_\odot(U)) \end{aligned} \tag{3.6}$$

From here it is simple to calculate the absolute magnitude,

$$M_\odot(F300W)_{AB} = m_\odot(F300W)_{AB} - 5[log(D_L) - 1] \tag{3.7}$$

The value determined for the solar absolute magnitude in the F300W WFPC2 filter is $M_{\odot}(F300W)_{AB} = 6.97$. Secondly, the FUV luminosity was calculate based upon the distance to each galaxy and the flux measured for each clump. This is defined as,

$$L = 4\pi D_L^2 F_{FUV} \tag{3.8}$$

where F_{FUV} is the FUV flux of the source in units of [erg/cm^2/s]. This is easily obtained by converting the FUV flux, f_{FUV}, in [counts/s] directly obtained from the photometric measurements to [erg/cm^2/s] by multiplying by the PHOTFLAM header value for the F300W filter and by the $\lambda_{eff} = 3000$Å. Using an area of a circle defined by one half the kiloparsec size of each clump, the surface brightness, I($L_{\odot}$ kpc^{-2}), was determined for each luminosity calculation. For each of the 18 selected clumpy galaxies Figures 3.10(a)–3.10(e) display the U-band image of the galaxy, the image with contours overlain, and the image with the boxes used for photometry marked with a clump reference number for that galaxy. Blue contours map the 2σ level, green contours map the 3σ level, yellow contours map the 4σ level, and orange contours map levels $\geq 5\sigma$. Table A.2 lists the measurements of size, apparent magnitude, absolute magnitude, luminosities, and luminosity densities for each clump.

3.4.1 Analysis

Figure 3.12 shows the size distribution of all 43 rest-UV sub-galactic clumps measured at intermediate redshifts. On the left of the plot the purple bar represents the range of sizes measured by E05 for rest-UV clumps at z $>$ 2 in the HST ACS i-band images of ten clump-clusters in the HUDF. They find average sizes between 1–2 kpc in diameter at the 10σ level above the background. The distribution of intermediate-redshift clumps drops off sharply below z = 2 and it is quite apparent that the clump sizes at these redshifts are much larger than the average range at high redshifts. Is this an effect of the lower resolution of the WFPC2 data (0.09″ drizzled pixel scale) with respect to the ACS data (0.03″ drizzled pixel scale)? In order to evaluate this question, Table 3.1 gives the minimum measurable size in the WFPC2 U-band image for each

(a)

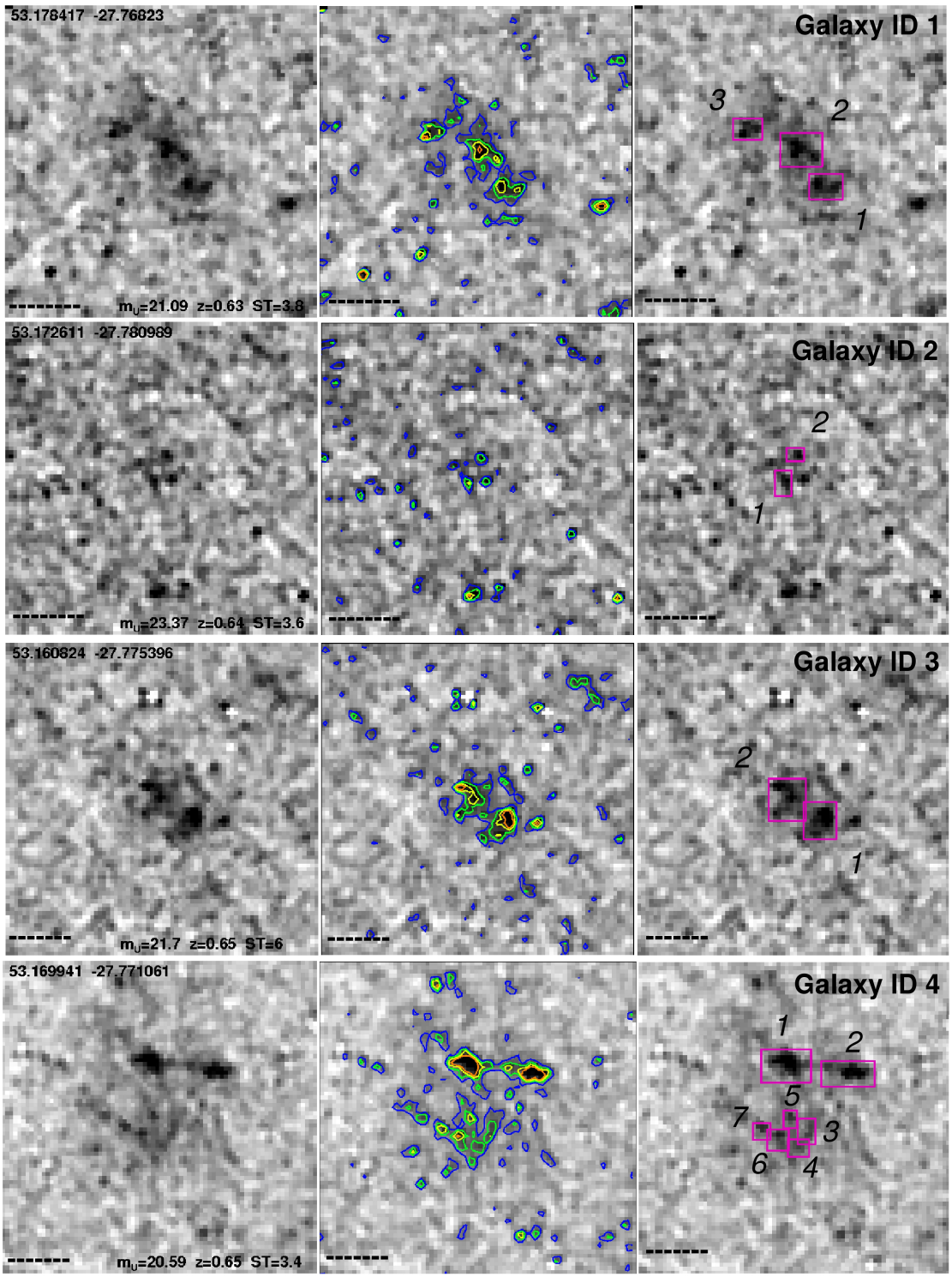

Figure 3.11 *Clumpy galaxy IDs 1–4. See (e) for full description of gallery.*

(b)

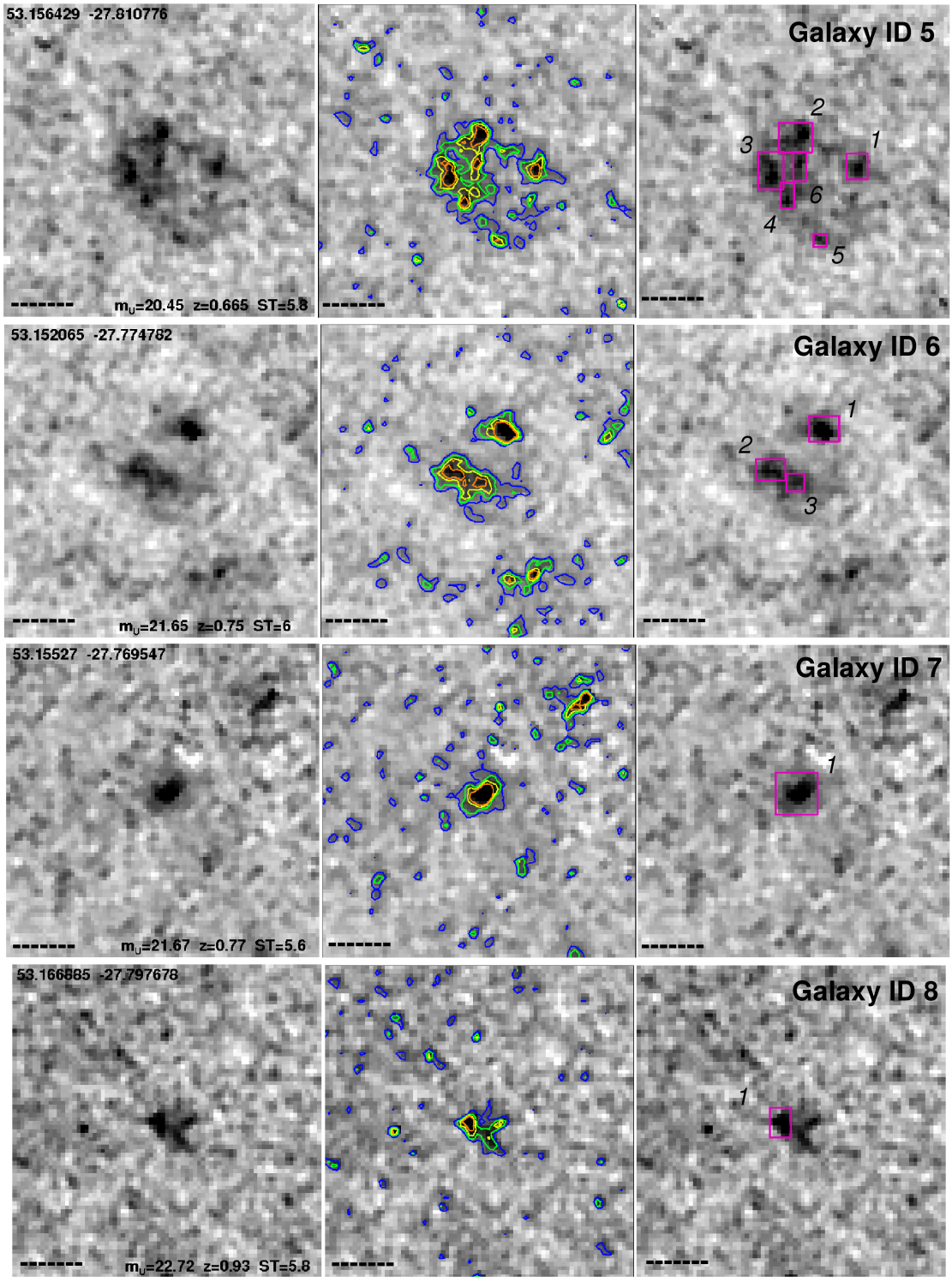

Figure 3.11 *Clumpy galaxy IDs 5–8. See (e) for full description of gallery.*

(c)

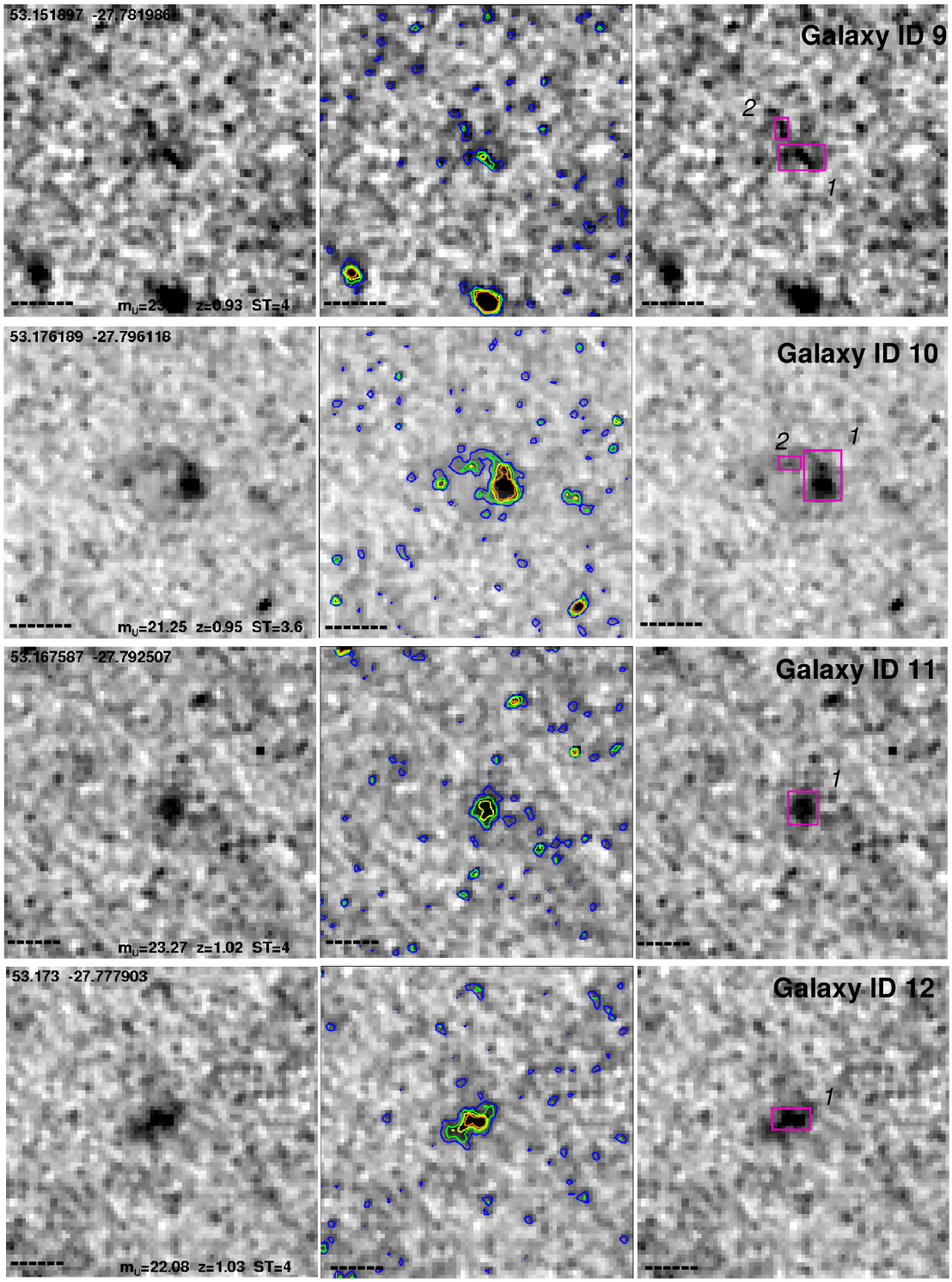

Figure 3.11 *Clumpy galaxy IDs 9–12. See (e) for full description of gallery.*

(d)

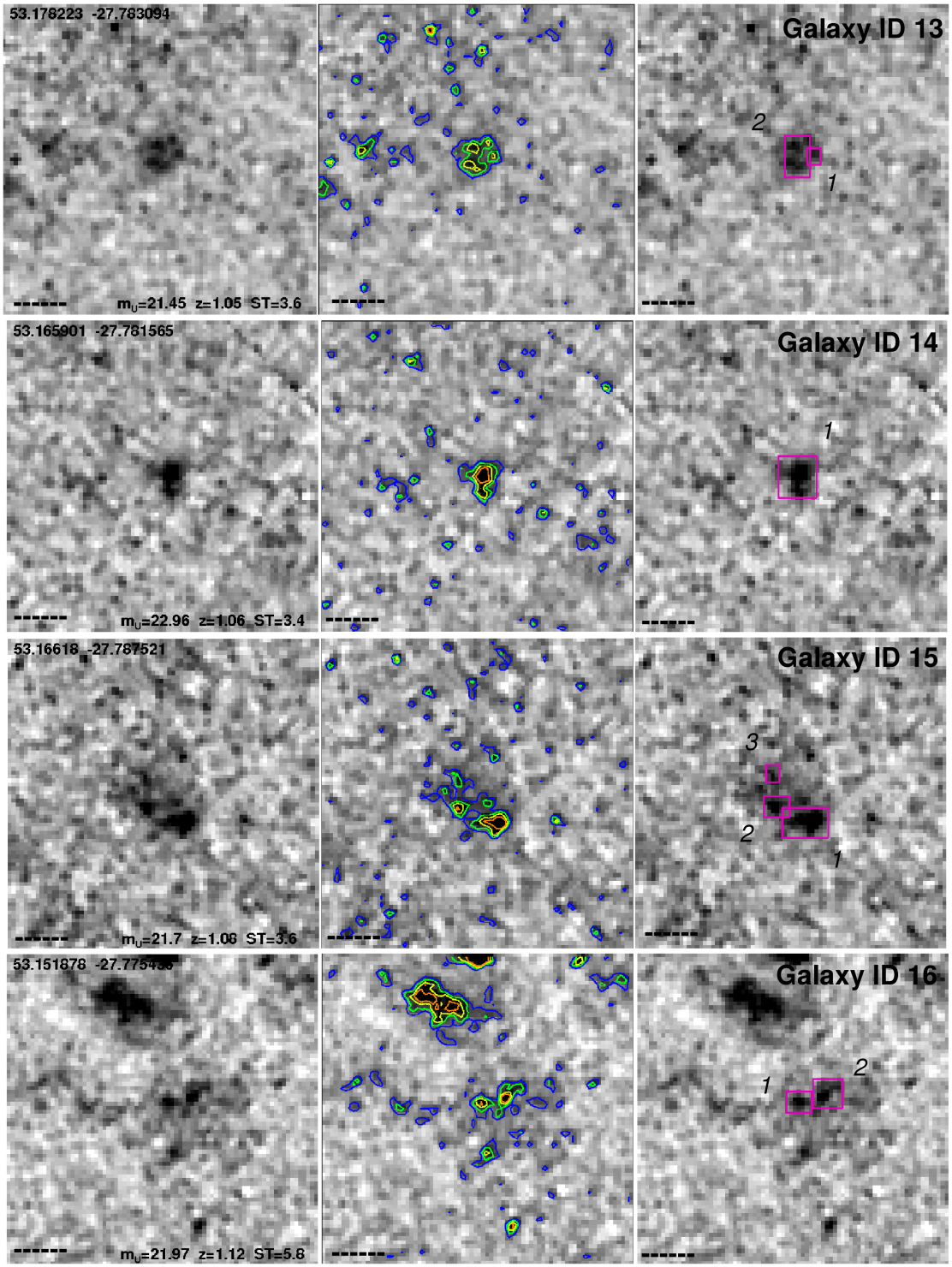

Figure 3.11 *Clumpy galaxy IDs 13–16. See (e) for full description of gallery.*

(e)

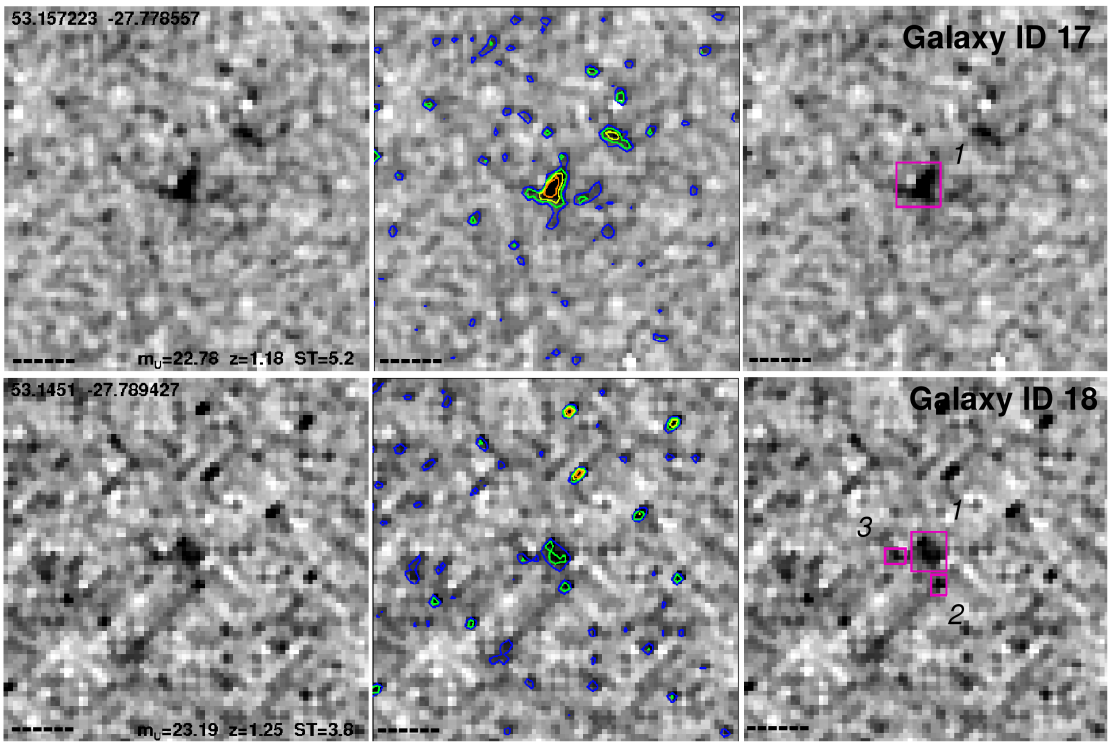

Figure 3.11 *Clumpy galaxy IDs 17 and 18. Gallery consists of 18 HUDF clumpy rest-frame UV ($\lambda_{rest} \sim$ 1200Å–1800Å) galaxies in order of ascending redshift. From left to right are WFPC2 F300W images alone, with contours between 2σ–5σ (blue to orange) above the background, and boxes defining the apertures for sub-galactic clump photometry. Images are 7″x7″ and dashed lines are 10 kpc at the given redshift.*

clumpy galaxy in the last column at its best measured redshift. This table is based on the conservative PSF FWHM (3 pixels or 0.27″) adopted for the cut off in spatial resolution of the measurable clump size in the image. For five clumpy galaxies sub-galactic sizes < 2 kpc can be measured. For the remainder of the galaxies minimum sub-galactic sizes measurable are between 6–10% higher than the 2 kpc threshold, except for source ID 12 which is exactly at 2 kpc. This conservative PSF FWHM cut-off in spatial resolution was chosen to reduce errors for very small clumps. If the actual, non-conservative, PSF FWHM of the U-band image is considered (2.18 pixels or 0.2″), then the minimum measurable sub-galactic sizes for all clumpy galaxies

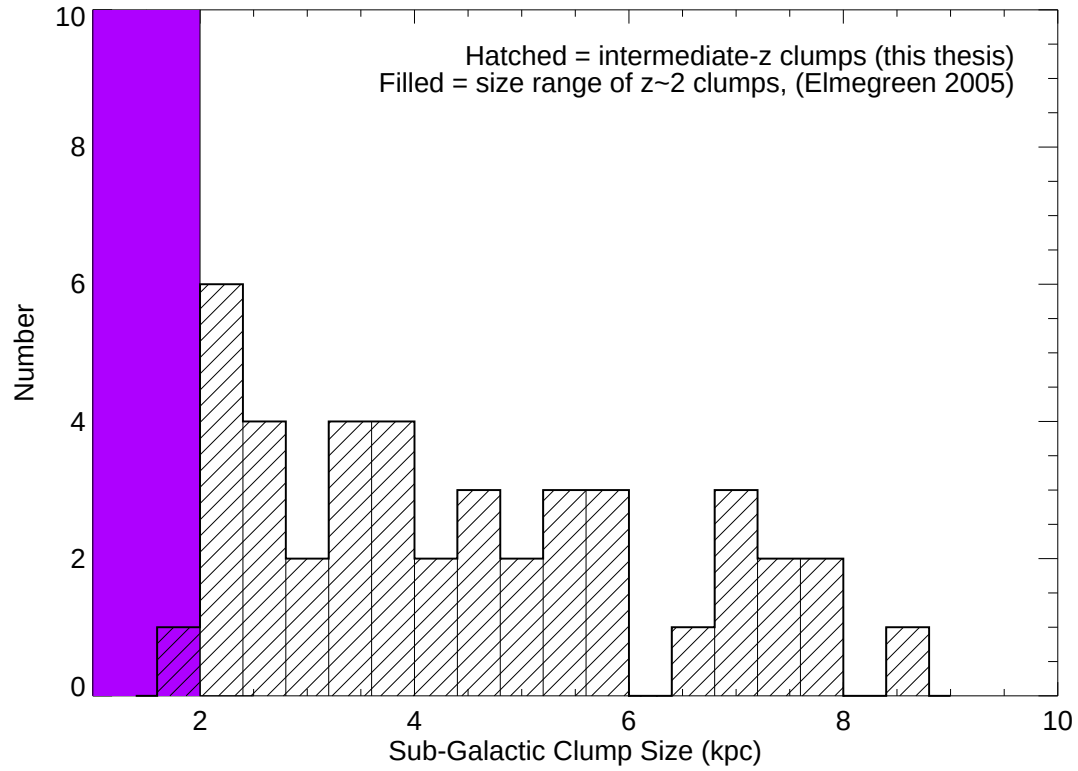

Figure 3.12 *Overall kiloparsec size distribution of all rest-UV sub-galactic clumps measured in selected HUDF clumpy galaxies (hatched). The bar on the left (filled) represents the kiloparsec size range of rest-UV sub-galactic clumps measured at* $z \sim 2$ *(Elmegreen & Elmegreen, 2005).*

drops below the 2 kpc threshold, ranging between 17–35% below 2 kpc. Thus sub-galactic clumps can be distinguish, but not necessarily accurately measured, that have physical sizes between 1–2 kpc in the U-band data enabling size comparisons for these data to high-redshift clumps. Thus, it can be said with confidence that there is a clear size evolution by a factor ∼2–3.5 towards larger rest-UV sub-galactic clumps at lower redshifts.

Of particular interest are the clumps > 6 kpc in size because these large sizes are not found at high redshift and potentially suggest size evolution of star-forming clumps with redshift. Figure 3.13 presents the individual kiloparsec sizes of clumps as a function of their host galaxy. These data are binned by clumpy galaxies containing the same total number of clumps, except for the bottom right plot that presents galaxies with 6 clumps or more. Same colors indicate that the sub-galactic clumps in that bin are within the same clumpy galaxy, and thus they appear in a vertical line on the plot. The range of E05 high-redshift clump sizes is marked by the hatched area at the bottom portion of each bin. It appears that the very large clumps (> 6) are found in every bin, but smaller clumps that are < 4 kpc in size are scarce in galaxies with single clumps. Also, while E05 found that at high-redshift clump-clusters contain ~ 5 sub-galactic clumps per galaxy, the majority of intermediate-redshift clumpy galaxies host only 1–2 star-forming clumps. This suggests that new star-forming regions of galaxies are not only becoming larger at intermediate redshifts, but also that they are fewer in number within their host galaxy. It could be a result of changing factors within the formation processes of these galaxies, such as larger amounts of available gas that are more widely spread throughout a galaxy at these lower redshifts, or it could be due to changes in the environment in which the galaxies live at these redshifts versus high redshifts. The larger clumps at intermediate redshifts may also be an indication of bulge formation or ongoing merger activity in a galaxy.

In the HUDF, E07 show that the dominant visual morphology between $z \sim 1$–2 is clump-cluster, thus at intermediate redshifts, and considering the large amount of cosmic time covered by this sample (∼8 Gyr) these clump-clusters should be transforming into disks and small ellipticals. E07 and also Law et al. (2007) suggest that

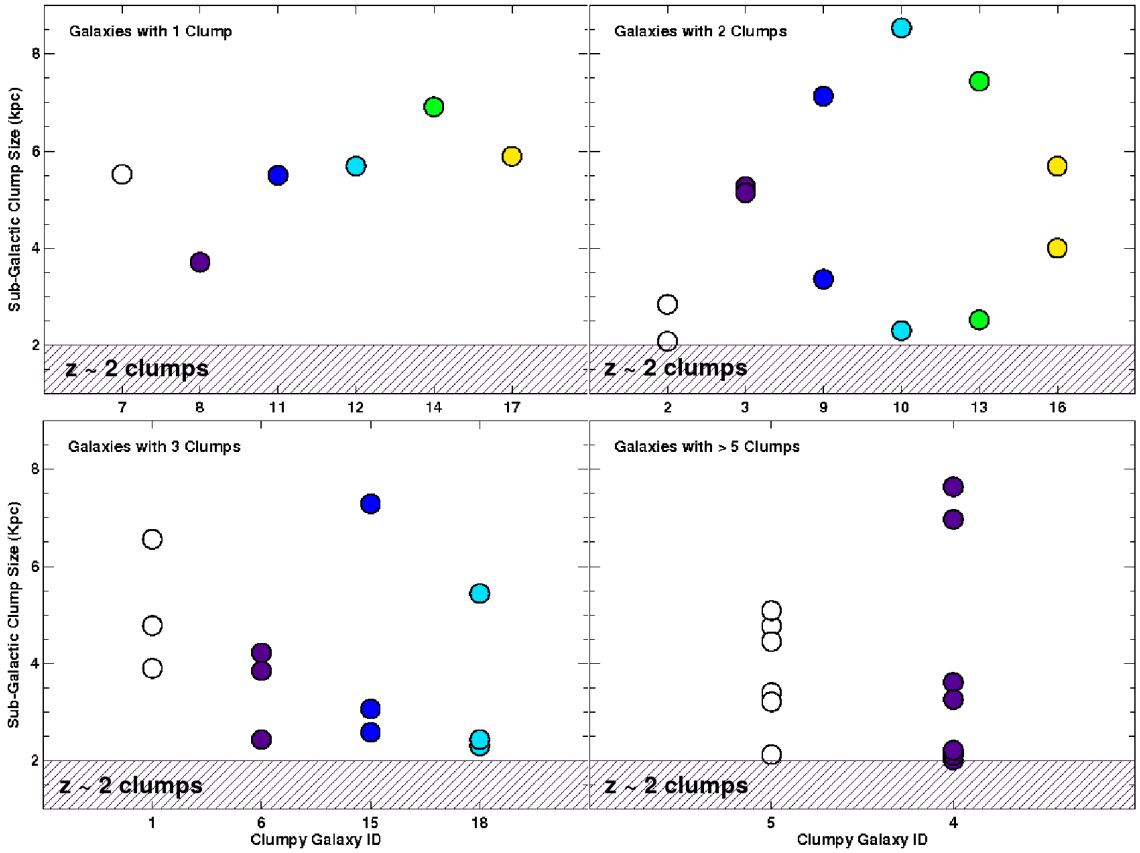

Figure 3.13 *Here the kiloparsec sizes of individual rest-UV sub-galactic clumps in the HUDF are presented by for each clumpy galaxy measured. They are split into bins of number of sub-galactic clumps per galaxy and the $z \sim 2$ rest-UV sub-galactic clump size range measured by Elmegreen & Elmegreen (2005) is overplotted for comparison.*

double and multiple star-forming clumps might be indications of mergers in progress. Such a scenario could ultimately result in the build up of smaller local elliptical galaxies (Bundy et al., 2005). With this in mind, the sizes of clumps are compared within each object and with the objects optical morphology from Figures 2.4(a)–2.4(k). Out of the objects with single clumps that could be bulges or ellipticals in formation, two of the objects (ID #'s 11 and 12) look potentially disky in optical bands, while the others look compact and irregular, but not quite spheroidal yet as their colors show distinct variations across their surfaces. Of those galaxies with two detected clumps, galaxy ID 10 is the only source that looks slightly disky and it also has the greatest difference in clump sizes. This serves as a good candidate for a disk in formation with its bulge not yet centered or done forming stars. The remaining double clump galaxies appear diffuse and irregular in their optical colors giving no clear indication of any sort of disk. With the exception of galaxy ID 18, objects containing three clumps all appear fairly disky, including one well formed spiral (ID #1). Both galaxies containing the greatest amount of star-forming clumps (ID #'s 4 and 5) are disky galaxies with clear indications of spiral arms. Despite the small sample, this suggests that perhaps galaxies containing more clumps at intermediate redshifts will, or have already evolved into disks, while those containing 1–2 clumps are the most likely candidates for low-redshift mergers and elliptical formation.

In the next section an attempt is made to put these intermediate-redshift star-forming galaxies in the context of galaxy evolution by investigating whether they are similar to high-redshift LBGs and their analogs studied at low redshifts.

3.5 Comparisons to Lyman Break Galaxies and Their Lower Redshift Analogs

Are these star-forming galaxies/clumps similar to LBGs? Ravindranath et al. (2006) analyze the rest-frame UV morphologies of 1333 LBGs (from a larger sample of 4700 LBGs) at $z > 2.5$, and 292 starbursts at $z \sim 1.2$ in the optical GOODS images,

looking for possible evolutionary connections. By analyzing their surface brightness profiles they find ∼70% of the LBG population is dominated by extended disk-like and irregular galaxies, as well as merger-like systems, while spheroidal profiles are only found for ∼30% of the LBG population. The percentage of spheroidal LBGs decreases from 44% at z∼5 to 27% at z∼3 and they find that only 16% of the lower redshift starbursts have spheroidal profile shapes, following the decreasing trend. By analyzing the ellipticity distributions of the LBGs with exponential disk-like profiles and the starburst populations, they find signatures of evolution from clumpy or merger morphologies at z = 4 to smooth disks at z = 3 which then could have evolved into the relatively flat spiral distributions they find for starbursts at z ∼ 1.2. Because the U-band sample is incomplete after z > 1 these data can not predict whether disks are dominating at these redshifts in the sample. However, Figures 3.6–3.9 show that the U-band sample at z < 1 consists primarily of objects with spiral morphologies, and secondarily, in terms of visual morphology, of spheroidal objects. These spirals could possibly be the evolved counterparts of disky starbursts observed at z ∼ 1.2, and thus evolved forms of LBGs at z > 2.5.

A population of LBGs at z ∼ 1 is studied in the rest-frame UV by Burgarella et al. (2007) (hereafter B2007) who analyze the dust attenuation of the population by comparing the luminosities of dusty IR-bright LBGs (RLBGs) (24μm) and blue LBGs (BLBGs). They have found that the total UV star-formation rate is dominated by RLBGs, however the BLBG objects are the number majority of their UV-selected galaxy sample. The average absolute magnitudes *(M_{1800})* of 15 U-band HUDF galaxies with rest-frame wavelengths between 1737–1833Å (z = 0.63–0.72) are calculated and compared with B2007's average value of M_{1800} for BLBGs (-20.3±1.0 mag) and RLBGs (-20.9±1.1 mag). The U-band sample has an average M_{1800} of -21.24±0.8 mag suggesting that the U-band selected objects are more luminous than B2007 LBGs.

Several authors (Papovich et al., 2001; Pettini et al., 2001; Giavalisco, 2002; Ferguson et al., 2004; Shapley et al., 2004) measured half-light radii for LBGs at $z \sim 3$ (rest-frame UV) between r_h = 1 kpc to 3 kpc. As shown in Table 3.2, there are objects in the U-band sample with sizes as small as LBGs, however, there are not a

Table 3.3. FUV Luminosities of Star-Forming Galaxies

Types	L_{FUV} ($L_\odot$)	Reference
35 objects[a]	$10^{9.06}$	Average from This Work
large UVLGs[b]	$10^{10.3}$–$10^{11.2}$	Hoopes et al. (2007)
compact UVLGs	$10^{10.3}$–$10^{11.0}$	Hoopes et al. (2007)
LBGs	$10^{10.3}$–$10^{11.3}$	Heckman et al. (2005)

[a]35 objects of U-band catalog sample observed with Hubble's ACS Solar Blind Channel which detects the rest-frame FUV at intermediate redshift.

[b]UVLGs are Ultraviolet Luminous Galaxies considered to be analogs of LBGs in the local universe.

large number of objects with $r_h > 3$ kpc. Most of them are spirals and clump-clusters. Approximately $\sim$1/2 of the U-band HUDF objects are similar to LBGs with respect to their r_h sizes. The U-band sample is also compared with the population of local LBG analogs, or Ultraviolet luminous galaxies (UVLGs). Heckman et al. (2005) and Hoopes et al. (2007) study a population of UVLGs ($z \sim 0$) that are thought to be a local analog to LBGs in luminosities and sizes. There are 12 U-band sources at $z < 0.3$ that have similar half-light radii sizes ($r_h \leq 3$kpc) to the compact UVLGs. Although, there is an overlap in size between our sample and these LBGs, the intermediate-redshift objects are not as luminous in the FUV as the LBGs or their local analogs (Table 3.3).

A comparison with local super star clusters is presented in the final section on future work in this chapter (3.6.1).

3.6 Summary

This chapter presented the sizes of star-forming galaxies and sub-galactic clumps at intermediate redshifts using the only U-band image available from space of the HUDF

to date. Through this analysis of intermediate-redshift clumpy star-forming galaxies it has been shown that large clumps dominate star-forming galaxies at the epoch when the star-formation rate density was declining. If those clumps are scaled up versions of earlier, smaller, clumps at high redshifts, they are not as UV bright as the ones at high redshift, which can be interpreted as an evolutionary effect since more gas was available at high redshift to form massive stars and a top-heavy IMF would be required (Iwata et al., 2009). Their large sizes fit with the scenario that these star-forming clumps are in the process of assembling the large local Hubble-type galaxies. The following main conclusions can be drawn from the study presented in this chapter:

1. U-band galaxies in the HUDF show no size evolution based on measurements of their r_h and r_p throughout the entire redshift range of the catalog. Size measurements for objects at $z < 1$ agree with what was found for the entire GOODS-S field between $0.25 \leq z \leq 1.25$ when selection effects were taken into account (Ravindranath et al., 2004). Due to the low-depth of our sample ($m_U < 23.5$) no conclusions can be made on the lack of size evolution for objects at higher redshifts.

2. The individual clump sizes of 18 objects between $0.63 \leq z < 1.5$ are measured. There are 1–7 star-forming clumps in each galaxy ranging between 1.6–10.9 kpc in diameter. These clumps are larger in size than clumps measured at higher redshifts in the rest-frame UV (Elmegreen & Elmegreen, 2005) that had sizes between ∼1–2 kpc. Thus an evolution in sub-galactic sizes to larger clumps at lower redshifts has been detected.

3. Our sample has 12 objects at $z < 0.3$ that have similar sizes to compact UVLGs and LBGs at $z \sim 3$ ($r_h \leq 3$kpc). Also, the U-band sample consists of mainly spiral morphologies at $z < 1$ that could possibly be the evolved counterparts of disk dominated starbursts observed at $z \sim 1.2$ that are connected to smooth disk LBGs observed at $z > 2.5$. However, our sample has a lower average FUV luminosity ($\log(L_{FUV}[L_\odot]) = 9.06$) than LBGs at $z \sim 3$ and all UVLGs.

3.6.1 Future Work

While the astronomical research community is making good progress in understanding the connection between the high-redshift and the intermediate-redshift populations of clumpy star-forming galaxies, it is still debatable how they connect with local types of galaxies. Intermediate-redshift star-forming clumps are a factor of 1–2 orders of magnitude larger than OB associations and super star clusters in the local universe. For comparison, NGC604 which is a very large OB association in M33, is only 140 pc in size. Larger and deeper samples in the rest-frame UV at intermediate redshifts are needed before the entire puzzle can be resolved. Also, high resolution rest-frame near-infrared data from space are necessary to evaluate extinction, mass, and age of sub-galactic clumps. The IR will provide access to the physical properties of the obscured star-forming regions. The current work presented in this chapter will be built upon in the future with high resolution UV imaging from the HST Wide Field Camera 3 (WFC3) Early Release Science (ERS) program. The improved resolution and deeper limiting magnitude of this data set (27.0 at 10σ in a $0.1''$ radius aperture) will allow for ample identification of clumpy galaxies in the ERS fields. In addition, UV data will soon be available from the CANDELS survey (see Section 1.1.1 for description) that will observe the GOODS-N field with slightly deeper exposures than the WFC3 ERS (27.6 magnitude depth at 10σ in a $0.1''$ radius aperture, Grogin et al. *in preparation*). With these data the current statistically small study of 18 clumpy intermediate-redshift galaxies will be expanded, providing increasing evidence of the transformations in size and morphology of star-forming galaxies over this epoch. Finally, it is critical to gain an understanding of rest-frame UV galaxy morphology and properties at lower redshifts in preparation for observations with ALMA and JWST. These state of the art observatories will see farther into the universe than ever before, probing the rest-frame UV at high redshift with deep IR observations.

4

Far-Ultraviolet Number Counts of Galaxies

This chapter presents a new measurement of the FUV number counts of galaxies. The FUV observations and the methodology of this measurement are described within and these new results are put in the context of past measurements of FUV number counts at both bright and faint magnitudes. This study addresses the following questions:

1. How has rest-frame UV star formation evolved since z $\sim$ 1?
2. Does empirical data of star-forming galaxies suggest a hierarchical ΛCMD formation evolution scenario?
3. To what degree does cosmic variance affect the measurements of galaxy number counts?

4.1 Introduction

Why is the night sky dark? The origins of the Universe itself are locked up in this one seemingly simple question. In the 19th century German physician Heinrich Olbers presented a paradox arguing that if the Universe were infinite, homogeneous, and static (i.e. Euclidean or flat) then the brightness of the sky should be constant and uniform, i.e. the night sky should not be dark. In this picture, any given line of sight would intersect a star in the infinite universe, thus causing stellar light to fill the entire

sky. The same conclusion could be drawn whether the stars were grouped in larger galactic structures or simply distributed throughout the Universe. Interestingly, steps towards the real resolution of this paradox were first conjectured by American poet Edgar Allen Poe in 1848 when he suggested that the Universe was not infinite, but had a beginning, and because observations of light from Earth are bound by time, due to light's finite velocity, not enough time has yet passed for light emitted at the beginning of the Universe to reach us. Thanks to modern observational studies of galaxies it is evident that the Universe has been expanding since the Big Bang and that this expansion has been accelerating over the last $\sim$7 Gyr. It is within this framework that the research field of observational cosmology emerged as astronomers sought to map the matter distribution of the universe in order to constrain the fundamental parameters that govern the evolution of cosmic space and time.

Measuring the number counts of field galaxies within an observed area as a function of magnitude is one of the fundamental techniques used to study galaxy evolution over time. Large surveys of galaxies are used to collect significant galaxy statistics down to faint levels in order to make measurements of number counts in multiple wavelengths of light. If the Universe were Euclidean in nature, measurements of number counts would show, a constantly increasing number density with increasing (fainter) apparent magnitudes, even in flux limited samples. The relations between galaxy number (N), flux (f), and distance (D) would be,

$$N \propto D^3 \tag{4.1}$$

$$f \propto \frac{1}{D^2} \tag{4.2}$$

Thus, for a Euclidean geometry, in the zero limit of the observed flux (fainter detections), the number of sources increases to infinite,

$$N \propto \frac{1}{f^{3/2}} \tag{4.3}$$

and the number apparent magnitude (m) relation would be derived as follows where

C is a constant,

$$m = C - \frac{5}{2} log(f) \rightarrow log(f) = C - \frac{2}{5} m \tag{4.4}$$

$$log(N) = -\frac{3}{2} log(f) + C \tag{4.5}$$

$$log(N) = \frac{3}{5} m + C \tag{4.6}$$

$$N = 10^{0.6m} + C \tag{4.7}$$

In reality, the Universe is governed by a non-Euclidean expansion cosmology where the comoving volume of space changes with redshift. Up to z $\sim$ 1 the slope of the brightest galaxy number counts are close to Euclidean geometry, however at higher redshifts the slope of the number counts begins to turn over, becoming more sensitive to the actual cosmology of the Universe. Thus, galaxy number counts are primarily used to test the predictions of theoretical models of galaxy and cosmological evolution; changes in the slope of number count distributions reflect physical changes in the underlying galaxy populations. Such models can predict galaxy properties in various bandpasses and for various redshift distributions.

Number counts have been well constrained in the observed optical and infrared bands as a result of the large number of ground- and space-based galaxy surveys performed in recent years (Madau & Pozzetti, 2000; Saracco et al., 2001; Yasuda et al., 2001; Barro et al., 2009). These studies probe both the evolved and star-forming stellar populations of galaxies depending on the galaxy's redshift. At local and low redshifts observations made in the optical and IR primarily detect light emitted by lower mass stars evolving along the main sequence as well as gas and dust emission in the IR that is re-processed light (longer wavelengths) from these stars. When the light from galaxies at higher redshifts (z $\gtrsim$ 0.5) is observed in the optical and IR it has been band-shifted into this region of the spectrum as the light has traveled towards Earth and therefore the emitted light is actually at shorter wavelengths. Thus, galaxies included in optical and IR number counts that are at z $\gtrsim$ 0.5 (varing slightly depending on the wavelength region observed) are star-forming

galaxies since it is their band-shifted emitted UV light that is being observed. As described previously, this light comes from the short-lived, massive, O and B stars that dominate the UV emission in new star-forming regions.

At observed far-ultraviolet (FUV) wavelengths, galaxy counts probe light from only unobscured star formation for $z \lesssim 1$, after which the Lyman limit (912Å) shifts into the observed bandpass. Little to no UV light is detectable blue-ward of this limit because it is used in ionizing HI gas in the interstellar and intergalactic medium between the galaxy and the observer. This has been shown in several studies attempting to constrain the Lyman continuum escape fraction at various redshifts (i.e., Siana et al., 2010, 2007; Bridge et al., 2010; Cowie et al., 2009). The majority of the detected FUV light is radiated by hot, massive, O and B stars, that have spectral energy distributions peaking at these wavelengths. Due to their short lifetimes, the UV light from O and B stars traces the star-forming regions within galaxies. For this reason, number counts of UV-detected galaxies provide a window into ongoing extragalactic star-formation history of the Universe.

FUV number count studies are only possible with space-based observations since the Earth's atmosphere is opaque to UV light. Over the past two decades, only a handful of space-based field galaxy surveys have been carried out at UV wavelengths (Milliard et al., 1992; Deharveng et al., 1994; Gardner et al., 2000a; Iglesias-Páramo et al., 2004; Xu et al., 2005; Teplitz et al., 2006; Hoversten et al., 2009) since long integration times are required to reach faint magnitudes. The first UV galaxy counts were measured by Milliard et al. (1992) using the balloon-borne FOCA instrument at 2000Å and bright magnitudes 15–18.5, covering a large area of sky ($\sim$6 deg^2). Later, two studies used deep imaging from the Hubble Space Telescope (HST) to measure faint UV galaxy counts. Gardner et al. (2000b) measured NUV (2365Å) and FUV (1595Å) counts over smaller areas (1.54 arcmin^2) for magnitudes 24.5–29.5 in the Hubble Deep Fields North and South (HDF-N & -S). Teplitz et al. (2006) measured FUV (1600 Å) counts for magnitudes 20.5–28.5 in the HDF-N, covering 3.77 arcmin^2. Bright UV galaxy counts (NUV: 2310, FUV: 1530), between 14–23.8 mag, were measured by Xu et al. (2005) using 36 Medium-depth Survey fields (MIS) and

3 Deep Survey fields (DIS) obtained with the Galaxy Evolution Explorer (GALEX). They cover a total area ∼20 deg^2. More recently, Hoversten et al. (2009) used the *Swift* UV/Optical Telescope to measure NUV (1928Å, 2246Å, 2600Å) galaxy counts in a 289 arcmin^2 area of the Chandra Deep Field South (CDF-S) between 21–26 mag. However, the only two studies measuring the faint end slope (24.5–29.5 mag) of the FUV galaxy counts are subject to cosmic variance effects, due to the small areas surveyed, and known overdensities in the HDF-N (Cohen et al., 2000).

This chapter presents a study of FUV (1614Å) galaxy number counts from deep images obtained with the Solar Blind Channel (SBC) on the Advanced Camera for Surveys (ACS). These observations sample a magnitude range of 21.5–29.5 and cover an area ∼4 times larger (15.9 arcmin^2) than the most recent FUV study that previously covered the largest area at these wavelengths and magnitudes (Teplitz et al., 2006). Section 4.2 presents the data used for this study. Section 4.3.1 discusses the measurement of the number counts and corrections to the counts due to observational biases. The number counts are compared with previous studies in Section 4.3.3 and theoretical models in Section 4.3.4. Finally, cosmic variance is discussed in Section 4.3.5. Results of this study are summarized in Section 4.3.3.

4.2 The Data

For this study FUV observations from three different data sets were used: the HDF-N area of the GOODS-N field, the HUDF area of the GOODS-S field, and smaller fields in various parts of the GOODS-N and -S fields (see Figure 4.1 and 4.2 and Section 1.1.1 for explanation of these fields). The HDF-N data is from the HST General Observer Program 9478, the HUDF data is from the HST Cycle 13 Treasury Program 10403, and the smaller GOODS-N and -S fields are from the HST Cycle 15 General Observer Program 10872. All observations were obtained with the SBC detector on Hubble's ACS.

The ACS SBC detector is a Multi-Anode Microchannel Array (MAMA) with a field of view of 34″.6×30″.8. MAMAs are photon-counting detectors equipped to

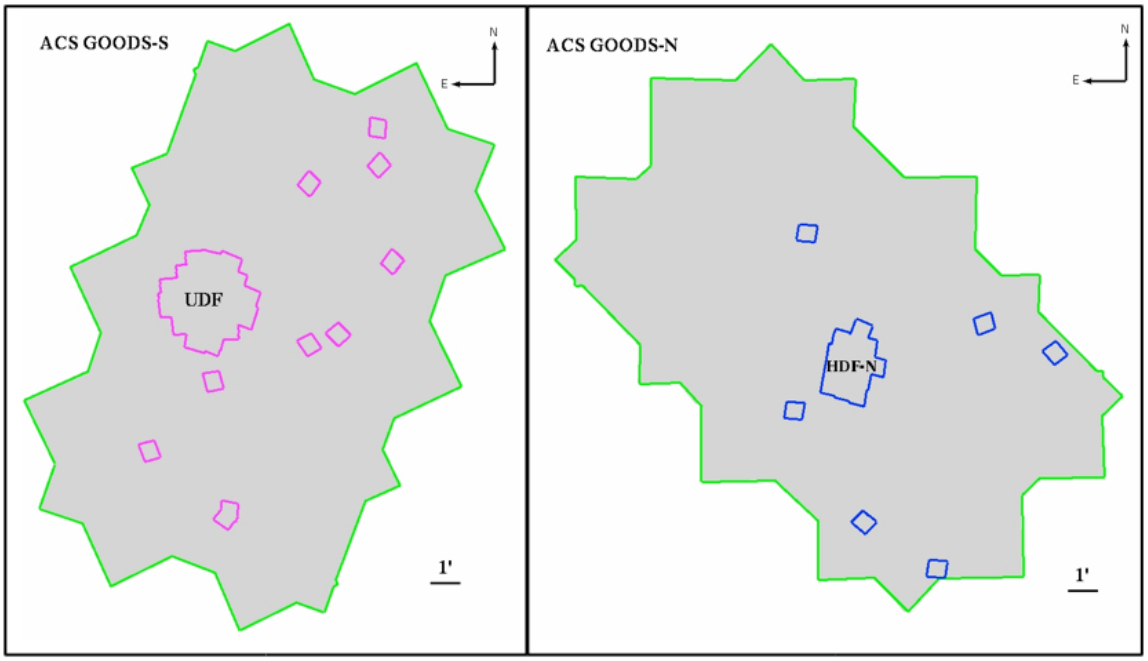

Figure 4.1 *Footprints of regions observed with the ACS SBC within the ACS GOODS-N and -S fields.*

produce 2D images on a scale of 0.03″/pixel. They are also only affected by noise due to temperature dependent dark current since they have no read noise and are not susceptible to cosmic rays. All observations were taken through the long-pass quartz filter, F150LP, that peaks ∼1500Å, has a bandwidth of ∼550Å, effective wavelength of 1614Å, and a FWHM=177Å. The SBC transmission curve is shown in Figure 4.3. At z ∼ 0.6 the Lyman limit, 912Å, is bandshifted to 1500Å, thus the SBC F150LP is only sensitive to the brighter galaxies beyond z > 0.7 and should not detect sources at all after z ∼ 1.2 where the Lyman limit is shifted to the far-right end of the F150LP throughput curve (∼2000Å).

Final images of the HDF-N and HUDF used for source detection were constructed using the DRIZZLE package in IRAF[1]. The smaller GOODS-N and -S images were tiled onto the original GOODS areas for source detection. Photometry is performed

[1]IRAF is distributed by the National Optical Astronomy Observatories, which is operated by the Association of Universities for Research in Astronomy, Inc., under cooperative agreement with the National Science Foundation.

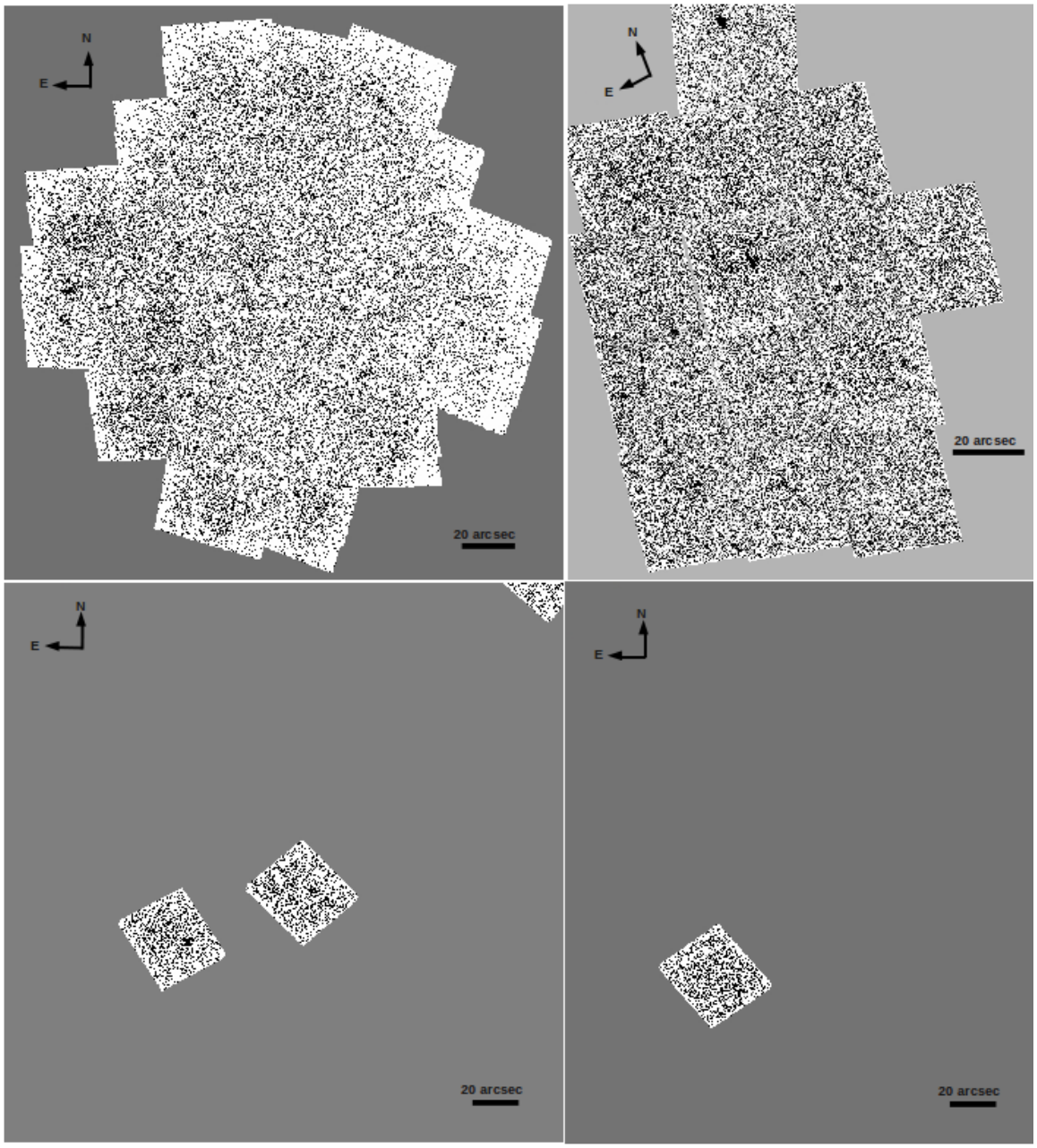

Figure 4.2 *Examples of FUV data taken with the ACS SBC F150LP. Top Left: HUDF image. Top Right: HDF-N image. Bottom Left: Small (< 1 arcsec^2) regions in GOODS-S tile 33. Bottom Right: Small (< 1 arcsec^2) region in GOODS-N tile 53.*

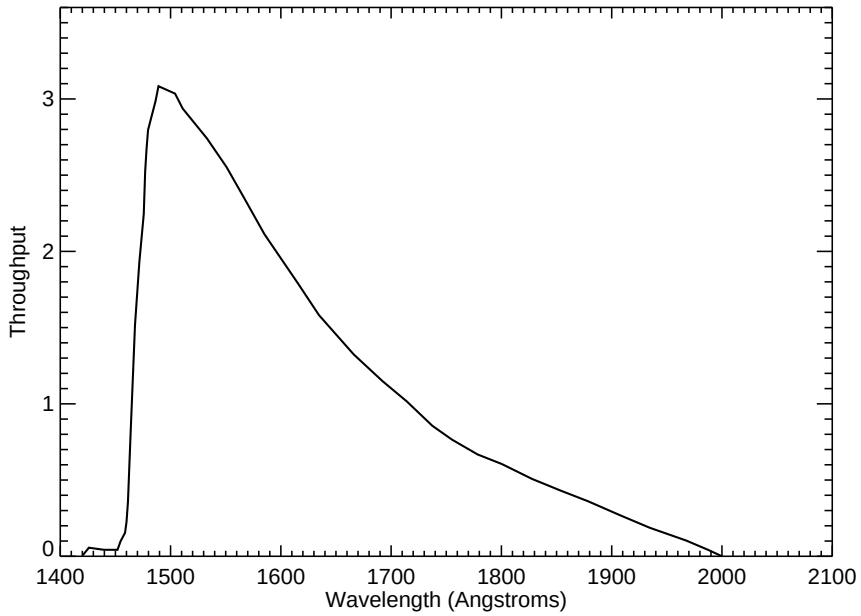

Figure 4.3 *Throughput of the HST ACS/SBC F150LP filter from the ACS Instrument Handbook.*

using similar procedures to those in Gardner et al. (2000a) and Teplitz et al. (2006) where optical segmentation maps produced with the SExtractor software package (Bertin & Arnouts, 1996) are used to determine the pixels that are included in the FUV flux measurement (Figure 4.4). SExtractor has difficulty working on low background data (Gardner et al., 2000a), such as the FUV images, thus in order to prevent false segmentation of sources, the optical image is used for detection because galaxies morphologies are less clumpy in the rest-frame optical than in the UV (Teplitz et al., 2006). Sources in the GOODS-N & -S fields ACS F606W (V-band) images were detected using SExtractor and extraction isophotes were defined to extend out to where the galaxy flux per pixel is 0.8 times the background RMS (σ). The 0.8σ apertures are then used to extract fluxes in the FUV images. The F606W images (Beckwith et al., 2006; Giavalisco et al., 2004) are more than one magnitude deeper than the FUV images (in AB mags).

Galactic extinction does not vary significantly over the areas we observe because

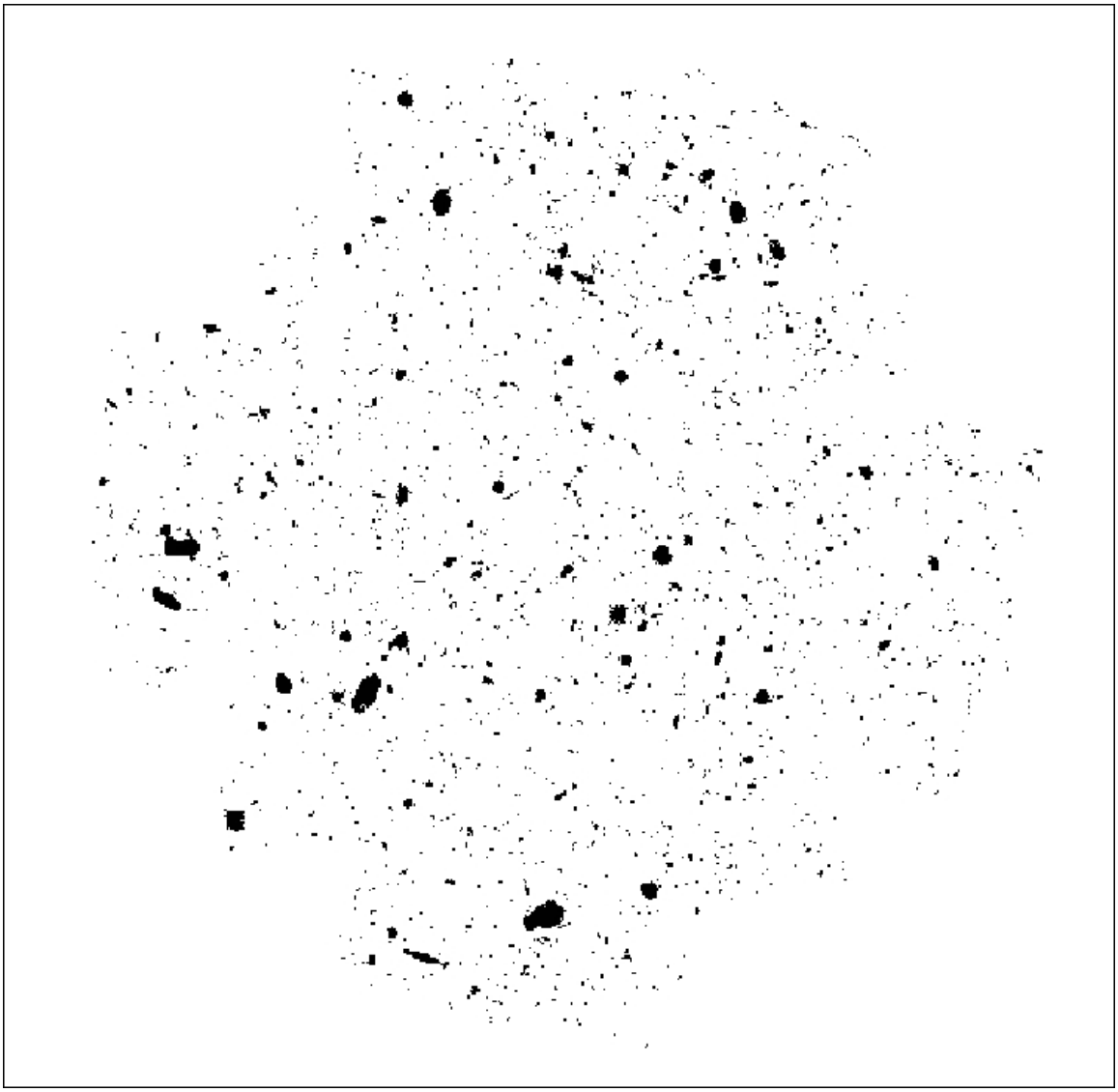

Figure 4.4 *Example of segmentation map with 0.8σ ACS/F606W (V-band) isophote areas in the observed SBC HUDF field.*

the GOODS fields were selected in part for the low extinction along their sight-lines (Beckwith et al., 2006; Williams et al., 1996). The range of extinction is found to be small over the GOODS-N & -S fields, varying between $0.0347 \leq A_V{}^2 \leq 0.0381$ and $0.0236 \leq A_V \leq 0.0298$, respectively. These values are from the Galactic dust maps of Schlegel et al. (1998)[3] based on the 100μm COBE/DIRBE and IRAS/ISSA maps. From these dust maps A_V is found at the central coordinate of each FUV source and the corresponding amount of extinction is calculate in the FUV, A_{1610}, via the ratio given in Siana et al. (2010) based on the extinction curve of Cardelli et al. (1989): $A_{1610}/A_V = 2.55$. None of the corrections for Galactic extinction are larger than 10%. Traditionally, when number counts are measured the detection areas of sources that have apparent brightnesses within a single increment of magnitude, or magnitude "bin" (e.g. $21.0 \leq m_{FUV} < 22.0$), are combined as a single data point plotted at the center of the magnitude bin on the horizontal axis. The extinction correction affects the final number counts measurement by shifting sources on the bright edge of a magnitude bin into the next brighter bin. However, only 9.3% of all FUV sources are shifted into a brighter bins after this extinction correction is made so this does not cause a major adjustment to the counts.

There are 114 FUV sources detected in the HUDF area of GOODS-S, 113 FUV sources detected in the smaller GOODS-N and -S images, and 116 FUV sources detected in the HDF-N area of GOODS-N. Ten sources were removed because they are too close to the edges of the images causing a certain amount of their area to be cut off. Thus, they can not be included accurately in the number counts measurement. This leaves 333 sources to be included in the measurement of the number counts. Three FUV sources in the sample are also X-ray detections and no stars were detected.

The three X-ray sources are *Chandra* detections CXO J123648.0+621309, CXO J033239.0-274602, and CXO J333213.2-274241 (Evans et al., 2010) located in the HDF-N area of GOODS-N, the HUDF area of GOODS-S, and a smaller area of

[2] A_V is the extinction in visual (V-band) light due to the reprocessing of light to redder wavelengths by gas and dust along the line of sight. It would be added to the magnitude to recover its intrinsic value.

[3] Accessed via the NASA/IPAC Infrared Science Archive (IRSA) Galactic Dust Extinction tool.

GOODS-S, respectively. Nandra et al. (2002) have done a study on the X-ray emissions of star-forming LBGs at z $\sim$ 3 and Balmer break galaxies[4] at z $\sim$ 1 in the HDF-N. They find an AGN (active galactic nuclei) fraction of $\sim$3% in this high-redshift LBG sample and an average stacked X-ray luminosity of 3x10^{41} erg s^{-1} for the remaining LBGs in their sample. Eight of the intermediate-redshift Balmer break sample show 2 AGNs in their spectra, and the remaining sources have a mean X-ray luminosity that is $\sim$5 times lower than the high-redshift LBGs. Interestingly, through analysis of the UV-to-X-ray luminosity ratio, L_{UV}/L_X, for both populations of star-forming galaxies they find no change between $1 < z < 3$, demonstrating that X-ray emission in star-forming high to intermediate-redshift sources follows the UV *SFR*. Lehmer et al. (2008) also confirm this finding at lower intermediate redshifts (up to z $\sim$ 1.4) in a study surveying 2,568 X-ray sources the CDF-N and the extended CDF-S. By measuring the mean X-ray-to-*SFR* ratio, L_X/SFR for galaxies with *SFR* = 1-100 $M_\odot$ they find that this ratio is constant over their entire redshift range, demonstrating that X-ray emisson can be used to trace star formation at intermediate to low redshifts as well. Thus, it is quite interesting that only three sources in the SBC/FUV sample also have X-ray detections. This could suggest that the star formation in these galaxies is smooth, not rapid, and that few (i.e. up to three) SBC/FUV galaxies have dominant AGNs.

The total SBC/FUV sample covers an FUV_{AB} magnitude range from 21–29 and its magnitude distribution begins to drop-off at $\sim$28.5 as shown in Figure 4.5. Reliable z_{phot} (photometric redshifts) are available for 212 sources and z_{spec} (spectroscopic redshifts) are available for 123 sources (Barger et al., 2008; Dahlen et al., 2010, T. Dahlen private communication). The redshift distribution for the FUV sample is shown in Figure 4.6 and a comparison of z_{phot} with z_{spec}, where available, is shown in Figure 4.7.

[4]Balmer break galaxies are star-forming sources detected by means of the rest-frame Balmer 3646Å + 4000Å break in their spectra. This criteria was introduced to identify galaxies at z $\sim$ 1–2 using their observed J-K color criteria. See Section 2.6 for further details on the Balmer 3646Å + 4000Å breaks.

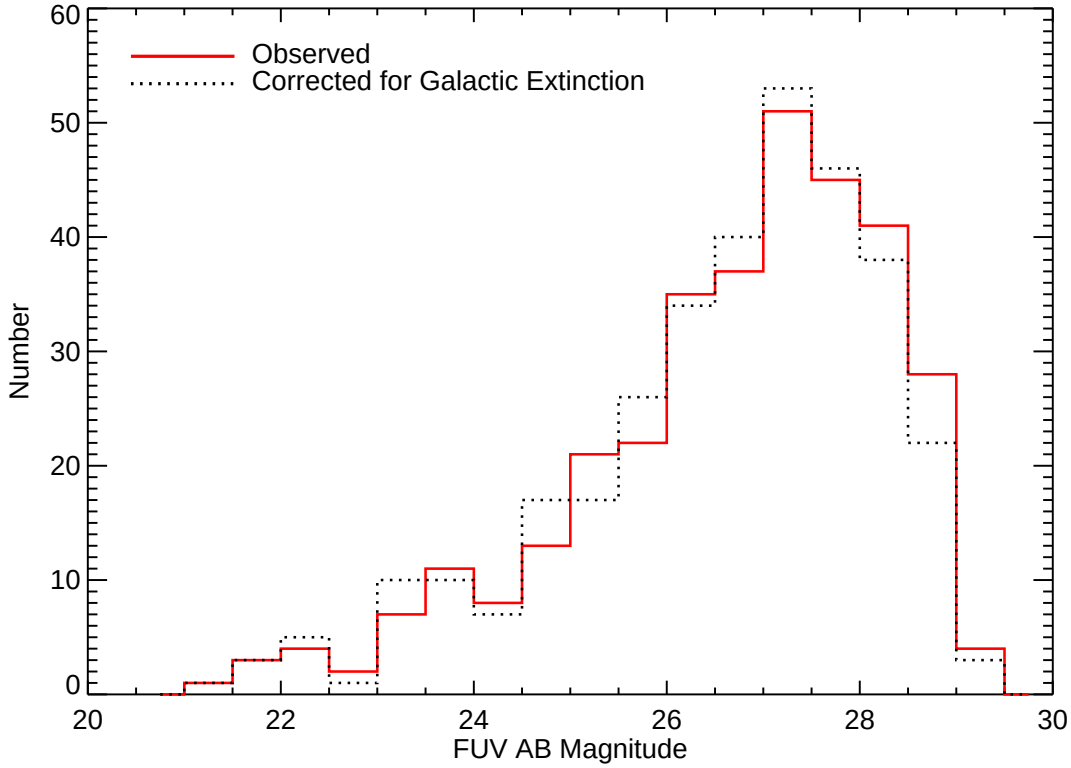

Figure 4.5 *FUV magnitude distribution for the 333 sources included in FUV number counts. Both the magnitude distribution as observed and the magnitude distribution corrected for Galactic extinction are shown. The extinction correction was done with* A_V *values from the Schlegel et al. (1998) Galactic dust maps and the ratio of* A_{1610}/A_V*=2.55 calculated in Siana et al. (2010).*

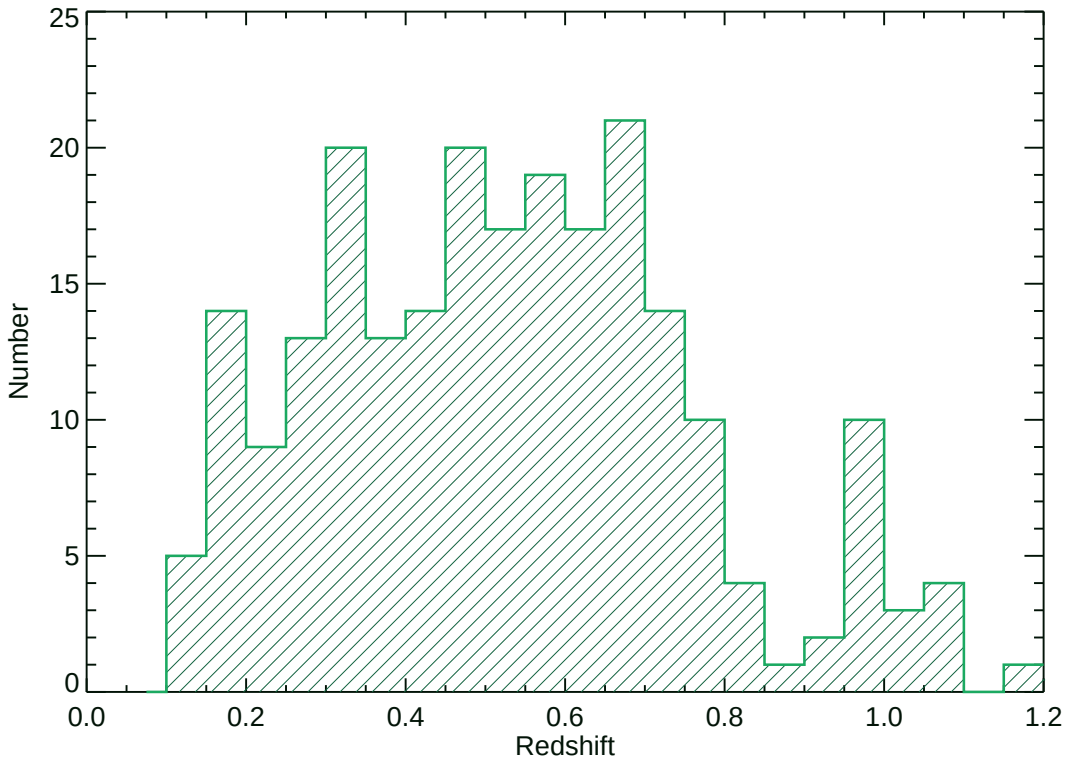

Figure 4.6 *Distribution of redshifts, where available, for 237 sources from the FUV number counts sample. The best quality redshift between z_{phot} and z_{spec} is used for each source (Barger et al., 2008; Dahlen et al., 2010, T. Dahlen private communication).*

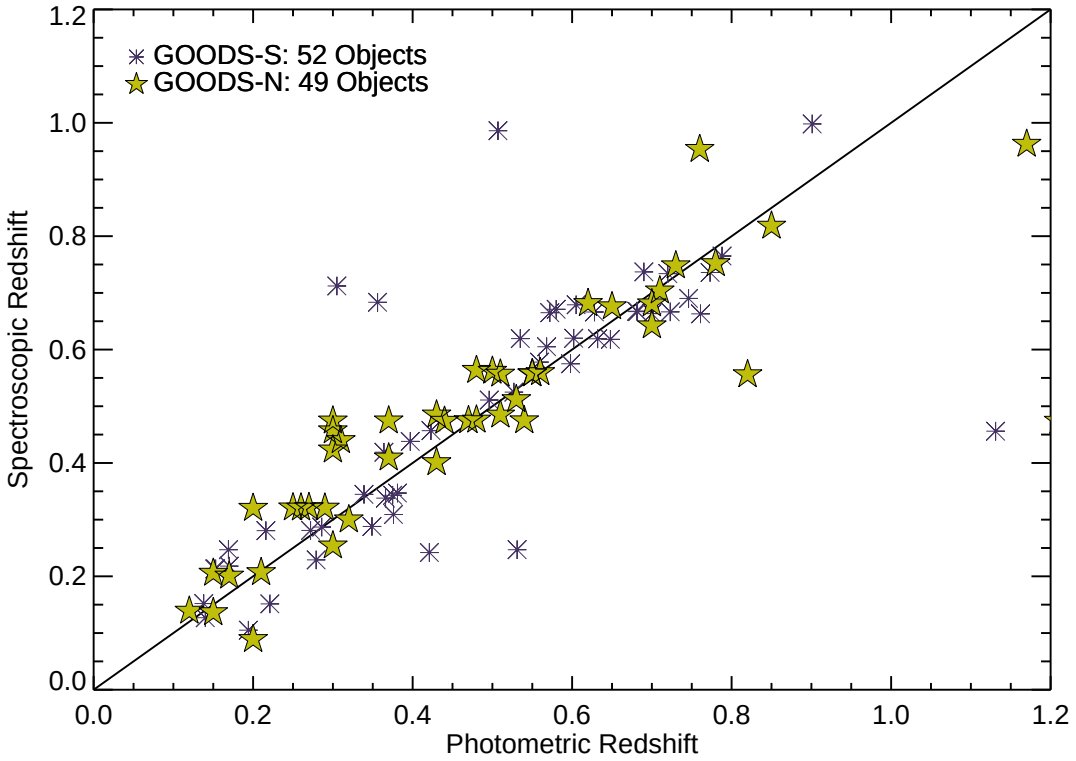

Figure 4.7 *Comparison of spectroscopic to photometric redshfits for 101 SBC/FUV sources. The z_{spec} quality flags of outlying sources have been checked and in the case of good quality the z_{spec} is used over the z_{phot}.*

4.3 Number Counts in the FUV

4.3.1 Measurement of Number Counts

In order to measure the number counts of galaxies in the sample the method developed for similar FUV data in Gardner et al. (2000b) is followed. Because there are variations in depth across the FUV images, each FUV source would not necessarily be detectable over everywhere within each image.The total area in which it would have been be detected in each image must be calculated for each source. The root-mean-square (RMS) error (i.e. variance) maps produced from the weight maps[5] of the drizzled SBC images are used to determine these areas. The RMS maps are defined as $1/(\sqrt{WeightMap})$. Small-scale-variations created during the image drizzling process are accounted for by smoothing the RMS maps with a $0''.4 \times 0''.4$ median filter. Each sources FUV_{AB} magnitude and size are required to calculate the total possible detection area in an image for that source. FUV_{AB} magnitudes of the sources in all observed fields were obtained from photometric catalogs produced with SExtractor as described in Section 4.2. The size of each source was determined from the SExtractor segmentation maps used for the catalog photometry. Using the size and magnitude of each source the maximum RMS error of a pixel at 3σ is calculated in the following way: $flux/(3\times\sqrt{size})$. Pixels in the RMS map with errors less than or equal to this value make up the total area over which the source would have been be detected at 3σ.

In order to be consistent, and not overestimate the detection area of the other sources, the edges of each RMS map are cut down by a length equal to the radius of the circular area of each source (discussed in Section 4.2) before calculating their detection areas. This includes both the outer edges of images, as well as edges on the inner parts of the images where drizzled fields do not overlap in the HUDF and HDF-N.

[5]Generally, a weight map is a map of the bad pixels in an image. Weight maps produced as output when drizzling multiple dithered images together are maps of the variations in exposure time, or depth, across the final image.

4.3.2 Incompleteness

In any given magnitude bin there is always some difference between the actual number of galaxies at that magnitude and the number counts as they have been measured from the data. This effect is largely due to variations in the surface brightnesses of extended sources that have a certain apparent magnitude. Sources having bright magnitudes may be largely extended with a smooth light profile and thus be generally low in surface brightness causing them to be detected as a fainter magnitude object or not be detected at all. However, this incompleteness effect tends to become larger towards fainter magnitudes.

For this study two independent methods are used to correct for incompleteness: bootstrap-sampling from a larger catalog of real data and detection of artificially introduced galaxies. For the first method the size distribution of the version 2.0 GOODS-S V-band catalog[6] is bootstrap-sampled starting with a randomly generated FUV galaxy sample. First, 2000 FUV magnitudes are randomly generated for each FUV magnitude bin. Next, following the procedure in Gardner et al. (2000b) the mean and standard deviation parameters of a Gaussian distribution fit to the FUV-V color distribution in GOODS-S between $24 \leqslant m_{AB} \leqslant 28$ is used to randomly generate FUV-V colors. This distribution is presented in Figure 4.8. Even though the completeness correction is ultimately applied to all magnitude bins from 21.5–29.5, this range ($24 \leqslant m_{AB} \leqslant 28$) is selected for determining the Gaussian distribution because the magnitude distribution of the FUV sample drops off at $\sim$28.5, and there are very few galaxies in the HUDF with magnitudes brighter than 24. Thus, including bins brighter or fainter than these magnitudes would introduce unnecessary errors in the distribution. Because the color distribution does not vary greatly between the different SBC fields only the HUDF is sampled. With these random FUV magnitudes and FUV-V colors the optical magnitudes of the randomly generated sample are calculated (i.e. FUV_{AB} - (FUV_{AB}-V_{AB}) = V_{AB}) and matched them to the closest optical magnitudes of sources in the GOODS-S V-band catalog effectively boot-strap

[6]http://archive.stsci.edu/prepds/goods/

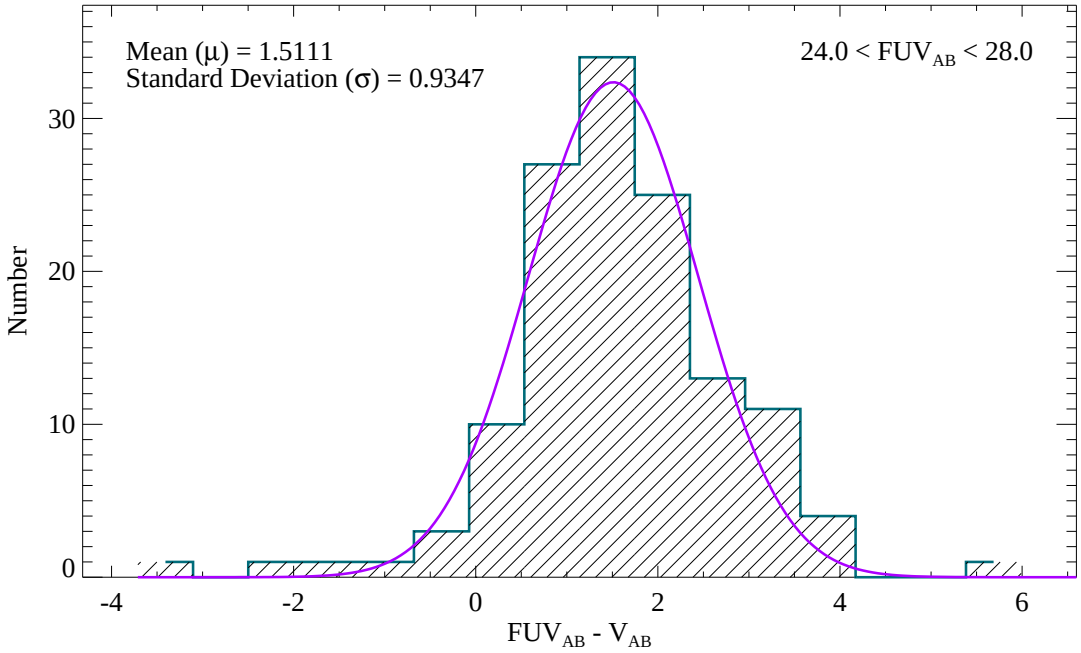

Figure 4.8 *The ultraviolet - optical color distribution of all FUV sources in the GOODS-S data. A Gaussian profile is fit to the distribution and its parameters are listed. These parameters are used to generate random optical magnitudes for completeness correction simulations.*

sampling the catalog. The sizes of these objects are then sampled from segmentation maps produced from public GOODS-S V-band images with SExtractor using 0.8σ isophotes to define the source areas. These are isophotes within which each pixel in the V-band images is 0.8σ above the background noise. Isophotes of size 0.8σ are used to be consistent with the isphotes used for the actual FUV photometry. Next, the maximum RMS pixel error below which each simulated object would be detected from the sizes and FUV magnitudes of the random sample are calculated. Using these errors the total detection area for each simulated object in the SBC RMS maps is determined (Figure 4.9). Finally, to get the completeness correction factor for each magnitude bin, the average of the detection areas per magnitude bin is calculated for

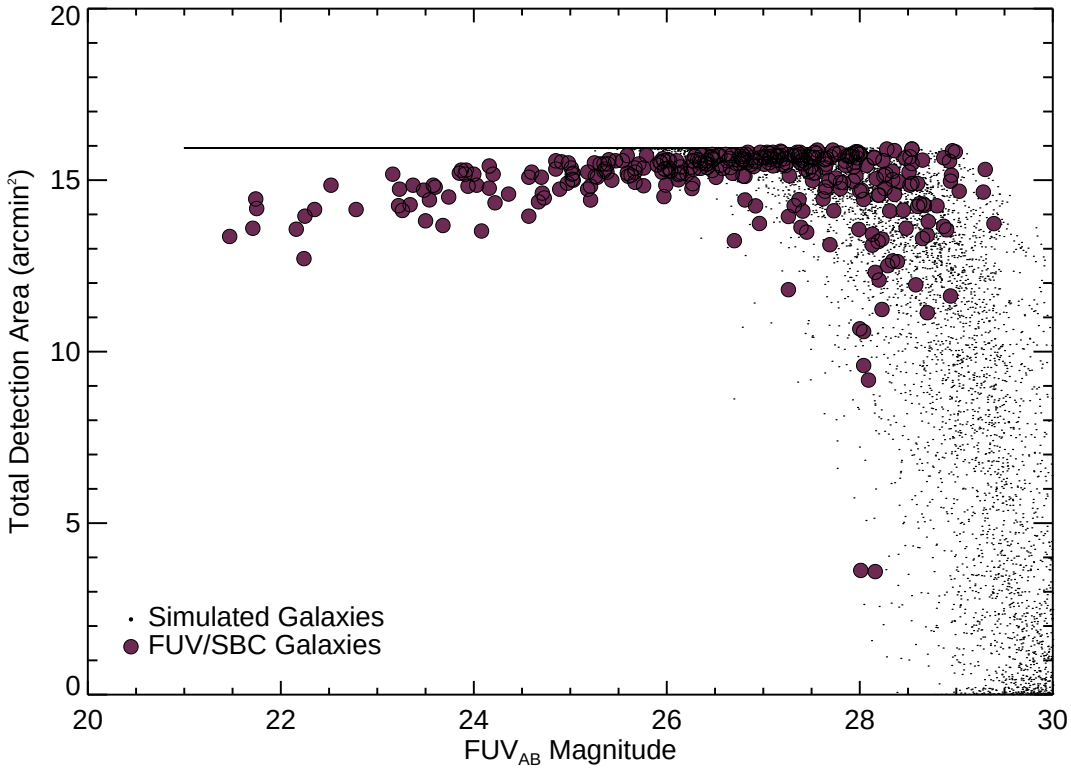

Figure 4.9 *Comparing the detection areas for real SBC/FUV galaxies and simulated galaxies used to calculate the completeness correction in method 1 (boot-strap sampling). These are the total areas over which these sources could be detected in the SBC data at 3σ. Bright galaxies are detected over the entire area producing the constant area line at bright magnitudes.*

the simulated objects (including galaxies with zero detection area), and its ratio with the average detection area of all real FUV sources in corresponding bins is taken. The number counts in each bin are multiplied by this factor to correct for incompleteness.

The second incompleteness correction method introduces 500 artificial FUV galaxies into the SBC data for each magnitude bin and recovers them with the same photometry algorithm used for the real data (Figure 4.10). The artificial sources are simulated using the IRAF task ARTDATA in the NOAO package. The same number of V-band galaxies are also simulated with ARTDATA in order to use their isophotal sizes to provide the area in which to measure the flux of the artificial FUV sources.

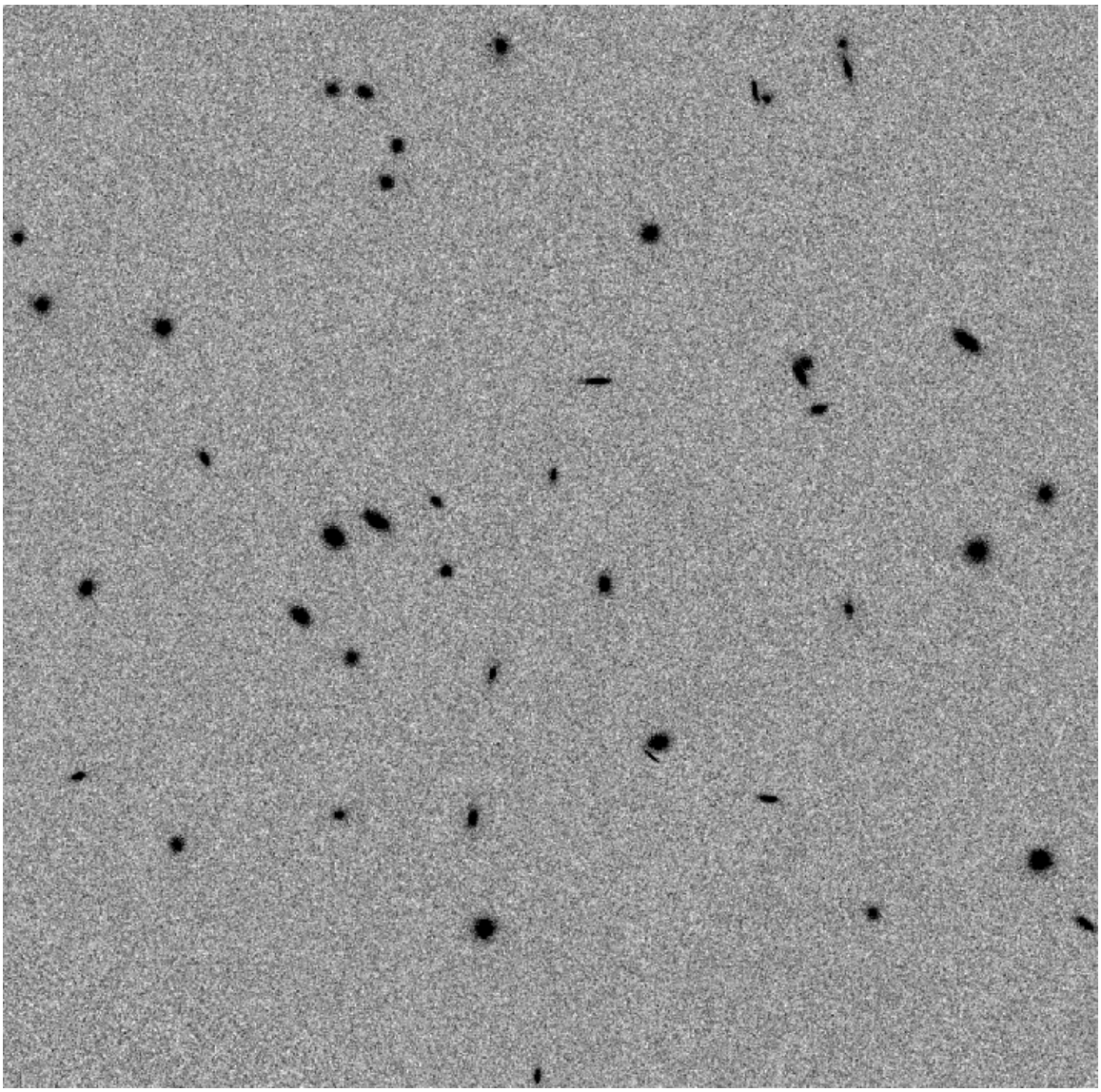

Figure 4.10 *Example of artificial sources simulated with V-band magnitudes in ART-DATA and dropped into an all background image.*

Essentially, this approach mimics the procedure of the actual FUV photometry. To determine the correct magnitudes of the artificial V-band galaxies, we use the parameters of the same Gaussian FUV-V color distribution discussed above. ARTDATA is given a V-band magnitude range calculated by adding and subtracting the standard deviation of the fitted distribution (σ) from an optical V-band magnitude equal to the center of that FUV magnitude bin minus the mean of the fitted distribution (μ). To make sure the artificial V-band and FUV sources are located at the same coordinates in the data the same seed value is used for the random number generation in ARTDATA. Next, a GOODS-S V-band tile is chosen at random and all real galaxies are removed from the image by subtracting segmentation maps created with GOODS SExtractor parameter files. The "holes" in the image are replaced with background noise by taking count values of the pre-existing background pixels, randomizing their order, and combining them back in the image at these locations. This same procedure is done for the SBC/FUV data in order to prepare a "clean" image of only background in which to drop the artificial sources. An advantage of the ARTDATA task is that it convolves the artificial galaxies with a user provided point-spread-function (PSF) before placing them in the data. The program TinyTim[7] was used to create PSF images to be convolved with both the optical and FUV data. TinyTim was developed specifically to generate PSFs for HST instruments/data. Once the artificial V-band sources were dropped into the all-background image, SExtractor was again used to create segmentation maps of the artificial sources using the same 0.8σ detection threshold as with the real data. After the artificial FUV sources were generated into the background image with ARTDATA, photometry was performed using the artificial V-band areas. An artificial FUV source that has S/N > 3.5 is a detection, where S/N = *(Sky Subtracted Flux) / (*$\sqrt{(RMSError)^2 + (PoissonError)^2 + (SkyError)^2}$*)*. The final detection ratio equals the number of sources recovered over 500 (total sources simulated). This entire procedure was carried out for each magnitude bin (21.5-29.5). Finally, to correct for incompleteness the number counts are divided by the determined detection ratio in each magnitude bin.

[7]http://www.stsci.edu/software/tinytim/tinytim.html

Table 4.1. Comparison of Completeness Correction Methods

FUV_{AB} (mag)	Method 1	Method 2	Difference
21.5	1.107	1.000	0.107
22.5	1.111	1.000	0.111
23.5	1.053	0.998	0.055
24.5	1.039	0.998	0.041
25.5	1.014	1.000	0.014
26.5	1.005	1.000	0.005
27.5	0.972	0.972	0.000
28.5	0.858	0.850	0.008
29.5	0.364	0.270	0.094

As described in Section 4.3.1, completeness method 1 uses boot-strap sampling of real galaxies in optical GOODS catalog for simulations and method 2 tests the recovery of large samples of artificially generated galaxies dropped into the real data.

Both of these methods yield similar incompleteness corrections, within a few percent of one another, in each bin. The results of each method are given in Table 4.1. An average of these two methods is used for the final correction to the number counts.

4.3.3 Comparison with Previous FUV Number Counts

Figure 4.11 presents the completeness corrected and the raw FUV number counts from this work and from past FUV number count studies in the literature. Their measured values, errors, completeness, and detection areas per magnitude bin are provided in Table 4.2. Small number Poisson statistical errors are calculated for each point from Gehrels (1986) at the 1σ level. The filled circles represent the completeness corrected counts. The open circles represent the raw counts. The upside-down

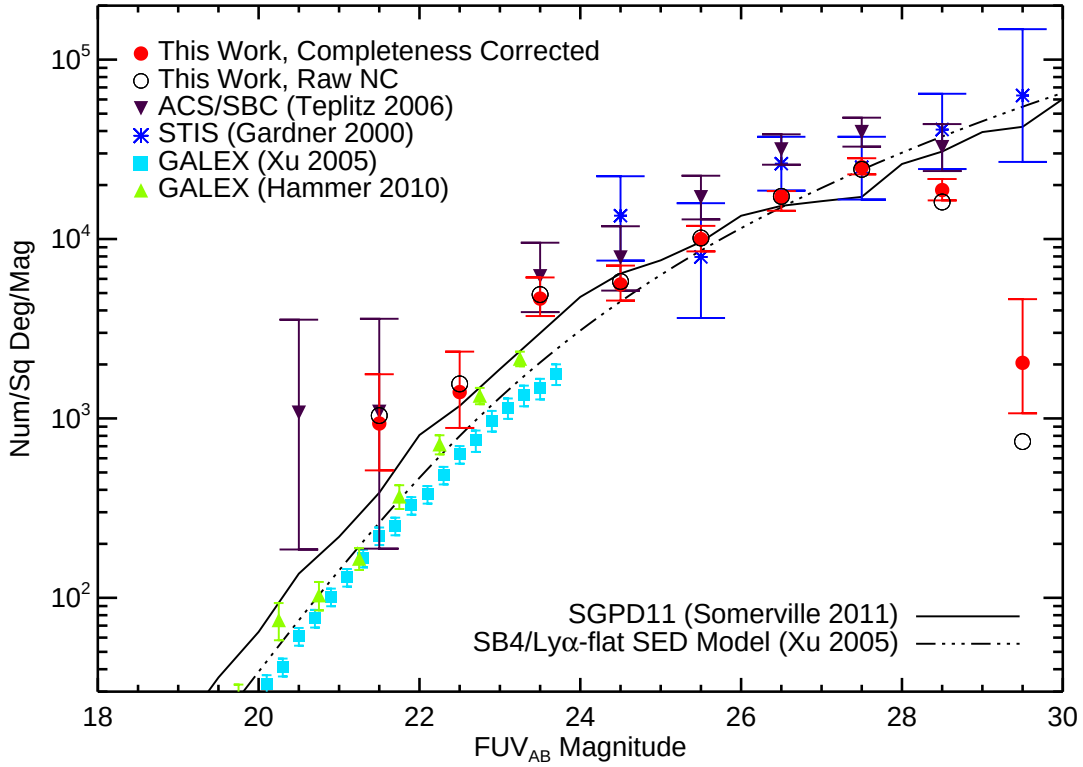

Figure 4.11 *FUV number counts of field galaxies from this work shown with FUV number counts from previous studies and compared to semi-analytic models. Error bars are Poisonnian from Gehrels (1986). The caps of the error bars do not reflect an error in magnitude, but have been manually varied in length to better distinguish amongst them.*

triangles represent counts done with SBC images of the HDF-N from Teplitz et al. (2006). The asterisks represent counts done with HST Space Telescop Imaging Spectrograph (STIS) in the HDF-N and HDF-S from Gardner et al. (2000b). The squares represent counts done with GALEX from Xu et al. (2005) (hereafter XU05 fields), and the upright triangles represent counts done with GALEX from Hammer et al. (2010) (hereafter HAM10 field). No color corrections are made between the SBC filter which has a central wavelength of 1614Å (filter peak is λ=1500Å) and the STIS and GALEX filters that have FUV central wavelengths at 1595Å and 1530Å respectively. As discussed in Teplitz et al. (2006), the color correction between the SBC

Table 4.2. FUV Galaxy Counts

FUV_{AB} (mag)	NC (No. deg^{-2} mag^{-1})	log NC	σ_{low}	σ_{high}	Raw No.	Completeness	Area ($arcmin^2$)
21.5	937	2.97	0.26	0.27	4	1.054	13.89
22.5	1402	3.15	0.20	0.23	6	1.056	13.89
23.5	4656	3.67	0.10	0.12	20	1.026	14.70
24.5	5582	3.75	0.09	0.11	24	1.019	14.91
25.5	9996	4.00	0.07	0.07	43	1.007	15.28
26.5	17207	4.24	0.08	0.03	74	1.003	15.42
27.5	25166	4.40	0.04	0.05	99	0.972	15.20
28.5	18752	4.27	0.06	0.06	60	0.854	14.33
29.5	2041	3.31	0.28	0.36	3	0.317	14.56

Note—Magnitudes represent the center of the bins, errors are 1σ Poisonnian (Gehrels, 1986), and areas are the average total detection areas of all objects within each magnitude bin.

and GALEX FUV filters would be significant for galaxies at z > 0.50 because the SBC filter is sensitive to a larger volume (∼30%) than the GALEX filter. This color difference results in no more than a factor of ∼2 (∼ half a magnitude) between the SBC and GALEX number counts. They also discuss that Lyα emitting sources at z < 0.15 could have the opposite effect resulting from the bluer wavelength coverage of the GALEX filter. About 54% of the FUV sample with z_{phot} are at $z_{phot} > 0.50$ and ∼ 2.3% are at $z_{phot} < 0.15$. The majority (98%) of sources at $z_{phot} > 0.5$ are not comparable to GALEX bins because they have fainter magnitudes ($FUV_{AB} >$ 24). Thus, comparisons with GALEX FUV number counts are not largely affected by ignoring the filter color correction.

The SBC/FUV galaxy sample selected and presented in this thesis probes the faint-end of the number counts, with the majority of sources occupying magnitude bins 23.5-28.5. This is reflected in the error bars of these plotted points. A power law is fit to the data in these bins with a slope of 0.14 ± 0.04 and an intercept of 0.40 ± 1.0. The three faintest objects in the sample have $FUV_{AB} = 29.19$, 29.21, and 29.33 and their ACS/F606W V-band and SBC/FUV images are shown in Figure 4.12. Although these sources are fainter than the magnitude drop-off of the FUV data (∼28.5), they

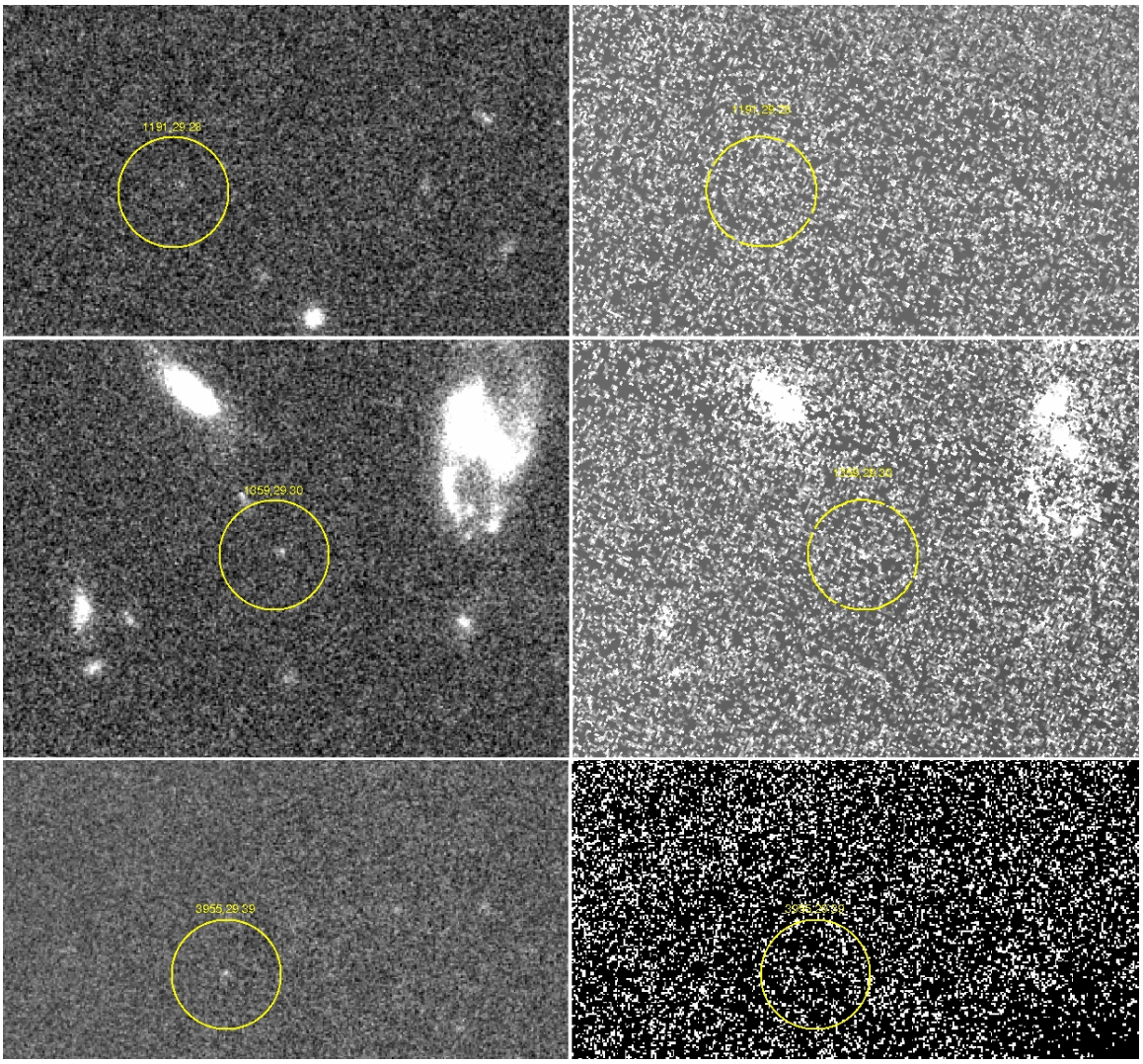

Figure 4.12 *Three FUV sources in the 29th magnitude bin of the number counts with extinction corrected magnitudes 29.19(top), 29.21(middle), and 29.33(bottom). The ACS V-band image is shown on the left and the SBC FUV image is shown on the right. The location of each source is within the yellow circle.*

are detected in the GOODS V-band catalog and are above the detection threshold of 0.8σ and have S/N > 3.5. Thus, they are included in these number counts. However, due to the few sources detected, the measurement does not accurately represent the number counts at this very faintest level. The large discrepancy between the Gardner et al. (2000b) 29th bin count and the 29th bin count measured here is due to longer

exposure times and to the higher sensitivity of STIS as compared to the ACS SBC detector. The measured counts are lower than previous faint HST FUV counts from Gardner et al. (2000b) and Teplitz et al. (2006) by an average standard deviation of ∼35% and ∼36%, respectively. The differences in the measurements are likely the result of cosmic variance which is discussed in more detail in Section 4.3.5.

At the 22.5 magnitude bin the slope of the FUV number counts intersects the faint end of the GALEX HAM10 field counts but not the XU05 field counts, remaining higher than these at all overlapping magnitudes. It is not well understood why the GALEX counts diverge from each other after FUV_{AB} ∼21.25, but Hammer et al. (2010) show the divergence can not be due to their source detection/photometry methods, AGN, or cosmic variance between fields. Also, while cluster members in the HAM10 field bias the bright bins of these number counts, they only compose ∼2% of objects in the faintest bin, which represents the limiting depth of the survey. However, massive clusters are known to be associated with many filaments and the number of filaments has been found to directly correlated with cluster mass (Pimbblet & Drinkwater, 2004). Thus, Hammer et al. do not rule out large scale structure behind the massive Coma Cluster as the culprit of their excess galaxy counts.

4.3.4 Comparison with Number Counts Models

A primary use of galaxy number counts is to test and constrain models of galaxy evolution. Initial galaxy counts were tested against models based on the null hypothesis that galaxy populations did not evolve over time and thus are appropriately called "no-evolution" models. In the simplest way these models, when plotted with empirical data, show that there is evolution in the properties of the underlying galaxy population. Other models can be developed simply to test for number evolution or luminosity evolution of a given sample of number counts. However, the most important results come from comparing complex models based on the theory of the ΛCDM hierarchical formation scenario (see Section 1.3 for basic discussion) that will thoroughly test cosmological parameters and evolutionary predictions of multiple galaxy proper-

ties. Such models start by simulating density fluctuations consistent with a designated primordial power spectrum parameter, σ_8, as predicted for the early Universe. In this framework baryonic matter assembles and condenses in gravitational potential wells of aggregations of dark matter, developing stars and galaxies as formulated by set timescales, star-formation histories, and endpoint morphological distributions. The intricacies of these models are adjusted to fit the results of real observations.

In Figure 4.11 the FUV number counts are compared with two different models, a simple luminosity evolution model from Xu et al. (2005) and a cosmological semi-analytic model (SAM) from Somerville et al. (2011, hereafter SGPD11). The first model is labeled on the plot as the SB4/Lyα-flat SED model. This model is characterized by a UV luminosity evolution, $L^* \sim (1+ z)^{2.5}$, and is constructed from a local FUV luminosity function (Wyder et al., 2005) with an estimated K-correction based on the UV starburst 4 (SB4) SED from Kinney et al. (1996) with a flat spectrum between 1200Å and 1000Å. It was selected as a initial check that the measured number counts were within reason since this model is in good agreement with evolution models derived from observed luminosity functions at high redshift (Arnouts et al., 2005). When plotting the SB4/Lyα-flat SED model it was not color corrected from the GALEX FUV effective wavelength at 1530Å to the SBC effective wavelength at 1614Å (see further discussion in Section 4.3.3).

The second model, SGPD11, makes use of the latest version of the SAMs developed by Somerville and collaborators (Somerville et al., 2008, 2001; Somerville & Primack, 1999). The backbone of these SAMs are dark matter "merger trees" representing the hierarchical build-up of structure in the Λ Cold Dark Matter (ΛCDM) paradigm. The model shown here is the "fiducial WMAP5" model presented in SGPD11, and adopts cosmological parameters consistent with the five year WMAP analysis (WMAP5; Ω_m=0.2383, Ω_Λ=0.7617, h=0.732, σ_8=0.82; Komatsu et al., 2009). The physical processes included in this model are radiative cooling of gas, photoionization squelching, star formation in quiescent and burst modes, morphological transformation via mergers, supernovae feedback, chemical evolution, black-hole growth, AGN-driven winds, and radio-mode feedback. The UV luminosities for the SAM galaxies are cal-

culated from synthetic SEDs created by convolving the star-formation and chemical enrichment histories for each galaxy with Bruzual & Charlot (2003) stellar population models using a Chabrier initial mass function. A two-component model for extinction by dust in diffuse cirrus and in dense "birth clouds", following Charlot & Fall (2000), is also applied. SGPD11 found, in agreement with other studies, that they had to adopt dust parameters that varied with redshift in order to match the UV and B-band luminosity functions at high redshift. Note that unlike simple pure luminosity evolution models, SAMs have many physical sources of scatter in galaxy number densities and properties. This causes bin-to-bin variation just as in a real survey. Therefore the predicted counts are not perfectly smooth.

The FUV number counts are compared to the SGPD11 model for several reasons. This model includes what are believed to be the key physical processes that shape galaxy formation and evolution. In particular, the FUV number counts are expected to provide an important constraint on the processes that trigger and regulate star formation, which are highly uncertain. The FUV number counts are also highly sensitive to dust extinction, which is another uncertain ingredient in SAMs.

The measured FUV number counts are broadly consistent with the SGPD11 and the SB4/Lyα-flat SED model over all magnitudes. As seen in Figure 4.11, the SB4/Lyα-flat SED model appears lower than the SGPD11 SAM up to FUV_{AB} $\sim$26.5 after which the trend is reversed and the SGPD11 model is lower. The differences in the bright end of the models are most likely due to the fact that the SB4/Lyα-flat SED model is derived from a single spectral-energy distribution. Both sets of GALEX counts are lower than the SGPD11 model at the bright end, however the HAM10 field counts start to coincide with the models at $\mathrm{FUV}_{AB} > 22.5$. This is consistent with the fact that the SGPD11 model is known to overproduce bright galaxies compared to GALEX data (Gilmore et al., 2009; Somerville et al., 2011), due to a small degree of residual "overcooling" in massive halos. The number counts do not match the SB4/Lyα-flat SED model at all magnitudes, but begin to coincide only after 24.5 mag. As discussed by Teplitz et al. (2006), the discrepancies with this model, especially towards bright magnitudes, may suggest a need for number density

evolution in FUV galaxy number count models because this model only takes into account luminosity evolution.

4.3.5 Effects of Cosmic Variance

If one could imagine the classic metaphor of the cosmic expansion of the universe as the growing volume of a balloon being filled with air, observations from any location on the balloon would be limited to a surface area within one's horizon. Any area beyond this curvature would never be seen by the observer. Additionally, observations of the viewable area may also be bias due to the non-uniform distribution of matter in the universe. Uncertainties in measurements of galaxy number counts can arise as a result of overall large-scale structure variation, or cosmic variance (Somerville et al., 2004; Trenti & Stiavelli, 2008). In deep galaxy surveys spatial area is often sacrificed for longer integration times at a single "pencil beam" pointings in the sky. This results in any statistics derived from those observations to be a product of the specific structure dominating that location in the universe. If an observer could examine a volume on the order of several times the scale of these structural variations then a bias due to cosmic variance would be insignificant in their measurements. Thus, it is important for studies measuring the number counts of galaxies to be aware of and take into account these effects on their measurements. Statistically the correction for cosmic variance on a set of number counts is expressed as,

$$\sigma_v \equiv \frac{< N^2 > - < N >^2}{< N >^2} - \frac{1}{< N >} \tag{4.8}$$

where the mean of the number counts is $< N^2 >$ and the the variance of the counts is $< N >^2$. One way in which the issue of cosmic variance can be relatively circumvented is by making several observations over small "pencil beam" areas that probe a variation of lines of sight in the sky and doing number statistics on these combined fields.

The observations used for this study were designed to significantly reduce the effects of cosmic variance by including data from various sight-lines and covering a larger area than any previous FUV number counts study at these wavelengths and

magnitudes. The observations cover a total area of 15.9 arcmin^2, while the Gardner et al. (2000b) STIS observations in the HDF-N and -S cover only 1.54 arcmin^2 and the Teplitz et al. (2006) SBC observations in the HDF-N cover only ∼3.77 arcmin^2. Also, the HDF-N has galaxy overdensities at z ∼0.45 and z ∼0.8 (Cohen et al., 2000) that bias the number counts in that field. To demonstrate the effects of cosmic variance Figure 4.13 compares the total FUV number counts with the number counts as calculated in the GOODS-N and GOODS-S SBC fields separately. The red circles represent the total number counts, blue upside down triangles represent the number

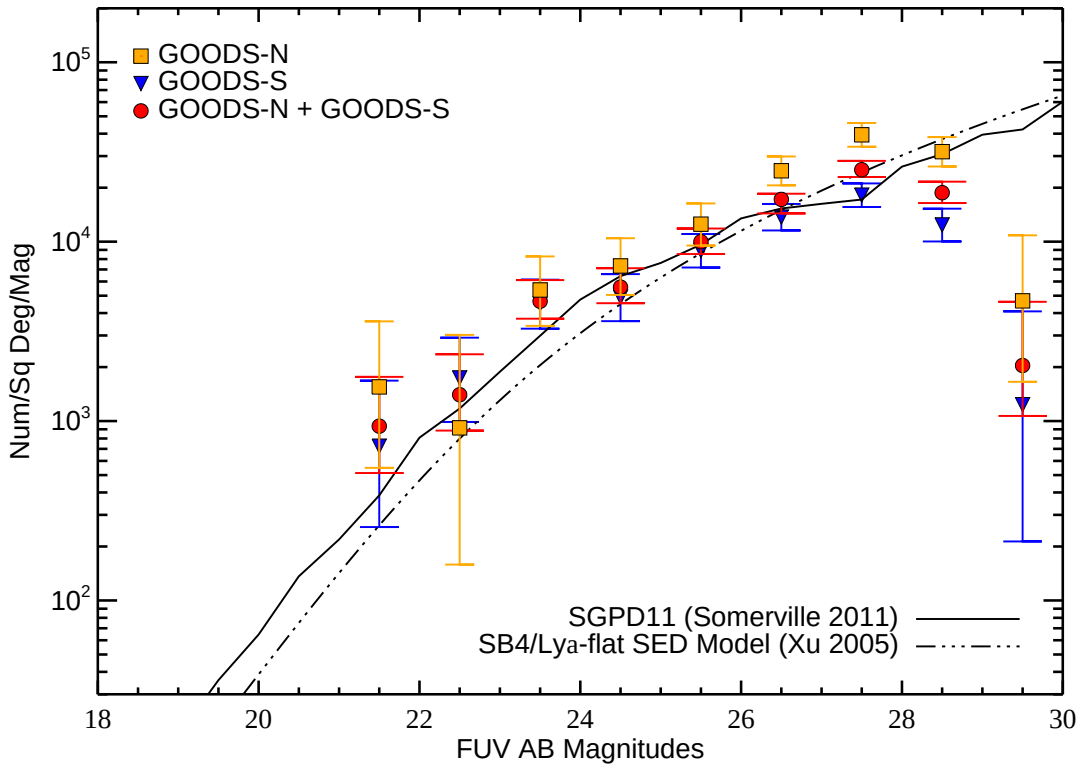

Figure 4.13 *FUV number counts for individual GOODS fields. We excluded the brightest (21.5 mag) and the faintest (29.5 mag) magnitude bins from this plot because there is not enough signal-to-noise to make a comparison between fields at these magnitudes. HDF-N counts are from Teplitz et al. (2006). The caps of the error bars do not reflect an error in magnitude, but have been manually varied in length to better distinguish amongst them.*

counts in the GOODS-S area, and the orange squares represent the number counts in the GOODS-N area. The counts in the GOODS-N area are consistently higher than those in GOODS-S in every magnitude bin except 22.5. The total number counts are a rough average of the number counts in these two fields over the entire magnitude range. This result demonstrates that using large areas and various sight-lines to make measurements of number counts reduces bias due to cosmic variance, and ideally these types of data sets provide the best comparisons for SAMs.

4.4 Summary

This chapter presented FUV galaxy number counts at 1614Å measured from deep HST ACS/SBC observations of the HUDF area of the GOODS-S field, the HDF-N area of the GOODS-N field, and 15 smaller fields at various pointings in GOODS-N and -S. These data sample the faint-end of the FUV number counts out to FUV_{AB} $\sim$29, with the majority of the sources in magnitude bins 23.5-28.5, and cover an area (15.9 arcmin^2) $\sim$4 times larger than the most recent deep FUV number counts survey (Teplitz et al., 2006) at these wavelength and magnitude ranges. The number counts distribution provides the following results:

1. A slope of 0.14 $\pm$ 0.04 (intercept of 0.40 $\pm$ 1.0) fits the faint-end of the logarithmic number counts distribution from FUV_{AB} = 23.5 to 28.5.

2. These number counts are $\sim$35% and $\sim$36% lower, on average, than the faint FUV counts measured in the HDF-N area of GOODS-N from Gardner et al. (2000b) and Teplitz et al. (2006), respectively. The differences are most likely due to cosmic variance.

3. The bright end of the number counts slope, at FUV_{AB} = 22.5, intersects the most recent GALEX FUV number counts from Hammer et al. (2010), but is higher than the GALEX FUV counts from Xu et al. (2005) at all common magnitudes.

4. The latest λCDM semi-analytic model based on the WMAP5 cosmology (Somerville et al., 2011) is in good agreement with the FUV number counts. Generally, the FUV counts are higher than the SB4/Lyα-flat single SED model (Xu et al.,

2005) but become more consistent at the faint-end. This may result from the model being based on a single starburst SED, thus offering evidence for number density evolution.

5. When the number counts are measured in the individual GOODS-N & -S fields they are clearly affected by cosmic variance. This may be due to overdensities along a given line of sight or simply from sampling smaller areas than used in the combined counts. This result confirms that previous faint HST FUV number counts were boosted due to the use of data only in the HDF-N field of GOODS-N. Clearly, in order to best asses the results of SAMs it is ideal to compare with number counts studies covering as large areas as possible over multiple sight-lines.

5

The Resolved Ultraviolet Background Light

This chapter presents new measurements for the extragalactic background light from resolved galaxies observed at FUV wavelengths. A detailed account of previous studies of the UV background is given to set the context for this new measurement. The basic derivation of the integrated light and the procedure of the new measurements are discussed within. Finally, resolved UV background measurements of previous studies are compared with these new values and they are discussed in the context of diffuse measurements of the UV background. This study addresses the following questions:

1. What is the total lower limit on the UV background set by the measurement of integrated light from resolved star-forming galaxies?
2. What is the contribution from only faint high-redshift star-forming galaxies to the background radiation?

5.1 Introduction

Measurements of background light essentially quantify the brightness of the sky at various wavelengths. They encompass the direct emissions from resolved sources as well as indirect (reprocessed or scattered) emissions internal and external to the

Galaxy. Studies on extragalactic background light (EBL) are particularly important in that they provide general quantitative information on earlier epochs in cosmic history where individual sources are out of the reach of our observational capabilities either due to technological limitations or physical limitations of our location in the Universe. Much work has been done to measure the background light at gamma-rays, X-rays, UV, optical, IR, microwave, and radio frequencies. Arguably, the most significant of these measurements is that of the cosmic microwave background (CMB) which reveals the uniform "glow" of the primordial material of the Universe over the entire sky, providing direct evidence for the Big Bang. At high-energies the gamma-ray background is primarily generated by interactions between cosmic rays and the interstellar medium (ISM), and the X-ray background by hot gas emissions within the Galaxy as well as extragalactic X-ray sources. The background light from UV to optical to IR wavelengths is due to direct stellar emissions internal and external to the Galaxy, indirect stellar emissions from the re-processing and/or scattering of stellar light in gas and dust, and redshifted stellar light. Together these data provide limits on the total energy density of the universe providing further constraints on models of cosmological and star-formation history.

5.2 The Ultraviolet Background Light

The total UV background light is composed of several ingredients, broadly including emissions from the Earth's atmosphere, or airglow, Galactic emissions, and extra-galactic emissions. The Galactic component has been shown to be dominated by interstellar UV radiation scattered isotropically by dust, but also includes molecular hydrogen fluorescence, HII two-photon emission, and hot gas line emission, in smaller quantities (Murthy, 2009; Bowyer, 1991). The extragalactic component is dominated by UV flux from resolved sources (i.e. galaxies), but may also include weak emission from the intergalactic medium (IGM). Measurements of the resolved UV EBL can be determined from catalogs of extragalactic sources, and can be interpreted as an average measurement of the star-formation rate density over cosmological time, setting a

lower limit for the total UV background light. Commonly, measurements of the UV background radiation that do not directly include these resolved sources are termed 'diffuse background' measurements. Earlier studies making measurements of the diffuse FUV background are discussed in thorough reviews by Bowyer (1991) and Henry (1991), while more recent work has been reviewed by Murthy (2009). The definition of FUV wavelength coverage for each study varies between 912–1740Å, depending on the detector used.

Several techniques have been imparted in order to measure the diffuse FUV background. First, many studies have measured Galactic dust scattering, removing airglow effects, and fitting models to diffuse observations, extrapolating the signal down to zero column density (N_{HI}=0) which provides levels for what is interpreted as the FUV extragalactic background (i.e. galactic sources and potentially diffuse IGM emission). Henry & Murthy (1993) used this technique to reanalyze data from the Johns Hopkins UVX experiment for observations above $|b| = 40^\circ$ (where b is Galactic latitude). An improved model simulating scattering of diffuse galactic light in the ISM was developed and used by Witt & Petersohn (1994) to re-measure the extragalactic background in Dynamic Explorer 1 observations from Fix et al. (1989). This same model was used by Witt et al. (1997) to re-evaluate the extragalactic background extrapolation from Far-Ultraviolet Space Telescope (FAUST) observations (Sasseen et al., 1995). Schiminovich et al. (2001) derived the extragalactic FUV background with data from the Narrowband Ultraviolet Imaging Experiment (NUVIEWS), the first experiment primarily designed to map the FUV background. Most recently, this extrapolation technique has been used by Seon et al. (2010) to measure the FUV extragalactic background with the Spectroscopy of Plasma Evolution from Astrophysical Radiation instrument (SPEAR/FIMS). A second technique, that measures the truly diffuse extragalactic background, has been imparted by Brown et al. (2000) who masked the resolved FUV sources down to $m_{AB} = 29$ in HST STIS HDF-N and -S, and HDF-N parallel imaging (Gardner et al., 2000a). They found a large unresolved diffuse background component.

Other studies have used FUV spectra and imaging from large data sets to map the

FUV background over a large range of Galactic latitudes, revealing patchy skymaps of the background due to variations in intensities of the flux at different latitudes. Murthy et al. (1999) mapped the FUV background over the sky from 17 years of Voyager observations with the Voyager Ultraviolet Spectrometer (UVS), unique in that they are not partial to airglow effects, and Murthy & Sahnow (2004) mapped the FUV background intensity with Far-Ultraviolet Spectroscopic Explorer (FUSE) observations in 71 independent fields. Most recently, Murthy et al. (2010) used archival GALEX imaging to map the diffuse FUV background over ∼75% of the sky. This technique is used to put an upper limit on the extragalactic FUV background from values determined in the darkest areas of these data sets, primarily, but not necessarily, found in the vicinity of the Galactic poles. These FUV background skymaps have also revealed that some of the brightest FUV intensities are correlated with Galactic structures such as molecular clouds and nebulae. Detailed analysis to disentangle components of and effects on the diffuse FUV background in the vicinity of these structures have been carried out by determining correlations with HI column, H_2 fluorescence, Galactic extinction, and dust scattering, in some cases, resulting in measurements of a FUV extragalactic background component (Sujatha et al., 2007; Lee et al., 2006; Sujatha et al., 2005). Measurements of the diffuse FUV background are complemented by measurements of the resolved FUV background from extragalactic sources.

5.3 New Measurements of the Resolved FUV Background Light

This section presents analysis and results for new measurements of the FUV extragalactic background light (EBL) from resolved sources in the GOODS-N and -S field areas observed with the HST ACS/SBC. The results are summarized in Table 5.1 along with all previous measurements of the resolved FUV EBL. Both sets of bright GALEX number counts are used in the calculation, giving us two possible values for

the resolved EBL. First, a slope of 0.13 ± 0.05 with an intercept of 0.68 ± 1.23 is fit to the FUV number counts for magnitudes 24.5–28.5, including only the faint-end of the SBC/FUV number counts distribution. A slope of 0.53 ± 0.01 with an intercept of -9.11 ± 0.28 is also fit to the Xu et al. (2005) (hereafter XU05) GALEX counts for magnitudes 14.2–23.7. For the Hammer et al. (2010) (hereafter HAM10) field GALEX counts the slope of 0.5 fitted to the FUV data by HAM10 with an intercept of -8.7 ± 0.81 is used for magnitudes 17.25–23.25. Next, these slopes, as well as the number counts, are converted to units of EBL per magnitude bin, I_ν [erg s^{-1} cm^{-2} Hz^{-1} sr^{-1}], using the formula from Madau & Pozzetti (2000),

$$I_\nu = 10^{-0.4(FUV_{AB}+48.6)} N(FUV_{AB}) \tag{5.1}$$

where the first term on the right side of the equation is the flux as a function of apparent magnitude, f(FUV_{AB}), and the second term is the differential number counts. In Figure 5.1 this conversion is shown for all FUV number counts compared in Chapter 4. The Teplitz et al. (2006) points and the data from this thesis in magnitude bins 20.5 and 21.5 are higher than the GALEX data at these magnitudes due to the low number of galaxies in these bins since these data targeted faint galaxies in very dark areas of the sky. To obtain the final EBL value the converted GALEX counts and the counts measured here are integrated as follows,

$$I_{EBL} = \int f(FUV_{AB}) N(FUV_{AB}) d(FUV_{AB}) \tag{5.2}$$

For the combined fit of the faint-end SBC/FUV data with the XU05 data (hereafter EBL I) the upper limit for the integral of the XU05 function and the lower limit for the integral of the SBC/FUV function is set to FUV_{AB} = 24.67 because this magnitude is the maximum in integrated light, i.e. the central intersection of the power law slopes fit to these data. From this model the integrated EBL is measured for the total magnitude range FUV_{AB} = 14.7–29.3 of $\nu I_\nu = 1.3^{+0.2}_{-0.2}$ nW m^{-2} sr^{-1}, or in photon units, $I_\lambda = 65.9^{+8}_{-8}$ photons s^{-1} cm^{-2} sr^{-1} $Å^{-1}$. The errors are 1 sigma

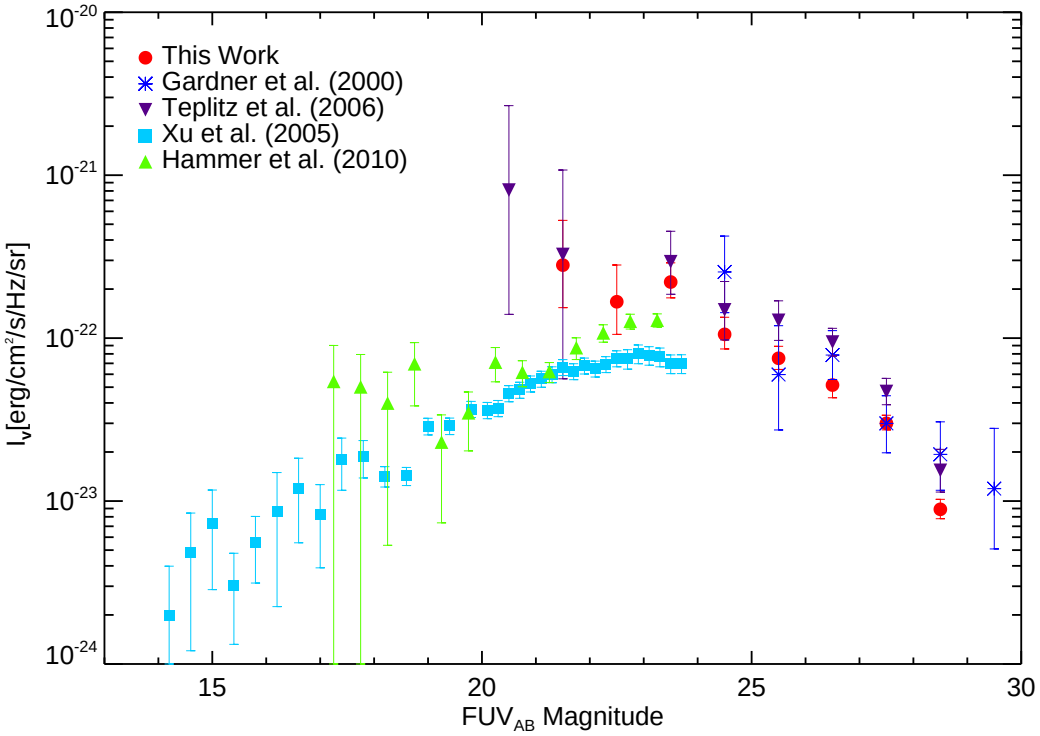

Figure 5.1 *Conversion of all FUV number count studies discussed in Section 4 converted to units of EBL per magnitude bin.*

uncertainties on the number counts. The model and data are plotted in Figure 5.2. The model for the GALEX data between FUV$_{AB}$=14-24.67 accounts for 66.5% of EBL I, measuring more of the resolved background light than the faint-end number counts. For the combined fit of the faint-end SBC/FUV data with the HAM10 data (hereafter EBL II) the upper limit for the integral of the HAM10 function and the lower limit for the integral of the SBC/FUV function are set to FUV$_{AB}$ = 24.28. From this model the integrated EBL is measured for the magnitude range FUV$_{AB}$ = 17.3–29.7 of $\nu I_\nu = 1.6^{+0.2}_{-0.2}$ nW m^{-2} sr^{-1}, or in photon units, $I_\lambda = 82.6^{+12}_{-12}$ photons s^{-1} cm^{-2} sr^{-1} Å^{-1}. Again, the GALEX portion of the model measures more resolved background light than the SBC/FUV number counts, accounting for 66% of EBL II, very similar to XU05. This similarity is due to a caveat in the data included from these two studies in that XU05 covers a larger magnitude range than HAM10, and

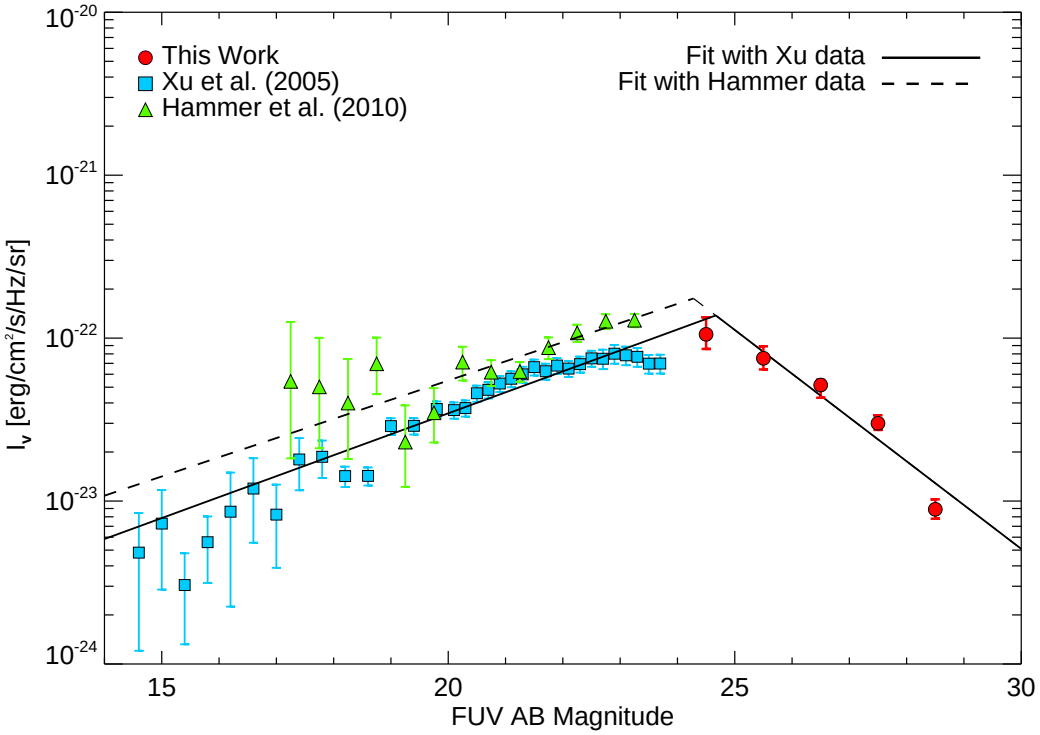

Figure 5.2 *Extragalactic background light from resolved sources per magnitude as a function of FUV magnitude. Two measurements are made from these data. The solid line measures the integrated EBL using the Xu et al. (2005) counts for the bright end (EBL I), while the dashed line makes this measurement using the Hammer et al. (2010) counts at the bright end (EBL II).*

the latter has higher I_ν. This can be clearly seen in Figure 5.2.

One of the first attempts at determining the resolved FUV background from light emitted by galaxies was carried out by Martin & Bowyer (1989). They obtained data from an FUV imaging experiment that used a rocket-mounted detector to observe signatures of galaxies in the integrated FUV background. The experiment covered wavelengths 1350–1900Å and determined a 1-sigma upper limit for the summed FUV intensity coming from sources ∼50 photons s^{-1} cm^{-2} sr^{-1} $Å^{-1}$, that is ∼25–40% lower than the measurements presented here. The UV EBL was measured at 2000Å by Milliard et al. (1992) from FOCA number counts and by Armand et al. (1994) from predictions of number counts (Armand et al., 1994). While our measurements are well

within the range of 40–130 photons s^{-1} cm^{-2} sr^{-1} $Å^{-1}$ predicted by Armand et al. (1994), they are much higher than the 23 photons s^{-1} cm^{-2} sr^{-1} $Å^{-1}$ determined from the FOCA number counts between magnitudes 15.0–18.5. Comparing the SBC/FUV measurements to those from Gardner et al. (2000b), EBL I and EBL II are ∼54–66% and ∼43–58% lower, respectively, than their measurements of $2.9^{+0.6}_{-0.4}$–$3.9^{+1.1}_{-0.8}$ nW m^{-2} sr^{-1} (144^{+28}_{-19}–195^{+59}_{-39} photons s^{-1} cm^{-2} sr^{-1} $Å^{-1}$) at 1595Å. Xu et al. (2005) extrapolated models fit to the GALEX FUV number counts (1530Å), integrated these functions to zero flux, and measured the total FUV EBL to be 1.03 ± 0.15 nW m^{-2} sr^{-1} which is ∼21% lower than EBL I, ∼37% lower than EBL II, and also below the Gardner et al. (2000b) range. All values for the resolved FUV EBL discussed in this section are summarized in Table 5.1.

5.4 Summary

In this chapter the EBL from resolved galaxies has been measured using the bright number counts from GALEX studies and the faint-end of the SBC/FUV number counts presented in Chapter 4 of this thesis. These values set a lower limit for the total UV background light. When these measurements are compared with the previous lower EBL value determined from bright GALEX counts (Xu et al., 2005) it is apparent that the faint-end data is higher than the model obtained from their faint-end extrapolations to zero I_ν. Thus, the inclusion of empirical data from the faint-end of the number counts function is quite important for obtaining a more realistic measurement of the overall resolved EBL quantity. Additionally, the reduction in cosmic variance in the SBC/FUV number counts, due to the large areas and various sight-lines covered, yields a lower contribution from the faint-end than originally measured from Gardner et al. (2000b) who measure FUV counts only within the HDF-N field of the larger GOODS-N area. The conclusion that can be drawn from these measurements is that the resolved EBL is unlikely to be much greater than ∼100 photons s^{-1} cm^{-2} sr^{-1} $Å^{-1}$. Therefore, diffuse EBL measurements done in space or at high Galactic latitudes that have significantly higher values (Schiminovich et al.,

2001; Brown et al., 2000; Witt et al., 1997; Witt & Petersohn, 1994; Henry & Murthy, 1993) most likely include Galactic contributions and potentially smaller contributions from airglow.

Table 5.1. Measurements of the Resolved FUV Background Light

Investigators	Instrument	λ (Å)	Magnitudes Covered (AB)	FUV BL (nW/m^2/sr)	FUV BL (phot/s/cm^2/sr/Å)
This Work: EBL I[a]	SBC/GALEX	1614/1530	14.70–29.30	$1.3^{+0.2}_{-0.2}$	65.9^{+8}_{-8}
This Work: EBL II[b]	SBC/GALEX	1614/1530	17.30–29.70	$1.6^{+0.2}_{-0.2}$	82.6^{+12}_{-12}
Xu et al. (2005)	GALEX	1530	extrap. to zero mag	1.03 ± 0.15	52 ± 7
Gardner et al. (2000b)	STIS/FOCA	1595	17.50–29.50	$2.9^{+0.6}_{-0.4}$ to $3.9^{+1.1}_{-0.8}$	144^{+28}_{-19} to 195^{+59}_{-39}
Armand et al. (1994)	...[c]	2000	15.00–18.50	0.8 to 2.6	40 to 130
Milliard et al. (1992)	FOCA	2000	15.00–18.50	0.4	23

[a]Bright end fit is from Xu et al. (2005) GALEX FUV number counts.

[b]Bright end fit is from Hammer et al. (2010) GALEX FUV number counts.

[c]his measurement is from a prediction of number counts based on galaxy evolution models and published galaxy SEDs.

6

Quantitative Morphologies of Far-Ultraviolet Detected Star-Forming Galaxies

In this chapter the rest-frame optical quantitative Sérsic morphologies of the SBC/FUV galaxy sample are presented and analyzed. They are compared against their SED based spectral type morphologies and evaluated as a function of galaxy redshift. This work addresses the following broad questions about galaxy evolution:

1. How do the optical morphologies of star-forming galaxies at intermediate redshifts compare to local star-forming galaxies?
2. Are there any important correlations between the quantitative optical morphologies of star-forming galaxies and their rest-frame UV morphologies?
3. Do SED based spectral type morphologies of galaxies agree with morphologies based on their functional light profiles? Does this vary depending on the epoch observed?
4. What can quantitative morphologies indicate about merger versus secular evolution of galaxies at intermediate redshifts?

6.1 Sample Selections and Data Preparation

The sample of galaxies for this study was selected from the larger sample of 333 sources detected in the SBC/FUV imaging of the GOODS-N and -S fields. The reddest edge of the SBC F150LP filter throughput is ∼2000Å, and it is only capable of detecting z < 1.2, after which the 912Å Lyman limit shifts to the red edge of the filter and no UV light can be detected after this point (see Section 4.2 for more detailed description of this effect). Therefore, only galaxies below this cut-off in redshift were included in this study. This provides a moderate size sample of 213 FUV detected galaxies for this work that also have STs. It was decided that the rest-frame V-band would be chosen for the analysis of these sources' optical morphologies. While many studies perform morphological analysis of star-forming sources in the rest-frame B-band (Conselice et al., 2004; Ravindranath et al., 2004), this band may still contain prominent areas of star formation in various morphologies (see U-band gallery in Chapter 2). For the purpose of this thesis the rest-frame V-band was chosen in the tradition of the Hubble classification scheme to provide a better overall view of the galaxies optical appearance, providing a bandpass of morphology unbiased by new star formation. Rest V-band images for the FUV sources were retrieved from the GOODS-N and -S public data sets available online[1]. A range of 5000Å $< \lambda <$ 7000Å was chosen to define the rest V-band for the purpose of this thesis. This range was selected because it is not overlapped by the HST ACS λ ranges for the B- and i-band filters which cover 3700Å $< \lambda <$ 4800Å and 7000Å $< \lambda <$ 8600Å respectively. In some cases the rest V-band wavelength range of a source fell in both the ACS i- and z-band wavelength ranges (6600Å $< \lambda <$ 8600Å and 8000Å $< \lambda <$ 11000Å, respectively). If this happened then the band containing the λ closest to the V-band filter center (6060Å) was selected.

In preparation for sending these sources through the GALFIT algorithm (see next section) 3″x3″ cut-outs were made for each source. In a few cases the sources were larger than this area, so 6″x6″ cut-outs were done for these galaxies (list numbers

[1]http://www.stsci.edu/science/goods/DataProducts/

here). In one case for object ID 159 (see Figure 6.1(h)) a 9″x9″ cut-out was made. Root-mean-square error maps of the same size were produced for each source from the weight image (RMS = 1 / $\sqrt{weight}$).

6.2 Quantitative Morphologies with GALFIT

GALFIT (Peng et al., 2002, 2010) was used to determine the quantitative rest V-band morphologies for the star-forming sample of galaxies. This program was originally designed for determining the morphologies of local galaxies, but had been found to also work quite well at high redshifts. Thus, it is a popular tool in high-redshift galaxy research. The program is designed to provide the user with much flexibility in the measured quantities desired for their data. Its basic function is to produce a two-dimensional fit to an input FITS image of a galaxy and output the model image, the residual between the model and the real image, and any 2D light profile models desired by the user including, the "Nuker" law, the Sérsic profile, an exponential disk, and Gaussian or Moffat functions. One of the advantages of using the GALFIT software is that it is able to convolve a given PSF with the input image to be fit before applying its algorithm, thus taking into account variations in images due to instrument design and seeing.

For this study the Sérsic profile has been chosen to model the morphologies of the galaxy sample in GALFIT. The functional form of this profile is,

$$lnI(R) = lnI_o - kR^{1/n} \tag{6.1}$$

where n is termed the "Sérsic index", I_o is the intensity (or surface brightness) of light at zero radius of an object, I is the measured surface brightness at radius R, and k is a constant. Figure 6.1 displays several examples of Sérsic surface brightness profiles with varying degrees of n[2]. One can see that for values of $n = 1$ the profile is quite flat and has the sharpest turnover towards longer radii. This value of n is

[2]Values of n are not limited to the range 1–10, as shown in Figure 6.1, but can also have values < 1 depending on the measured light profile.

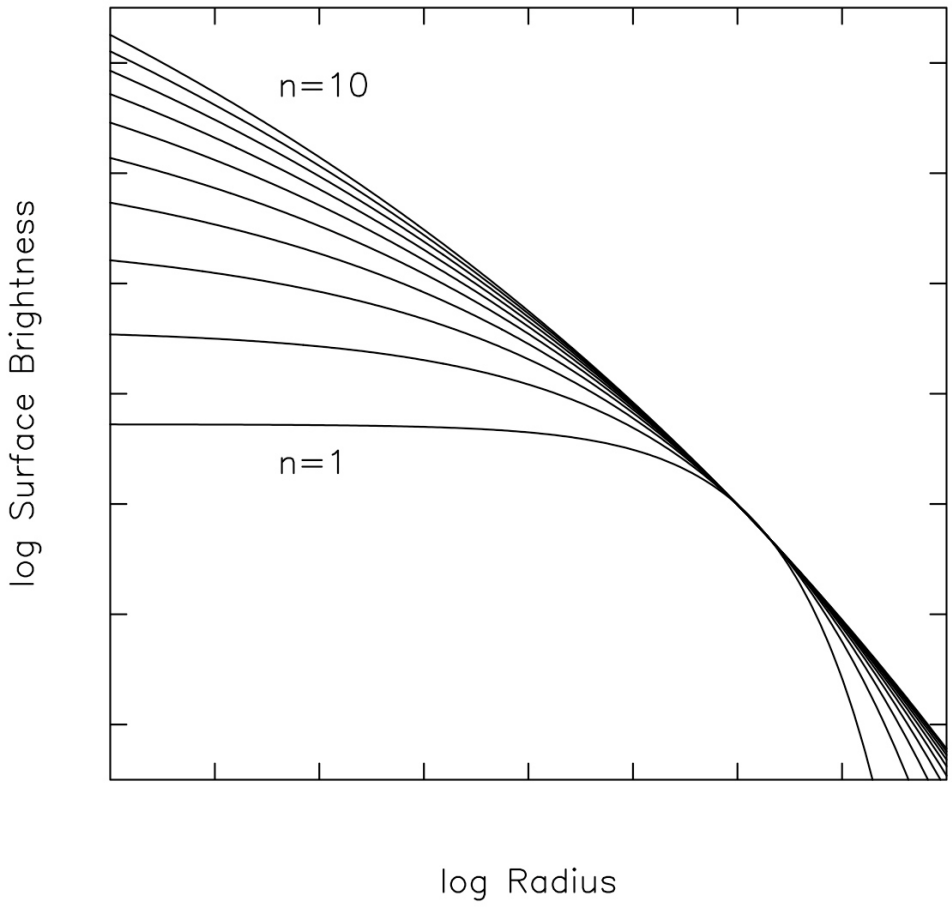

Figure 6.1 *The variation of Sérsic light profiles with varying Sérsic index n.*

used to define disk galaxies with elliptical bulges and exponential disks. As n increases from this value the Sérsic profile rounds steadily to $n = 10$ as the distribution models show less of a turnover from central to outer radii. Thus, higher values of n model more elliptical/spheroidal galaxies. Note that when $n = 4$ the profile becomes the classic elliptical profile defined by de Vaucouleurs (1959). Recently, several authors have discussed that galaxies can be classified morphologically into bins of Sérsic index as follows: $n < 0.8$ are clumpy merger or tidal morphologies, $0.8 < n < 2.5$ are exponential disks, and $n > 2.5$ are spheroid-like and centrally concentrated (Ravindranath et al., 2006; Petty et al., 2009). The subdivision between exponen-

tial disks and spheroid-like galaxies was initially defined by Shen et al. (2003) using Sloan Digital Sky Survey (SDSS) images of ∼140,000 low-redshift optically detected galaxies. The $n = 2.5$ value is the average of the de Vaucouleurs elliptical designation ($n = 4$) and the exponential disk definition ($n = 1$) of the Sérsic index. They find that this threshold correlates well with the cut by the concentration parameter (c) between early- and late-type galaxies of $c = 2.86$. Ravindranath et al. (2006) determined the same subdivision between disk and spheroid-like profiles ($n = 2.5$) using a large Monte Carlo simulation of ∼50,000 galaxies that were divided equally between $r^{1/4}$ ellipticals and exponential disks. However, from visual inspection of fits to the rest-UV morphologies of their sample they caution that such sources may still show signs of clumpy and/or merger-like morphologies but these do not depart to a great extent from the exponential disk or spheroid-like n designations. Furthermore, the division between exponential disks and clumpy merger/tidal-like morphologies at $n = 0.8$ was selected by Ravindranath et al. (2006) from visual inspection of the rest-UV images (∼1600Å) of their high-redshift ($z > 3$) LBG sample in which they find objects below this division to have multiple cores, tadpole, chain, diffuse, and low surface brightness galaxies that lack apparent central concentrations. They claim that based on Dickinson et al. (2000) and Papovich et al. (2003) there is not a significant morphological k-correction for galaxies with very young stellar populations at high redshift and thus they expect the divisions of n to hold for rest-frame optical as well as rest-UV morphologies. In the following sections these bins are used in order evaluate the Sérsic indices determined for the rest-frame V-band images of the FUV detected sample, and for quantitative comparisons with STs.

6.2.1 Image Gallery and GALFIT Results

Figure 6.2 presents images of the FUV sample of 230 sources with $z < 1.2$ along with their rest-frame V-band image, their GALFIT output model image, and the GALFIT residual image between the V-band and the fitted model. The majority of cut-outs are 3″x3″ in size, however IDs 8, 10, 58, 62, 93, 98, 129, 130, and 185 have 6″x6″

size cut-outs due to the larger optical sizes of these sources, and largest cut-out is 9″x9″ for ID 159. Each objects R.A. and Decl. are listed along the top of each panel and the objects, best redshift, spectral type (where available), apparent m_{FUV}, and Sérsic index, and χ^2 of the Sérsic fit are listed along the bottom. At the top of each rest-frame V-band image (second image in) the observed optical band and the field in which the object was detected is given. If the object is in one of the smaller ($< 1.0'$) SBC/FUV images in GOODS-N or -S then the GOODS tile number is also given to better identify the field. Figure 6.3 and 6.4 show, respectively, the distributions of ST and n for the FUV sources presented in the gallery. There are 18 sources in GOODS-N that do not have STs thus providing only 212 of the 230 sources for this distribution. The ST distribution shows that the majority of FUV sources are Scd (51.9%) types and Im types and all starbursts (SB1 and SB2 combined) are equally the next most numerous spectral types (18.9% and 20.2%, respectively). This is in agreement with the results found for the ST distribution of the smaller HUDF U-band detected star-forming sample in Section 2.6. The n distribution peaks below $n = 1.0$ with a skewed drop-off towards higher values. The dotted purple line marks the threshold at $n = 0.8$ between clumpy merger/tidal-like morphologies and exponential disks, and the orange dot-dashed line marks the threshold at $n = 2.5$ between exponential disks and spheroid-like morphologies. The majority of sources, 52.6%, have exponential disk n-values, while 40% of sources have n-values indicative of clumpy merger/tidal-like morphologies, and only 7.4% have n-values indicative of spheroid-like morphologies which is only slightly higher than the 2.4% of sources with E STs (1).

Inspecting the gallery it is clear that large sample of intermediate-redshift FUV sources is represented by a wide variety of optical morphologies. There is a large presence of traditional Hubble morphologies including extremely compact or elliptical-like morphologies (e.g., IDs 88, 114, 141), lenticular morphologies (e.g., IDs 62, 116), spirals varying in tightness of their arms (e.g., IDs 21, 64, 159, 165), and irregular morphologies (e.g., IDs 61, 139). There are also non-traditional morphologies including clumpy morphologies (e.g., IDs 46, 58, 130), tadpole morphologies (e.g., IDs 16, 169), and diffuse morphologies (e.g., IDs 85, 113). This demonstrates that star formation is

(a)

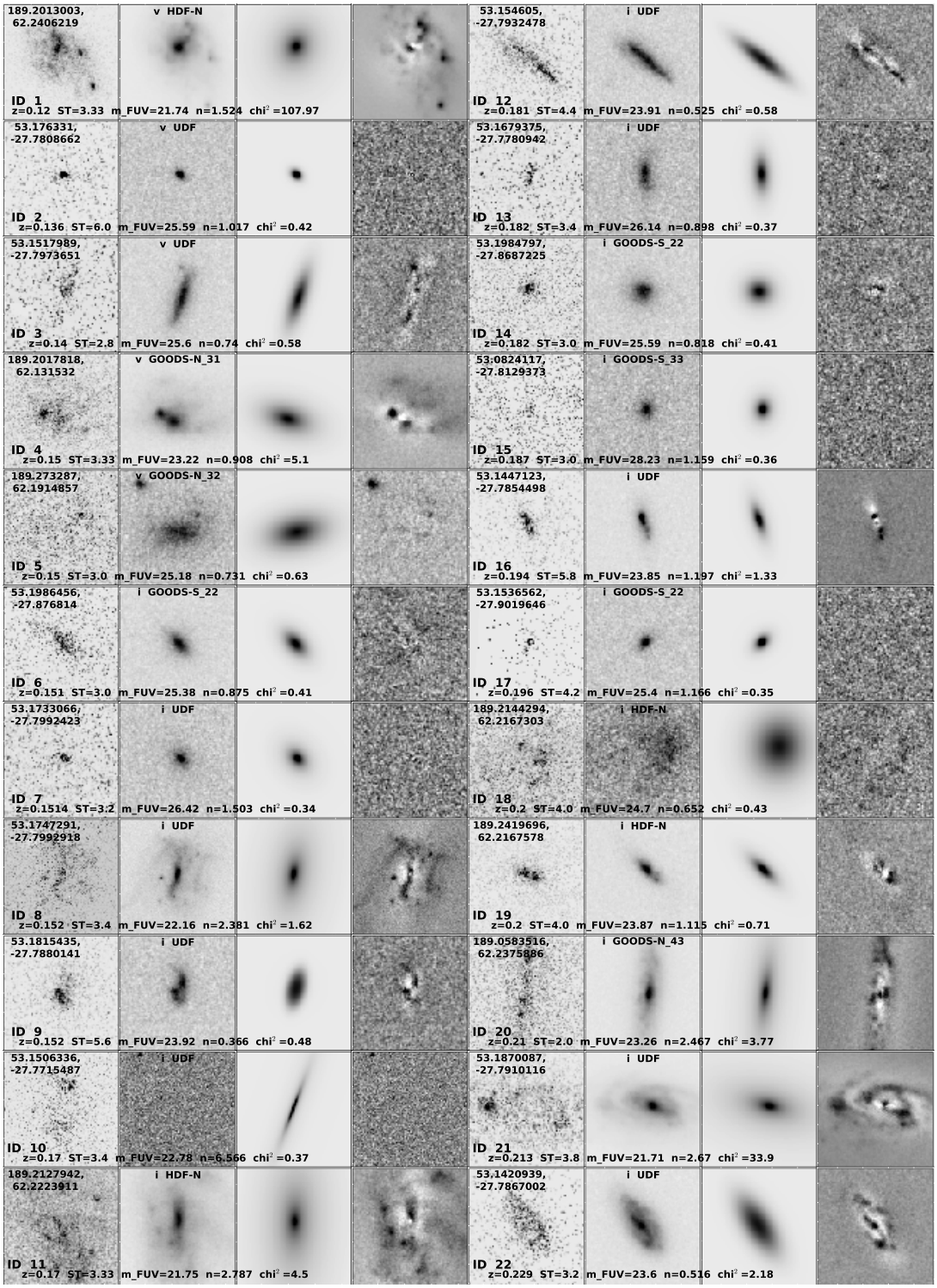

Figure 6.2 *FUV source IDs 1–22. See (k) for a full description of this gallery.*

(b)

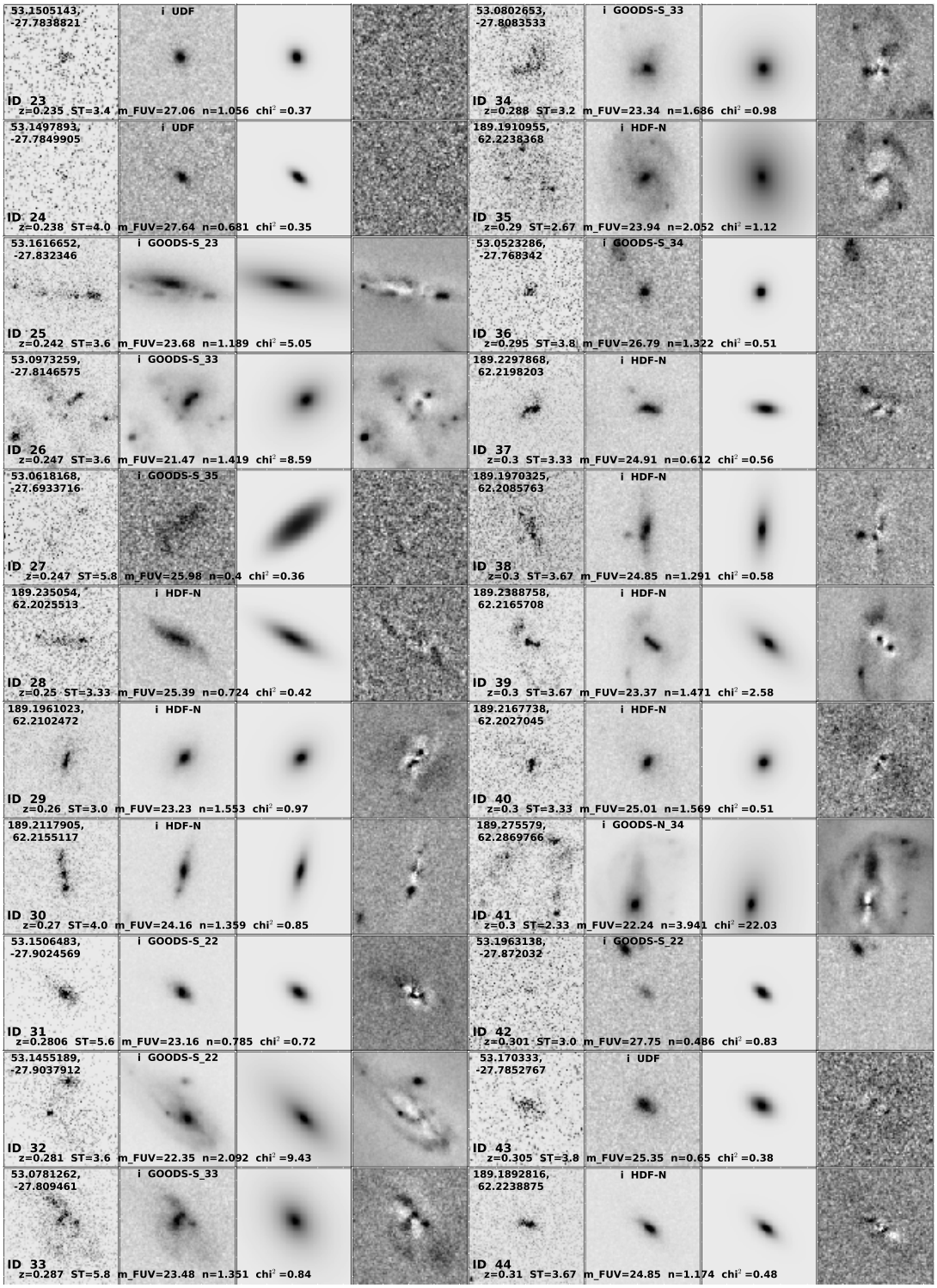

Figure 6.2 *FUV source IDs 23–44. See (k) for a full description of this gallery.*

(c)

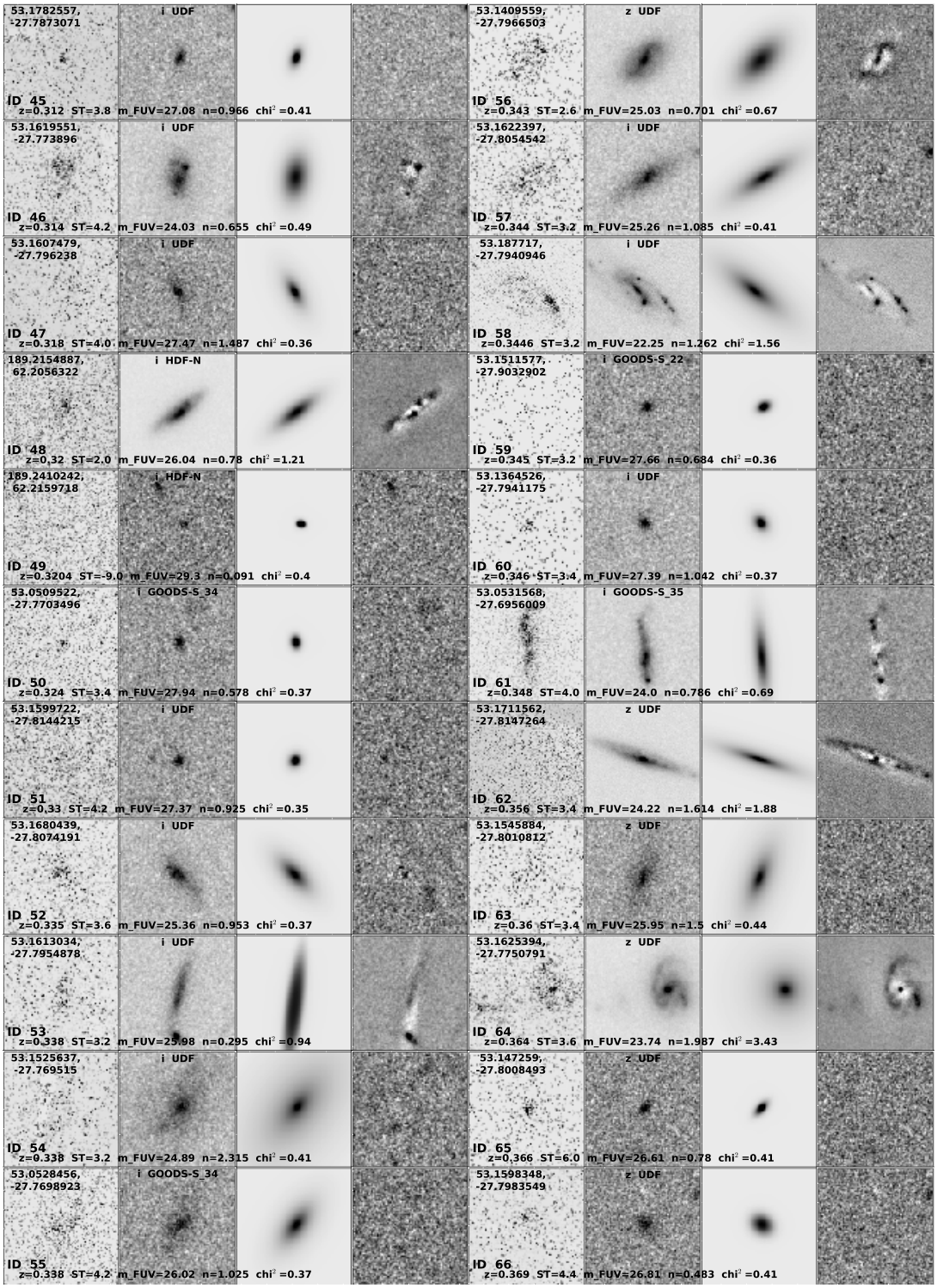

Figure 6.2 *FUV source IDs 45–66. See (k) for a full description of this gallery.*

(d)

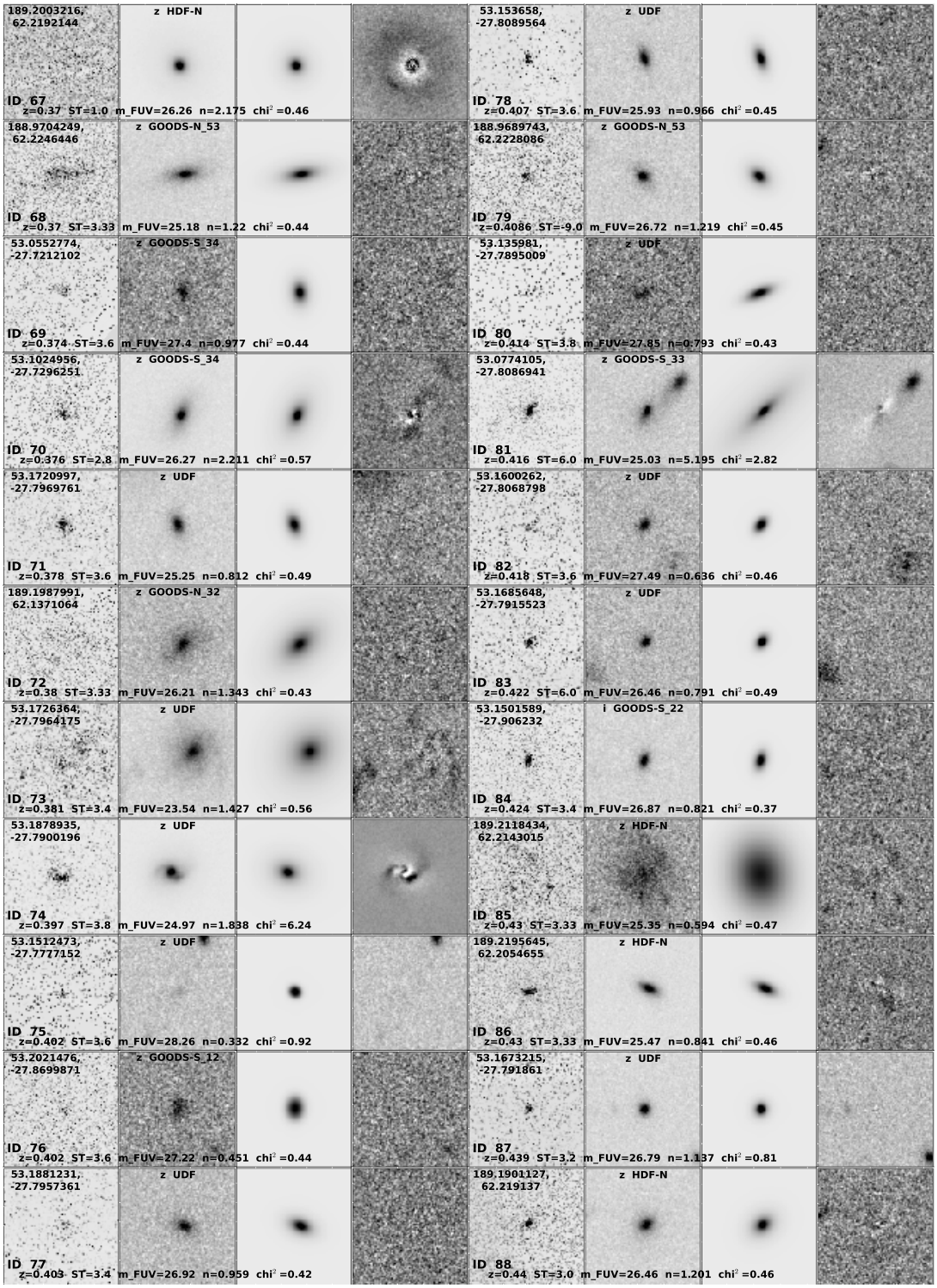

Figure 6.2 *FUV source IDs 67–88. See (k) for a full description of this gallery.*

(e)

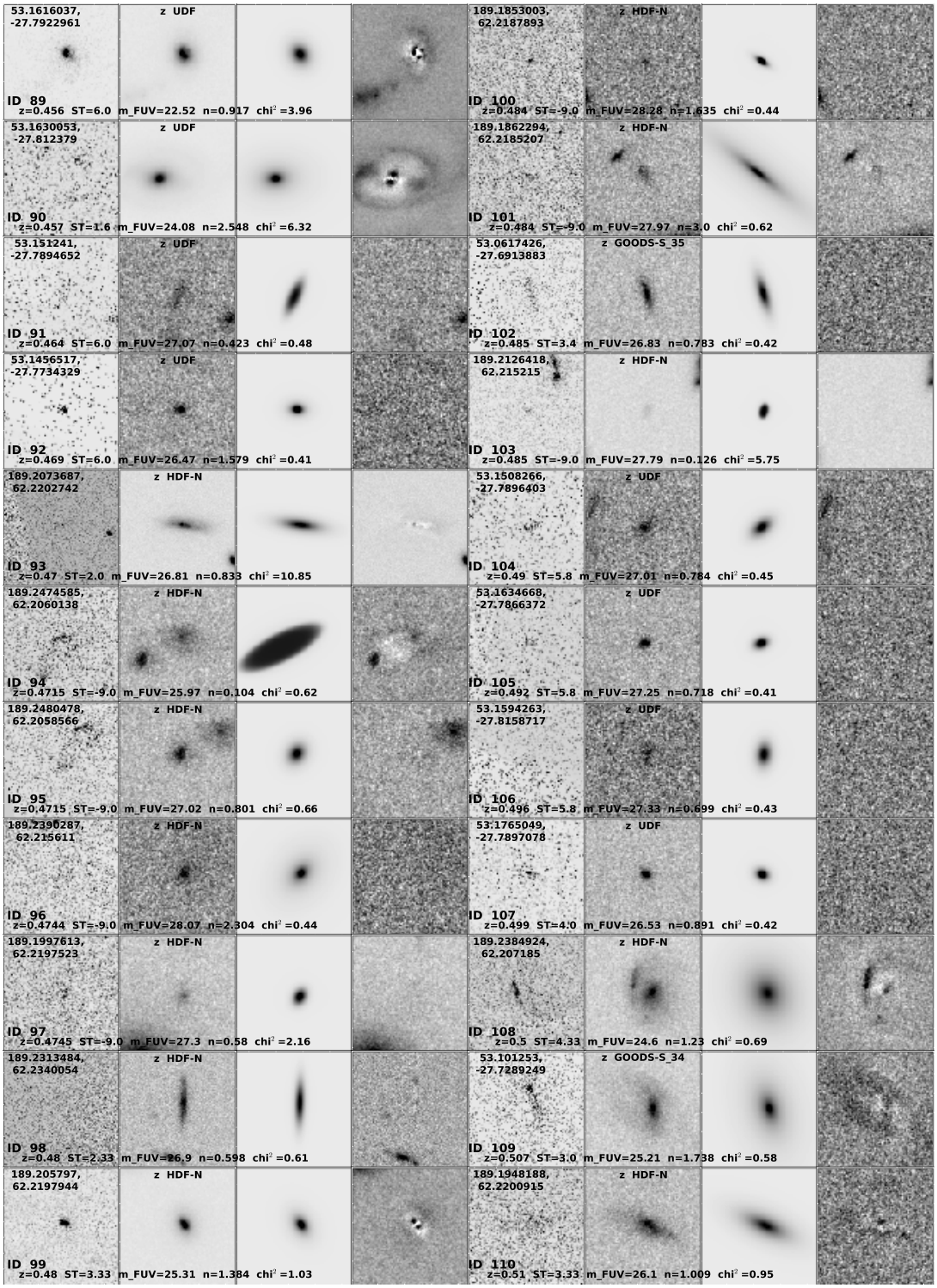

Figure 6.2 *FUV source IDs 89–110. See (k) for a full description of this gallery.*

(f)

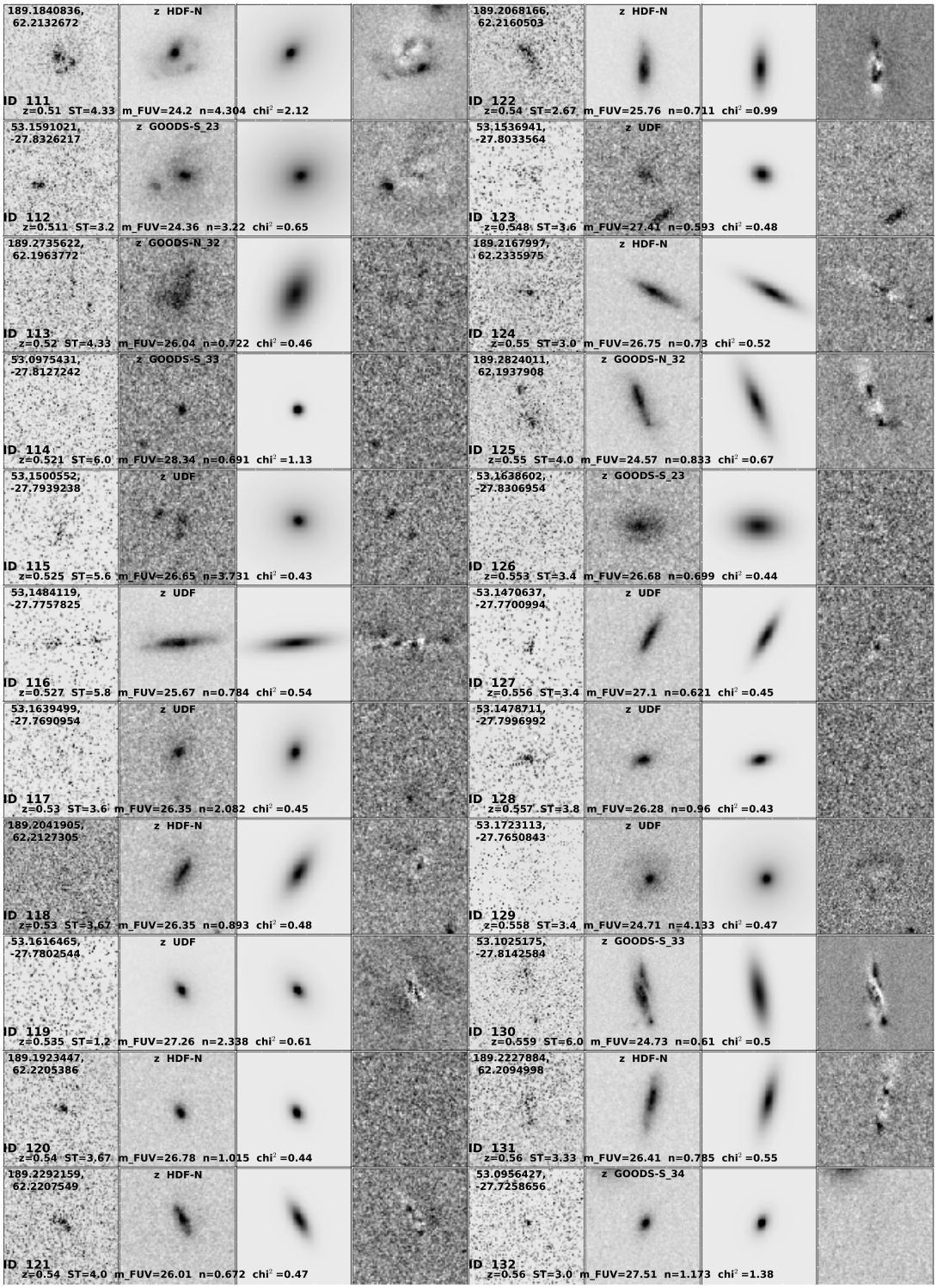

Figure 6.2 *FUV source IDs 111–132. See (k) for a full description of this gallery.*

(g)

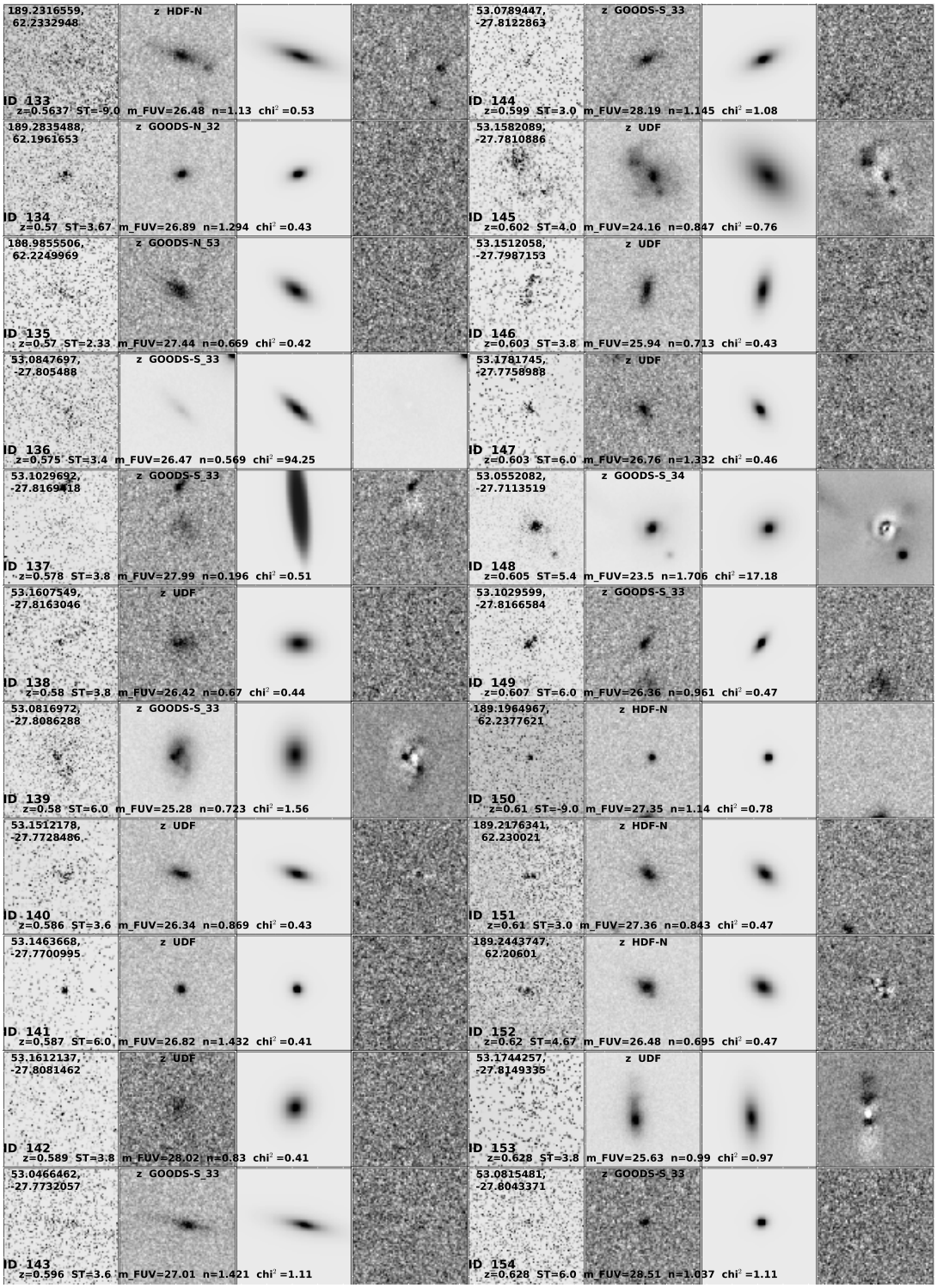

Figure 6.2 *FUV source IDs 133–154. See (k) for a full description of this gallery.*

(h)

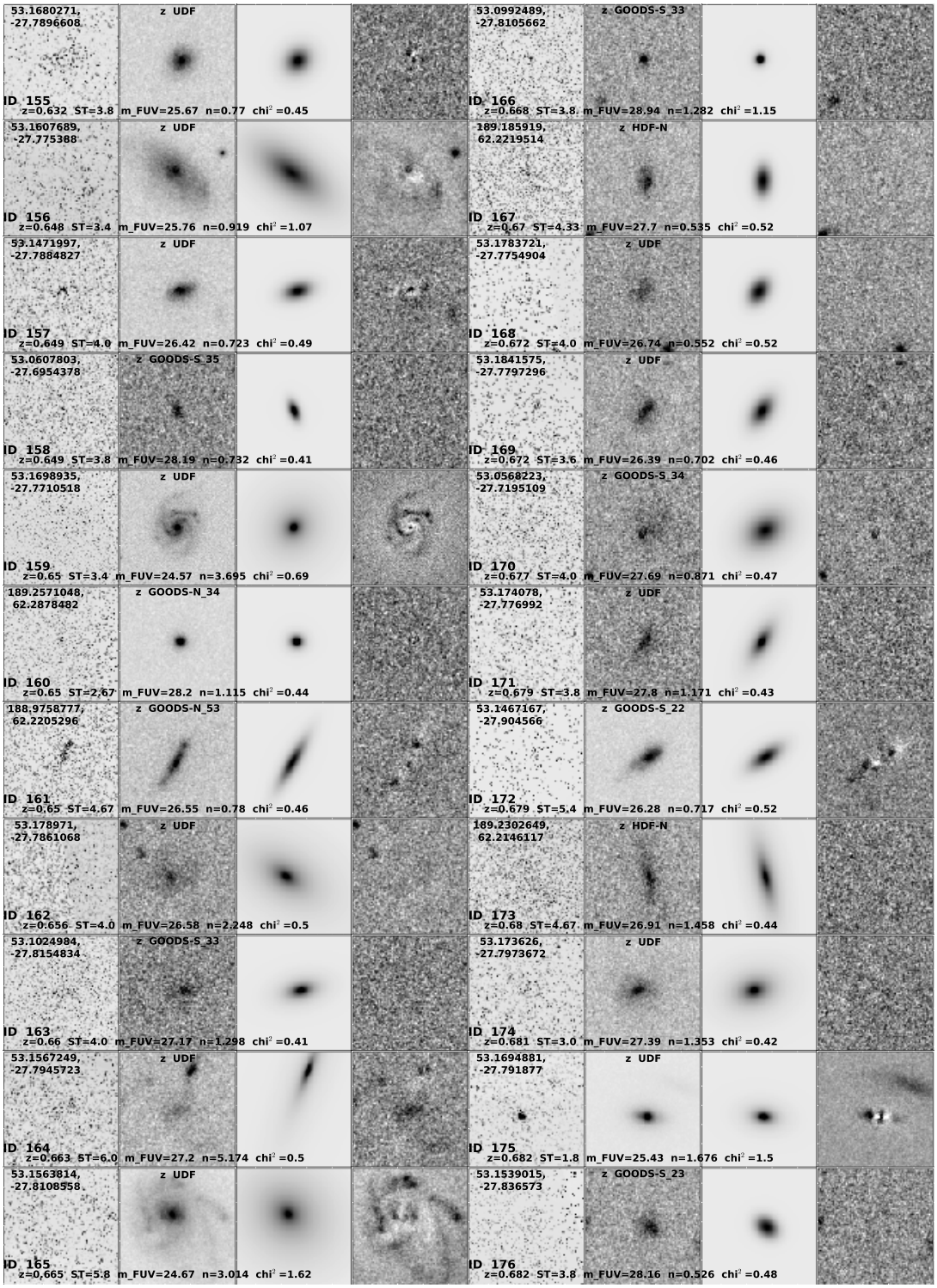

Figure 6.2 *FUV source IDs 155–176. See (k) for a full description of this gallery.*

(i)

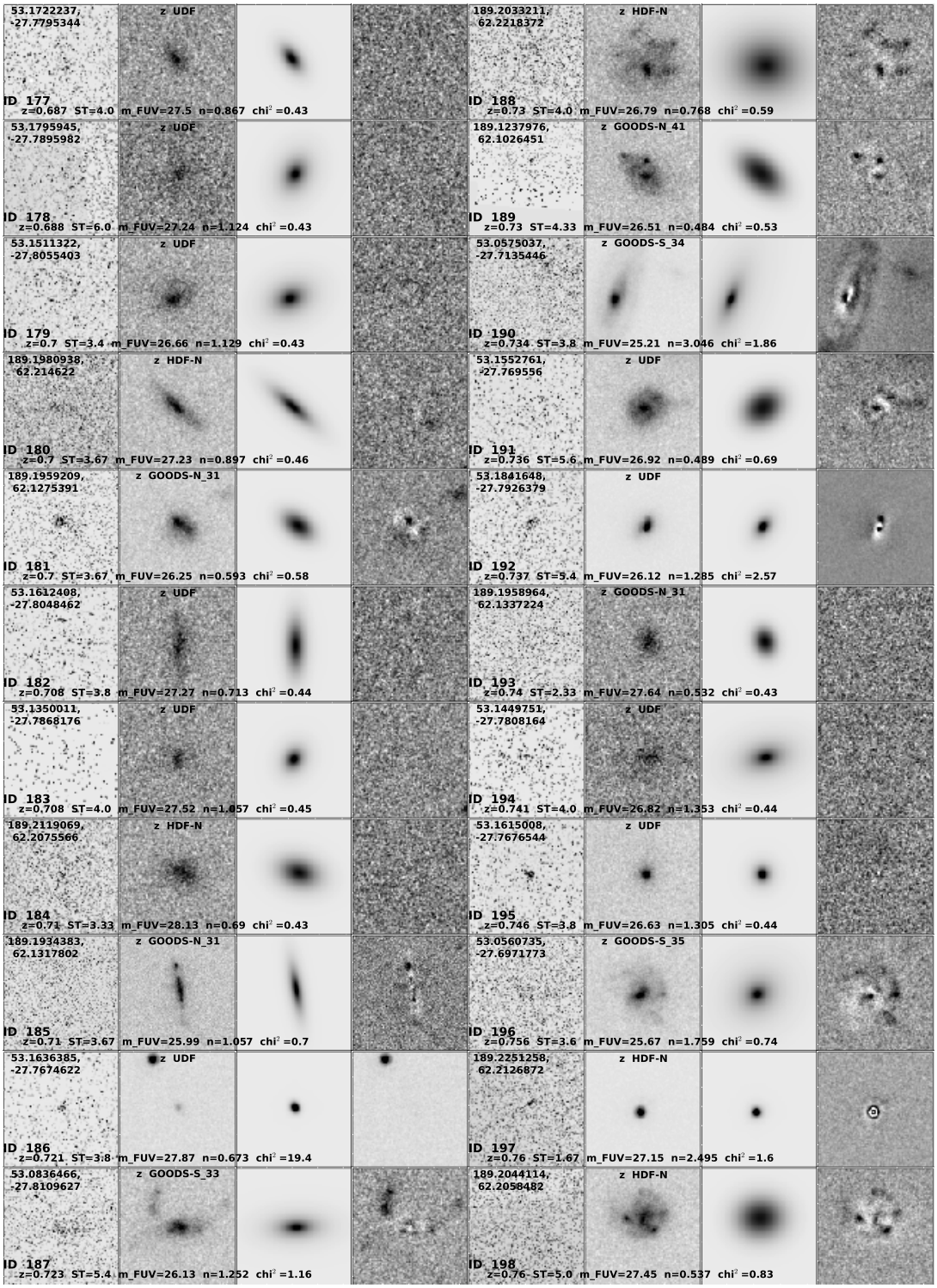

Figure 6.2 *FUV source IDs 177–198. See (k) for a full description of this gallery.*

(j)

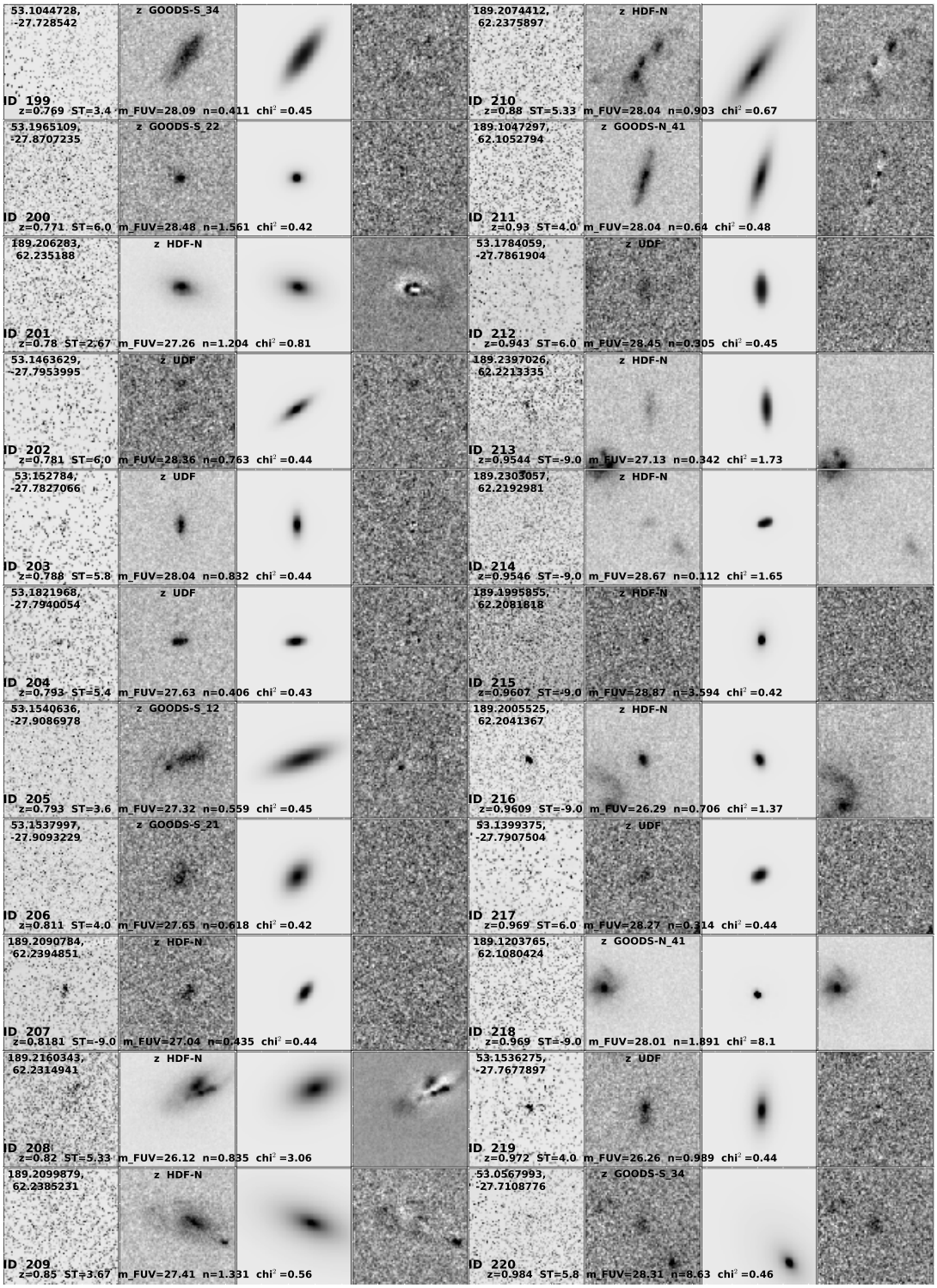

Figure 6.2 *FUV source IDs 199–220. See (k) for a full description of this gallery.*

(k)

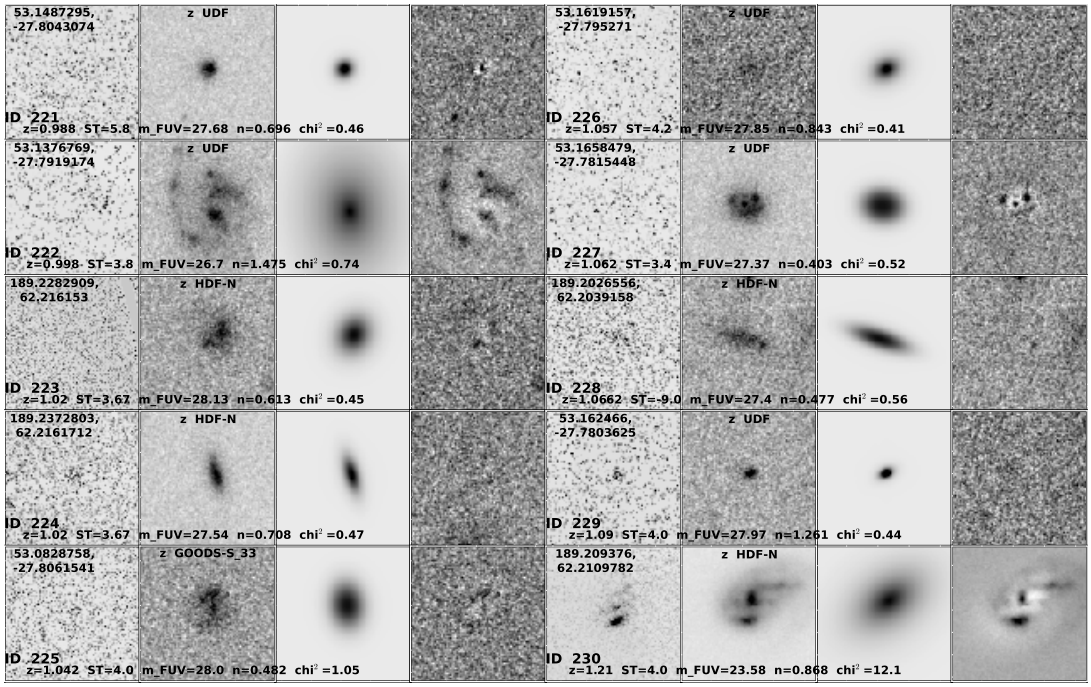

Figure 6.2 *FUV source IDs 221–230. This gallery visually displays the quantitative morphologies of sources in the SBC/FUV sample that have reliable redshifts ($z < 1.2$). Each panel has two columns of sources. The images of a single object from left to right are the SBC/FUV image, the rest-frame V-band image (varies between V, i, and z depending on the redshift), the GALFIT light profile model of that source, and the residual between the optical and GALFIT images. Object's IDs are order by redshift and the redshift, ST, apparent FUV magnitude, Sérsic index (n), and normalized χ^2 from GALFIT are printed at the bottom of each image. Most images are 3″x3″ in size, except for larger sources which have images 6″x6″ in size.*

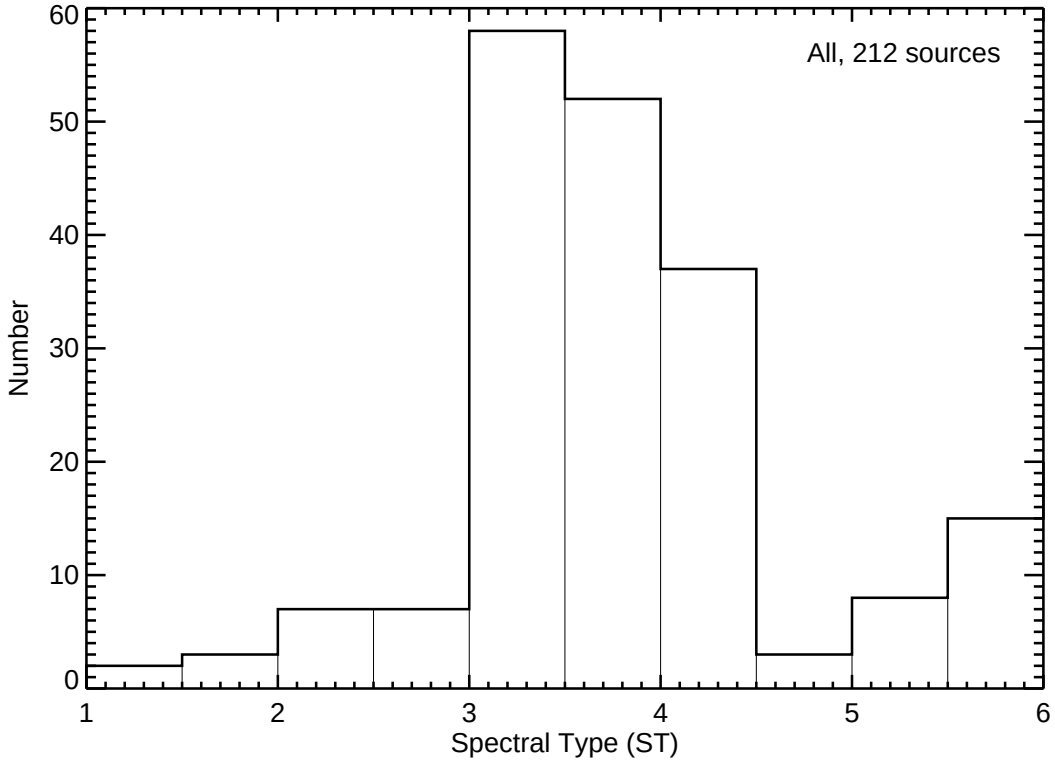

Figure 6.3 *Distribution of Spectral Types for FUV detected sources, where available (Dahlen private communication; Dahlen et al., 2010). Here, 1 = E; 2 = Sbc; 3 = Scd; 4 = Im; 5 = SB1; 6 = SB2.*

occurring in all types of galaxies at intermediate epochs. For most sources with high S/N in their FUV images there is a direct correlation with the morphology of the residual image, i.e. the residual picks out regions of star formation. ID 41 is a beautiful example of this where its FUV image shows an upside-down U shape of diffuse emission with three small star-forming knots dispersed about it, and the rest-frame V-band image shows a very faint disk with a large central bulge and a brighter inner exponential disk. While GALFIT models both the bulge and and inner disk quite well, the residual shows the diffuse U shaped disk and the three star-forming knots from the FUV image, as well as an over-subtracted bar where the bulge was, and a larger clump above this feature that is visible, but faint in the optical image. Thus,

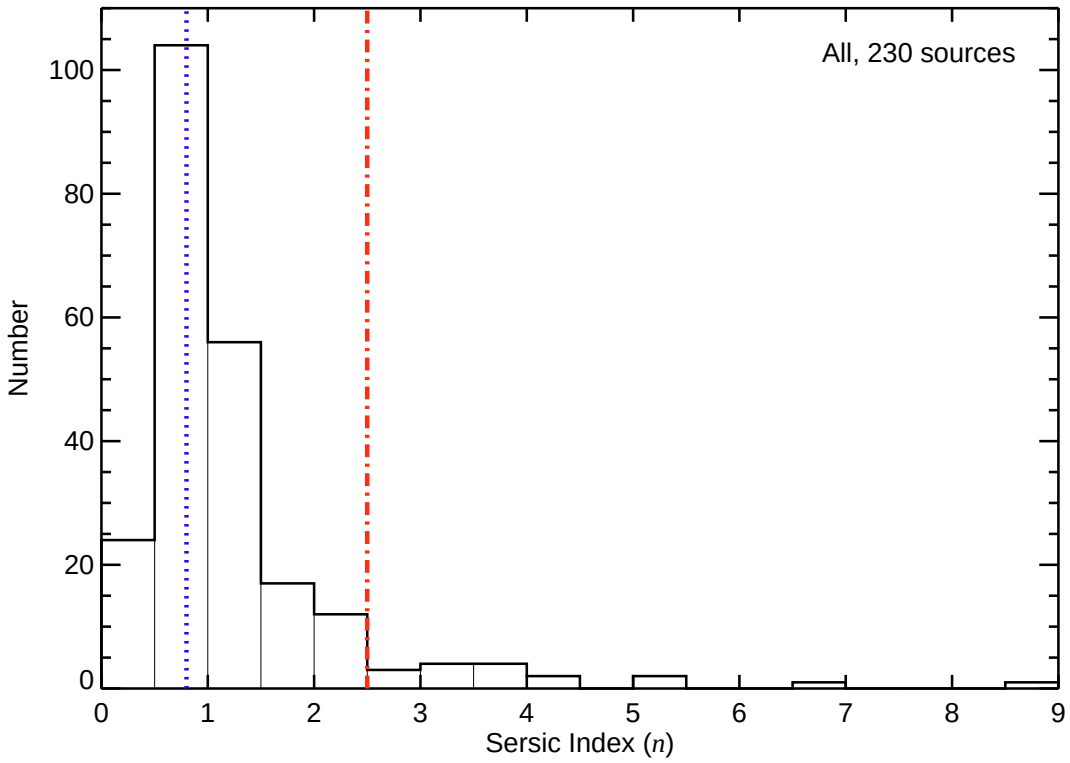

Figure 6.4 *Distribution of Sérsic indices for all FUV detected sources with $z < 1.2$. Dotted line (purple) at $n = 0.8$ represents threshold between clumpy merger/tidal-like morphologies($n < 0.8$) and exponential disks ($0.8 < n < 2.5$). The dot-dash line (orange) at $n = 2.5$ represents the threshold between exponential disks and spheroid-like/centrally concentrated morphologies ($n > 2.5$).*

for morphologies with non-smooth light profiles the GALFIT model removes the underlying disk and bulge component while revealing the intricacies of the morphology in the residual image.

As mentioned previously, the Sérsic index is designed to differentiate between the steepness in the Sérsic light profiles of galaxies which has been found to be a good indication of morphology. GALFIT provides a χ^2 goodness of fit value for the Sérsic model fits to each galaxy, and these values were inspected as compared to the visual model fits and the residual images. The majority of sources, 77.8%, have χ^2 values that are < 1.0. There are 34 sources (14.8%) with χ^2 between $1.0 \leq \chi^2 < 4.5$,

and there are 22 sources (7.4%) with $\chi^2 \geq 4.5$. However, by looking at a handful of GALFIT model fits as compared to their χ^2 values it is not straight forward as to the differences between the high and low χ^2 values in the gallery nor to what degree or for what criteria a bad χ^2 is calculated. A detailed visual and parametric evaluation was done to try and sort out the meanings of the variations in χ^2 of the Sérsic models. First, the group of 22 sources with extremely high χ^2 were evaluated keeping track of their GALFIT output magnitudes, n-values, and V-band morphologies. From this inspection it appears that there are three potential reasons for such high χ^2 values. First, the galaxy is very bright, with a low GALFIT output optical magnitude ($<$ 20) and is a very large disk on the image with under-subtracted dust lanes and over-subtracted clumpy knots showing up in the residual image. This could suggest that in reality these disks not have non-smooth profile shapes and they are also extremely bright. If this is the case, the differences between the model and actual galaxy pixel counts would quite large, increasing the errors between the two. Second, if the galaxy has a fainter, higher, magnitude and $n < 0.8$ then there was another object in the same field-of-view (FOV). This was the case for four of the 22 high χ^2 sources. None of the fields run through GALFIT were masked in order to remove additional objects so this could potentially bias a small percent of the results of this study. In the future these additional sources will be masked out. Third, galaxies that have average optical GALFIT magnitudes and have exponential disk n-values may produce high χ^2 due to either being disky and producing large residuals, or having an intrinsic double knotted core that can either be seen in the optical image and residual, or just shows up in the residual image only.

Next, it was noticed that there are several galaxies with low χ^2 (< 1.0), that have additional sources in the same optical FOV that also appeared as over-subtracted areas on the outskirts of the residual images. Some examples include IDs 5, 36, 37, 75, and 91. The majority of these sources (with an exception of a couple) have $n <$ 0.8, suggesting that the GALFIT algorithm could have potentially overestimated the number of sources with clumpy merger/tidal-like morphologies due to an additional source in the FOV. This has not yet been tested for, but the majority of these sources

appear to be split between extremely compact and very diffuse morphologies in their rest-frame V-band images with GALFIT model fits doing a good job at reproducing these morphologies for the most part. This visual inspection re-affirms that GALFIT most likely calculated the best n-values for these sources, and they are not expected to severely overestimate the population with $n < 0.8$. In addition, only 14% of the sample with $\chi^2 < 4.5$ falls within this scenario and most have STs of either Scd or SB2. It remains unclear why these sources have low χ^2 compared to the 4 sources with extremely high χ^2 that also have another source in the FOV. This could potentially result from the S/N value of the additional source in the images. In conclusion, the χ^2 values should be considered with caution when evaluating the goodness of profile fits using GALFIT.

6.3 Sérsic Profiles Compared to Spectral Types of Star-Forming Galaxies

Both photometric and spectral energy distribution signatures of galaxies have been used in the literature as indicators of morphology. One of the issues with the current variety of morphological classifications of galaxies is there are too many. At some point comparisons between galaxy samples from different studies become inaccurate due to the variations in the methods used to determine their morphologies. Because much information on galaxy evolution is concluded from morphological analysis, astronomers must take care to understand the caveats in comparisons between samples as a result of different methods used. Here a comparison is done between SED derived spectral types (STs; see Section 2.6 for further discussion) and GALFIT generated Sérsic indices in order to determine how well these two morphological indicators correlate with one another.

6.3.1 Statistical Comparisons of Morphologies

Two sets of distributions are tested in order to judge whether Sérsic index and ST provide the same information about the optical morphology of the star-forming galaxy samples. Figure 6.5 presents the ST distribution of the sample binned by range of n for the three ranges described in the previous section (6.2.1). Figures 6.6 and 6.7 present the n distributions in bins of ST and combined STs for all spirals (Sbc + Scd) and all starbursts (SB1 + SB2).

Statistical Kolmogorov–Smirnov (K-S) tests are performed within each set of distributions in order to determine whether the distributions represent the same or different morphological indicators between their bins. The K-S test is used to determine if two compared distributions are derived from the same parent distribution. It is a nonparametric test and thus is independent of a specific distribution function. By calculating the cumulative fractions of two sets of data and determining the greatest distance, D, between them a probability value, or P-value, can be derived for the K-S test providing the level or percentage of confidence (i.e., confidence interval, CI) that the distributions are not drawn from the same parent distribution,

$$CI = 100\%(1 - P) \tag{6.2}$$

Additionally, the range in standard deviation corresponding to the confidence interval can be determined with the assumption that the underlying distribution is normal (i.e., Gaussian),

$$n\sigma = \sqrt{2} erf^{-1}(CI) \tag{6.3}$$

where $erf^{-1}(CI)$ is the value of the inverse error function at the confidence interval. This provides a standard measure of whether the result of the K-S test is significant or not. Here, confidence intervals of 3σ or greater are considered significant enough to indicate two distributions are not from the same parent distribution, confidence intervals $< 1\sigma$ are considered to say that two distributions are definitely from the same parent distribution, and results between these require the additional consideration of

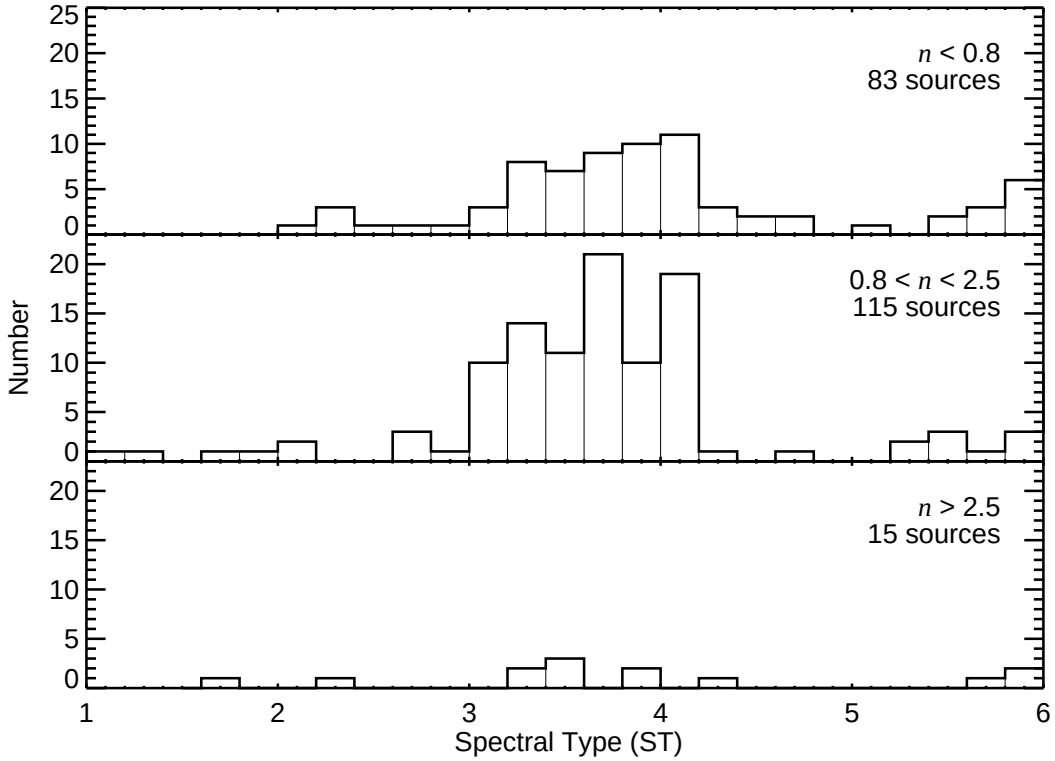

Figure 6.5 *Spectral Type distribution in bins of Sérsic index range. Top: clumpy merger or tidal morphologies. Middle: exponential disk morphologies. Bottom: spheroid-like and centrally concentrated morphologies*

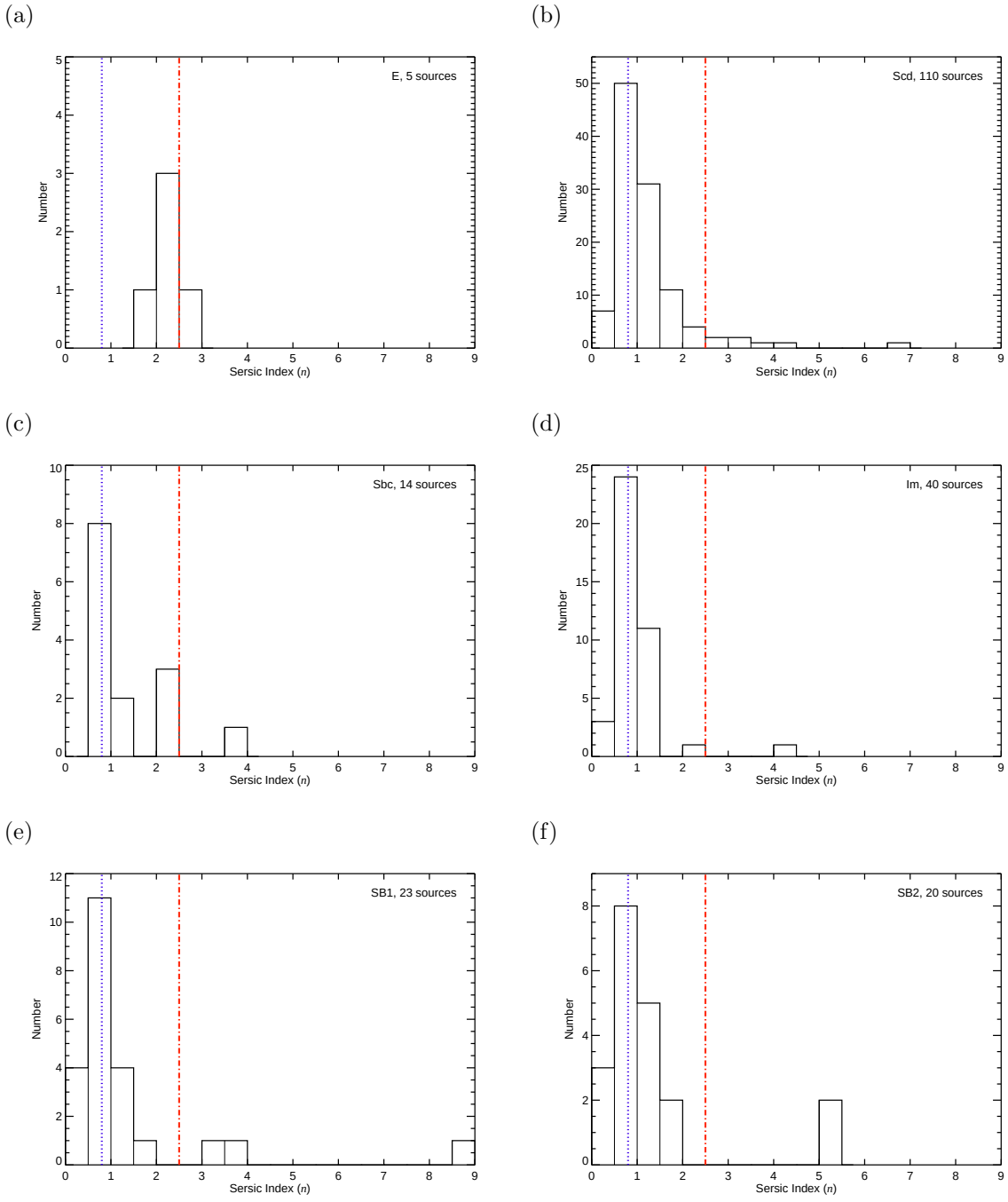

Figure 6.6 *Distributions of Sérsic index in bins of spectral types. Dotted line (purple) at $n = 0.8$ represents threshold between clumpy merger/tidal-like morphologies($n < 0.8$) and exponential disks ($0.8 < n < 2.5$). The dot-dash line (orange) at $n = 2.5$ represents the threshold between exponential disks and spheroid-like/centrally concentrated morphologies ($n > 2.5$).*

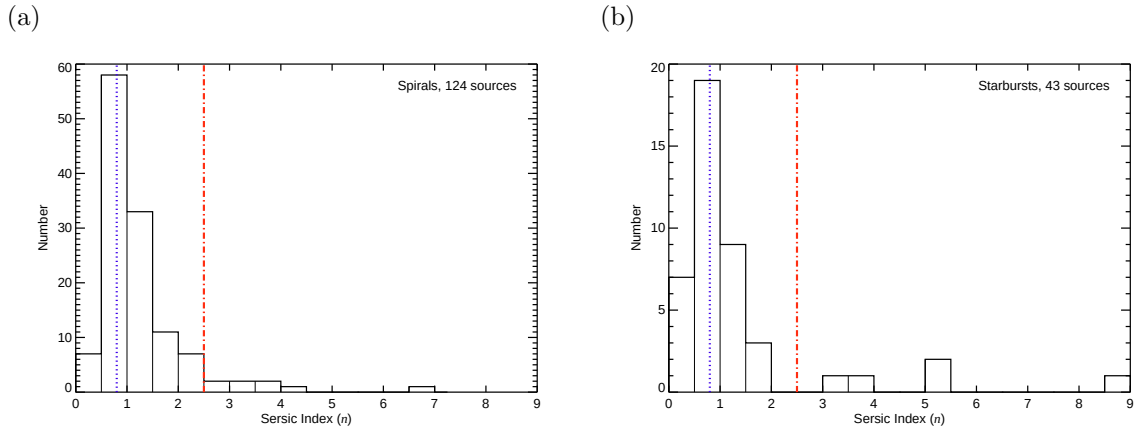

Figure 6.7 *Distributions of Sérsic index in bins of all spiral spectral types (Sbc + Scd) and all starburst spectral types (SB1 + SB2). Dotted line (purple) at $n = 0.8$ represents threshold between clumpy merger/tidal-like morphologies($n < 0.8$) and exponential disks ($0.8 < n < 2.5$). The dot-dash line (orange) at $n = 2.5$ represents the threshold between exponential disks and spheroid-like/centrally concentrated morphologies ($n > 2.5$).*

the distribution plot itself.

Table 6.1 shows the results of K-S tests between the three ST distributions in Figure 6.5. Tests (2) and (3) say that the ST distributions for n-values of exponential disks compared to spheroid-like sources and compact merger/tidal-like sources compared to spheroid-like sources most likely are derived from the same parent distribution, and thus these n ranges do not do a good job differentiating between ST morphological indicators. Test (1) is inconclusive as to whether the compact merger/tidal-like n-values and the exponential disk n-values come from the same parent distribution.

Table 6.2 provides the results of a larger series of K-S tests between the n distributions in Figures 6.6 and 6.7. For all tests that include the E bin, the results have a high significance ($> 3\sigma$) that the distributions are not drawn from the same parent distribution. This could either mean that galaxies with elliptical spectral types can be differentiated by Sérsic index from other types of morphologies, i.e. elliptical STs will always be , or that this test is biased due to small statistics in this bin. However,

Table 6.1. K-S Tests Between ST Distributions

Test #	n Range 1	n Range 2	D	P	CI %	σ
(1)	$n < 0.8$	$0.8 < n < 2.5$	0.164274	0.133748	86.62	1.10
(2)	$0.8 < n < 2.5$	$n > 2.5$	0.226087	0.453962	54.60	0.53
(3)	$n < 0.8$	$n > 2.5$	0.213655	0.554333	44.57	0.42

Table 6.2. K-S Tests Between Sérsic Index Distributions

Test #	ST 1	ST 2	D	P	CI %	σ
(1)	Im	Starbursts	0.136	0.801	19.85	0.25
(2)	Im	Spirals	0.198	0.167	83.31	1.38
(3)	Im	Scd	0.216	0.112	88.76	1.59
(4)	Im	E	0.950	$1.678\text{x}10^{-4}$	99.98	3.76
(5)	Im	Sbc	0.236	0.552	44.80	0.60
(6)	Im	SB1	0.125	0.962	3.80	0.05
(7)	Im	SB2	0.175	0.768	23.20	0.30
(8)	Spirals	Starbursts	0.130	0.607	39.28	0.51
(9)	Spirals	E	0.839	$7.778\text{x}10^{-4}$	99.92	3.35
(10)	Spirals	SB1	0.188	0.434	56.60	0.78
(11)	Spirals	SB2	0.119	0.955	4.48	0.06
(12)	Starbursts	Scd	0.150	0.447	55.25	0.76
(13)	Starbursts	E	0.864	$7.965\text{x}10^{-4}$	99.92	3.35
(14)	Starbursts	Sbc	0.172	0.881	11.93	0.15
(15)	Scd	E	0.855	$5.979\text{x}10^{-4}$	99.94	3.43
(16)	Scd	SB1	0.211	0.309	69.09	1.02
(17)	Scd	SB2	0.217	0.930	6.96	0.09
(18)	Scd	Sbc	0.199	0.660	33.96	0.44
(19)	SB1	SB2	0.202	0.724	27.60	0.35
(20)	SB1	E	0.826	0.003	99.70	2.97
(21)	SB1	Sbc	0.174	0.932	6.78	0.09
(22)	SB2	E	0.900	$9.392\text{x}10^{-4}$	99.91	3.32
(23)	SB2	Sbc	0.186	0.910	9.01	0.11
(24)	Sbc	E	0.714	0.023	97.75	2.28

the K-S test has been shown to work well with small statistical samples. Test (2) between Im and all spiral STs have 83% confidence that these two distributions are not drawn from the same parent distribution, thus their distributions of n can distinguish between these morphological STs. This is confirmed by looking at Figures 6.6(d) and 6.7(a) which show that Im types tend to be distributed about the $n = 0.8$ threshold while spirals are more spread throughout the n exponential disk range. K-S tests performed with the distribution in the starburst bins show that Im, Sbc, Scd, and all combined spiral spectral types are most likely derived from the same parent distribution, and thus the Sérsic index can not distinguish starbursts from other STs. Since starburst galaxies are found in many visual morphologies over all redshifts this result confirms what is found in the literature. In addition, results of K-S test between Im and Sbc distributions and Scd and Sbc distributions indicate that the Sérsic index can not differentiate between these individual ST. For the latter, this is understandable since it may be expected that n values for disk STs will all fall in the exponential disk range. But, for the former it suggests that galaxies with STs Im and Sbc have similar 2D light profiles which is not expected since Sbc galaxies have a well defined disk whereas Im galaxies are irregular galaxies. This could be due to the fact that the sample is UV-selected and therefore it picks Sbc galaxies that are not the classical types.

6.3.2 Sérsic Profiles and Spectral Types as a Function of Redshift

Figure 6.8 shows the Sérsic index as a function of redshift for all sources. The spectral type of each source is designated in the legend by a particular symbol. The colors of the sources signify the magnitudes of their reduced χ^2 values from the GALFIT output. Objects that are red have the largest χ^2 values > 5. Orange sources have $4 < \chi^2 < 5$, green have $3 < \chi^2 < 4$, blue have $2 < \chi^2 < 3$, violet have $1 < \chi^2 < 2$, and black have $\chi^2 < 1$. The dotted line divides the sample below $n < 0.8$ and the dot-dashed line divides the sample above $n > 2.5$. These mark the regions defined by

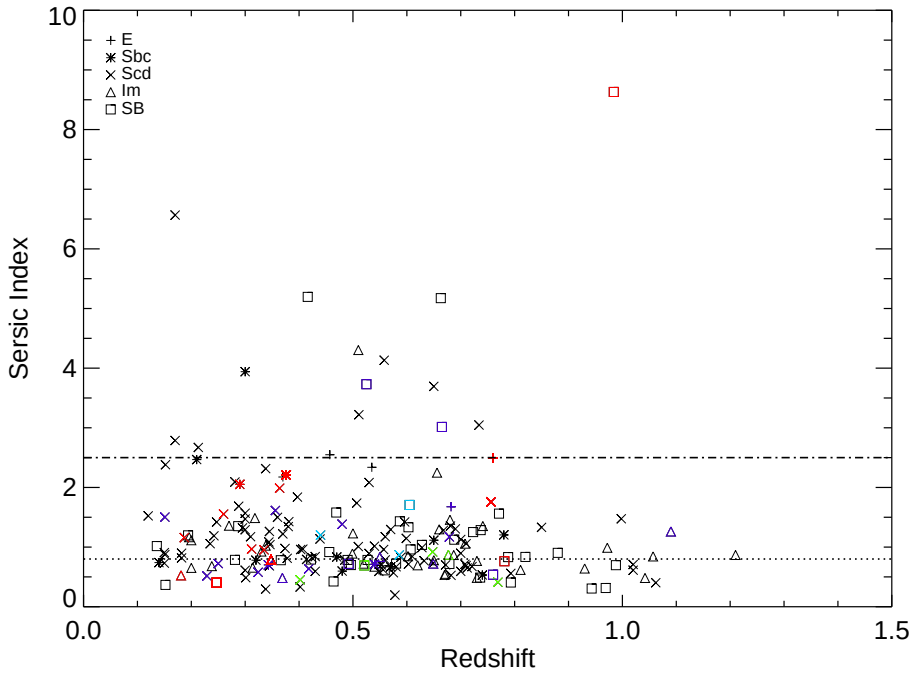

Figure 6.8 *Sérsic index (n) as a function of redshift for all SBC/FUV galaxies selected for this study in GOODS-S. Warmer to cooler colors indicate higher to lower* χ^2 *values. Red:* $\chi^2 > 5$. *Orange:* $4 < \chi^2 < 5$. *Green:* $3 < \chi^2 < 4$. *Blue:* $2 < \chi^2 < 3$. *Violet:* $1 < \chi^2 < 2$. *Black:* $\chi^2 < 1$.

Ravindranath et al. (2006) as light profiles of galaxies undergoing mergers ($0.8 < n$), exponential disk galaxies ($0.8 < n < 2.5$), and bulge systems (n > 2.5). The majority of sources have χ^2 values < 1, and 14 have $\chi^2 > 5$. As discussed in Section 6.2.1, it is not clear if high values of reduced χ^2 are necessarily bad fits to the galaxies. Only ∼7% of the sources have elliptical n indices covering all STs listed. While the majority of sources have n indices indicative of disks they seem to cluster around the dotted line marking the transition to mergers over the entire redshift range covered. Thus the distribution above and below this line seems constant for star-forming galaxies throughout the intermediate-redshift epoch. There is no clear trend in how sources with higher χ^2 Sérsic fits affect this distribution.

In Figures 6.9–6.11 the Sérsic index versus redshift plot has been split between ST to better distinguish if there are any clear correlations or anti-correlations between ST and n values as a function of redshift. Out of the five elliptical galaxies (IDs: 67,

90, 119, 175, 197) in Figure 6.9, four are distributed around the Sérsic disk/elliptical threshold while one has a definite exponential disk n value of 1.67. It is interesting to note that none of these sources have $n = 4$, the classic de Vaucouleurs value for ellipticals. This could suggest that star formation may be quenched once galaxies evolve to extremely elliptical morphologies by intermediate redshifts or that these sources are still in formation. Visually, all of these objects are extremely compact in their rest-frame V-band images, however there are slight signatures of diffuse emission on their outskirts which may cause the lower n value classification, while having an elliptical ST. Thus any hint of diffuse emission may greatly bias the Sérsic classification of the object. These two morphologies were originally defined in the *Revised Shapley-Ames Catalog of Bright Galaxies* (Sandage & Tammann, 1981). Visually Scd's spiral arms are more open and less pronounced compared to Sbc galaxies and they also differ in luminosity class. Many Scd sources are distributed around the merger line, but also fill out the area of between the two cut-offs. This indicates that n values of exponential disks have a decent correlation with Scd disk STs. Star-forming Scds only have a moderate merger population when compared with other STs, most of which are located at $z < 0.9$.

Figure 6.11(a) shows the Sérsic index distribution with redshift for the Im ST. This ST is not necessarily that of peculiar galaxies, such as tadpoles and clump-clusters, but those galaxies more similar to dwarfs like the Magellanic cloud (Coleman et al., 1980). The Sérsic indices of these sources seem well correlated with their ST as all except for two outliers appear to be distributed about the merger cut-off line. In Figure 6.11(b), the n index with redshift for starbursting galaxies is presented. These sources have the potential to be assigned a large variety of n values since they are seen in a mixed bag of types of galaxies at all redshifts (see Section 1.5.1 for a detailed description of starbursts). However, in this plot they also appear to be distributed around the merger line at all detected redshifts, with only 5 sources possessing highly elliptical n indices. This presents evidence that starbursts may be seen in mergers and disks at all redshifts.

6.4 Summary

It is clear that for rest-frame star-forming galaxies at intermediate redshifts there are discrepancies between SED based spectral type morphologies and Sérsic morphologies that are based only on the functional light profiles of these sources. Essentially this is a comparison of the galaxies spectral emissions, which is mapped out in its SED, to its visual appearance. Do these two characteristics correlate, and should they be used for the same purpose of determining morphology?

From the K-S test results presented in this section it has been discussed that Sérsic index best differentiates between Im and a combination of all spiral spectral types (Scd + Sbc). From these n distribution plots it can be seen that Im types are more on the compact merger/tidal-like side while spirals have more of a range of exponential disk profiles. Sérsic index may do a good job at picking out E STs, but give the small

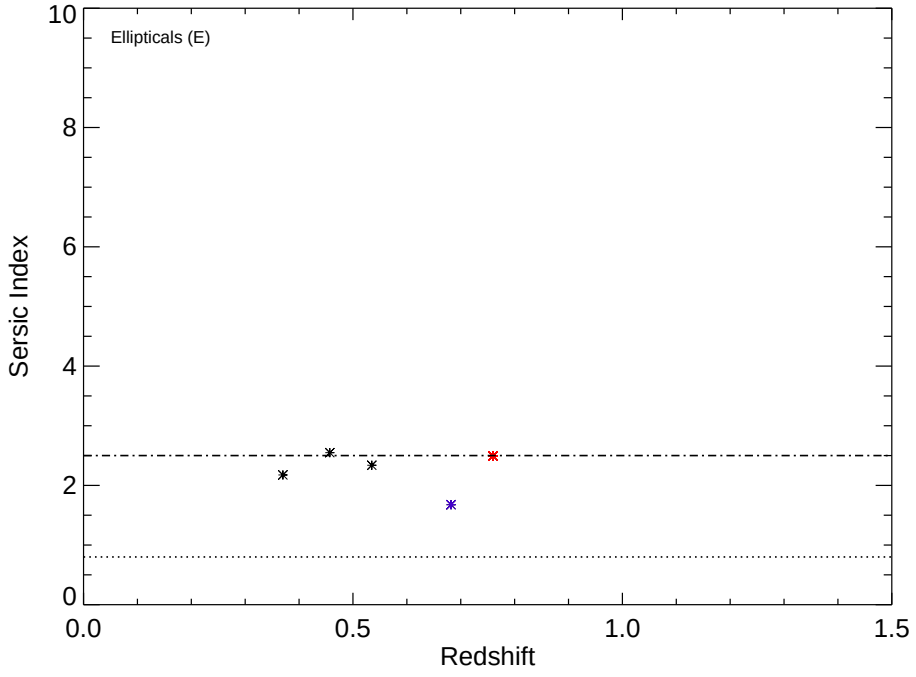

Figure 6.9 *Sérsic index (n) as a function of redshift for all SBC/FUV galaxies with elliptical spectral types. Warmer to cooler colors indicate higher to lower* χ^2 *values. Red:* $\chi^2 > 5$. *Orange:* $4 < \chi^2 < 5$. *Green:* $3 < \chi^2 < 4$. *Blue:* $2 < \chi^2 < 3$. *Violet:* $1 < \chi^2 < 2$. *Black:* $\chi^2 < 1$.

(a)

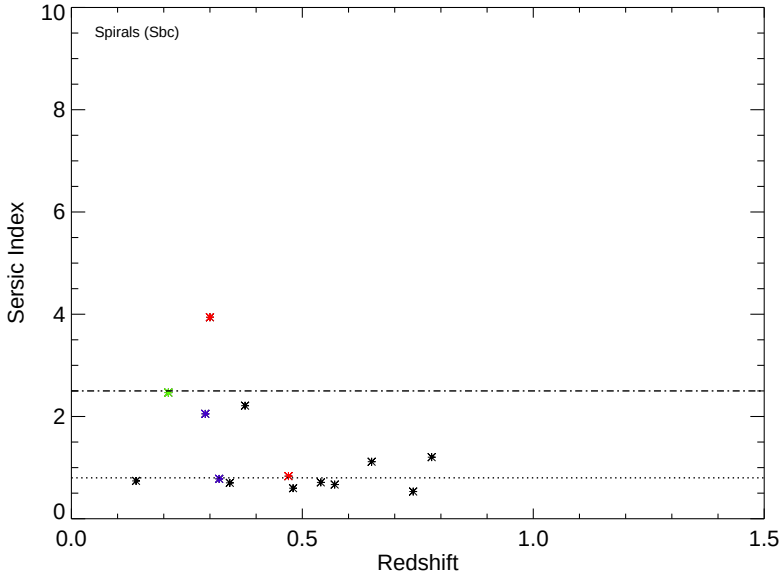

(b)

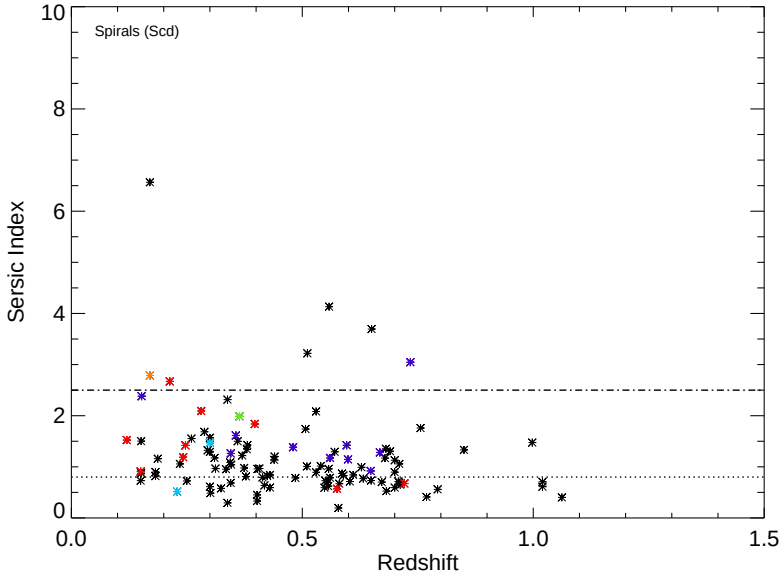

Figure 6.10 *Sérsic index (n) as a function of redshift for all SBC/FUV galaxies with (a) Sbc and (b) Scd spectral types. Warmer to cooler colors indicate higher to lower* χ^2 *values. Red:* $\chi^2 > 5$. *Orange:* $4 < \chi^2 < 5$. *Green:* $3 < \chi^2 < 4$. *Blue:* $2 < \chi^2 < 3$. *Violet:* $1 < \chi^2 < 2$. *Black:* $\chi^2 < 1$.

(a)

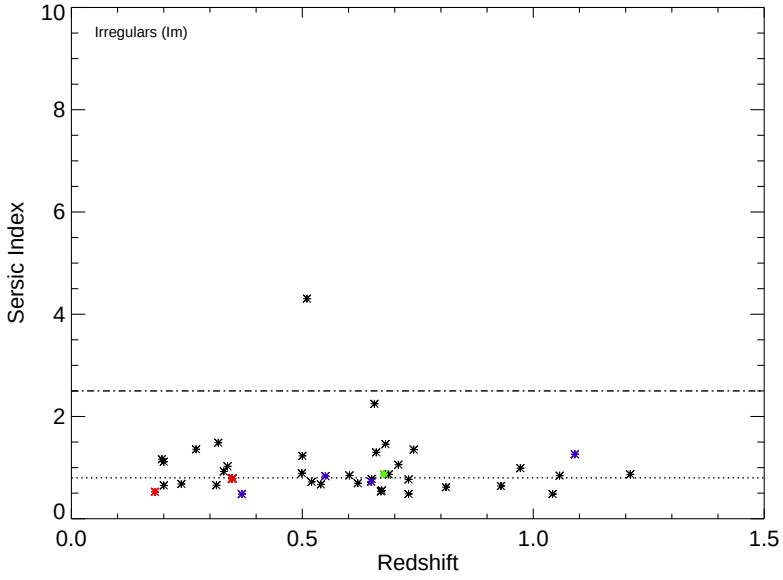

(b)

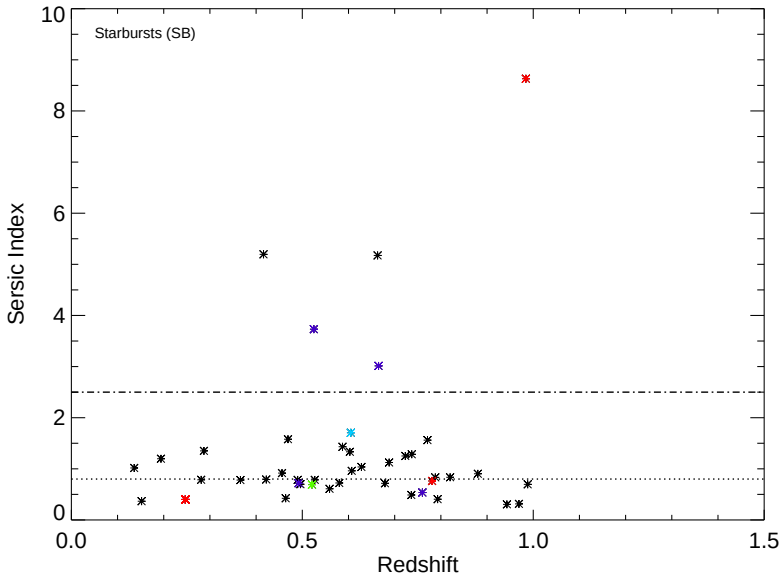

Figure 6.11 *Sérsic index (n) as a function of redshift for all SBC/FUV galaxies with (a) Magellanic irregular and (b) starburst spectral types. Warmer to cooler colors indicate higher to lower* χ^2 *values. Red:* $\chi^2 > 5$. *Orange:* $4 < \chi^2 < 5$. *Green:* $3 < \chi^2 < 4$. *Blue:* $2 < \chi^2 < 3$. *Violet:* $1 < \chi^2 < 2$. *Black:* $\chi^2 < 1$.

statistics of the FUV sample of E types this is difficult to state conclusively. Finally, Sérsic index can not differentiate between starburst and other STs since n is based on light profiles and starbursts occur in galaxies with a wide variety of morphologies as based on light profile. Thus any study needing a morphological indication of starbursts must rely on spectral, rather than quantitative, morphology.

The most striking feature of Figure 6.8 is that the 55% of star-forming galaxies of all STs have Sérsic indices < 1, and $\sim$81% have $n < 1.5$. Only $\sim$12% of the entire sample has $n > 2$ and these are randomly distributed between $n \sim$ 2–8.63 with no clear preference for any particular ST. Thus, it appears that the star formation is primarily occurring in disk or merger rest-frame V-band morphologies over $0.1 <$ z < 1.2. There are 45% of all Im types with $n < 0.8$ and $\sim$50% with $0.8 < n < 1.5$. Starbursts and Sbc STs are a similar case in that 47% and 50%, respectively, have $n < 0.8$, indicating mergers. However, when looking at Scd types only 33% have $n < 0.8$ and the rest highly vary between different Sérsic indices. Therefore, these STs demonstrate that the rest-frame optical light profiles of disks over intermediate redshifts span a wide range of exponential disk n-values although their SEDs do not show much variation during this epoch.

7

Concluding Remarks and Future Work

In order to understand the process of galaxy evolution over cosmic time it is vital to track its primary physical drivers including the formation of stars within galaxies. Studies have shown that the *SFR* density of the universe peaks between z $\sim$ 1–2, after which there is a sharp drop that coincides with the formation of the Hubble sequence of galaxy morphologies that exists in the local universe. Thus, it is vital to make observational connections between these two phenomena in order to piece together the puzzle of our cosmic past. In this thesis a comprehensive multiwavelength study of rest-frame UV detected star-forming galaxies was presented along with its analysis through several different observational approaches in order to achieve a better picture of the role of morphology and star formation in galaxy evolution during the intermediate-redshift epoch ($0.2 < z < 1.5$). This work adds evidence for the formation of the local Hubble sequence and the processes of disk formation over this period of cosmic history.

The first targeted space-based U-band image of the Hubble Ultra Deep Field has been presented here along with U-band catalog of the photometry of these sources measured using the Source Extractor software. A multiwavelength view of this initial intermediate-redshift star-forming sample was obtained by matching this catalog with sources in the large GOODS-S B-band catalog and comparing their morpholo-

gies from rest-frame UV to optical wavelengths. It has been shown that extremely compact sources do not vary in morphology across multiple bands but there is a large disconnect between rest-frame UV morphologies of optically detected spiral sources. This confirms what is also seen at high redshifts. Additionally, the visual morphologies of the intermediate-z sources were assessed with respect to the spectral types of these sources and showed that spiral galaxies dominate the galactic star-forming regime during this epoch as compared to clump-clusters, tadpoles, chains, and doubles which were much more numerous at high redshifts between z $\sim$2–3. This provides observational evidence which suggests clumpy galaxies transform over this epoch into more organized morphologies, as has also been shown in the most recent simulations of clumpy galaxy evolution.

Furthermore, the physical sizes of this sample were measured for both the overall galaxies and for sub-galactic clumps within a selection of clumpy galaxies that have redshifts placing their rest-frame directly within the far-ultraviolet range. This guaranteed that the sub-galactic features measured were pure star-forming regions and allowed for comparisons to high-redshift (z $>$ 2) clumps. Based upon the half-light and Petrosian radii of the U-band sample, no significant evolution in the overall sizes of galaxies is detected over intermediate redshifts in the HUDF field. This result is consistent with what has been observed in larger GOODS samples which include galaxies that do not have any significant star-formation activity. This suggests that both star-forming and quiescent galaxies stop building up their baryonic sizes after the epoch of the peak of *SFR* density in the Universe, suggesting that local disk and ellipticals are the result of secular evolution from that point onwards, perhaps with some minor mergers of small satellites as well. The measurements made here of sub-galactic star-forming clumps in the selected clumpy galaxies from the initial U-band sample have shown that there is an evolution in their sizes from high to intermediate redshifts by a factor of $\sim$2–3.5. It appears that star-formation is occurring in larger and fewer regions within star-forming galaxies at intermediate versus high redshifts. This is a sign that the physical processes driving the evolution of these galaxies made a transition between these two epochs. At intermediate redshifts there may be larger

amounts of gas available to fuel new star formation as a result of previous evolution, or there could be an increase in merger activity at this epoch. However, the later conflicts with the lack of overall galaxy size evolution during this time in cosmic history. These results add important information to the overall picture of galaxy evolution during this time.

This thesis has also presented the latest measurement of the FUV number counts of field galaxies from deep imaging of the GOODS-N and -S fields with HSTs ACS Solar Blind Channel detector. These data cover ∼4 times larger area than the most recent FUV counts measured at similar wavelengths (1614Å) and magnitudes (21–29). The number counts are found to be ∼36% lower than previous HST studies that also probe the faint-end of the FUV counts distribution. This is attributed to the reduction in cosmic variance in these counts due to the inclusion of observations that cover several lines of sight and larger areas than previously sampled by similar studies. The most recent semi-analytic ΛCDM models show good agreement with these counts. Additionally, new measurements of the FUV background light from resolved sources are presented and found to set an upper limit for this measurement of 100 photons s^{-1} sr^{-1} $Å^{-1}$ within the calculated errors.

Taking advantage of the large sample of star-forming FUV detected galaxies used for the number counts measurement, a study of the quantitative Sérsic morphologies of these sources has been performed using the GALFIT software. As compared to the initial morphological study of the HUDF U-band detected sample, these data have the advantage of observing pure rest-frame UV morphologies over the entire redshift range of the FUV sample. Comparing spectral and photometric morphological indicators, STs and Sérsic index (n), it has been shown that Sérsic index does a decent job differentiating between Magellanic irregular (Im) and all spiral STs combined (Sbc + Scd) as well as between ellipticals and all other STs as long as the comparison is not biased by low statistics. However, Sérsic index is not able to differentiate between starburst and other STs since starbursts are found in a wide variety of morphologies at all redshifts. It appears that the star formation is primarily occurring in disk or merger rest-frame V-band morphologies over the entire intermediate-redshift range,

$0.1 < z < 1.2$.

7.1 Future Work

Thanks to the success of the final servicing mission to the Hubble Space Telescope, improved UV observational capabilities have been provided to the astronomical community with the addition of the WFC3 camera and its Ultraviolet-Visible channel (UVIS). Deep UV astronomy has been extended into the next decade and this high resolution camera will reveal finer features in star-forming galaxies at low and high redshifts than ever before. Building upon the work of this thesis, the public WFC3 UV Early Release Science data will be utilized to search for a statistically larger sample of intermediate-redshift clumpy galaxies in the northern area of the GOODS-S field. These sources will be measured in order to further confirm the size evolution of sub-galactic star-forming clumps towards lower redshifts. The CANDELS survey has also planned to obtain deep (< 27.5 magnitudes) UV imaging of a larger area of the GOODS-S field in two WFC3 UV filters. These observations will also provide further data for this future clumps project. In addition, more work is needed in terms of analyzing the luminosities and luminosity densities of these clumps with respect to other star-forming phenomenon at all redshifts. It would be particularly interesting to make a detailed comparison of the stellar populations within sub-galactic clumps to those of local super-star clusters as a means of searching for potential evolution in the initial mass function of galaxies with cosmic time. The study of the large FUV-detected galaxy population in this thesis would also benefit from comparisons with star-forming populations at low redshift, selected from the SDSS, as well as non star-forming populations at intermediate redshifts. By doing so a visual Hubble sequence of star-forming galaxies at low and high redshift can be compared in order to determine what percentage of peculiar morphologies that existed during the intermediate epoch may have transformed into disks at the current epoch. This future work will provide further evidence of evolution in the physics of the formation mechanisms of galaxies.

A

Tables

Table A.1: HUDF U-band Sources

ID #	RA Deg.	Dec Deg.	U_{mag}	FUV_{mag}	B_{mag}	V_{mag}	i_{mag}	z_{mag}	GALEX NUV_{mag}	GALEX FUV_{mag}	z_{phot}	z_{spec}	ST
1	53.1306038	-27.7902641	20.50±0.05	...	22.46±0.02	21.80±0.01	21.16±0.01	21.01±0.01	23.52±0.07	25.69±0.25	0.56	0.6660	5.40
2	53.1376457	-27.7919559	21.70±0.07	26.70±0.17	23.54±0.04	23.13±0.02	22.44±0.02	22.04±0.02	...	...	0.90	0.9980	3.80
3	53.1409721	-27.7966537	22.12±0.05	25.03±0.06	23.54±0.04	22.47±0.01	21.95±0.02	21.69±0.02	24.63±0.24	...	0.38	0.3430	2.60
4	53.1421356	-27.7866974	21.02±0.03	23.60±0.03	22.11±0.01	21.15±0.01	20.73±0.01	20.57±0.01	23.18±0.09	23.90±0.16	0.28	0.2290	3.20
5	53.1445389	-27.7911339	21.58±0.06	...	24.22±0.07	24.16±0.05	24.04±0.09	23.84±0.09	...	...	1.44	1.4380	5.80
6	53.1447334	-27.7854404	20.97±0.03	23.85±0.04	23.20±0.02	22.58±0.01	22.47±0.02	22.51±0.02	23.44±0.07	23.78±0.08	0.19	0.1050	5.80
7	53.1450996	-27.7894268	23.19±0.11	...	24.15±0.06	23.96±0.04	23.58±0.06	23.07±0.05	...	...	1.25	1.3160	3.80
8[c]	53.1470947	-27.7784290	22.46±0.08	...	24.43±0.06	24.28±0.04	23.93±0.06	23.73±0.06	24.91±0.25	...	1.08	...	4.00
9	53.1472054	-27.7884884	22.71±0.08	26.42±0.16	24.52±0.06	23.98±0.03	23.35±0.04	23.19±0.04	...	...	0.65	...	4.00
10	53.1477814	-27.7769451	21.87±0.07	...	24.74±0.06	24.66±0.05	23.90±0.05	23.43±0.04	...	...	1.10	1.0860	3.60
11[c]	53.1478577	-27.7740345	20.58±0.03	...	22.59±0.02	22.33±0.01	21.76±0.02	21.30±0.01	23.03±0.07	...	1.11	1.0880	4.00
12	53.1479225	-27.7996845	23.00±0.10	26.28±0.10	25.06±0.15	24.35±0.07	23.75±0.08	23.58±0.08	...	...	0.56	...	3.80
13	53.1484451	-27.7757874	22.80±0.07	25.67±0.09	24.14±0.04	23.24±0.02	22.68±0.02	22.45±0.02	22.75±0.10	...	0.53	0.5250	5.80
14	53.1485405	-27.7968845	22.48±0.08	...	23.56±0.03	23.52±0.03	23.49±0.05	23.43±0.05	...	...	1.84	...	6.00
15	53.1506119	-27.7715912	20.51±0.04	22.78±0.02	22.24±0.02	21.54±0.01	21.26±0.01	21.19±0.01	22.62±0.07	22.93±0.09	0.17	0.2180	3.40
16	53.1512375	-27.7986679	21.51±0.06	25.94±0.09	24.93±0.08	24.37±0.04	23.64±0.04	23.83±0.09	...	...	0.60	...	3.80
17	53.1516838	-27.7964039	22.93±0.11	...	23.77±0.04	23.49±0.03	23.35±0.05	23.15±0.05	...	...	1.60	...	3.80
18[c]	53.1518784	-27.7754364	21.97±0.05	...	23.76±0.05	23.36±0.03	22.58±0.03	22.17±0.02	22.93±0.06	...	1.13	1.0470	5.80
19[c]	53.1518898	-27.7828751	22.73±0.04	...	24.44±0.04	24.14±0.03	23.45±0.03	23.23±0.03	24.11±0.13	...	0.84	...	3.60
20[c]	53.1518974	-27.7819862	23.17±0.08	...	24.60±0.06	24.32±0.04	23.72±0.05	23.32±0.04	24.19±0.18	...	0.93	0.8940	4.00
21[c]	53.1520653	-27.7747822	21.65±0.03	...	22.64±0.02	22.15±0.01	21.37±0.01	21.16±0.01	22.93±0.06	...	0.75	0.7650	6.00
22[c]	53.1523628	-27.7779751	22.99±0.06	...	24.71±0.08	24.84±0.07	24.96±0.16	24.29±0.10	22.93±0.06	...	1.34	1.4140	5.20
23[c]	53.1528244	-27.7826958	23.57±0.06	28.04±0.25	25.52±0.10	25.21±0.07	24.61±0.09	24.25±0.08	24.11±0.13	...	0.79	0.7650	5.80
24	53.1531296	-27.8120804	21.04±0.04	...	23.85±0.04	23.38±0.02	23.30±0.04	23.33±0.05	24.11±0.12	24.21±0.10	0.14	0.2140	5.60
25	53.1536751	-27.8089409	22.06±0.06	25.93±0.14	24.92±0.08	24.12±0.03	23.80±0.05	23.62±0.05	...	...	0.40	...	3.60
26	53.1546783	-27.7932301	21.29±0.04	23.91±0.03	23.44±0.02	22.86±0.01	22.65±0.02	22.62±0.02	23.18±0.09	23.79±0.09	0.18	...	4.40
27	53.1552696	-27.7695465	21.67±0.06	26.92±0.23	23.65±0.05	23.07±0.02	22.38±0.03	22.13±0.03	...	...	0.77	0.7360	5.60
28	53.1556816	-27.7793083	23.94±0.09	...	23.99±0.05	23.68±0.03	23.28±0.04	23.16±0.04	...	...	1.46	...	4.60

ID #	RA Deg.	Dec Deg.	U_{mag}	FUV_{mag}	B_{mag}	V_{mag}	i_{mag}	z_{mag}	GALEX NUV_{mag}	GALEX FUV_{mag}	z_{phot}	z_{spec}	ST
29[c]	53.1559105	-27.7948895	21.82±0.08	...	24.02±0.04	23.79±0.03	23.43±0.04	23.11±0.04	24.63±0.12	...	1.08	...	4.00
30	53.1564293	-27.8107758	20.45±0.02	24.67±0.08	22.20±0.02	21.62±0.01	20.97±0.01	20.84±0.01	22.90±0.08	...	0.57	0.6650	5.80
31[c]	53.1567726	-27.7955532	22.17±0.07	...	23.79±0.04	23.31±0.02	22.66±0.07	22.08±0.02	23.34±0.15	...	1.12	1.0970	3.60
32	53.1572227	-27.7785568	22.78±0.06	...	24.59±0.05	24.53±0.04	24.41±0.07	23.83±0.05	...	...	1.19	1.3070	5.20
33	53.1578369	-27.7974815	22.27±0.10	...	23.62±0.03	23.26±0.02	22.61±0.03	22.40±0.03	23.34±0.15	...	0.81	...	3.60
34	53.1580658	-27.7692299	21.91±0.02	...	21.18±0.01	20.40±0.00	20.02±0.01	19.91±0.00	23.79±0.14	...	0.06	0.0860	2.40
35	53.1581879	-27.7811279	21.00±0.02	24.16±0.04	22.93±0.02	22.43±0.01	21.93±0.02	21.90±0.02	23.22±0.09	25.13±0.34	0.60	0.6200	4.00
36	53.1583176	-27.7774792	22.76±0.04	...	24.77±0.06	24.79±0.05	24.75±0.09	24.64±0.10	...	...	1.61	...	6.00
37	53.1587791	-27.7705669	22.47±0.04	...	23.90±0.04	23.56±0.03	22.84±0.03	22.45±0.02	23.86±0.22	...	0.98	...	3.80
38	53.1599007	-27.7668762	23.39±0.27	...	24.76±0.07	24.72±0.06	24.02±0.07	23.59±0.06	21.86±0.04	...	0.99	...	3.60
39	53.1604424	-27.7903595	23.03±0.07	...	24.01±0.04	24.01±0.03	23.92±0.05	23.92±0.06	...	...	1.62	...	5.40
40	53.1604996	-27.7863064	23.83±0.07	...	25.50±0.15	25.36±0.11	24.55±0.11	24.28±0.10	...	...	0.96	...	3.80
41	53.1608238	-27.7753963	21.70±0.06	25.76±0.11	23.44±0.04	22.50±0.02	21.67±0.02	21.42±0.02	22.44±0.06	23.02±0.10	0.65	0.6180	3.40
42	53.1613579	-27.7957401	22.93±0.10	...	24.48±0.06	24.06±0.04	23.77±0.06	23.54±0.06	24.62±0.25	25.37±0.24	1.40	...	3.60
43[c]	53.1615295	-27.7676716	22.95±0.10	26.63±0.14	24.96±0.07	24.45±0.04	23.78±0.05	23.70±0.05	21.86±0.00	...	0.75	0.6902	3.80
44[a]	53.1615944	-27.7922535	20.89±0.02	22.52±0.02	21.81±0.01	21.37±0.01	21.02±0.01	20.77±0.01	21.98±0.04	23.08±0.09	1.13	0.4560	6.00
45[c]	53.1619873	-27.7925415	21.63±0.04	...	24.91±0.04	24.16±0.02	23.75±0.03	23.71±0.03	21.97±0.03	22.95±0.04	0.19	...	3.60
46[c]	53.1619949	-27.7739410	21.87±0.06	24.03±0.04	23.58±0.03	22.83±0.02	22.62±0.02	22.53±0.02	22.39±0.04	23.12±0.05	0.31	...	4.20
47[c]	53.1623802	-27.7750893	21.16±0.03	...	22.45±0.02	21.48±0.01	20.97±0.01	20.69±0.01	22.39±0.04	23.12±0.05	0.36	0.4190	3.60
48	53.1624947	-27.7709045	24.45±0.15	...	25.46±0.11	25.10±0.07	24.61±0.07	24.45±0.09	23.86±0.22	...	0.98	...	4.00
49[ac]	53.1628456	-27.7672405	21.16±0.03	26.96±0.25	21.17±0.01	20.94±0.01	20.87±0.01	20.84±0.01	21.96±0.03	...	2.64	1.2160	4.60
50	53.1635971	-27.7935085	21.89±0.07	...	25.17±0.07	25.09±0.05	24.98±0.08	24.47±0.07	...	...	1.21	...	4.20
51	53.1641121	-27.7873249	23.08±0.05	...	24.95±0.07	24.78±0.05	24.32±0.07	24.00±0.06	...	...	1.08	...	6.00
52	53.1648941	-27.7787838	23.27±0.12	...	25.31±0.10	25.34±0.08	24.89±0.11	24.63±0.11	...	...	1.01	...	4.00
53	53.1659012	-27.7815647	22.96±0.05	27.37±0.25	24.67±0.08	24.05±0.04	23.29±0.04	22.79±0.03	...	...	1.06	...	3.40
54	53.1661797	-27.7875214	21.70±0.05	...	23.02±0.03	22.64±0.02	21.98±0.02	21.41±0.01	...	...	1.08	1.1120	3.60
55	53.1662140	-27.7939320	21.99±0.10	...	24.56±0.06	24.54±0.04	23.99±0.05	23.63±0.04	23.48±0.24	...	1.03	...	3.80
56	53.1668854	-27.7976780	22.72±0.06	...	24.37±0.05	24.43±0.04	23.93±0.05	23.75±0.05	24.39±0.23	...	0.93	...	5.80
57[c]	53.1675873	-27.7925072	23.27±0.54	...	23.76±0.04	23.45±0.02	23.01±0.03	22.72±0.03	23.48±0.24	...	1.02	...	4.00
58	53.1679382	-27.7781277	23.47±0.12	26.14±0.09	24.86±0.08	24.05±0.03	23.70±0.05	23.63±0.06	...	...	0.18	...	3.40

ID #	RA Deg.	Dec Deg.	U_{mag}	FUV_{mag}	B_{mag}	V_{mag}	i_{mag}	z_{mag}	GALEX NUV_{mag}	GALEX FUV_{mag}	z_{phot}	z_{spec}	ST
59	53.1680222	-27.7896690	22.09±0.07	25.67±0.09	24.12±0.04	23.57±0.02	22.98±0.03	22.90±0.03	24.86±0.14	...	0.63	0.6190	3.80
60[c]	53.1680603	-27.8074017	22.91±0.11	25.36±0.08	24.77±0.09	23.97±0.04	23.72±0.06	23.70±0.07	24.35±0.17	25.89±0.27	0.34	...	3.60
61	53.1681747	-27.8128967	23.16±0.07	...	24.43±0.06	24.06±0.03	23.35±0.04	23.04±0.03	...	...	0.95	0.9630	3.60
62	53.1699409	-27.7710609	20.59±0.02	24.57±0.07	22.01±0.02	21.18±0.01	20.37±0.01	20.12±0.01	22.94±0.05	25.26±0.20	0.65	...	3.40
63	53.1703148	-27.7852764	23.07±0.09	25.35±0.07	24.86±0.07	24.15±0.03	23.90±0.04	23.67±0.04	...	...	0.31	0.7122	3.80
64[b]	53.1704826	-27.7613792	21.58±0.03	...	22.53±0.01	21.84±0.01	21.49±0.01	21.39±0.01	23.16±0.09	23.91±0.09	0.12	0.1510	3.20
65	53.1705437	-27.8065834	22.75±0.09	...	24.65±0.06	24.67±0.05	24.42±0.07	23.96±0.06	24.74±0.47	...	1.22	1.2440	4.00
66[bc]	53.1706848	-27.7579365	22.42±0.05	...	24.19±0.08	23.56±0.03	22.98±0.03	22.93±0.04	22.77±0.06	23.16±0.10	0.67	...	3.80
67	53.1707726	-27.8046780	23.14±0.09	...	24.06±0.05	23.91±0.04	23.71±0.06	23.63±0.07	25.04±0.24	...	1.84	...	6.00
68[bc]	53.1713791	-27.7574749	20.96±0.02	...	21.69±0.02	21.07±0.01	20.71±0.01	20.63±0.01	22.70±0.04	23.23±0.05	0.08	...	2.80
69[c]	53.1721077	-27.7969379	23.11±0.13	25.25±0.06	24.58±0.08	23.71±0.03	23.42±0.05	23.32±0.05	22.94±0.05	23.50±0.06	0.38	...	3.60
70	53.1721840	-27.8058681	22.21±0.06	...	23.94±0.06	23.83±0.04	23.71±0.08	23.24±0.06	...	...	1.15	1.3180	5.20
71	53.1722603	-27.7651482	22.41±0.08	24.71±0.09	23.34±0.04	22.64±0.02	22.01±0.02	21.88±0.02	23.98±0.16	24.65±0.25	0.56	...	3.40
72[c]	53.1725159	-27.7963371	21.05±0.06	...	23.01±0.03	22.15±0.01	21.85±0.02	21.67±0.02	22.89±0.08	23.27±0.10	0.38	0.3469	3.40
73	53.1726112	-27.7809887	23.37±0.15	...	24.04±0.06	22.90±0.02	22.05±0.02	21.71±0.01	...	...	0.64	...	3.60
74	53.1730003	-27.7779026	22.08±0.06	...	24.06±0.04	23.98±0.03	23.53±0.04	23.20±0.04	24.46±0.26	...	1.03	...	4.00
75[bc]	53.1730042	-27.7590351	20.62±0.02	...	21.51±0.01	20.76±0.01	20.37±0.01	20.26±0.01	22.69±0.06	22.99±0.08	0.12	...	3.20
76	53.1747513	-27.7992420	19.58±0.03	22.16±0.02	21.14±0.01	20.54±0.01	20.25±0.01	20.14±0.01	22.04±0.03	22.30±0.03	0.14	0.1520	3.40
77	53.1761894	-27.7961178	21.25±0.06	...	22.87±0.02	22.36±0.01	21.62±0.01	21.23±0.01	24.28±0.18	...	0.95	0.9961	3.60
78[d]	53.1767311	-27.7996502	22.52±0.12	...	22.53± ...	20.58± ...	18.93± ...	18.32±0.00	...	...	0.70	...	1.33
79	53.1777191	-27.7869625	22.52±0.07	...	25.15±0.08	25.08±0.07	24.52±0.08	24.41±0.08	...	...	0.94	...	4.00
80[b]	53.1778793	-27.7577496	23.50±0.12	...	25.02±0.05	25.05±0.05	24.44±0.06	24.27±0.06	...	...	0.93	...	5.40
81	53.1782227	-27.7830944	21.45±0.05	...	24.03±0.05	23.84±0.03	23.45±0.04	22.92±0.03	...	...	1.05	...	3.60
82	53.1784172	-27.7682304	21.09±0.05	...	22.39±0.02	21.54±0.01	20.68±0.01	20.39±0.01	...	...	0.63	0.6690	3.80
83[b]	53.1799660	-27.7573910	23.55±0.13	...	25.28±0.08	24.76±0.05	24.31±0.06	24.33±0.08	23.12±0.07	...	0.55	...	4.00
84	53.1815453	-27.7879925	22.07±0.04	23.92±0.03	23.94±0.04	23.48±0.02	23.35±0.03	23.44±0.04	...	...	0.15	0.2130	5.60
85	53.1821976	-27.7939968	23.18±0.09	27.63±0.22	25.70±0.09	25.59±0.06	25.07±0.08	24.93±0.08	23.57±0.14	23.55±0.19	0.79	...	5.40
86[d]	53.1826210	-27.7681408	19.44±0.00	...	...	...	...	17.74±0.00	...	...	0.30	...	6.00
87[b]	53.1841164	-27.7559299	22.82±0.13	...	24.89±0.06	24.73±0.05	24.41±0.07	24.33±0.08	...	...	0.68	...	4.40
88	53.1841660	-27.7926407	21.36±0.02	26.12±0.14	22.90±0.02	22.33±0.01	21.65±0.01	21.44±0.01	...	...	0.69	0.7370	5.40

ID #	RA Deg.	Dec Deg.	U_{mag}	FUV_{mag}	B_{mag}	V_{mag}	i_{mag}	z_{mag}	GALEX NUV_{mag}	GALEX FUV_{mag}	z_{phot}	z_{spec}	ST
89	53.1841698	-27.7915535	23.38±0.10	...	24.95±0.14	24.48±0.07	23.77±0.07	23.36±0.06	...	...	1.55	1.2200	3.20
90[b]	53.1855202	-27.7554283	22.01±0.07	...	23.96±0.03	23.07±0.01	22.52±0.02	22.36±0.02	...	...	0.54	...	3.40
91[c]	53.1869583	-27.7910004	19.03±0.01	21.71±0.01	20.21±0.01	19.19±0.00	18.65±0.00	18.44±0.00	21.32±0.02	21.89±0.02	0.15	0.2130	3.80
92[c]	53.1877899	-27.7940979	19.83±0.02	22.25±0.02	21.49±0.01	20.68±0.01	20.45±0.01	20.23±0.01	21.95±0.02	22.49±0.03	0.34	0.3446	3.20
93[b]	53.1879463	-27.7615261	21.55±0.06	...	21.50±0.01	20.61±0.01	20.22±0.01	20.05±0.01	23.59±0.11	24.47±0.21	0.08	...	1.80
94[ac]	53.1879768	-27.7900066	21.10±0.03	24.97±0.06	22.69±0.02	21.53±0.01	20.79±0.01	20.39±0.01	21.32±0.02	21.89±0.02	0.40	0.4380	3.80
95[b]	53.1898384	-27.7588539	20.64±0.03	...	21.84±0.01	21.41±0.01	21.17±0.02	21.17±0.01	22.43±0.04	22.65±0.03	0.12	...	3.60
96[b]	53.1901550	-27.7651958	20.49±0.06	...	22.01±0.02	20.95±0.01	20.52±0.01	20.29±0.01	22.82±0.07	23.69±0.13	0.37	0.3370	2.80

[a]X-ray source (Koekemoer et al. 2004)
[b]Source is outside the HUDF footprint
[c]Confusion in GALEX image
[d]Star
[e]Selected rest-frame UV clumpy galaxy

Table A.2: Properties of Rest-Frame UV Sub-Galactic Clumps

Galaxy ID	Clump	Level[a]	Size	m_U	M_U	f_U	S/N	log L_U[b]	log $L_{U_{bol}}$[c]	log I_U[d]	log $I_{U_{bol}}$[d]
#	#	σ	kpc	AB	AB	10^{-15} erg/cm^2/s/Å		$L_\odot$	$L_\odot$	$L_\odot$ kpc^{-2}	$L_\odot$ kpc^{-2}
(1)	(2)	(3)	(4)	(5)	(6)	(7)	(8)	(9)	(10)	(11)	(12)
1	1	3	5.89	23.23	-21.69	6.35	3.11	11.46	10.74	9.75	9.02
1	2	3	7.44	22.76	-22.15	12.22	3.20	11.65	10.92	9.74	9.01
1	3	3	2.52	23.65	-20.02	11.98	3.25	10.80	10.07	9.68	8.95
2	1	2	5.69	24.20	-21.15	4.17	3.40	11.25	10.52	9.62	8.89
2	2	2	4.00	24.75	-20.41	1.95	3.17	10.95	10.22	9.65	8.92
3	1	3	7.64	22.76	-21.40	4.72	3.30	11.35	10.62	9.39	8.66
3	2	3	3.61	22.62	-20.01	5.57	2.52	10.79	10.07	9.98	9.25
4	1	3	2.10	22.58	-19.88	21.87	2.78	10.74	10.01	9.87	9.14
4	2	3	2.09	22.79	-19.37	2.62	2.40	10.54	9.81	10.09	9.36
4	3	3	3.26	24.18	-20.14	11.02	2.70	10.84	10.12	10.03	9.30
4	4	3	2.15	24.32	-19.65	27.41	3.80	10.65	9.92	9.50	8.77
4	5	3	5.52	24.82	-21.22	1.56	3.57	11.28	10.55	9.47	8.75
4	6	3	4.78	24.06	-19.80	1.88	2.15	10.71	9.98	10.19	9.46
4	7	3	6.56	24.55	-20.27	11.83	2.61	10.90	10.17	9.91	9.18
5	1	4	3.40	23.21	-19.81	4.43	2.51	10.71	9.98	10.24	9.51
5	2	4	4.77	22.50	-20.52	1.77	2.50	10.99	10.27	9.99	9.26
5	3	4	5.09	22.52	-20.49	10.49	2.56	10.99	10.26	9.85	9.12
5	4	4	3.21	23.66	-19.35	6.78	1.86	10.53	9.80	9.49	8.77
5	5	4	2.12	24.49	-18.52	1.67	2.01	10.20	9.47	9.54	8.81
5	6	4	4.45	23.53	-19.48	2.53	1.76	10.58	9.85	9.47	8.74
6	1	5	4.22	22.90	-20.49	1.54	2.13	10.98	10.25	9.52	8.79
6	2	5	3.85	23.28	-20.10	7.47	3.02	10.83	10.10	9.84	9.11
6	3	5	2.43	24.09	-19.29	3.62	2.68	10.51	9.78	9.85	9.13
7	1	4	3.90	22.06	-19.38	6.01	2.73	10.54	9.81	9.77	9.04
8	1	4	3.71	23.35	-20.56	8.43	4.51	11.01	10.28	9.84	9.11
9	1	3	2.84	23.14	-18.71	5.91	3.79	10.27	9.54	9.76	9.03
9	2	3	2.08	24.66	-18.16	2.81	3.94	10.05	9.33	9.84	9.11

Galaxy ID	Clump	Level[a]	Size	m_U	M_U	f_U	S/N	log L_U[b]	log $L_{U_{bol}}$[c]	log I_U[d]	log $I_{U_{bol}}$[d]
#	#	σ	kpc	AB	AB	10^{-15} erg/cm^2/s/Å		$L_\odot$	$L_\odot$	$L_\odot$ kpc^{-2}	$L_\odot$ kpc^{-2}
(1)	(2)	(3)	(4)	(5)	(6)	(7)	(8)	(9)	(10)	(11)	(12)
10	1	3	8.54	21.86	-22.10	9.55	2.57	11.63	10.90	9.48	8.75
10	2	3	2.30	24.17	-19.80	10.87	2.34	10.71	9.98	9.55	8.82
11	1	3	5.50	22.61	-21.55	11.33	3.68	11.41	10.68	9.85	9.12
12	1	4	4.19	23.03	-20.43	9.33	3.73	10.96	10.23	9.69	8.96
13	1	3	6.91	22.08	-21.60	2.59	3.37	11.43	10.70	9.78	9.06
13	2	3	7.13	24.21	-20.77	2.29	3.57	11.10	10.37	10.20	9.47
14	1	3	3.36	22.66	-19.25	1.44	3.74	10.49	9.76	10.00	9.28
15	1	3	7.29	22.53	-21.86	2.91	3.63	11.53	10.80	9.92	9.19
15	2	3	3.06	23.60	-20.79	1.85	3.61	11.10	10.38	10.09	9.36
15	3	3	2.58	24.60	-19.79	18.26	2.97	10.70	9.98	9.90	9.17
16	1	3	3.82	23.82	-20.05	6.22	4.34	10.81	10.08	9.45	8.73
16	2	3	2.42	23.27	-19.24	9.58	4.01	10.48	9.76	9.37	8.64
17	1	3	5.69	22.86	-20.96	4.23	4.05	11.17	10.44	9.46	8.74
18	1	2	7.68	22.86	-20.94	8.75	2.63	11.16	10.44	10.03	9.30
18	2	2	1.88	24.43	-17.83	17.94	2.45	9.92	9.19	10.01	9.28
18	3	2	2.43	24.53	-20.17	2.52	2.58	10.86	10.13	10.10	9.37

[a]Standard deviation above the median background level providing the boundaries at which size and photometry were measured.

[b]Luminosity calculated from the absolute magnitude of the sub-galactic clump and the conversion to standard Johnson-Cousins U-band filter ($3650\lambda_{eff}$).

[c]Bolometric luminosity calculated from the F300W U-band flux of the sub-galactic clump.

[d]The surface brightness is calculated by taking the luminosity over the area of a circle with its radius defined by the size of the clump diameter (column 4).

Bibliography

Abraham, R. G., van den Bergh, S., & Nair, P. 2003, ApJ, 588, 218

Agertz, O., Teyssier, R., & Moore, B. 2009, MNRAS, 397, L64

—. 2011, MNRAS, 410, 1391

Alexander, D. M., et al. 2003, AJ, 126, 539

Arimoto, N., & Yoshii, Y. 1987, A&A, 173, 23

Armand, C., Milliard, B., & Deharveng, J. M. 1994, A&A, 284, 12

Arnouts, S., et al. 2005, ApJ, 619, L43

Arp, H. 1966, ApJS, 14, 1

Barger, A. J., Cowie, L. L., & Wang, W. 2008, ApJ, 689, 687

Barro, G., et al. 2009, A&A, 494, 63

Beckwith, S. V. W., et al. 2006, AJ, 132, 1729

Bertin, E., & Arnouts, S. 1996, A&AS, 117, 393

Bouwens, R. J., Illingworth, G. D., Blakeslee, J. P., & Franx, M. 2006, ApJ, 653, 53

Bouwens, R. J., Illingworth, G. D., Franx, M., & Ford, H. 2007, ApJ, 670, 928

Bouwens, R. J., et al. 2003, ApJ, 595, 589

—. 2009, ApJ, 705, 936

Bowyer, S. 1991, ARA&A, 29, 59

Bridge, C. R., et al. 2010, ApJ, 720, 465

Brown, T. M., Kimble, R. A., Ferguson, H. C., Gardner, J. P., Collins, N. R., & Hill, R. S. 2000, AJ, 120, 1153

Bruzual, G., & Charlot, S. 2003, MNRAS, 344, 1000

Bundy, K., Ellis, R. S., & Conselice, C. J. 2005, ApJ, 625, 621

Bunker, A. J., Stanway, E. R., Ellis, R. S., & McMahon, R. G. 2004, MNRAS, 355, 374

Burgarella, D., Le Floc'h, E., Takeuchi, T. T., Huang, J. S., Buat, V., Rieke, G. H., & Tyler, K. D. 2007, MNRAS, 380, 986

Capak, P. L. 2004, PhD thesis, UNIVERSITY OF HAWAI'I

Cardelli, J. A., Clayton, G. C., & Mathis, J. S. 1989, ApJ, 345, 245

Carruthers, G. R., Opal, C. B., & Heckathorn, H. M. 1978, ApJ, 225, 346

Casertano, S., et al. 2000, AJ, 120, 2747

Charlot, S., & Fall, S. M. 2000, ApJ, 539, 718

Chiosi, C., Bressan, A., & Fagotto, F. 1994, Mem. Soc. Astron. Italiana, 65, 881

Code, A. D., Houck, T. E., McNall, J. F., Bless, R. C., & Lillie, C. F. 1970, ApJ, 161, 377

Coe, D., Benítez, N., Sánchez, S. F., Jee, M., Bouwens, R., & Ford, H. 2006, AJ, 132, 926

Cohen, J. G., Hogg, D. W., Blandford, R., Cowie, L. L., Hu, E., Songaila, A., Shopbell, P., & Richberg, K. 2000, ApJ, 538, 29

Coleman, G. D., Wu, C., & Weedman, D. W. 1980, ApJS, 43, 393

Combes, F. 2010, ArXiv e-prints

Connolly, A. J., Szalay, A. S., Dickinson, M., Subbarao, M. U., & Brunner, R. J. 1997, ApJ, 486, L11+

Conselice, C. J., Bershady, M. A., Dickinson, M., & Papovich, C. 2003, AJ, 126, 1183

Conselice, C. J., et al. 2004, ApJ, 600, L139

Cowie, L. L., Barger, A. J., & Trouille, L. 2009, ApJ, 692, 1476

Cowie, L. L., & Hu, E. M. 1998, AJ, 115, 1319

Cowie, L. L., Hu, E. M., & Songaila, A. 1995, AJ, 110, 1576

Cowie, L. L., Songaila, A., Hu, E. M., & Cohen, J. G. 1996, AJ, 112, 839

Dahlen, T., Mobasher, B., Dickinson, M., Ferguson, H. C., Giavalisco, M., Kretchmer, C., & Ravindranath, S. 2007, ApJ, 654, 172

Dahlen, T., Mobasher, B., Somerville, R. S., Moustakas, L. A., Dickinson, M., Ferguson, H. C., & Giavalisco, M. 2005, ApJ, 631, 126

Dahlen, T., et al. 2010, ApJ, 724, 425

de Mello, D. F., Dahlen, T., Gardner, J. P., & Grogin, N. A. 2006a, AJ, 132, 2014

de Mello, D. F., Wadadekar, Y., Dahlen, T., Casertano, S., & Gardner, J. P. 2006b, AJ, 131, 216

de Vaucouleurs, G. 1959, Handbuch der Physik, 53, 275

Deharveng, J., Sasseen, T. P., Buat, V., Bowyer, S., Lampton, M., & Wu, X. 1994, A&A, 289, 715

Delgado-Serrano, R., Hammer, F., Yang, Y. B., Puech, M., Flores, H., & Rodrigues, M. 2010, A&A, 509, A78+

Dickinson, M., et al. 2000, ApJ, 531, 624

Eggen, O. J., Lynden-Bell, D., & Sandage, A. R. 1962, ApJ, 136, 748

Ellis, R. S., Abraham, R. G., Brinchmann, J., & Menanteau, F. 2000, Astronomy and Geophysics, 41, 020000

Elmegreen, B. G., Bournaud, F., & Elmegreen, D. M. 2008, ApJ, 688, 67

Elmegreen, B. G., & Elmegreen, D. M. 2005, ApJ, 627, 632

Elmegreen, D. M., Elmegreen, B. G., & Hirst, A. C. 2004, ApJ, 604, L21

Elmegreen, D. M., Elmegreen, B. G., Marcus, M. T., Shahinyan, K., Yau, A., & Petersen, M. 2009, ApJ, 701, 306

Elmegreen, D. M., Elmegreen, B. G., Ravindranath, S., & Coe, D. A. 2007, ApJ, 658, 763

Epinat, B., Amram, P., Balkowski, C., & Marcelin, M. 2010, MNRAS, 401, 2113

Evans, I. N., et al. 2010, ApJS, 189, 37

Ferguson, H. C., et al. 2004, ApJ, 600, L107

Fix, J. D., Craven, J. D., & Frank, L. A. 1989, ApJ, 345, 203

Förster Schreiber, N. M., et al. 2006, ApJ, 645, 1062

—. 2009, ApJ, 706, 1364

Gardner, J. P., Brown, T. M., & Ferguson, H. C. 2000a, ApJ, 542, L79

Gardner, J. P., et al. 2000b, AJ, 119, 486

Gehrels, N. 1986, ApJ, 303, 336

Genzel, R., et al. 2008, ApJ, 687, 59

Giacconi, R., et al. 2001, ApJ, 551, 624

Giavalisco, M. 2002, ARA&A, 40, 579

Giavalisco, M., Steidel, C. C., & Macchetto, F. D. 1996, ApJ, 470, 189

Giavalisco, M., et al. 2004, ApJ, 600, L93

Gilmore, R. C., Madau, P., Primack, J. R., Somerville, R. S., & Haardt, F. 2009, MNRAS, 399, 1694

Gordon, K. D., et al. 2004, ApJS, 154, 215

Hammer, D., Hornschemeier, A. E., Mobasher, B., Miller, N., Smith, R., Arnouts, S., Milliard, B., & Jenkins, L. 2010, ApJS, 190, 43

Heckman, T. M., et al. 2005, ApJ, 619, L35

Henry, R. C. 1991, ARA&A, 29, 89

Henry, R. C., & Murthy, J. 1993, ApJ, 418, L17+

Holmberg, E. 1958, Meddelanden fran Lunds Astronomiska Observatorium Serie II, 136, 1

Hoopes, C. G., et al. 2007, ApJS, 173, 441

Hopkins, A. M. 2004, ApJ, 615, 209

Hopkins, A. M., & Beacom, J. F. 2006, ApJ, 651, 142

Hoversten, E. A., et al. 2009, ApJ, 705, 1462

Hu, E. M., & McMahon, R. G. 1996, Nature, 382, 231

Hubble, E. P. 1936, Realm of the Nebulae, ed. Hubble, E. P.

Iglesias-Páramo, J., Buat, V., Donas, J., Boselli, A., & Milliard, B. 2004, A&A, 419, 109

Ishizuki, S., Kawabe, R., Ishiguro, M., Okumura, S. K., & Morita, K. 1990, Nature, 344, 224

Iwata, I., Ohta, K., Tamura, N., Ando, M., Wada, S., Watanabe, C., Akiyama, M., & Aoki, K. 2003, PASJ, 55, 415

Iwata, I., et al. 2009, ApJ, 692, 1287

Kassin, S. A., et al. 2007, ApJ, 660, L35

Kauffmann, G., & Charlot, S. 1998, MNRAS, 294, 705

Kennicutt, Jr., R. C. 1998, ApJ, 498, 541

Kinney, A. L., Calzetti, D., Bohlin, R. C., McQuade, K., Storchi-Bergmann, T., & Schmitt, H. R. 1996, ApJ, 467, 38

Kitzbichler, M. G., & White, S. D. M. 2007, MNRAS, 376, 2

Koekemoer, A. M., Fruchter, A. S., Hook, R. N., & Hack, W. 2002, in The 2002 HST Calibration Workshop : Hubble after the Installation of the ACS and the NICMOS Cooling System, ed. S. Arribas, A. Koekemoer, & B. Whitmore, 337–+

Koekemoer, A. M., et al. 2004, ApJ, 600, L123

Komatsu, E., et al. 2009, ApJS, 180, 330

Koo, D. C. 1998, Highlights of Astronomy, 11, 468

Kormendy, J., & Kennicutt, Jr., R. C. 2004, ARA&A, 42, 603

Krumholz, M. R., & Dekel, A. 2010, MNRAS, 406, 112

Kulkarni, V. P., Woodgate, B. E., York, D. G., Thatte, D. G., Meiring, J., Palunas, P., & Wassell, E. 2006, ApJ, 636, 30

Larson, R. B. 1974, MNRAS, 166, 585

Larson, R. B., & Tinsley, B. M. 1978, ApJ, 219, 46

Law, D. R., Steidel, C. C., Erb, D. K., Pettini, M., Reddy, N. A., Shapley, A. E., Adelberger, K. L., & Simenc, D. J. 2007, ApJ, 656, 1

Le Fèvre, O., et al. 2004, A&A, 417, 839

Lee, D., et al. 2006, ApJ, 644, L181

Lehmer, B. D., et al. 2008, ApJ, 681, 1163

Lilly, S. J., Le Fevre, O., Hammer, F., & Crampton, D. 1996, ApJ, 460, L1+

Liu, C. T., & Kennicutt, Jr., R. C. 1995a, ApJS, 100, 325

—. 1995b, ApJ, 450, 547

Lotz, J. M., Madau, P., Giavalisco, M., Primack, J., & Ferguson, H. C. 2006, ApJ, 636, 592

Lotz, J. M., Primack, J., & Madau, P. 2004, AJ, 128, 163

Madau, P. 1995, ApJ, 441, 18

Madau, P., Ferguson, H. C., Dickinson, M. E., Giavalisco, M., Steidel, C. C., & Fruchter, A. 1996, MNRAS, 283, 1388

Madau, P., & Pozzetti, L. 2000, MNRAS, 312, L9

Martin, C., & Bowyer, S. 1989, ApJ, 338, 677

Martin, D. C., et al. 2005, ApJ, 619, L1

McLure, R. J., Cirasuolo, M., Dunlop, J. S., Foucaud, S., & Almaini, O. 2009, MNRAS, 395, 2196

Milliard, B., Donas, J., Laget, M., Armand, C., & Vuillemin, A. 1992, A&A, 257, 24

Moller, P., & Warren, S. J. 1993, A&A, 270, 43

Morgan, W. W. 1958, PASP, 70, 364

—. 1959a, PASP, 71, 394

—. 1959b, PASP, 71, 92

Morgan, W. W., & Osterbrock, D. E. 1969, AJ, 74, 515

Morrissey, P., et al. 2007, ApJS, 173, 682

Mouri, H., & Taniguchi, Y. 2006, A&A, 459, 371

Moustakas, L. A., et al. 2004, ApJ, 600, L131

Murthy, J. 2009, Ap&SS, 320, 21

Murthy, J., Hall, D., Earl, M., Henry, R. C., & Holberg, J. B. 1999, ApJ, 522, 904

Murthy, J., Henry, R. C., & Sujatha, N. V. 2010, ApJ, 724, 1389

Murthy, J., & Sahnow, D. J. 2004, ApJ, 615, 315

Nandra, K., Mushotzky, R. F., Arnaud, K., Steidel, C. C., Adelberger, K. L., Gardner, J. P., Teplitz, H. I., & Windhorst, R. A. 2002, ApJ, 576, 625

Neistein, E., van den Bosch, F. C., & Dekel, A. 2006, MNRAS, 372, 933

Nilsson, K. K., & Møller, P. 2009, A&A, 508, L21

Nonino, M., et al. 2009, ApJS, 183, 244

Oesch, P. A., et al. 2010, ApJ, 709, L21

O'Neil, K., Bothun, G. D., & Schombert, J. 1998, AJ, 116, 2776

Overzier, R. A., Heckman, T. M., Schiminovich, D., Basu-Zych, A., Gonçalves, T., Martin, D. C., & Rich, R. M. 2010, ApJ, 710, 979

Overzier, R. A., et al. 2008, ApJ, 677, 37

—. 2009, ApJ, 706, 203

Page, T., & Carruthers, G. R. 1981, ApJ, 248, 906

Papovich, C., Dickinson, M., & Ferguson, H. C. 2001, ApJ, 559, 620

Papovich, C., Dickinson, M., Giavalisco, M., Conselice, C. J., & Ferguson, H. C. 2005, ApJ, 631, 101

Papovich, C., Giavalisco, M., Dickinson, M., Conselice, C. J., & Ferguson, H. C. 2003, ApJ, 598, 827

Peng, C. Y., Ho, L. C., Impey, C. D., & Rix, H. 2002, AJ, 124, 266

—. 2010, AJ, 139, 2097

Petrosian, V. 1976, ApJ, 209, L1

Pettini, M., Shapley, A. E., Steidel, C. C., Cuby, J., Dickinson, M., Moorwood, A. F. M., Adelberger, K. L., & Giavalisco, M. 2001, ApJ, 554, 981

Petty, S. M., de Mello, D. F., Gallagher, J. S., Gardner, J. P., Lotz, J. M., Matt Mountain, C., & Smith, L. J. 2009, AJ, 138, 362

Pimbblet, K. A., & Drinkwater, M. J. 2004, MNRAS, 347, 137

Ravindranath, S., et al. 2004, ApJ, 604, L9

—. 2006, ApJ, 652, 963

Reddy, N. A., & Steidel, C. C. 2009, ApJ, 692, 778

Rix, H., et al. 2004, ApJS, 152, 163

Roberts, M. S., & Haynes, M. P. 1994, ARA&A, 32, 115

Sandage, A., & Tammann, G. A. 1981, A revised Shapley-Ames Catalog of bright galaxies, ed. Sandage, A. & Tammann, G. A.

Saracco, P., Giallongo, E., Cristiani, S., D'Odorico, S., Fontana, A., Iovino, A., Poli, F., & Vanzella, E. 2001, A&A, 375, 1

Sasseen, T. P., Lampton, M., Bowyer, S., & Wu, X. 1995, ApJ, 447, 630

Savaglio, S., et al. 2005, ApJ, 635, 260

Schiminovich, D., Friedman, P. G., Martin, C., & Morrissey, P. F. 2001, ApJ, 563, L161

Schinnerer, E., Böker, T., & Meier, D. S. 2003, ApJ, 591, L115

Schlegel, D. J., Finkbeiner, D. P., & Davis, M. 1998, ApJ, 500, 525

Scoville, N., et al. 2007, ApJS, 172, 1

Seon, K., et al. 2010, ArXiv e-prints

Shapley, A. E., Erb, D. K., Pettini, M., Steidel, C. C., & Adelberger, K. L. 2004, ApJ, 612, 108

Shen, S., Mo, H. J., White, S. D. M., Blanton, M. R., Kauffmann, G., Voges, W., Brinkmann, J., & Csabai, I. 2003, MNRAS, 343, 978

Siana, B., et al. 2007, ApJ, 668, 62

—. 2010, ApJ, 723, 241

Somerville, R. S., Gilmore, R. C., Primack, J. R., & Dominguez, A. 2011, *In Preparation*

Somerville, R. S., Hopkins, P. F., Cox, T. J., Robertson, B. E., & Hernquist, L. 2008, MNRAS, 391, 481

Somerville, R. S., Lee, K., Ferguson, H. C., Gardner, J. P., Moustakas, L. A., & Giavalisco, M. 2004, ApJ, 600, L171

Somerville, R. S., & Primack, J. R. 1999, MNRAS, 310, 1087

Somerville, R. S., Primack, J. R., & Faber, S. M. 2001, MNRAS, 320, 504

Stanway, E. R., Bunker, A. J., & McMahon, R. G. 2003, MNRAS, 342, 439

Steidel, C. C., Adelberger, K. L., Giavalisco, M., Dickinson, M., & Pettini, M. 1999, ApJ, 519, 1

Steidel, C. C., Adelberger, K. L., Shapley, A. E., Pettini, M., Dickinson, M., & Giavalisco, M. 2003, ApJ, 592, 728

Steidel, C. C., Giavalisco, M., Dickinson, M., & Adelberger, K. L. 1996, AJ, 112, 352

Steidel, C. C., & Hamilton, D. 1992, AJ, 104, 941

—. 1993, AJ, 105, 2017

Steidel, C. C., Pettini, M., & Hamilton, D. 1995, AJ, 110, 2519

Straughn, A. N., Cohen, S. H., Ryan, R. E., Hathi, N. P., Windhorst, R. A., & Jansen, R. A. 2006, ApJ, 639, 724

Sujatha, N. V., Murthy, J., Shalima, P., & Henry, R. C. 2007, ApJ, 665, 363

Sujatha, N. V., Shalima, P., Murthy, J., & Henry, R. C. 2005, ApJ, 633, 257

Teplitz, H. I., et al. 2006, AJ, 132, 853

Trenti, M., & Stiavelli, M. 2008, ApJ, 676, 767

van den Bergh, S. 1960a, ApJ, 131, 558

—. 1960b, ApJ, 131, 215

van den Bergh, S., Abraham, R. G., Ellis, R. S., Tanvir, N. R., Santiago, B. X., & Glazebrook, K. G. 1996, AJ, 112, 359

Vorontsov-Vel'Yaminov, B. A. 1959, in Atlas and catalog of interacting galaxies (1959), 0–+

Vorontsov-Velyaminov, B. A. 1977, A&AS, 28, 1

Vorontsov-Vel'Yaminov, B. A., & Arkhipova, V. P. 1963, Trudy Gosudarstvennogo Astronomicheskogo Instituta, 33, 1

—. 1968, Trudy Gosudarstvennogo Astronomicheskogo Instituta, 38, 1

—. 1974, Trudy Gosudarstvennogo Astronomicheskogo Instituta, 1

Vorontsov-Vel'Yaminov, B. A., & Krasnogorskaya, A. A. 1962, Trudy Gosudarstvennogo Astronomicheskogo Instituta, 32, 207

Wadadekar, Y., Casertano, S., & de Mello, D. 2006, AJ, 132, 1023

Williams, R. E., et al. 1996, AJ, 112, 1335

Witt, A. N., Friedmann, B. C., & Sasseen, T. P. 1997, ApJ, 481, 809

Witt, A. N., & Petersohn, J. K. 1994, in Astronomical Society of the Pacific Conference Series, Vol. 58, The First Symposium on the Infrared Cirrus and Diffuse Interstellar Clouds, ed. R. M. Cutri & W. B. Latter, 91–+

Wyder, T. K., et al. 2005, ApJ, 619, L15

Xu, C. K., et al. 2005, ApJ, 619, L11

Yasuda, N., et al. 2001, AJ, 122, 1104

Yoshii, Y., & Peterson, B. A. 1994, ApJ, 436, 551